Capability Demonstration of 3D CdZnTe Gamma-Ray Detectors in Extreme Environments

by

Sara A. Abraham

A dissertation submitted in partial fulfillment
of the requirements for the degree of
Doctor of Philosophy
(Nuclear Engineering and Radiological Sciences)
in the University of Michigan
2023

Doctoral Committee:

Professor Zhong He, Chair
Professor Fei Gao
Professor Igor Jovanovic
Professor Susan Lepri

Sara Abraham
abrasara@umich.edu
ORCID iD: 0000-0001-9316-3420

Acknowledgments

First and foremost, I would like to thank Professor Zhong He. I am extremely grateful that he decided to take me on as a student. Professor He has been the best advisor anyone could ask for. He has challenged me yet so kindly supported me. He expertly guided me but gave me freedom to grow on my own. He has pushed me to be a better researcher and to always strive to answer "why?". None of this work would have been possible without Professor He, the technology he cultivated over decades, the hard work of his past students, and current Orion group members. I am also thankful for the many opportunities he has provided me outside of research as well, such as various group activities, my first experience skiing, and travel abroad to conferences.

The advice of Dr. Yuefeng Zhu has been essential to this work. There are many times when I was confused but his expertise quickly pushed me back on track. I would like to thank Dr. Matthew Petryk for taking the time to teach me and for thoughtful discussions on research. I am grateful to Dr. Daniel Shy for welcoming me into the group and being a mentor to me even when I decided not to join him on the "imaging team". Many of the interesting topics studied were motivated by the work and suggestions of Dr. Jiawei Xia. Peter Hotvedt provided very helpful feedback on a couple chapters of this thesis. James Berry provided much advice (and entertaining anecdotes) over the years. I would like to thank all Orion group members that I have worked with—it has been a joy to spend time with so many intelligent and interesting people.

I would like to thank my thesis committee members Professor Fei Gao, Professor Igor Jovanovic, and Professor Susan Lepri for challenging me and providing feedback on my work.

For the high-altitude balloon flight project, I would like to thank the group at Los Alamos National Laboratory: Dr. Suzanne Nowicki, Dr. Alexei Klimenko, Dr. Peter Bloser, Benigno Sandoval, Sara Lanctot, Jonathan Deming, and George Duran. Suzanne and Alexei accompanied me on many trips to the lovely Santa Rosa and Fort Sumner,

making sure our detector had a chance to fly. Benigno and Sara provided much support and advice. George Duran's high-level skill in crafting high-voltage boards amazed me and was critical to the success of the operation of the detector in near-vacuum. From the University of Michigan side, Dr. Yuefeng Zhu provided guidance on major design considerations, Dr. Matthew Petryk helped greatly with troubleshooting issues, James Berry was very helpful during the construction of Orion Eagle, and Damon Anderson helped with software updates.

I would like to thank H3D Inc. for lending me detectors to experiment with and for discussions on CZT temperature sensitivity.

I am thankful for my family. My parents for financial support and providing an example of a strong work ethic. Bret for his advice and intellectual conversations. Jenni for home-cooked meals, a place to stay, and many fun times. Matt for having me as an older sister. Additionally, this work is in memory of late extended family members who would have been very proud to see me earn my PhD.

Last but far from least, I would like to thank my fiancé Jack Kuchta for his limitless unwavering support. He has always seen the best in me, never minded how late I worked (and often joined me), introduced me to Laufey, and willingly proofread this entire thesis. Not only has he helped me reach this point, but he has made it all more enjoyable.

The majority of this work was supported by the Defense Threat Reduction Agency under Contract # HDTRA1-18-C-0073. Any opinions, findings and conclusions or recommendations expressed in this material are those of the author(s) and do not necessarily reflect the views of the Defense Threat Reduction Agency.

The CZT high-altitude balloon flight project was supported by the National Nuclear Security Administration Defense Office of Nuclear Nonproliferation Research and Development. Los Alamos National Laboratory is operated by Triad National Security, LLC, for the National Nuclear Security Administration of the U.S. Department of Energy.

Table of Contents

List of Figures

List of Tables

List of Acronyms

ASIC Application-Specific Integrated Circuit.

CAR Cathode-to-Anode Ratio.

CSBF Columbia Scientific Balloon Facility.

FET Field-Effect Transistor.

FPGA Field-Programmable Gate Array.

FWHM Full Width at Half Maximum.

HPGe High-Purity Germanium.

PCA Principal Component Analysis.

SRF System Response Function.

TRL Technology Readiness Level.

Abstract

Over the last two decades, advancements in 3D CdZnTe (CZT) gamma-ray detector technology have led to its use in a wide range of applications such as nuclear non-proliferation, defense, nuclear power, environmental monitoring, and medical imaging. Excellent energy resolution, 4π Compton imaging capability, and room-temperature operation make 3D CZT detectors ideal for the characterization and localization of radioactive sources. This work aims to explore the feasibility of operating CZT in tougher, more challenging environments and in applications with stringent requirements in terms of the detector's stability, power consumption, weight, and size. The effects of extreme ambient temperatures, neutron damage, and space-like environments were investigated to help benchmark and advance the capabilities of CZT detector technology.

Removal of the temperature regulation used to keep CZT at room temperature can help minimize the power consumption, weight, and size of detector systems. However, this also introduces some technical challenges, as the behavior of CZT detector systems at extreme temperatures is not yet well understood. Temperature-related effects were studied for several 3D CZT detectors for ambient temperatures ranging from 20°C to 60°C. Detector leakage increases exponentially with temperature, making operation more difficult. Nonetheless, it was demonstrated that with minor adjustments, not only is operation at 60°C possible, but satisfactory energy resolution can still be achieved without any active temperature regulation. Issues were identified and resolved to help minimize the degradation of performance at high temperatures. Also, decreased efficiency for some detectors below room temperature (-10°C) was investigated and found to be related to distortions in the detector's internal electric field. The effect of annealing on CZT detectors with and without neutron damage was explored. Annealing at 80°C improved the quality of several detectors without previous radiation damage and helped recover performance for CZT detectors exposed to a neutron fluence of 10^{12} neutrons/cm^2. Nonuniformity of neutron damage and unexpected instability over time

was further studied.

Gamma-ray detectors can be useful in space applications such as planetary science; however, the 3D CZT technology developed at the University of Michigan has not yet been space-qualified. In collaboration with Los Alamos National Laboratory, a 3D CZT detector system, Orion Eagle, was specifically designed for near-space environments. Orion Eagle was integrated into a gondola and launched on a NASA high-altitude balloon. The detector measured atmospheric radiation during a 9 h flight reaching a float altitude of nearly 40 km, verifying the effectiveness of the design and demonstrating the first successful operation of this technology in a near-space environment. The dataset obtained from the flight was used to develop algorithms to discriminate between gamma-ray and cosmic ray interactions in the CZT detector. Overall, this work led to a greater understanding of fundamentals related to 3D CZT performance in extreme environments, which is essential for guiding the development of future detector systems.

Chapter 1

Background

1.1 Radiation Detectors

Ionizing radiation exists in many forms and places. It is in space, in the Earth's atmosphere, in the ground, and even within the human body. While this sounds alarming, it is simply the nature of the world. Ionizing radiation interactions, that are usually invisible to the human eye, are constantly occurring. Therefore, it goes without reason that scientists have sought out ways to detect radiation to help see where and what exactly it is.

There are two key factors important for choosing a material for radiation detection. Firstly, the radiation must interact with the material in some form with a reasonable frequency. The probability of interaction (i.e. cross-section) depends heavily on the radiation type and energy, as well as the properties of the material. In this work, gamma-ray detection is the focus. Gamma rays are more likely to interact with dense, high atomic number (high-Z) materials. The three primary interactions that gamma rays undergo in matter are photoelectric absorption, Compton scattering, and pair production. The interaction cross-sections depend heavily on the gamma-ray energy and the Z of the material. Photoelectric absorption dominates at low energies, Compton scattering occurs at mid-range energies, and pair production is dominant at high energies, as shown in Fig. 1.1. Increasing the detector size can also help improve the likelihood of interactions (i.e. increase efficiency).

Second, the energy deposited from a radiation interaction must be measurable by some means. In scintillators, the energy is converted to light which is then detected by

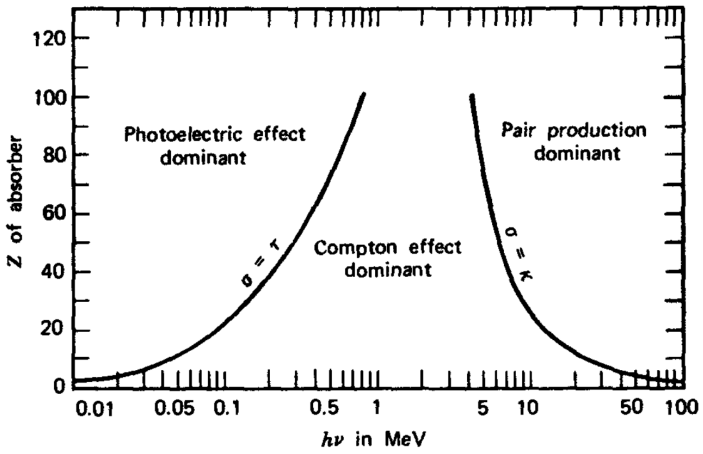

Figure 1.1: The relative importance of the three types of gamma ray interactions as a function of the incoming gamma ray energy and Z of the detection material. [1]

a light detector such as photo-multiplier tube or silicon-photomultiplier. In gas detectors (i.e. ionization chamber, proportional counter, Geiger-Mueller tubes), the energy from radiation interactions leads to ionization of the gas and an electronic charge that can be measured by a meter.

In this work, semiconductors are used for radiation detection. In a semiconductor crystal, atoms are arranged in a periodic lattice. For this lattice, there are set energy bands that define where electrons can exist (energetically) within the solid. The defining feature of a semiconductor is the band gap, or the separation between the energy of the lowest conduction band and the energy of the highest valence band, as shown in Fig. 1.2. The band gap is a forbidden region where electrons cannot exist. However, if an electron in the valence band gains enough energy (e.g. through an ionizing radiation interaction), it can be elevated above the band gap to the conduction band. In the conduction band, the electron is free to migrate through the crystal. The excitation of the electron will also lead to a vacancy in the valence band, which is referred to as a hole. This hole will also be free to drift, and has the opposite charge of an electron. The excited electron and corresponding hole are called an electron-hole pair. The number of electron-hole pairs created is proportional to the energy deposited in the interaction, and they are often referred to as charge carriers. If left undisturbed, the electron and hole will eventually recombine. Therefore, for semiconductor radiation detectors, an external electric field

is applied to cause the charges to drift in opposite directions. The drift of the charge carriers can induce signals on electrodes that are attached to the semiconductor, which can be measured (or read out) by the connected circuitry (also referred to as the readout electronics). The induction of signals can be described by the Shockley-Ramo theorem, which is described in detail in Section 1.3. The electronic signal can be used to derive information about the radiation interaction.

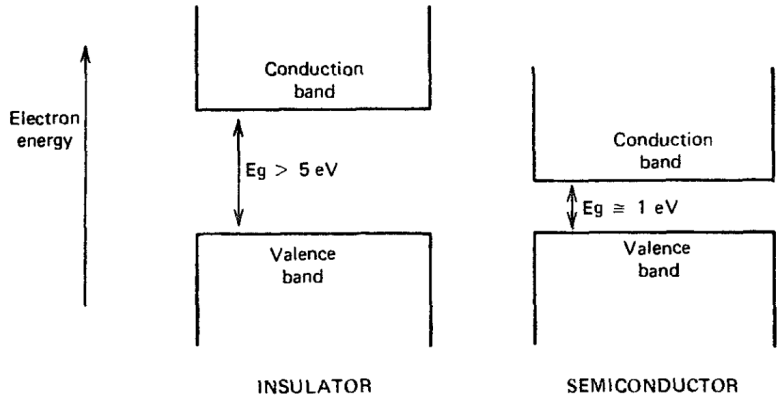

Figure 1.2: Simplified band structure of electron energies of a semiconductor compared to an insulator. [1]

The main motivation for using semiconductor detectors is that they can achieve better energy resolution than other common radiation detectors, and thus it is easier to identify the energy of incoming radiation. In terms of the Full Width at Half Maximum (FWHM) of the 662 keV peak from ^{137}Cs, semiconductors can achieve below 1% energy resolution whereas the next-best energy resolution is achieved by scintillators, which typically are at 3% or worse. There are many factors that can influence energy resolution. However, the main reason that higher energy resolution is possible for semiconductor detectors than for scintillators is statistical fluctuation in the generation of information carriers (charge carriers in semiconductors, photoelectrons in scintillators) [1]. In scintillators, far fewer information carriers are generated in a radiation interaction compared to the number generated in semiconductors, resulting in a limitation in the best energy resolution that can be achieved.

1.2 Cadmium Zinc Telluride

Cadmium zinc telluride (CdZnTe or CZT) is a wide band gap semiconductor commonly used for gamma-ray detection. The key feature of CZT is that the band gap is relatively large (or "wide") for a semiconductor material. At any finite temperature, there is a probability that an electron in the valence band can be excited to the conduction band (just as described for a radiation interaction) due to the thermal energy. The probability increases with temperature and with smaller band gaps, as less energy is needed to reach the conduction band. Because CZT has a wide band gap (1.6 eV), the probability of thermal generation is low enough that room-temperature operation is possible, which is why CZT is also commonly referred to as a "room-temperature" semiconductor. When the band gap of a semiconductor is narrow, such as in the case of germanium (0.67 eV), cryogenic cooling is required to prevent the thermal generation of charge carriers. It can take hours to cool germanium detectors before they can be used, whereas CZT can be ready in minutes. Additionally, CZT has a higher average atomic number (Z=$\sim$50) than other common semiconductor detector materials such as germanium (Z=32) and silicon (Z=14). This means that the same volume of CZT will have greater stopping power and higher sensitivity to incoming gamma rays. Since CZT does not require a cyrostat, it can be used to create compact, hand-held detectors that are convenient for users.

Some shortcomings of CZT lay in the charge collection properties. Since the charge is proportional to the energy deposited, it would be ideal if all charge could be fully collected, as there would be less statistical uncertainty in the measured energy and higher energy resolution. In CZT, the mobility-lifetime product ($\mu\tau$) of electrons is orders of magnitude larger than the $\mu\tau$ of the holes. The holes typically do not travel very far before being trapped, so their contribution to the total signal induced is negligible. To account for this, an electrode geometry resulting in sensitivity to only electrons is desirable, which will be discussed in Section 1.4. Electrons will travel much farther than holes; however, some charge will be trapped along the drift due to material defects (i.e. electron charge trapping). If the trapped electrons do not detrap within the event timing window, the charge is essentially lost, and the energy deposited will be underestimated. The amount of electron charge trapping will depend on the distance of the electron drift path, so the energy loss is variable and will lead to spread in the full-energy peak

toward the low-energy side (called low-energy tails). If electrons are detrapped within the event timing window, it will affect timing characteristics of the induced signal. Therefore, techniques to correct for nonuniform charge loss are needed to improve the energy resolution.

1.3 Shockley-Ramo Theorem

To understand the output signal from a semiconductor radiation detector, it is important to understand how signals are induced by the free moving charge. Traditionally, the signal induced Q on an electrode by a free moving charge q can be calculated by integrating the normal component of the electric field E over the surface S as described by the equation

$$Q = \oint \varepsilon E \cdot dS \tag{1.1}$$

where ε is the dielectric constant. This requires calculating the instantaneous E for each location along the path of q which can be very tedious and incredibly difficult for complex electrode geometries.

Shockley [2] and Ramo [3] introduced a more simplistic way to calculate the induced signal, the Shockley-Ramo Theorem. While this theorem was originally used to describe induced charge on an electrode in a vacuum tube, it is also valid in the presence of stationary space charge [4] [5] and can be extended to include cases in which a magnetic field is present and when the device medium is heterogeneous [6]. Therefore, it can be applied to semiconductor radiation detectors.

According to the Shockley-Ramo Theorem, the charge Q and current i induced on an electrode by a moving point charge q are

$$Q = -q\varphi_0(\vec{x}) \tag{1.2}$$

and

$$i = q\vec{v}\overrightarrow{E_0}(\vec{x}) \tag{1.3}$$

where $\vec{v}$ is the instantaneous velocity of charge q, φ_0 is the weighting potential, and $\overrightarrow{E_0}(\vec{x})$ is the weighting field. The weighting potential and the weighting field are the

electrostatic potential and field that would theoretically exist at q's instantaneous position $\vec{x}$ under the following conditions:

- The electrode of interest is at unit potential (1V).
- All other electrodes are a zero potential (0V).
- All charges are removed.

The weighting field is independent of the actual operating electric field, and instead depends only on the geometry of the electrodes and the uniformity of the detector's dielectric constant. This greatly reduces the amount of computation required, as only one field (the weighting field) needs to be calculated (per electrode of interest), and can be used to find the signal for a variety of radiation interactions. The Shockley-Ramo Theorem assumes that magnetic effects are negligible and the electric field propagates instantaneously. The change in the induced charge ΔQ_L on an electrode of interest L due to the movement of charge q from an initial position $\vec{x}_i$ to a final position $\vec{x}_f$ is

$$\Delta Q_L = \int_{\vec{x}_i}^{\vec{x}_f} q\vec{E_0} \cdot d\vec{x} = -q[\varphi_0(\vec{x}_f) - \varphi_0(\vec{x}_i)] \tag{1.4}$$

and therefore only depends on the initial and final position and the value of q.

In a semiconductor detector, a radiation interaction will create a large number of electron-hole pairs or "clouds" of charge carriers. For simplicity, this cloud is often approximated as a point charge. However, in cases where the electron cloud is very large (e.g. high-energy interactions), this may not be a good approximation. In any case, the cloud could be divided into many point charges. Based on the superposition principle, the signal induced by the whole cloud is equal to the summation of the induced signal from each point charge in the cloud.

For many semiconductor detector systems, the output of the readout electronics is the value of ΔQ_L, which is considered the amplitude of the radiation event. However, for the detector system discussed in this work, $Q_L(t)$ or how Q_L changes with time is recorded as well, in the form of a digitized waveform. $Q_L(t)$ depends on the drift trajectory, and the drift trajectory is determined by the actual operating electric field. Therefore, the waveform $Q_L(t)$ contains a wealth of information. It provides details of

the charge cloud drift which can be used to determine properties of the detector material such as the uniformity and degree of trapping.

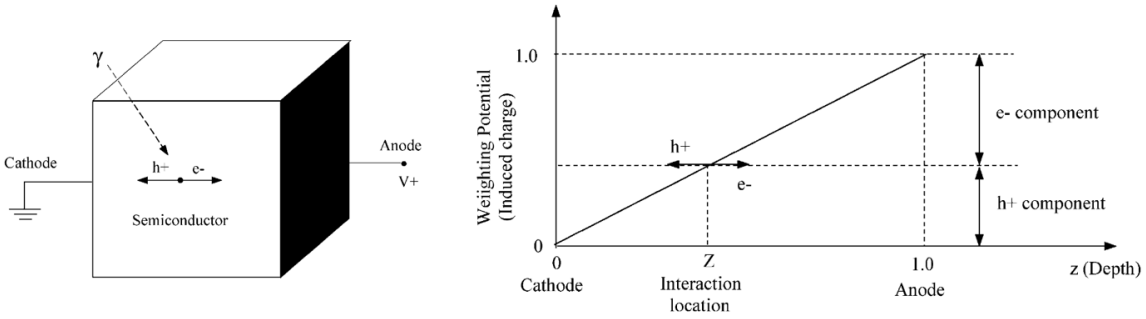

Figure 1.3: The planar electrode configuration and the corresponding weighting potential. [6]

1.4 Single-Polarity Charge Sensing

Since the electrode configuration determines the signals induced, it is a very important feature in the design of any semiconductor detector. The most simple configuration consists of a semiconductor material sandwiched between two planar electrodes, called the cathode and the anode. If the potential of the anode is set to 1V and the cathode set to 0V, the weighting potential is a linear function of depth (z) as shown in Fig. 1.3. When a bias is applied, holes drift to the cathode, and electrons drift to the anode. The total charge induced ΔQ on the anode is described as the sum of two components, the movement of n holes (from Z to 0) and the movement of n electrons (from Z to 1). Based on Eq. 1.4, the charge induced is

$$\Delta Q = -(ne_0)(0 - Z) + (ne_0)(1 - Z) = ne_0 \tag{1.5}$$

where e_0 is the charge of an electron and Z the depth of interaction. In this case, the induced charge (pulse amplitude) is always proportional to the number of electron-hole pairs generated and the energy deposited in the radiation interaction, regardless of where the interaction occurs inside the detector. The issue with this configuration is that it relies on all charge carriers reaching the electrodes, which is typically not the case due

to charge trapping or poorer mobility of one of the charge carriers. For example, the holes in CZT are practically immobile, so the induced charge would instead be

$$\Delta Q \approx (ne_0)(1 - Z) \tag{1.6}$$

which depends on the depth of interaction, and no spectroscopic information can be gained from the pulse amplitude if gamma rays interact with all depths randomly. Therefore, this motivated the need for an electrode configuration capable of providing sensitivity to just one type of charge carrier type, i.e. capable of single-polarity charge sensing.

For semiconductors, there are many ways to achieve single-polarity charge sensing such as using a Frisch-grid style configuration [7] [8], coplanar grid [9] [10] [11], and pixelated anodes [12]. Fig 1.4 shows a few examples of single-polarity charge sensing CZT detector designs. In these designs, the weighting potential for the anode (or the difference in weighting potential between collecting and non-collecting anodes in coplanar grid detectors) is close to zero in the bulk and rises to 1V only in close proximity to the collecting anode. The output anode signal should be approximately proportional to the number of electrons collected, and approximately independent of the movement of holes in the bulk. It is desirable for the rise of the weighting potential to be as steep as possible. For pixelated detectors, the "small pixel effect" helps produce a desirable weighting potential for anode pixels, as shown in Fig. 1.5.

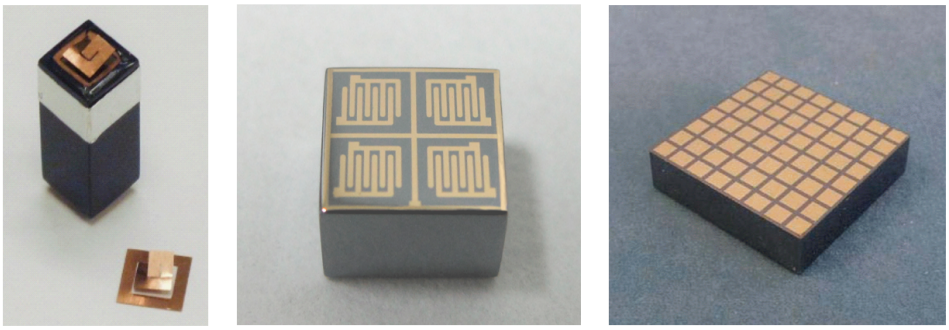

Figure 1.4: Examples of CZT detectors with different electrode designs: (left) virtual Frisch-grid [8], (center) coplanar quad-grid [13], and (right) pixelated [14].

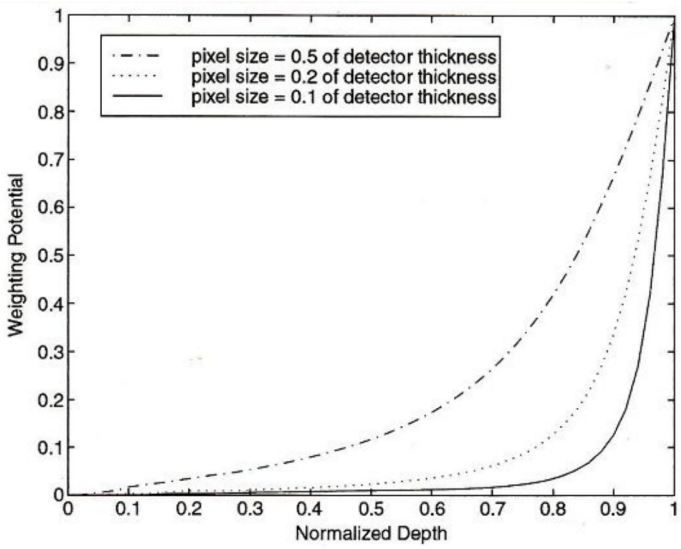

Figure 1.5: The weighting potential for three different pixel electrode sizes. The small pixel effect is enhanced by using smaller pixel sizes relative to detector thickness. [1]

1.5 3D CZT

This work will focus on 3D position-sensitive, pixelated CZT detectors developed by the University of Michigan over the last two decades. These detectors will be referred to as "3D CZT" or just "CZT" in the rest of this work. Advancements in electrode designs, crystal growth and fabrication, low-noise front-end readout electronics, and radiation event reconstruction algorithms have led to a drastic improvement in the performance of 3D CZT. In 1999, energy resolution near ∼2% FWHM at 662 keV was achieved for 1 cm^3 cubic CZT [12]. In the past several years, large-volume 2×2×1.5 cm^3 CZT with energy resolution consistently below 0.5% have become standard in research detector systems [15]. Additionally, these detectors have very good 3D position resolution, which allows them to be used for Compton imaging and coded aperture imaging. Since cyrogenics are not required, compact, hand-held 3D CZT detectors are useful for performing high-resolution spectroscopy and imaging for in-field source localization and characterization. 3D CZT technology was commercialized in 2011 and has since gained widespread use in a broad range of terrestrial applications (i.e. national security, nuclear power plants, medical imaging, defense, nuclear nonproliferation), replacing High-Purity Germanium (HPGe) in many instances.

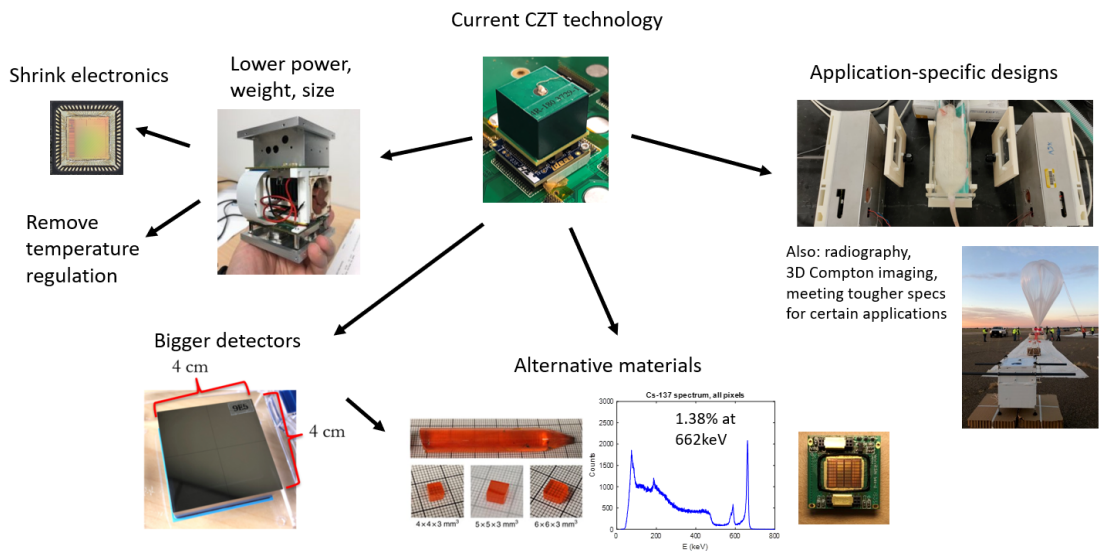

Figure 1.6: The multiple directions of current/future research related to 3D CZT technology. Figures courtesy of Orion group members.

1.6 Recent Advancements and Future of 3D CZT

Though 3D CZT technology has already made significant progress over the past two decades, there are still many interesting research opportunities and ways in which the detector systems can be further advanced. Fig. 1.6 shows a few possible directions of research. In the first "branch", there is the desire to even further reduce the size, weight, and power consumption of the detector system. One way to do this is to remove temperature regulation which has traditionally been used to cool electronics to keep the system at room temperature. Detector calibrations are temperature sensitive, so temperature corrections must be made when the temperature is left to float without temperature regulation. This subject was recently studied by Xia [16], and many commercial systems no longer use temperature regulation. Another way to greatly reduce the size and power consumption is to shrink the readout electronics. During the past few years, there have been efforts to develop an Application-Specific Integrated Circuit (ASIC) for digital signal processing, as discussed by Chen [17] and Petryk [18].

The second branch indicates that while it is desirable to physically minimize the detector system, this refers to everything outside of the CZT detector material, as bigger detectors are of interest. For many years, large-volume $2\times2\times1.5$ cm^3 CZT has

been the standard detector size used at University of Michigan. However, there have been efforts to move towards even bigger "larger"-volume $4\times4\times1.5$ cm^3 CZT detectors. Since 2018, the group at the University of Michigan has received many larger-volume $4\times4\times1.5$ cm^3 CZT detectors and Zhu and He demonstrated that they are a feasible option for practical applications [19]. This is currently the world's largest single-crystal volume CZT. Bigger single-volume detectors are advantageous as opposed to arrays of detectors due to higher efficiency, reduced artifacts in coded aperture imaging, potential for better spectroscopic performance, and potential for reduced cost [19]. They may also be beneficial for high-energy event reconstruction due to improvements in the uniformity of the weighting potential [20].

While thinking about detector size, it should also be considered that the future of 3D CZT may not actually include CZT. Other room-temperature semiconductors are of interest (third branch in Fig. 1.6), as they have the potential for easier growth (i.e. larger sizes, cheaper), higher stopping power, or perhaps better performance at high temperatures due to lower leakage. TlBr has been studied for many years [21] [22] [23]. Recently, promising energy resolution has been demonstrated for perovskites (a relatively new material for radiation detection) [18]. However, these alternative materials often suffer from issues with stability and are not close to being as mature as CZT. Though another material could eventually replace CZT, the readout electronics and event reconstructions algorithms developed for CZT would still be instrumental in those detector systems.

The final branch is labeled "application-specific designs". For many years, CZT research was focused on improving the energy and position resolution, which helped enable its use in a broad range of applications. Now that near-HPGe energy resolution and very good angular resolution have been achieved, new areas of research focuses on other aspects of the detector system in order to improve the benefits and convenience of CZT in its current applications and to push forward into even more challenging applications. This has already been touched on in the other branches. Reducing the detector's size, weight, and power will make for better hand-held detectors (in current applications) but could also lead to its use in space applications (a new application). Same applies for the larger-volume CZT. Other projects in progress are specifically tailored to medical applications, radiography, and source search (i.e. 3D Compton imaging). In general, there is a desire to advance 3D CZT technology to meet tougher specs for certain applications. The work discussed in this thesis is most relevant to this final branch.

1.7 Overview of Thesis

The research in this thesis falls under three topics that are interconnected: temperature effects, radiation damage, and space applications. The current 3D CZT technology and analysis techniques used throughout this work are described in Chapter 2.

The effect of temperature on 3D CZT is discussed in Chapters 3, 4, and 5. Understanding the effect of temperature is very important because detector stability and performance over a broad range of temperatures is important to meet military specs and International Atomic Energy Agency (IAEA) standards.

Chapter 3 serves as an introduction to the effect of high temperatures. In this chapter, results from annealing several CZT detectors at 80°C are discussed. Changes in CZT material properties and the electrode contacts observed after annealing (in room-temperature measurements) are discussed in detail to help build upon previous work.

In Chapter 4, the focus moves to the operation of 3D CZT at high temperatures, as measurements taken at ambient temperatures ranging from 20°C to 60°C are described. Prior to this study, the highest temperature of operation recorded for pixelated CZT was 40°C [20], so these experiments entered a territory not previously explored. Issues that arise during high-temperature operation are identified, and potential solutions to improve performance are discussed. Again, changes in CZT material properties and the electrode contacts are observed due to high temperature. This time, the observations were made over the course of the experiment, with some changes even happening within a single calibration measurement.

Next, the temperature discussion pivots to the effect of low temperatures on CZT in Chapter 5. In contrast to the high temperature experiments where reducing the degradation in energy resolution is the primary goal, the leakage at low temperatures is so low that very high energy resolution can be achieved. However, issues arise below 0°C, when the photopeak efficiency drops significantly for some CZT detectors. This is an elusive problem that was identified only in the past few years and has not yet been explained despite significant efforts, prompting a detailed analysis on the matter in Chapter 5.

In Chapter 6, the topic of the thesis switches to radiation damage. The effects of temperature are still pertinent here because annealing at 80°C is used to help recover the performance of two CZT detectors exposed to a neutron fluence of 10^{12} neutrons/cm^2.

This large fluence could represent an "emergency" scenario or long term use near a nuclear reactor or in space. While energy resolution could be almost fully recovered, unexpected degradation in performance over time under bias was observed and analyzed. Such behavior has not been reported in other CZT radiation damage studies. Also discussed in Chapter 6 is a quick experiment to address a mystery regarding non-uniformity of damage observed in pixelated CZT detectors.

For the rest of the thesis, the focus is on developments for space applications, though it could be argued that the whole thesis falls under this category, as an understanding of temperature effects and radiation damage is critical for space applications as well. In Chapter 7, the feasibility of using CZT in space is approached from an engineering perspective as a custom 3D CZT detector system is designed, built, and tested on a high-altitude balloon flight. This was the very first time this technology has been successfully operated in a near-space environment. Chapter 7 introduces the concept of charged particle detection in 3D CZT, and Chapter 8 expands on this by exploring charged particle discrimination techniques using data from the balloon flight.

Lastly, in Chapter 9, the contributions of this work are summarized and future work is proposed.

Chapter 2

Overview of Digital 3D CZT Detector System

2.1 Hardware

2.1.1 Pixelated CZT Detector

Various CZT detectors were used throughout this work. Each detector has an array of 11×11 anode pixels surrounded by a guard ring anode, with a single planar cathode on the opposite side. The detector design is illustrated in Fig. 2.1. The width (W) and length (L) are equal, and the height (H) is typically the smallest dimension, and is referred to as the "thickness" of the detector. Two different sizes of detectors were used: 2×2×1.5 cm^3 and 2.2×2.2×1.0 cm^3. The pixel side of the CZT material is bonded to a carrier board that has three rows of pins on the opposite side. Each anode (pixels and guard ring) is connected to a pin so that the induced signal can be read out via an ASIC. During operation, a negative bias is applied to the cathode surface to create a strong electric field. The standard voltage applied is 2,000V per centimeter of detector thickness. The detectors used in this work were sourced from two different CZT vendors, either Redlen Technologies or Kromek (formerly eV Products).

2.1.2 ASIC

The VAD UM v2.2 ASIC, which was developed in collaboration between the University of Michigan and Integrated Detector Electronics AS (Ideas), was used for signal

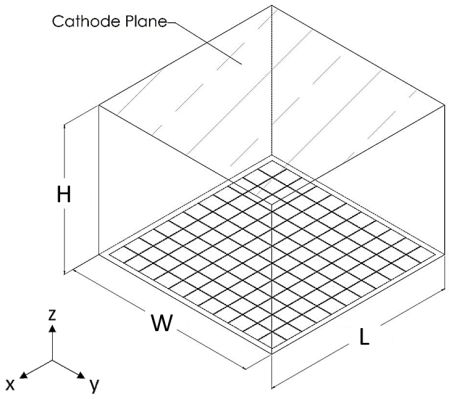

Figure 2.1: Schematic of the 3D CZT electrode design consisting of 11×11 anode pixels and a single cathode plane.

readout in this study. The ASIC has 130 inputs or "channels". Each channel has a charge-sensitive pre-amplifier, 160-cell analog sample-and-hold pipeline, a shaper, and a comparator. It can provide readout of waveforms of up to 130 channels simultaneously, depending on the selected readout mode. In trigger-only readout mode, only anode pixels with waveforms reaching an adjustable low-energy threshold are read out in addition to the cathode and guard ring anode signals. In trigger+4 mode and trigger+8 mode, either 4 or 8 of the anode pixels that neighbor the triggered anode are also readout, respectively. In this work, radiation events will be referred to by the number of anode pixels triggered (i.e. single-pixel events for events triggering one anode pixel). In forced readout mode, all channels are read out which can be useful for gauging the baseline noise. The ASIC has an adjustable dynamic range from 700 keV to 9 MeV per channel. The sampling rate is adjustable as well, but 40 MHz was used in this work. The ASIC provides these many capabilities with low noise (∼1.5 keV), and in a very small package (as shown in Fig. 2.2). More information on the ASIC design can be found in Ref. [24].

2.1.3 Test Systems

At the University of Michigan, there is a variety of detector systems that were built in-house and used in conjunction with the ASIC. In this work, both the VAD UM Bench-top system and the Single Board system were used. Both systems use the same back-end electronics, but the front-end varies as shown in Fig. 2.3. In the Bench-top system front-end, the VAD UM v2.2 Ideas ASIC (v7038 or v7081) can be plugged in (and

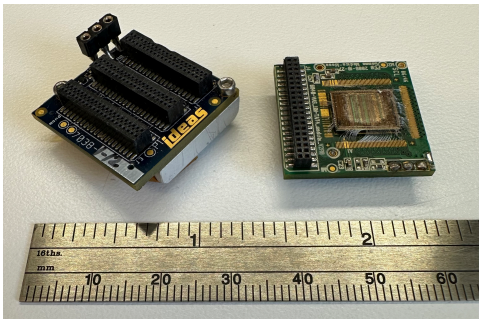

Figure 2.2: The VAD UM v2.2 Ideas ASIC module that the CZT can be plugged into (left) and the flip-side with the chip exposed (right).

CZT is plugged into the ASIC), and it can accommodate up to a 3×3 array of detectors. There are Peltier coolers below each ASIC slot and a fan to keep the ASICs cool. In the Single Board system, a VAD UM v2.2 Ideas ASIC is already incorporated into the front-end board, and a single CZT detector can be directly plugged in. Below the ASIC is a heat sink, and there is no form of active temperature regulation in this design. External power supplies are needed to power both systems and provide high-voltage power. There is also the "Orion" generation of detector systems that were developed after the VAD UM systems. The designs of Orion-α, Orion-β, and Orion-γ are described in Ref. [18]. They have an on-board high-voltage generator and only require a 12V input. All of the detector systems communicate over Ethernet with an in-house data acquisition program installed on a desktop computer or laptop. Through this communication, the user can control the ASIC settings and receive data. For calibration measurements, the data is saved for post-processing analysis. If a calibration is already on file, spectroscopy and imaging can be performed on-the-fly.

In general, the Orion systems are much more compact than the older VAD UM systems. Orion-α, Orion-β, and Orion-γ are all nearly identical. They each have a 3×3 array of 2×2×1.5 cm^3 detectors contained in a package much smaller than the VAD UM Benchtop system. The newest generation of detector systems (H3DD UM) are even more compact. The H3DD UM Array houses a 2×2 array of 2×2×1.5 cm^3 detectors (or alternatively one 4×4×1.5 cm^3 detector). All three generations are shown in Fig. 2.4.

Orion Solo is less compact than the other Orion detector systems and only holds a single detector. The main components of Orion Solo are the motherboard, microZed, high-voltage generation/thermoelectric cooling board, Peltier cooler and fan, and the

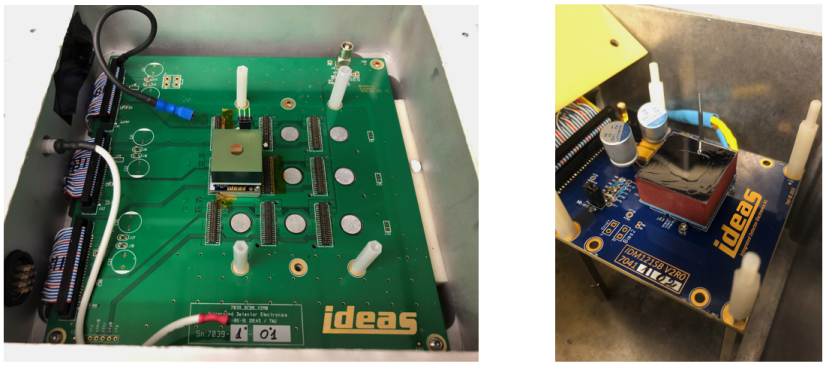

Figure 2.3: Comparison of the (opened) front-end for the Bench-top system (left) and the Single Board system (right). For scale, the CZT detector in both figures is the same size.

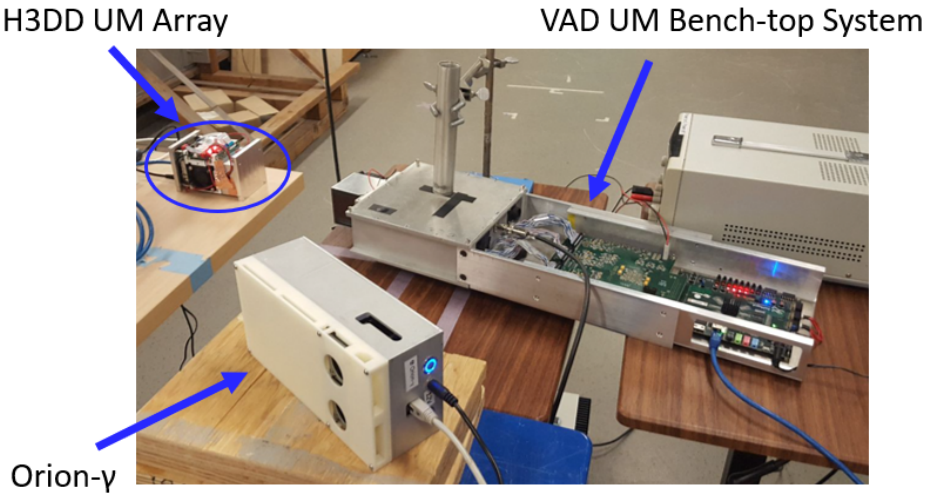

Figure 2.4: The VAD UM Bench-top system, Orion-γ, and the H3DD UM Array system pictured together.

crystal enclosure with the ASIC, CZT, and high-voltage distribution board. The microZed is a commercial off-the-shelf system-on-module, which includes a central processing unit and Field-Programmable Gate Array (FPGA), and is the component that consumes the most power, around 3 to 4 W. The Peltier cooler requires 1 to 3 W depending on the cooling needs. The ASIC consumes less than 300 mW, and the rest of the components consume less than 1 W. The main components are labeled in Fig. 2.5. Orion Eagle (discussed in Chapter 7) is similar to this design except the Peltier and fan were removed, the handling of high voltage components was modified, the motherboard

was made larger to include a voltage step-down regulator and to make room for mounting holes (to be able to add extra mechanical support), enclosures were added/changed, along with a few other modifications.

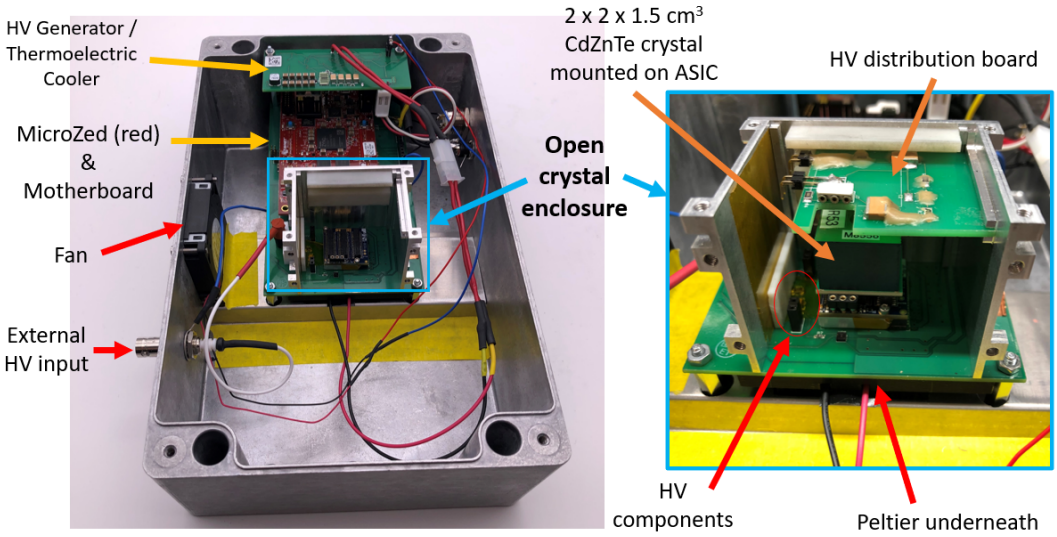

Figure 2.5: Orion Solo with the major components labeled and a closer view of the crystal enclosure.

2.2 Software

2.2.1 Digital Filtering

Digital signal filtering is used to extract amplitude and timing information from the digitized waveforms (160 samples at 40 MHz or 4 μs time window). Example waveforms are shown in Fig. 2.6. The amplitude of a waveform is usually determined or "picked off" by a trapezoidal filter or sometimes by simple subtraction (the mean of samples in the tail minus the mean of samples in the baseline). The timing of the waveforms is picked off using a fourth order CR-RC filter. Since the cathode signals rise slower than the anode signals, different filter settings are used for the anode and cathode waveforms. For the trapezoidal filter, the rising and falling edges of the trapezoid are 1600 ns and the top stage is 400 ns for anode waveforms. For cathode waveforms, this is adjusted to 1400 ns and 800 ns, respectively. The maximum value of the filtered waveform gives

the amplitude. For the fourth order CR-RC filter, the shaping times are 100 ns and 250 ns for the anode and cathode waveforms, respectively. For both filtered signals, a 50% threshold is used to pick off the timing. The timing of the cathode signal is considered the start of the electron drift, and the timing of the anode signal is considered the end, so the difference in timing gives the estimated drift time. The optimal filters and settings were determined by Zhu [24].

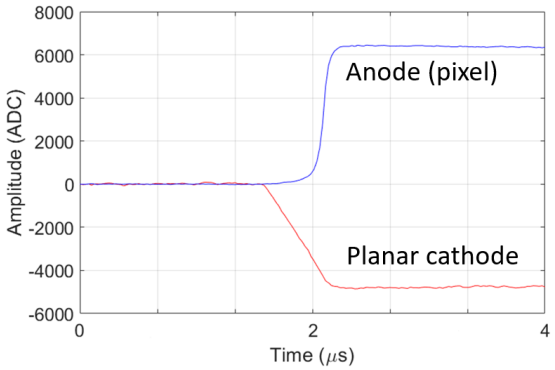

Figure 2.6: Example of raw waveforms recorded by the pixelated CZT detector.

2.2.2 3D Event Reconstruction

After digital filtering, every triggered pixel will have at a minimum the following data associated with it: anode amplitude, cathode amplitude, drift time, and the channel number corresponding to the pixel that triggered. This information is used to reconstruct the 3D position. Sometimes timestamps, ASIC temperature readings, and dead time were saved as well.

Due to the detector geometry and electrode configuration, the weighting potential of an anode pixel is near-zero everywhere except very close to the pixel, and the cathode weighting potential is linear. An example of the weighting potential for a pixelated detector (with a 3×3 array of pixels) is shown in Fig. 2.7. Note that for the detectors used in this study, the weighting potential follows the same shape but the magnitude will be much lower outside of the near-anode region. For a pixel detector, the slope of the weighting potential outside the near-anode region is roughly proportional to one divided by the number of pixels.

Due to the weighting potentials, the cathode amplitude depends on the depth of the radiation interaction whereas the anode amplitude does not. Therefore, the ratio of these signals, the Cathode-to-Anode Ratio (CAR), can be used to determine the depth of interaction. The depth of interaction will often be referred to as "depth" or "z" in this work. The x-y location of the interaction is given by the triggered pixel index, but can also be determined on a finer, subpixel scale (resolution of ~300 μm at 662 keV) if neighboring non-collecting pixel signals are processed [25]. Though charge is not collected by the neighboring pixels, there will still be some small signals induced on them from the charge passing through their weighting field in the near-anode region (demonstrated on right in Fig. 2.7). The amplitude of these signals are related to the x-y subpixel location of the interaction.

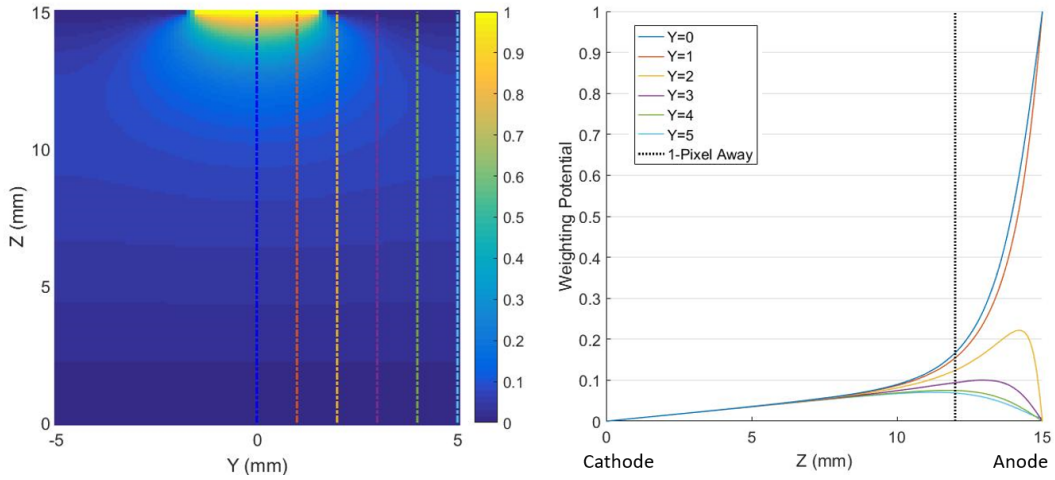

Figure 2.7: The weighting potential simulated for the center pixel of a 0.5×0.5×1.5 cm^3 detector with a 3×3 array of anode pixels and planar cathode (left). The weighting potential as a function of depth for different y-positions (right).

Since the position (x,y,z) of radiation interactions in the CZT volume can be determined, spatial variations in gain can be accounted for to help improve energy resolution. To do so, a calibration measurement is performed, which is simply a ^{137}Cs flood irradiation. The data from this measurement is sorted based on the 3D position. In the x-y dimension, the volume of the detector is split up by anode pixel. Under each pixel (in the z direction), the detector is typically divided into 40 artificial "depth bins". An example of an anode spectrum separated by depth bin is shown in Fig. 2.8. In all, the

detector is artificially split into 4,840 voxels in the 3D space, and the single-pixel event data is binned by voxel.

For each voxel, the raw anode spectrum is produced, and the high energy cutoff of the spectrum ("anode cutoff") is determined. The anode cutoff is considered to be the "gain". The gain as a function of depth under a single pixel will always vary in the near-anode region due to changes in the weighting potential. In the bulk of the detector, variation in gain with depth is typically related to trapping. Gain will be lower, especially towards the cathode side, when there is more trapping. Each pixel anode has its own pre-amplifier, so the electronic gain can vary pixel-to-pixel as well. The anode cutoff of each anode spectrum (including all depths) can help correct for the variation in electronic gain. This value should be less sensitive to trapping, as the events with the least trapped charge determine the high energy cutoff. The pixel-by-pixel gain can also be useful for judging the uniformity of the detector. Sometimes in this work, the photopeak centroid was used to determine the gain. This is because the anode cutoff is very sensitive to noise. If there is high noise (e.g. in high-temperature measurements), the anode cutoff will be overestimated due to greater spread in the photopeak.

Previously, pixels with unexpectedly low gain have been observed, as described by Kaye [26]. This phenomenon is referred to as "gain deficit" and was initially proposed to be due to an issue at the anode surface, as no depth dependence was observed. While this issue does not significantly affect single-pixel energy resolution, Xia showed it is a significant problem for high-energy multi-pixel event reconstruction [20]. Xia proposed that the issue was due to thermal tension built up in the adhesive between the detector's anode electrodes and the PCB board that carries the detector.

After all depth-dependent and pixel-to-pixel variations in gain are corrected, much better energy resolution can be achieved. The final spectrum is referred to as the "depth-corrected" single-pixel spectrum or sometimes just the "corrected" single-pixel spectrum. Energy resolution for these corrected spectra can be very good, near 0.3% FWHM at 662 keV for the best detectors, as shown in Fig. 2.8.

For multi-pixel events, CAR is no longer an accurate estimate of depth because the cathode signal will be affected by all interactions and the anode signal corresponds to a single interaction in most cases. The drift time is another measure of depth, but is only accurate if the electric field is uniform. However, the relationship between CAR and drift time for single-pixel events can be used as a lookup table for multi-pixel events.

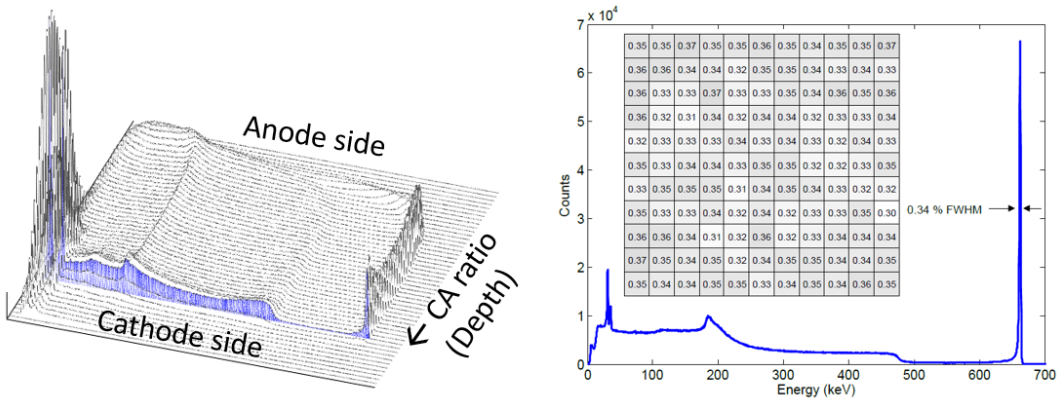

Figure 2.8: The depth-separated anode spectra, an intermediate step during the calibration process (left). The depth-corrected anode spectrum for single-pixel events in a high-quality detector (right).

The number of triggered pixels represents the number of anode positions (x-y locations) detecting a significant amount of charge. For gamma ray events, the number of triggered pixels usually describes the number of discrete interactions (i.e. number of locations where a scatter, photoelectric absorption, or pair-production event occurred). However, sometimes charge originating from a single interaction can trigger more than one pixel, which is often referred to as "charge sharing". This can happen if the x-y position of the interaction is in the gap between pixels (or close to the gap) or if the charge cloud diffuses significantly. It also becomes more likely if an interaction deposits a large amount of energy, as the electron clouds from the interaction may be large enough to span across multiple pixels [24] [20] [27]. There are algorithms that can be used to correct for charge sharing. Typically, only events involving up to 4 triggered pixels are saved to optimize data storage, as the probability of 5 or more interactions becomes unlikely for most gamma-ray events. For high-energy measurements, this setting can be changed.

2.2.3 Waveform Analysis

Once the 3D position has been determined, the waveforms can be re-examined by calculating the average waveform corresponding to 662 keV photopeak events in each voxel. The average waveform is referred to as the System Response Function (SRF). Averaging many waveforms is beneficial for identifying and comparing subtle features in the

system response that could be concealed by noise in individual waveforms. The SRFs are calculated for all depths of interaction but for ease of plotting/viewing usually just the SRFs corresponding to interactions at the cathode side (z=40) are used. This depth bin is most advantageous because the cathode SRF represents the drift path through all of the detector. If there is non-uniformity in the detector at any depth, it will show up in the cathode-side SRFs. However, this technique relies heavily on the accurate reconstruction of the 3D position and uniformity within the voxel volume. For example, in some waveforms there was unexpected decay in the cathode tail. This led to inaccurate depth estimation and poorly reconstructed SRFs. Also, if the system response is different in a small volume within a voxel, it may go unnoticed unless it is dramatically different.

While reducing the waveforms to just timing and amplitude values or the SRFs helps reduce the size of the data for easier analysis, it does not take full advantage of all the information contained in the waveform. To address this limitation, Williams introduced a new approach for performing energy calibrations that utilizes Principal Component Analysis (PCA) [28]. PCA also reduces the dimensionality of the waveform data yet does so in a fundamentally different way. The conventional methods rely on human intuition (i.e. knowledge of detector physics) for selecting attributes to identify and quantify waveforms (e.g. amplitude, 3D position). On the other hand, PCA can be used to exploit the statistical properties of the underlying data to determine which attributes account for the most variance between waveforms in a data set. In this algorithm, pre-processed waveforms from ^{137}Cs photopeak events are compiled into a data matrix, and singular value decomposition is used to extract eigenvectors. Waveform are then projected along these eigenvectors to yield principal component values. This transforms the data into a new coordinate system that has fewer dimensions yet still retains most of the variance. The principal component values are regressed against the amplitude reconstructed using the conventional methods, and since the energy is known (662 keV), the regressions can be made to match up with the calibration value. Williams was able to improve the energy resolution of CZT by 10% compared to any other method, and Petryk had success applying this technique to TlBr and perovskite detector data [18]. In general, PCA has applications in many fields, and plotting principal components against each other can be helpful for visually identifying clusters of related data.

2.2.4 Imaging

The CZT detector is sensitive to gamma rays that primarily interact via Compton scattering so Compton imaging can be performed. If the position and energy deposited for every radiation interaction is measured, the incident angle of scatter can be determined by considering the Compton kinematics. The scattering angle is given by

$$\theta = arccos\left(1 - \frac{m_e c^2 E_1}{E_0(E_0 - E_1)}\right) \tag{2.1}$$

where E_0 is the total deposited energy and E_1 is the energy deposited in the first interaction. Then a Compton cone with angle θ can be projected into a 4π space along a normalized axis direction c as given by

$$c = \frac{d_1 - d_2}{\|d_1 - d_2\|} \tag{2.2}$$

where d_1 is the coordinate of the first interaction and d_2 is the coordinate of the second interaction. This is visualized in Fig. 2.9. The projected Compton cone creates a "ring" of potential source locations. When many interactions occur, many Compton cones can be projected. The rings from the Compton cones will overlap and eventually converge in the direction of the source.

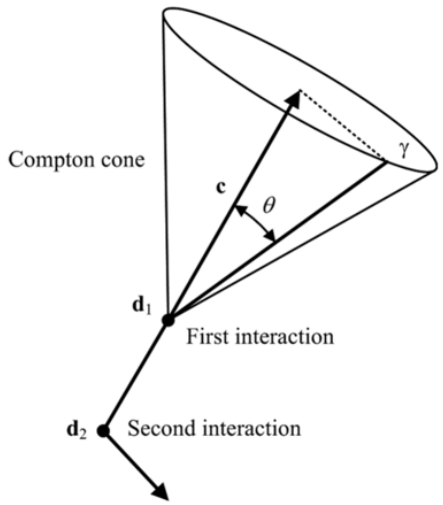

Figure 2.9: Visualization of the projection of a Compton cone. This figure is from Ref. [29].

In order to project the Compton cone in the correct direction, the sequence of interactions must be known. Traditionally, Compton imagers consist of two layers of detectors: the first layer used to scatter the gamma ray, and second layer absorbs the scattered gamma ray. In this setup, it is assumed that events forward scatter, and backward scatters degrade the imaging performance. In 3D CZT, multiple interactions within the same detector volume can be reconstructed, thus only one detector is required to perform Compton imaging. However, the timing resolution of CZT is not good enough to determine the sequence of interactions, so a variety of algorithms can be implemented to reconstruct the sequence. Therefore, CZT can provide Compton images in a compact form factor, making it ideal for in-field source localization.

At low energies, gamma rays are more likely to interact only a single time in the CZT material via photoelectric absorption (as shown earlier in Fig. 1.1). In this case, Compton imaging cannot be performed so coded aperture imaging is used instead, which involves placing a coded aperture mask (radiation shielding material with patterned cutouts) between the source and detector [30]. The mask will stop gamma rays unless they pass through the cutouts, casting a "shadow" on the detector. Knowledge of the mask's pattern and the shadow recorded by the detector can be used to locate a source. Since the spatial resolution of CZT is very good (i.e. the shadow can be well reconstructed), low energy gamma-ray sources can be imaged with high angular resolution using 3D CZT and a coded aperture mask. Time-encoded imaging, which is performed by moving the coded aperture mask, temporally modulates the gamma-ray signal and helps improve image quality by reducing artifacts [31]. The 3D distribution of extended sources can be estimated as well [32]. On the high-energy side, gamma rays can undergo pair production. These events can create artifacts in Compton images, as discussed by Shy [33]. Petryk showed that pair production events can be imaged with 3D CZT by exploiting asymmetries in pair production and charge induction physics [18].

Chapter 3

Annealing of CZT

3.1 Introduction

It is well known that elevating the detector temperature can help heal radiation damage in semiconductor detectors, which is a process referred to as "annealing". This has been demonstrated for CZT in previous work [34] [35] [36] [37] [20] and is further discussed in Chapter 6. Xia [20] found that annealing could help improve detectors beyond the state prior to neutron damage. The improvement in depth-corrected energy resolution was significant (0.68% to 0.56%) for one detector (#5R-32). This motivated the study of the effect of annealing on CZT detectors in the absence of radiation damage.

3.2 Annealing for 60 h at 80°C

3.2.1 Experimental Details

In this study, several 2×2×1.5 cm^3 Redlen CZT detectors (without electronics) were placed in an environmental chamber and heated at 80°C for 60 h. This annealing time and temperature were selected based on findings from Ref. [20]. These detectors had previously displayed below average performance to some degree either overall or in certain sections of the detector (i.e. high leakage, gain deficit, heavy trapping, or dead layer). Also, a couple detectors were selected because they were received in the same batch of detectors as detector #5R-32. Calibration measurements were taken using ^{137}Cs before and after annealing for comparison. Performance was analyzed by looking

at both the raw and corrected single-pixel energy resolution; resolution and peak gain as a function of depth; and resolution and gain deficit on a pixel-by-pixel basis.

3.2.2 Performance After Annealing

In general, annealing for 60 h at 80°C appeared to either positively impact the performance or not affect the performance much at all. The results in terms of energy resolution are summarized in Table 3.1. The improvement in raw single-pixel energy resolution was as great as -1.99% for detector #5R-37. Annealing appeared to improve "problem" pixels in most cases, alleviate gain deficit, and/or reduce trapping, which helped improve the raw energy resolution. For four detectors the change was -0.04% or less, which could be considered insignificant compared to the variation measurement-to-measurement. The change in the depth-corrected energy resolution was very small, -0.03% in the best case. While a change in raw energy resolution indicates that annealing clearly does affect a detector's properties, the minimal change in the depth-corrected energy resolution demonstrates that the depth-correction already almost fully compensates for most issues prior to annealing anyways. The affect of annealing varied detector-to-detector, so specific examples are discussed in the remainder of this section.

Table 3.1: Raw and depth-corrected single-pixel energy resolution (1-P ER) in terms of % FWHM at 662 keV before and after annealing detectors for 60 h at 80°C. Only detector #5R-32 had previous neutron exposure.

Detector #	Serial #	Date Received	Raw 1-P ER (%)			Corrected 1-P ER (%)		
			Before	After	Net	Before	After	Net
5R-20	M4022	4/2/2014	1.43	1.39	-0.04	0.47	0.46	-0.01
5R-32	M4282	10/2/2014	–	–	–	0.68	0.56	-0.12[1]
5R-33	M4283	10/2/2014	1.42	1.27	-0.15	0.55	0.53	-0.02
5R-35	M4320	10/2/2014	2.5	2.22	-0.28	0.64	0.64	0
5R-37	M4322	10/2/2014	6.94	4.95	-1.99	0.68	0.66	-0.02
5R-53	M8556	5/19/2016	1.79	1.45	-0.34	0.51	0.49	-0.02
5R-69	M9492	12/21/2016	1.2	1.18	-0.02	0.51	0.5	-0.01
5R-70	M9491	12/21/2016	2.43	2.42	-0.01	0.55	0.54	-0.01
5R-72	M9490	12/21/2016	1.11	1.07	-0.04	0.45	0.46	0.01
5R-73	M9601	12/21/2016	2.19	1.84	-0.35	0.64	0.61	-0.03

[1]Results for detector #5R-32 are from Ref. [20].

3.2.3 Resolution Improvement on a Pixel-by-Pixel Basis

Annealing was able to improve the energy resolution of pixels with very poor performance as shown in Fig. 3.1. For example, approximately a third of detector #5R-73 displayed poorer energy resolution than the rest of the detector. Pixels in this section showed significant improvement after annealing, as great as -2.34% change in the depth-corrected energy resolution for the most improved pixel. The resolution was initially poor for all depths of interactions, and improved uniformly with depth, so this could suggest that annealing may have helped improve the pixel contacts, or a material issue close to the pixels.

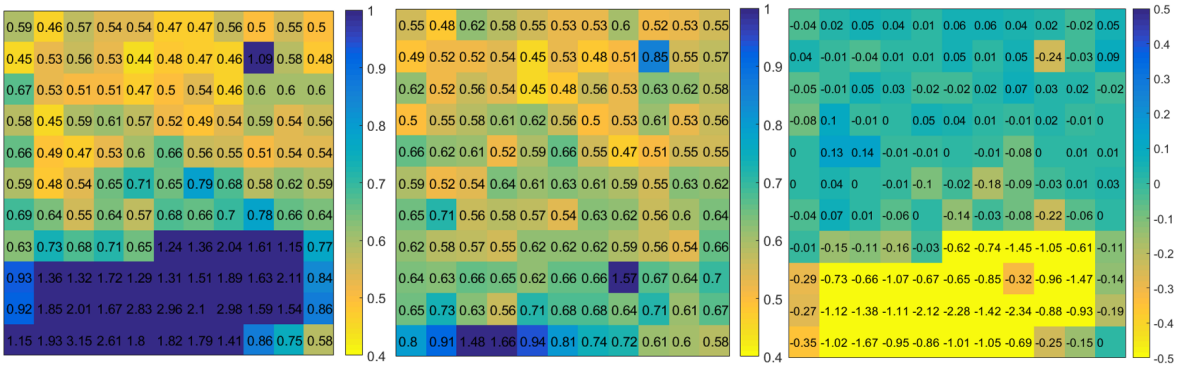

Figure 3.1: The pixel-by-pixel energy resolution (% FWHM at 662 keV) for detector #5R-73 before (left) and after (middle) annealing, and the net change in energy resolution (right).

3.2.4 Electron Trapping

For a few detectors, there was a significant reduction in electron trapping. The level of trapping can be gauged by looking at the gain as a function of depth or the energy resolution as a function of depth. If there is significant trapping, the gain and resolution will get worse (i.e. decrease in gain, increase in FWHM) towards the cathode side because the drift distance is longer and there is more opportunity for charge to be lost/trapped. Fig. 3.2 shows that trapping in detectors #5R-37 and #5R-53 was improved by annealing. For detector #5R-53, the trapping was relatively uniform, and the gain slowly decreased toward the cathode side. For detector #5R-37, there appeared to be a layer of heavy trapping mid-way through the detector bulk for many of the pixels, which can

be clearly seen in terms of resolution as a function of depth too, shown in Fig. 3.3. In both cases, annealing helped reduce trapping. Detector #5R-72 initially had a group of pixels with a dead layer which caused very poor resolution and few counts. Fig. 3.4 shows that annealing helped improve the energy resolution in this region and extended the active area. However, it was not a full recovery, as there was still a diminished response beyond a certain depth in a few pixels.

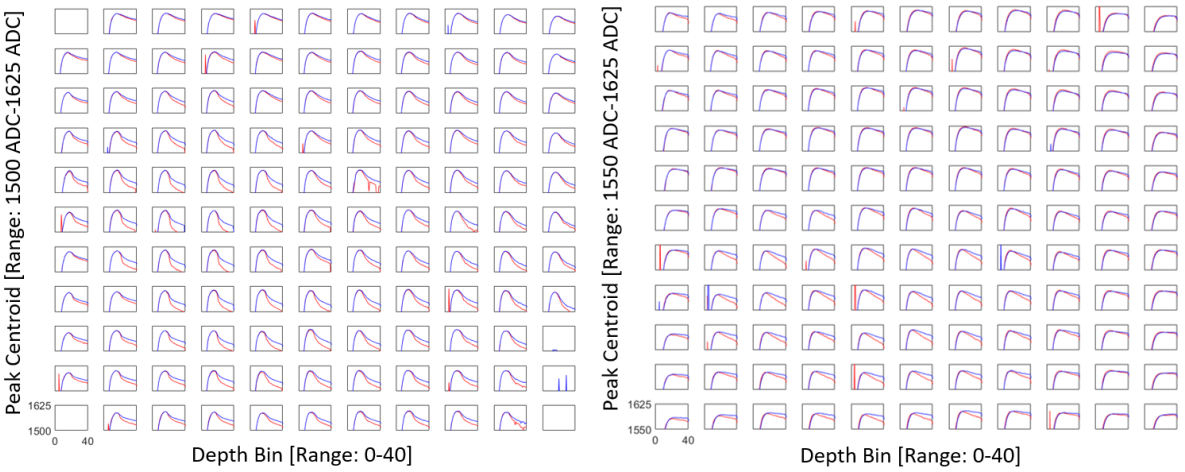

Figure 3.2: Gain (peak centroid) as a function of depth for detectors #5R-37 (left) and #5R-53 (right) before (red) and after (blue) annealing.

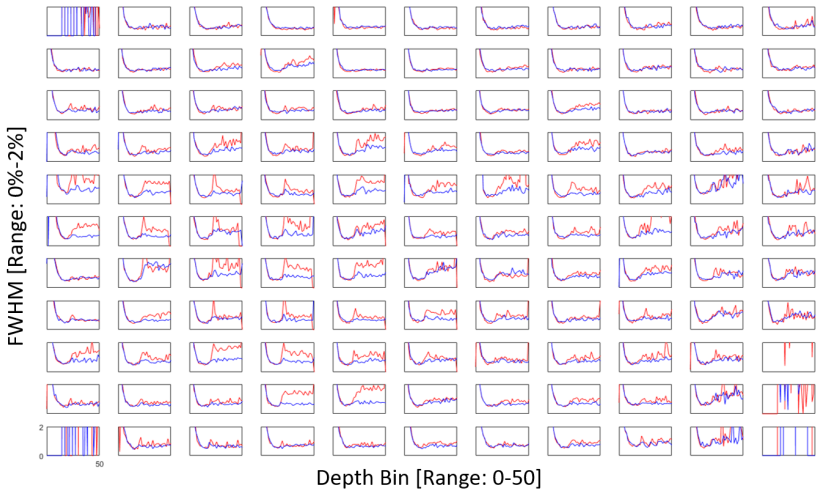

Figure 3.3: Energy resolution (% FWHM at 662 keV) as a function of depth before (red) and after (blue) annealing for detector #5R-37.

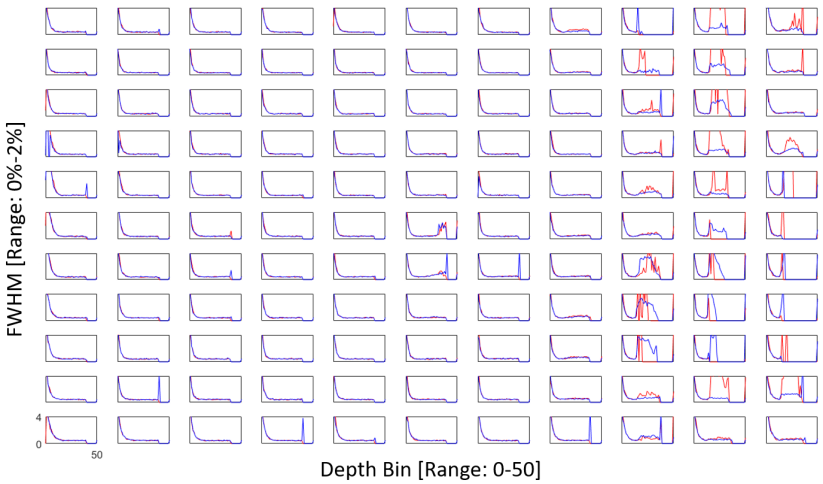

Figure 3.4: Energy resolution (% FWHM at 662 keV) as a function of depth before (red) and after (blue) annealing for detector #5R-72.

3.2.5 Gain Deficit

Similar to previous studies [20], proof that annealing can alleviate gain deficit was observed in this study. For example, detector #5R-20 initially had several edge pixels with gain deficit that were healed by annealing, as shown in Fig. 3.5. Only one pixel (row 10, column 1) still had significantly reduced gain.

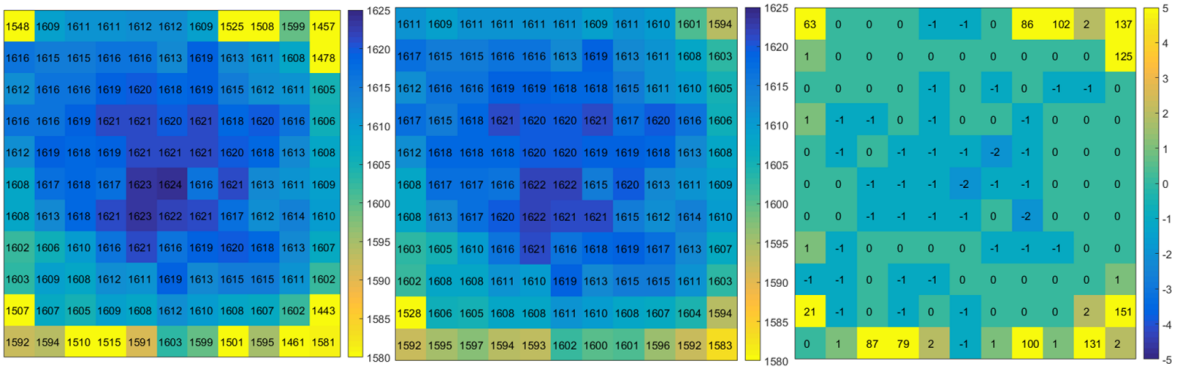

Figure 3.5: Pixel-by-pixel gain (anode cutoff) for detector #5R-20 before (left) and after (middle) annealing, and the net change (right).

3.3 Multiple Annealing Sessions

The post-annealing (60 h at 80°C) calibration data for detector #5R-37 suggested that while uniformity had improved due to annealing, some non-uniformities remained. This can been seen in the cathode SRF for cathode-side interactions, as shown for four pixels from detector #5R-37 in Fig. 3.6. A straight cathode SRF would indicate a uniform electric field. Since there was an obvious bend in the cathode SRFs, it indicates that there is a weak electric field in the middle of the detector. This is likely due to the layer of heavy trapping (i.e. material defects) noted earlier. Annealing helped straighten the cathode SRF (i.e. improved uniformity), but it was still not completely straight. Thus, this detector was subject to further annealing and testing to see if the performance could be improved more.

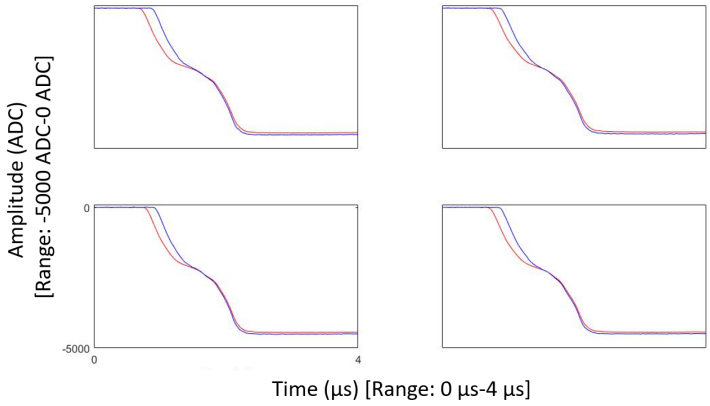

Figure 3.6: Cathode SRFs for cathode-side events in detector #5R-37 before (red) and after (blue) annealing at 80°C for 60 h.

Prior to further annealing, the detector was tested again to verify that the improvement due to annealing was unchanged, as a notable amount of time had passed since the last measurement (45 days). Once this measurement was taken, two additional annealings both at 80°C for 60h were performed, with calibration measurements taken after each. The timeline of testing and the corresponding raw and corrected single-pixel energy resolution are given in Table 3.2. Each annealing improved the corrected single-pixel energy resolution by 0.02%, and oddly an improvement of 0.03% was seen after 45 days at room-temperature after the first annealing. Overall, this detector was annealed a total 180 h at 80°C and saw a 3.22% improvement in raw single-pixel energy resolution

Table 3.2: Timeline of testing of detector #5R-37.

Date:	6/13	6/14-6/16	6/17	8/1	8/2-8/5	8/5	8/9-8/12	8/15
Raw 1-P ER (%):	6.94	80°C 60 h	4.95	5.08	80°C 60 h	4.07	80°C 60 h	**3.72**
Corrected 1-P ER (%):	0.68	80°C 60 h	0.66	0.63	80°C 60 h	0.61	80°C 60 h	**0.59**

and a 0.09% improvement in the corrected single-pixel energy resolution. The transformation of the anode photopeak region over the course of testing is shown in Fig. 3.7. The change in photopeak shape is most drastic after the first annealing compared to the two annealing sessions afterward, indicating that the effect of annealing plateaus for repeated annealing sessions. Further analysis of the SRFs showed that the uniformity of the electric field improved, but the electric field was still weaker in the middle of the detector.

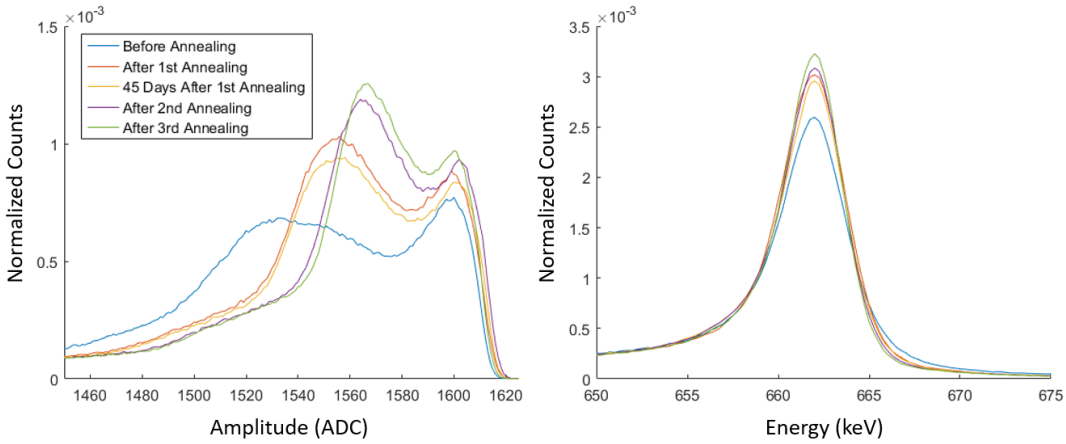

Figure 3.7: The transformation of the 662 keV photopeak region in the raw (left) and corrected (right) single-pixel spectra throughout testing of detector #5R-37.

3.4 Damage from Annealing

In later studies, a Kromek/eV detector #4E-3 was exposed to neutrons from a PuBe source. The neutron fluence was so low ($<\sim 10^8$ n/cm^2) that trapping only slightly

increased. However, it was noted that prior to neutron exposure, several pixels had gain deficit, and trapping was significant. Since it was shown that annealing Redlen CZT detectors to 80°C can help reduce trapping and reduce gain deficit, detector #4E-3 was annealed at 80°C for 91 h in the environmental chamber. Calibration measurements were made with ^{137}Cs before and after. Unfortunately, the gain issue became much worse. The gain deficit spread to around half of the pixels and other pixels had a slight reduction in gain, as shown in Fig. 3.8. Single-pixel energy resolution did not change significantly, but over 5% fewer counts were in the final corrected energy spectrum. The damage from annealing was too significant to continue to use it in neutron damage studies. It should be noted that the annealing temperature of 80°C was chosen based on recommendations for the 5R-generation Redlen CZT, not Kromek CZT. It is likely that this detector was fabricated differently.

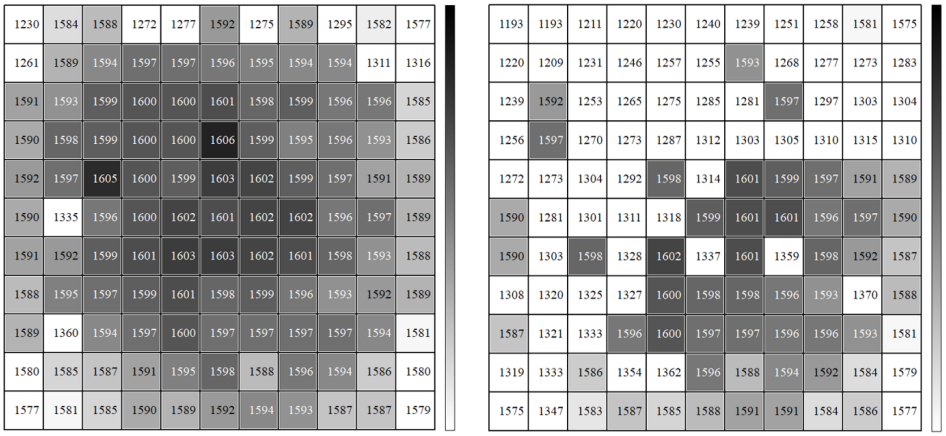

Figure 3.8: Gain (anode cutoff) before (left) and after (right) annealing detector #4E-3 at 80°C. The color bar scale is 1580 ADC - 1610 ADC for both plots.

3.5 Conclusions

Overall, it was shown that annealing Redlen CZT detectors at 80°C helped "heal" issues in the bulk (i.e. trapping) and at the contacts (i.e. gain deficit) for some detectors. Typically, the effect of annealing for 60 h at 80°C was mainly reflected in the raw energy resolution (up to 2% improvement) and minimally in the corrected energy resolution

(up to 0.03% improvement). For a detector with electric field non-uniformity due to very heavy trapping, multiple annealings led to greater improvement in the detector's performance. After a total 160 h at 80°C, there was a 3.22% improvement in raw single-pixel energy resolution and a 0.09% improvement in the corrected single-pixel energy resolution. The improvement in raw spectra does not provide a huge benefit for pixelated CZT because the depth-correction already accounts for most non-uniformities. However, for CZT detectors that are not 3D position-sensitive or have less fine position resolution (i.e. co-planar or virtual Frisch grid CZT), the improvement due to annealing at 80°C could be more beneficial.

For the series of Redlen CZT detectors tested, annealing provided an avenue to improve detector properties with minimal risk; however, for the Kromek CZT, annealing at 80°C damaged the detector contacts. This emphasizes the importance in considering the detector fabrication when selecting an annealing temperature: 80°C is not necessarily a fix-all for all CZT detectors. It also suggests that fabrication may affect detector performance over a wide range of temperatures, which is a subject matter discussed further in Chapter 4. The change in the raw spectra after annealing indicates that new calibrations must be taken afterwards. While this helps improve performance once re-calibrated, it also poses an issue because calibration factors may change during a measurement if a CZT detector is operated at a temperature high enough for annealing to occur. Therefore, it may be important to choose detectors without any issues that could be affected by annealing or possibly pre-anneal detectors prior to temperature cycling so that further heating has a minimized effect.

Chapter 4

High-Temperature Operation

4.1 Introduction

3D CZT detector systems typically employ some sort of temperature regulation to remove excess heat generated by electronics and keep the temperature stable, as energy calibrations are temperature-sensitive. Removal of temperature regulation would greatly reduce the power consumption, weight, and size of detector systems, making CZT better suited for in-field operational use.

Previous studies have shown that pixelated 3D CZT can operate well at ambient temperatures in the range of 0°C to 30°C [16]. Prior to this work, the highest that pixelated 3D CZT detectors had been tested at was 40°C [20]. Coplanar CZT has been tested up to 50°C [38], but the only details given were that resolution degraded at 50°C and remained degraded until the detector was at room-temperature again. Therefore, this work aimed to address the lack of knowledge on the behavior of CZT detectors at extreme temperatures (i.e. up to 60°C). The main goals of this study were to assess the viability of high-temperature operation of CZT, test experimental CZT detector electrode designs, and see if results were consistent for CZT detectors fabricated by different vendors. An understanding of how the detector and its electronics behave with temperature is important for guiding the development of future CZT detectors as well as determining techniques to improve performance above room-temperature.

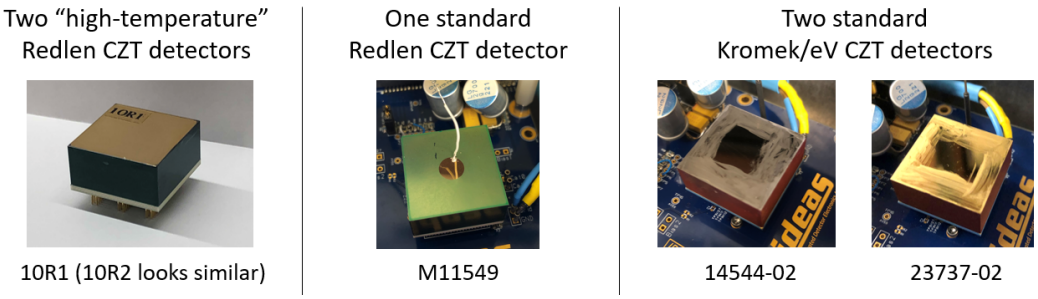

Figure 4.1: Pictures and descriptions of the CZT detectors tested at high temperatures.

4.2 Standard Experimental Setup and Methods

Five 2.2×2.2×1.0 cm^3 CZT detectors (Fig. 4.1) were used in this study: two “high-temperature” Redlen CZT detectors (#10R1 and #10R2), one standard Redlen CZT (M11549), and two standard Kromek/eV CZT detectors (#14544-02 and #23737-02). The high-temperature Redlen CZT detectors were the product of experiments involving changes to contact design and fabrication processes to develop CZT sensors capable of high-temperature operation. The Kromek detectors have different appearances because detector #23737-02 has a Au finish on the cathode contact and detector #14544-02 has a Pt finish. However, the semiconductor and metal interface is the same. The VAD UM v2.2 digital ASIC and the single board system were used for readout with the dynamic range on the ASIC set to 700 keV. The front-end enclosure of the single board system, containing the CZT and ASIC, was placed inside an environmental chamber for testing, as shown in Fig. 4.2. The front-end enclosure has neither cooling nor ventilation, so the temperature of the ASIC and detector is not controlled and is heavily influenced by environmental conditions.

Calibration measurements (1.5 h with ^{137}Cs and ^{241}Am check sources) and noise measurements (no source) were taken at a series of environmental chamber temperature settings, ranging from 20°C to 60°C during a warming (denoted as ↑) and cooling (denoted as ↓) cycle for all detectors. At each temperature, measurements were taken once the temperature was stable. The detector was biased to -2000V. At 20°C and 60°C, additional measurements were taken at -1000V and -1500V. The method used to apply cathode bias varied throughout the experiments, which is discussed in Section 4.3.

There were three measures of temperature during these experiments (listed in order

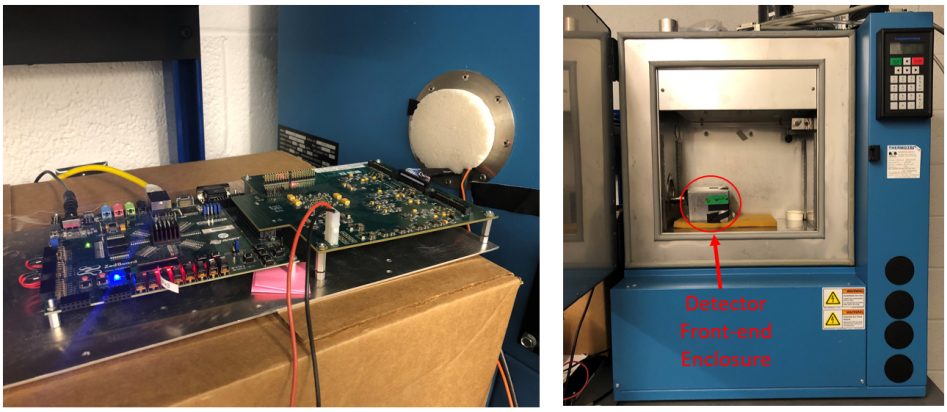

Figure 4.2: The front-end enclosure inside the thermal chamber (right), and the rest of the VAD UM system outside of the thermal chamber (at room temperature) (left).

from least to most precise): (1) the temperature setting on the environmental chamber, (2) the front-end enclosure temperature measured by a thermocouple in air readout via a multimeter, and (3) the reading (in ADC) from the ASIC temperature sensor. The ASIC temperature sensor reading was used to determine whether the temperature was stable. For simplicity, temperature values given in this work will typically refer to the temperature set on the environmental chamber, unless otherwise specified.

4.3 Leakage and Electronic Noise

The relationship between leakage I and absolute temperature T is

$$I \propto e^{-E_g/k_b T} \tag{4.1}$$

where E_g is the band gap and k_b is the Boltzmann constant. This causes leakage to increase significantly as temperature is increased, as shown in Fig. 4.3. The leakage typically varies detector-to-detector. At 20°C, the total leakage was low for all the detectors, with values ranging from 27 nA to 45 nA. Due to the exponential increase of leakage with temperature, the total leakage was extremely large, between 1,325 nA and 2,140 nA, at 60°C. The leakage of the high-temperature CZT (#10R1 and #10R2) was comparable to the leakage of the other detectors. The detector with lowest leakage was

from Kromek; however, the detector with the highest leakage was also from Kromek. It should be noted that the sample size is small, and the leakage of these detectors does not necessarily represent the average leakage for all detectors from each vendor. The detectors used in this experiment were not pre-selected based on their leakage.

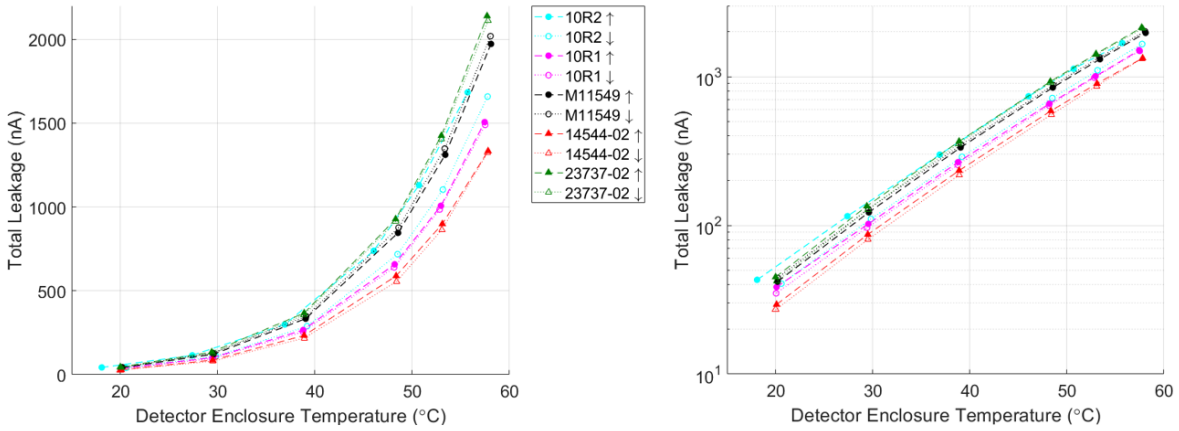

Figure 4.3: Total leakage as a function of front-end enclosure temperature for all five detectors on a linear scale (left) and log scale (right). The bias was -2000V, and the detector thickness was 10 mm. Circle and triangle markers indicate detectors from Redlen and Kromek, respectively.

In these leakage measurements, a high-voltage power supply was used to apply -2000V to the cathode surface of the 10 mm thick detectors, and the total leakage was measured by the power supply. Thus, the total leakage measured here is comprised of both the bulk and surface leakage. Unfortunately, the leakage per pixel cannot be measured with the ASIC used in this study, making it impossible to get an independent measure of the bulk leakage. However, the detector's surface leakage can be estimated by measuring the leakage on the guard ring that surrounds the 11×11 anode pixel array. This leakage is referred to as the grid leakage and is shown in Fig. 4.4. The grid leakage was a very small fraction (roughly 10% or less) of the total leakage for all detectors. While the difference between the measured total leakage and grid leakage may not exactly equal the bulk leakage, the measurement of the grid leakage indicates that the bulk leakage is the main contributor.

Another interesting observation in Fig. 4.3 and Fig. 4.4 is that leakage was usually slightly lower during "cooling cycle" measurements than "warming cycle" measurements taken at the same temperatures. A decrease in leakage (for the same applied bias) could

indicate an increase in material resistivity or an improvement in material quality. This suggests that the temperature cycling process or high temperatures (as low as 60°C) may slightly affect material properties, which is discussed more in Section 4.7.

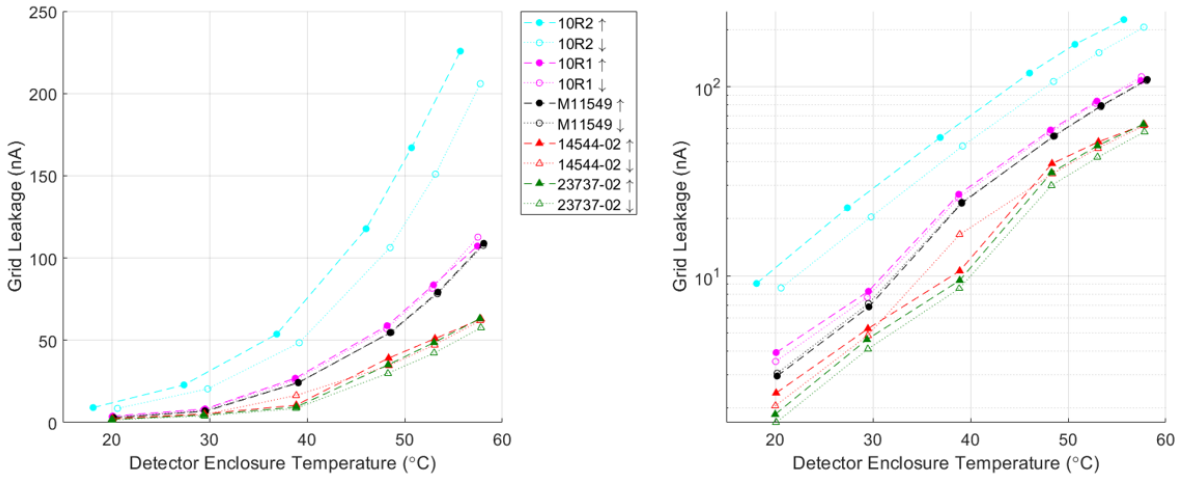

Figure 4.4: Grid leakage as a function of front-end enclosure temperature for all five detectors on a linear scale (left) and log scale (right). The bias was -2000V, and the detector thickness was 10 mm. Circle and triangle markers indicate detectors from Redlen and Kromek, respectively.

High leakage leads to high electronic noise. The increase in electronic noise is most significant for the cathode channel (Fig. 4.5) as it experiences the full effect of the leakage. Detector #10R2 was the first detector to be tested, thus some lessons learned from its testing were incorporated during the remainder of the experiment. The cathode noise did not recover for detector #10R2 during the cooling cycle. This was due to an issue with the foam used to make the connection between the cathode surface and the high-voltage pad on the high-voltage distribution board. While normally easily compressible, the temperature cycling caused the foam to become stiff, resulting in a poor cathode connection. The cathode connection was improved (i.e. connected via a wire or foam wrapped with metallized film) for testing of the remaining detectors. For detector M11549, the cathode signal became unstable over time at 60°C, leading to an inaccurate estimation of the FWHM at 60°C and 55°C during the cooling cycle. The distribution of the noise was no longer Gaussian. A similar effect occurred for detector #23737-02 at 55°C and 60°C.

The benefit of using the pixelated anode design at high temperatures is that the bulk

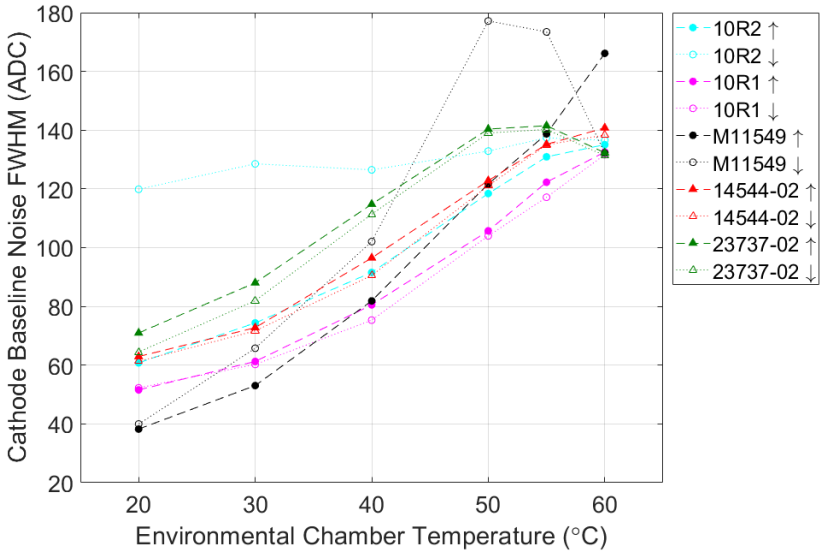

Figure 4.5: The cathode electronic noise in ADC as a function of temperature while warming (↑) and cooling (↓). Circle and triangle markers indicate detectors from Redlen and Kromek, respectively. For scale, 40 ADC corresponds to roughly 5 keV.

leakage is shared between 121 pixels and the guard ring captures the surface leakage, so the leakage for each pixel/channel is just a small fraction of the total leakage. The input capacitance for the pixels is much smaller than for the cathode, which also keeps electronic noise low. The average pixel electronic noise was ∼1.7 keV for all the detectors at 20°C and rose to typically around 4 to 5 keV at 60°C (Fig. 4.6). The pixel noise was lowest for the high-temperature Redlen CZT. The increase in noise above 50°C was much larger for detector #10R2 during the warming cycle compared to all the other measurements. This is because the default ASIC settings were used. During the cooling measurements for detector #10R2 and for the testing of the rest of the detectors, the pre-amplifier feedback resistance was adjusted depending on the leakage during the measurement. When the leakage is very large, increasing the pre-amplifier feedback resistance setting can help stabilize the anode channel baselines. While improving the stability of the baselines helps reduce noise, adjusting this setting is not without drawbacks. Increasing the pre-amplifier feedback resistance increases the pre-amplifier decay time constant, leading to decay in the tails of the waveforms which will

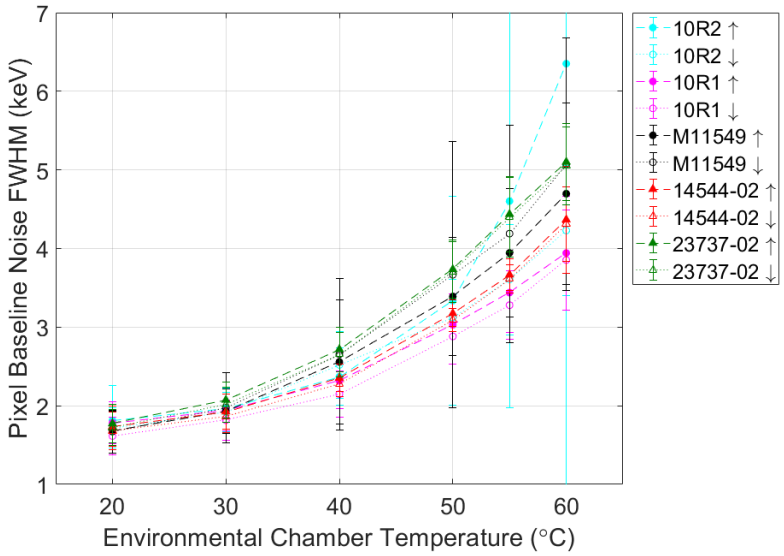

Figure 4.6: The average electronic noise in keV from all pixels as a function of temperature while warming (↑) and cooling (↓). Error bars represent the standard deviation. Circle and triangle markers indicate detectors from Redlen and Kromek, respectively.

consequently cause the amplitude to be underestimated. Thus, the setting was only adjusted when necessary, typically at 50°C or higher, depending on the detector. The pixel noise at 60°C for various pre-amplifier feedback resistance settings and biases is shown in Fig. 4.7. Reducing bias can help reduce the electronic noise, and the improvement seen by selecting an appropriate pre-amplifier resistance setting is even more drastic at high bias.

The stability of the baseline at high temperatures can vary channel-to-channel, but the pre-amplifier feedback resistance setting cannot be adjusted individually for each channel. During this experiment, there were typically a few channels that were more noisy than the rest of the channels at high temperatures. In the worst case, the noise/unstable baselines could flood a channel with false triggers, and the channel would need to be disabled. Increasing the pre-amplifier feedback resistance high enough to stabilize these channels would result in decay of the tails for the majority of pixels, which could possibly be more detrimental to the overall energy resolution. If an ASIC were to be designed specifically for high-temperature use, the option to adjust the pre-amplifier feedback for

each channel would be desirable.

A secondary effect of the increase in leakage is a decrease in the effective applied bias. The high-voltage distribution board, which is location between the high-voltage power supply and cathode connector, features some very large resistors (∼108 MΩ) used in conjunction with capacitors to filter the signals. At high temperatures, the leakage becomes large enough that the voltage drop across these resistors is no longer negligible. At 60°C, the effective applied bias was reduced by ∼10% as shown in Fig. 4.8. The effective applied bias is the estimated bias applied to the detector when considering the loss of voltage to the resistors.

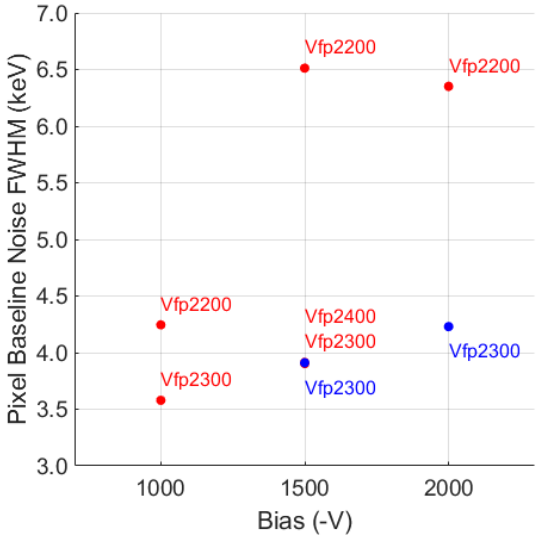

Figure 4.7: The average electronic noise in keV as a function of applied cathode bias and anode pre-amplifier feedback resistance setting (Vfp) for detector #10R2 at 60°C. In chronological order, measurements were taken at -2000V, -1500V, and -1000V (shown in red) and then at -1500V and -2000V (shown in blue). The Vfp ASIC setting value is given in ADC. Higher values indicates higher feedback resistance. Three data points overlap at -1500V.

4.3.1 Additional Electronic Noise Measurements and Analysis

So far in this section, it has been implied that the increase in electronic noise at high-temperature is due to detector leakage. While detector leakage can play a role, there are

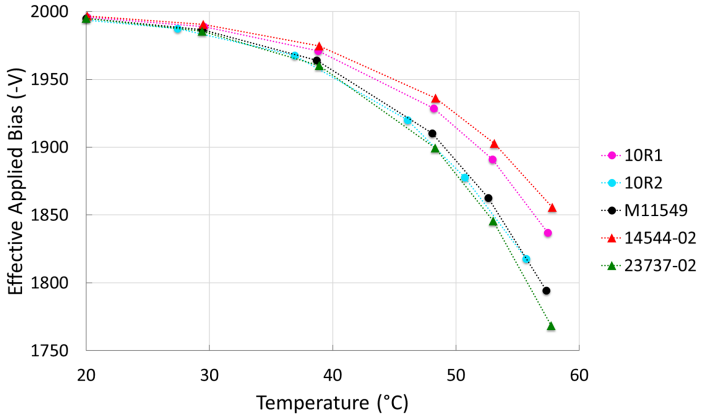

Figure 4.8: The estimated effective applied bias as a function of temperature. The bias supplied by the high-voltage power supply was -2000V.

other factors in the circuit that contribute to the electronic noise as well, such as detector thermal noise, Field-Effect Transistor (FET) leakage noise, FET channel thermal noise, FET 1/f noise, and feedback resistor thermal noise, as outlined by Zhu in Ref. [24]. Additional measurements and analysis were performed to confirm that leakage was the dominant factor at high temperatures.

To further investigate the source of the noise, the readout system was tested without a detector in order to get a measurement of the ASIC noise in the absence of detector leakage. The high-voltage distribution board was present, with the cathode pin connected. The ASIC baseline noise FWHM for anode pixel channels as a function of temperature is shown in Fig. 4.9. The noise (in ADC) declined with increasing temperature. Initially, it was thought this may have been caused by the decrease in pre-amplifier gain with temperature; however, accounting for gain did not fully compensate for the effect. This indicates that noise related to FETs and feedback resistors are not significant contributors at high temperature.

The electronic noise with the detector plugged in with and without bias was measured at 20°C and 60°C. Fig. 4.10 shows that without bias at 60°C, the electronic noise is much lower than the electronic noise with bias at 60°C, comparable to that at 20°C with -2000V applied bias and slightly greater than that at 20°C without bias. The minimal increase in noise from 20°C 0V to 60°C 0V compared to the increase seen when -2000V bias is applied at 60°C suggests that detector leakage is the main contributor to noise and other noise sources (i.e. detector thermal noise) only slightly contributes to the

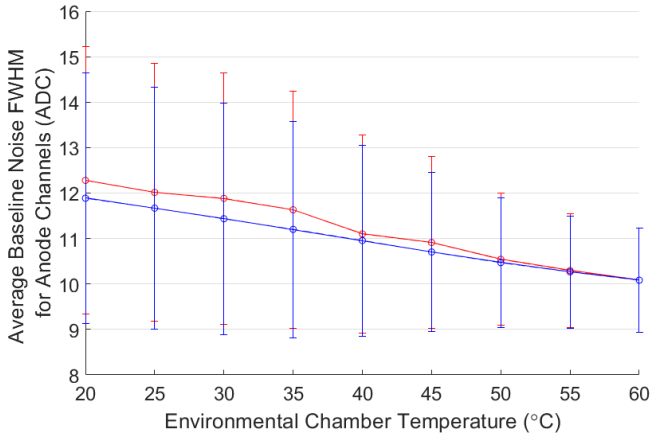

Figure 4.9: The average measured ASIC baseline noise FWHM for anode channels when warmed up (red) from 20°C to 60°C, and then cooled down (blue) to 20°C in 5°C increments. The error bars represent the spread of values (standard deviation) among the channels.

increase in noise with temperature. This means that if the leakage of the detectors could be reduced, lower noise and thus higher resolution could be achieved.

More information can be gained about the electronic noise by determining how it varies as a function of shaping time. Fig. 4.11 shows the results for all anode pixels/channels at 20°C and 60°C, and Fig. 4.12 shows the results for the cathode and for an example anode channel (to demonstrate how series and parallel noise is observed qualitatively). At 20°C, the noise is primarily series noise, which was seen in previous measurements [24]. The cathode has some parallel noise as well. At 60°C, parallel noise dominates. This matches our expectations because parallel noise includes thermal and leakage noise, which both increase with temperature. At 20°C, the electronic noise is mostly comprised of serial noise and the parallel noise is very low. As the temperature increases, parallel noise becomes the dominant contributor due to the huge increase in detector leakage current.

Because the composition of the noise contributions changes significantly at high temperatures, the filters used for timing and amplitude pick-off may not be optimal. The default filters and their settings were optimized for room-temperature measurements, when the series noise is dominant. The energy resolution shown in Figs. 4.14 and 4.17 was calculated using the default filtering methods (same filtering at all temperatures), which means there may be some room for improvement. For example, shortening the

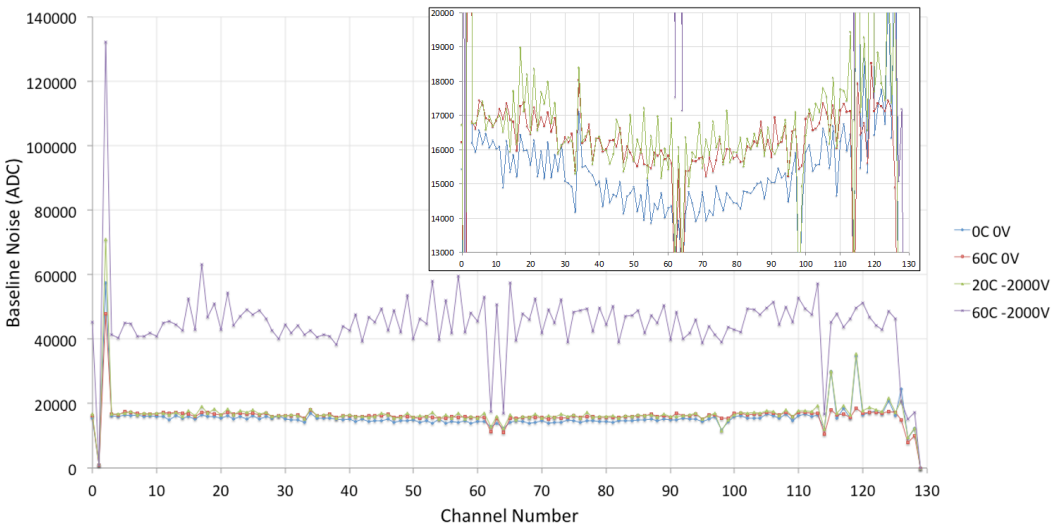

Figure 4.10: The electronic noise measured at 20°C and 60°C with and without the detector #23737-02 biased to -2000V. The inset shows a zoomed in view. Channel 0 corresponds to the average noise over all channels and channel 3 corresponds to the cathode. The remaining channels correspond to individual anode pixels except for several channels that are disconnected (channels 1, 62, 64, 114, 127, 128, and 129).

shaping time of the trapezoidal filter for picking off the anode amplitude can be beneficial, as it reduces the integration of noise. For detector #23737-02 at 60°C, this improved the depth-corrected energy resolution by 0.1% for single-pixel events, and more significantly for multi-pixel events.

Lastly, the noise at different dynamic ranges at 60°C was measured, as shown in Fig. 4.13. The noise increases by almost 2 keV when the dynamic ranges is increased from the smallest to largest, which is very similar to the increase seen at 20°C [20]. The fact that there appears to be no extra noise at high dynamic ranges due to the increase in temperature is promising for high-energy measurements at high temperatures.

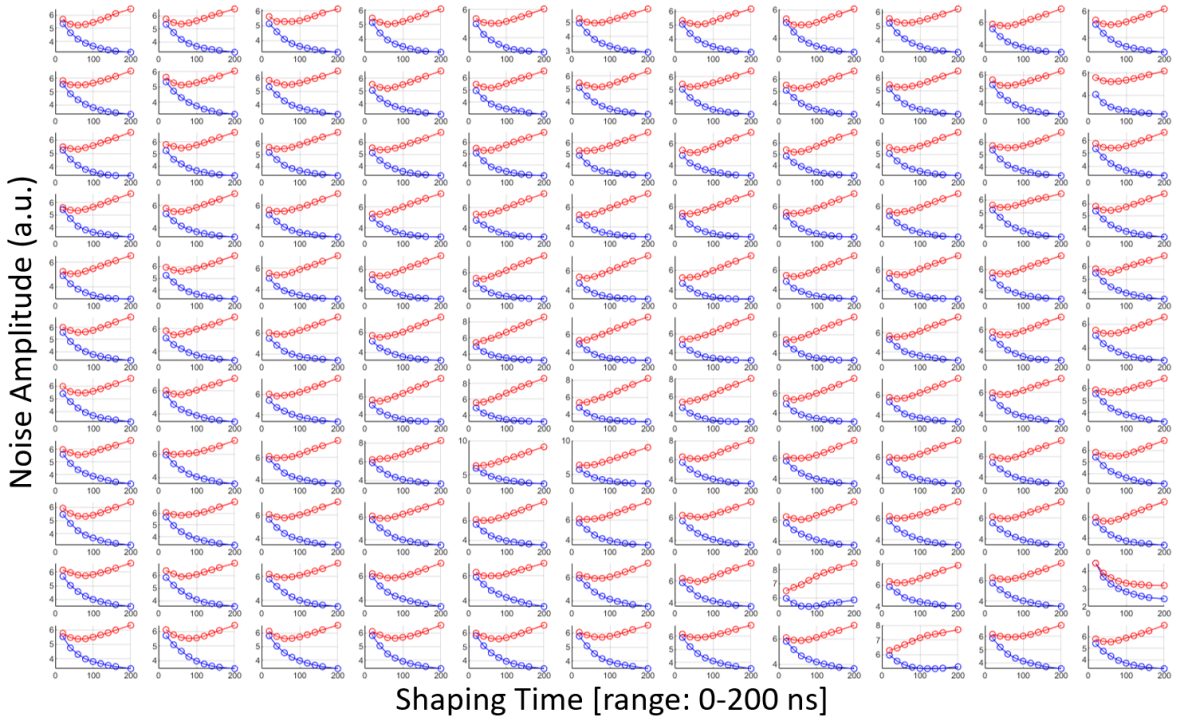

Figure 4.11: Noise as a function of shaping time (CR-RC^4 filter) at 20°C (blue) and 60°C (red) for all anode channels. Detector #23737-02 was plugged in and biased to -2000V and the dynamic range was 700 keV.

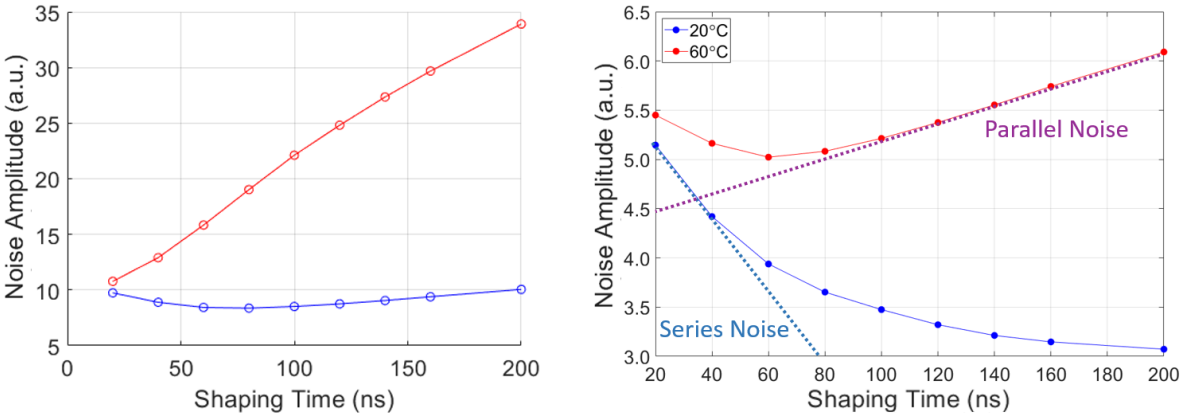

Figure 4.12: Noise as a function of shaping time (CR-RC^4 filter) at 20°C (blue) and 60°C (red) for the cathode channel (left) and for an example anode channel with series and parallel noise labeled (right). Detector #23737-02 was plugged in and biased to -2000V and the dynamic range was 700 keV.

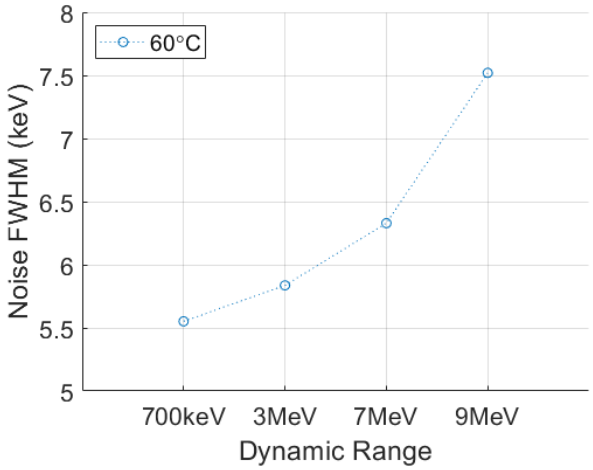

Figure 4.13: Noise as a function of dynamic range at 60°C for detector #23737-02 biased to -2000V.

4.4 Energy Resolution

The depth-corrected single-pixel energy resolution FWHM at 662 keV is shown in Fig. 4.14. At 60°C, resolution was ∼0.85% for the high-temperature Redlen CZT, ∼1% for the standard Redlen CZT, and just below 1.3% for the standard Kromek CZT. The difference in resolution between the two measurements of #10R2 at 60°C shows the importance of optimizing the anode pre-amplifier feedback resistance (it was not optimized during the warming cycle for #10R2). While the resolution at room-temperature was similar for all detectors (within a range of ∼0.1%), it appears that small differences in resolution at room-temperature become more dramatic at high-temperature. For example, the resolution of the Kromek detectors was just slightly worse than the other detectors at 20°C (by 0.04% to 0.1%), but was much worse at 60°C (by 0.23% to 0.45%). In the future, detectors with better resolution at room temperature could be selected for high-temperature measurements to help yield better results. The room-temperature energy resolution of the detectors used in this study was not the best possible (i.e. the best detectors can achieve near 0.3%).

High leakage can degrade energy resolution because it will increase the noise; however, it is not the only factor to consider. For example, the performance of Kromek detectors #14544-02 and #23737-02 can be compared. At 60°C, detector #23737-02 had the highest leakage and detector #14544-02 had the lowest leakage, yet they both had

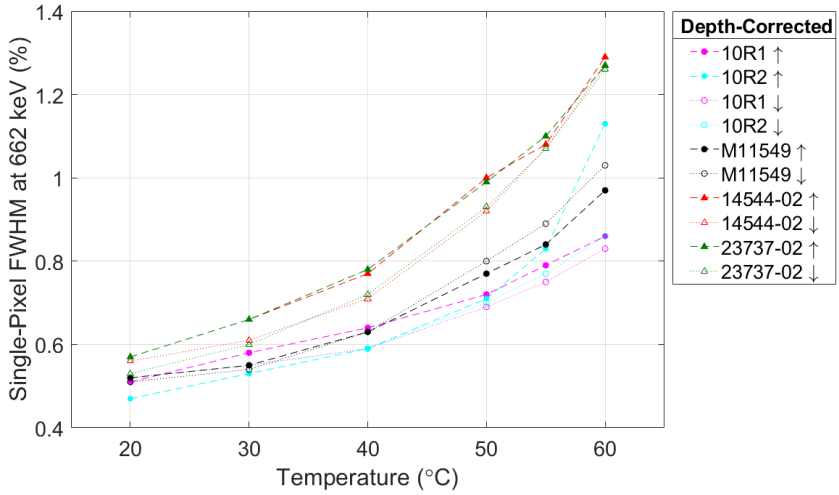

Figure 4.14: Depth-corrected single-pixel energy resolution FWHM at 662 keV measured during the warming (↑) and cooling (↓) cycle for all detectors while at -2000V bias. Circle and triangle markers indicate detectors from Redlen and Kromek, respectively.

the same energy resolution. The pixel-by-pixel performance (Fig. 4.15) can shine some light on this discrepancy. At 20°C, detector #23737-02 had very uniform resolution, whereas detector #14544-02 was non-uniform. Several pixels of detector #14544-02 had better resolution than pixels in detector #23737-02, but towards one side of the detector, the resolution was much worse. The poor resolution in this region was not related to electronic noise. At 60°C, the resolution in the poor region becomes much worse, over 2% for many pixels, whereas the resolution is very good on the other side of the detector, <0.9% for several pixels. On the other hand, the resolution of detector #23737-02 remains uniform but even the best pixels are still above 1%.

As shown previously in Fig. 4.5, the cathode noise degrades at high temperatures. This will worsen the position resolution of the depth of interaction estimate. The effect this has on energy resolution will depend on the amount of electron trapping. The heavier the electron trapping, the greater the variation in amplitude as a function of depth, and the more important it is to accurately calculate the depth of interaction to prevent a degradation in energy resolution. In general, the amount of electron trapping was relatively low for all the detectors temperature-tested in this study (i.e. the resolution did not degrade towards the cathode-side for the majority of pixels). Detector

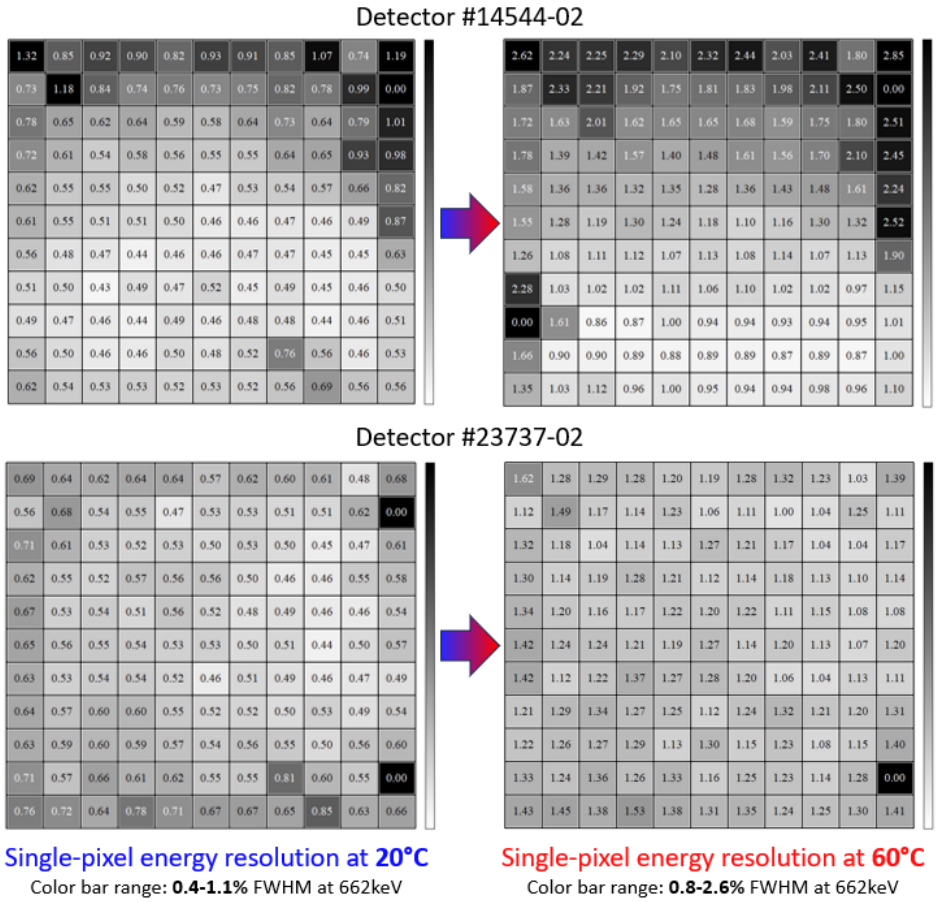

Figure 4.15: Depth-corrected single-pixel energy resolution FWHM at 662 keV on a pixel-by-pixel basis at 20°C (left) and 60°C (right) for Kromek CZT detectors #14544-02 (top) and #23737-02 (bottom). Bias was -2000V. The color bar range is consistent for each temperature.

M11549 had higher cathode noise during the cooling cycle compared to the warming cycle (Fig. 4.5). Though electron trapping was low, there was still a small degradation in energy resolution (<0.06%, shown in Fig. 4.14) when the cathode noise was most severe, at 50°C and above. For a detector with heavy electron trapping, an even more significant degradation in energy resolution would be expected. So while leakage is a limiting factor for resolution in terms of electronic noise, its effect on depth-estimation should be considered as well. Therefore, if CZT vendors are unable to find a way to minimize detector leakage, reducing electron trapping in CZT would be another way to minimize energy resolution degradation at high temperatures.

One easy way to reduce leakage, and thus electronic noise, is to reduce the applied bias. Fig. 4.16 shows the energy resolution measured at 60°C as a function of applied bias. For all of the detectors, the best resolution was achieved from measurements at either -1000V or -1500V, not at -2000V. The best depth-corrected single-pixel energy resolution achieved at 60°C was 0.78% for detector #10R1 at -1500V. The bias should not be reduced too much, as there is balance between reducing leakage to improve noise and degrading the charge carrier properties. Lowering the bias reduces the strength of the electric field and reduces the electron drift velocity. This increases the probability of electron charge trapping so the amplitude of events will decrease, worsening the signal-to-noise ratio and energy resolution (especially if the increase in trapping is not fully corrected for by the depth-correction). At room temperature, energy resolution typically degrades when the bias is reduced, which was also observed in this study. Because detector leakage is not the main contributor to noise at room temperature, decreasing the leakage/bias does not provide much benefit.

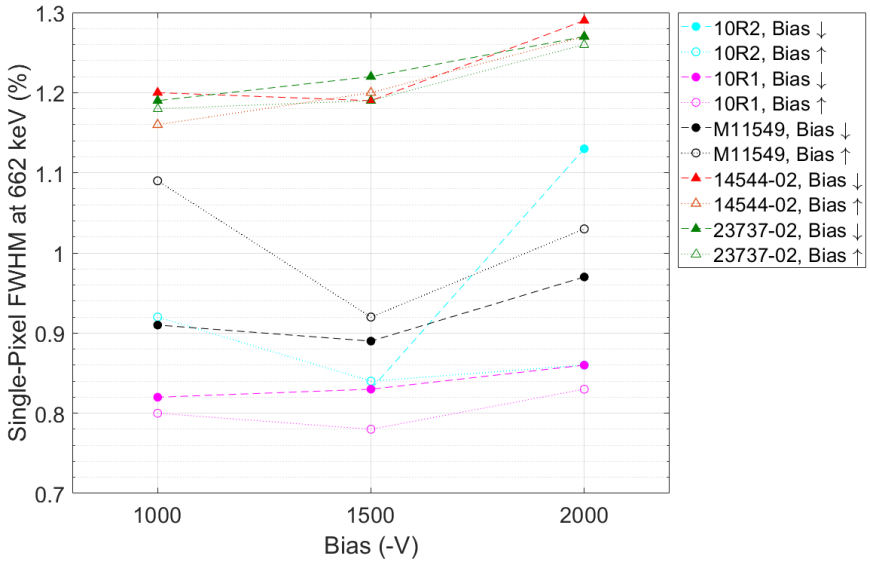

Figure 4.16: Depth-corrected single-pixel energy resolution FWHM at 662 keV as a function of applied cathode bias at 60°C. In chronological order, measurements were taken at -2000V, -1500V, and -1000V (Bias ↓) and then at -1000V, -1500V and -2000V (Bias ↑). Circle and triangle markers indicate detectors from Redlen and Kromek, respectively.

Another way to improve energy resolution at high temperatures is to compensate for

changes in photopeak centroid (662 keV) location over the time of the measurement (called time-correction). The depth and time-corrected single-pixel energy resolution FWHM at 662 keV is shown in Fig. 4.17. With depth-correction, the resolution at 60°C ranged from 0.83% to 1.29%. When the time-correction is added, the range in resolution improved to 0.75% to 1.15%. For detector systems with temperature regulation used in the lab (and not in the environmental chamber), this correction usually does not improve resolution and is therefore not typically used. Because some improvement in energy resolution was seen in this experiment, it indicates fluctuations in gain during each measurement were significant. The gain is very sensitive to temperature, which is discussed further in Section 4.6. The temperature in the environmental chamber may oscillate over time due to how the air is cycled in the enclosed area of the environment chamber, whereas the temperature may be more stable in a large open area. There can also be drift in the temperature if the measurement was taken too soon after a temperature setting change. The time-correction provides an estimate of the performance if changes with gain over time are corrected properly. In reality, systematic changes in gain with temperature would need to be calibrated ahead of time for on-the-fly measurements, as the presence and identity of sources may be unknown. The time-correction also corrects for any unexpected changes in gain that would not be fixed during in-field measurements even with a temperature calibration.

4.5 System Response Functions

The mean SRFs at 20°C and 60°C are shown for the Redlen and Kromek detectors in Figs. 4.18 and 4.19, respectively. The mean SRFs are the average cathode-side event waveforms for the center 5×5 pixels. The cathode SRFs represent the full drift of the electron cloud. For all detectors, the cathode signal takes longer to rise at 60°C, which indicates the electron drift is slower by ∼10%. There are two reasons for this. First, as mentioned in Section 4.3, the effective applied bias is reduced at high temperatures, which weakens the electric field (E). Secondly, the electron mobility (μ_e) will decrease with increasing temperature, due to an increase in lattice (phonon) scattering. Both of these factors are proportionally related to the electron drift velocity v_d (i.e. $v_d = \mu_e E$), thus a decrease in either will decrease the drift velocity and increase the total drift time. Since the leakage and resistor value is known, the effective applied bias and the expected

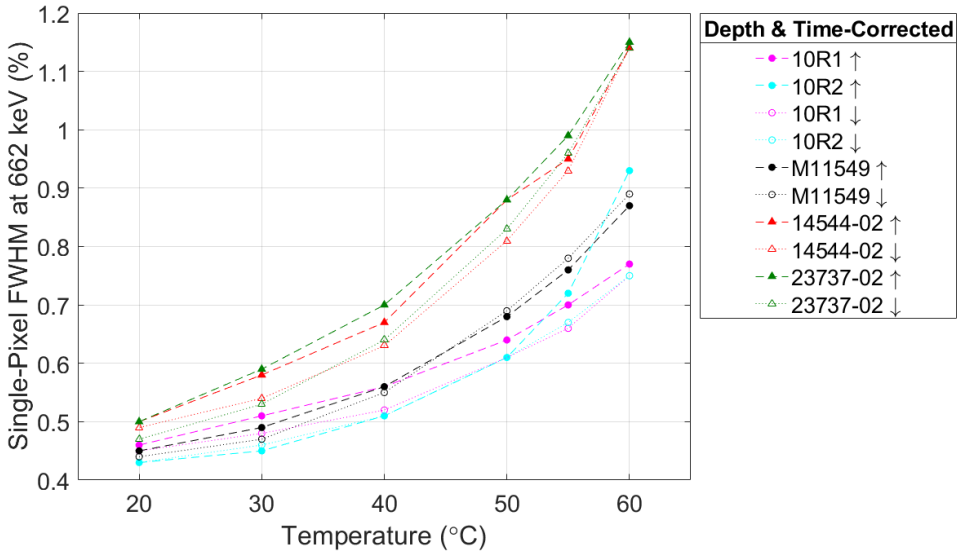

Figure 4.17: Depth and time-corrected single-pixel energy resolution FWHM at 662 keV measured during the warming (↑) and cooling (↓) cycle for all detectors while at -2000V bias. Circle and triangle markers indicate detectors from Redlen and Kromek, respectively.

increase in drift time due to the reduced electric field can be estimated. From this, it is estimated that the increase in drift time is mostly due to the reduced bias, and only slightly due to a decrease in electron mobility.

For the Redlen CZT detectors (Fig. 4.18), the rise in the anode SRFs is just slightly more rounded at high temperature, likely due to the slower electron drift. For the Kromek CZT detectors (Fig. 4.19), the anode SRFs are much rounder towards the end of the signal rise at 20°C than at 60°C. The rounder signal at 20°C suggests that the electron detrapping rate was significantly slower at 20°C for the Kromek CZT. As shown in Fig. 4.20, the change in the shape of the anode SRF was most significant when the temperature was increased from 20°C to 30°C and was minimal at higher temperatures. The transition temperature may be related to the corresponding energy level of the electron traps. Changes in detrapping rate was not seen for the Redlen CZT (direct comparison in Fig. 4.21), indicating there are differences in the material properties of CZT from the two vendors.

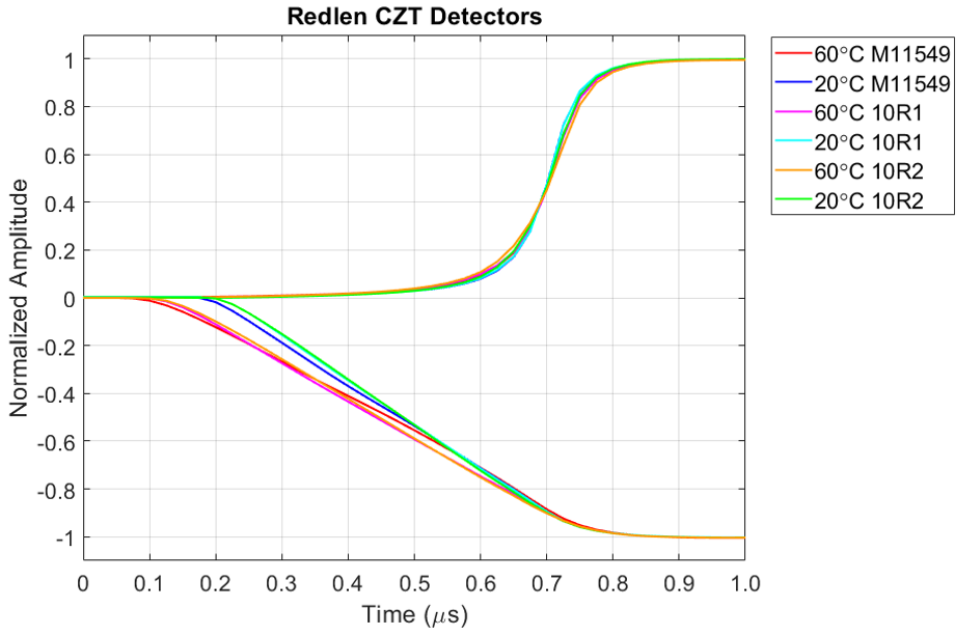

Figure 4.18: The mean anode (positive) and cathode (negative) SRFs at 20°C and 60°C for the Redlen CZT detectors.

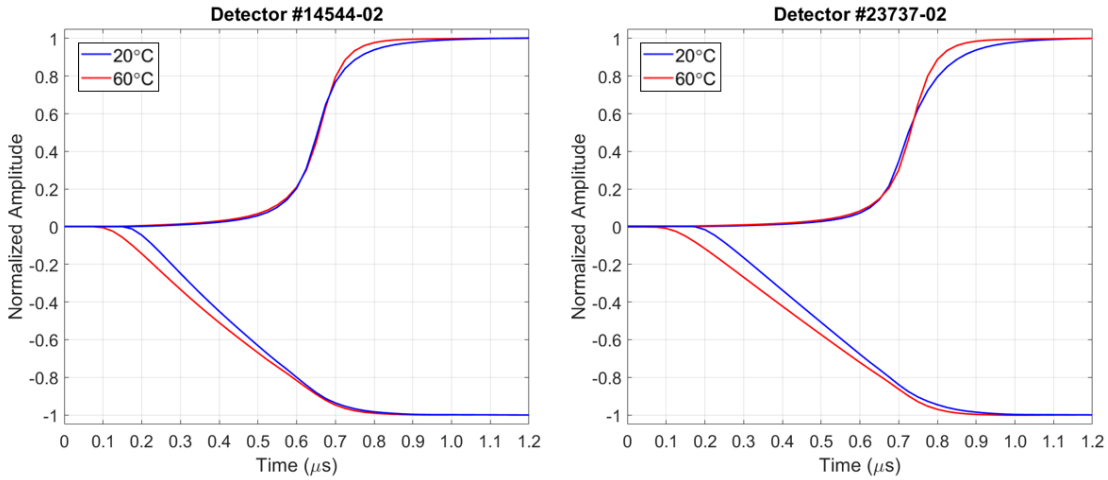

Figure 4.19: The mean anode (positive) and cathode (negative) SRFs at 20°C and 60°C for the Kromek CZT detectors.

4.5.1 Anode Tail Rise Issue

Also evident in Fig. 4.21 is a change in the anode tail slope. As temperature increased, the slope of the anode tail signal typically became more positive, as shown in Fig. 4.22

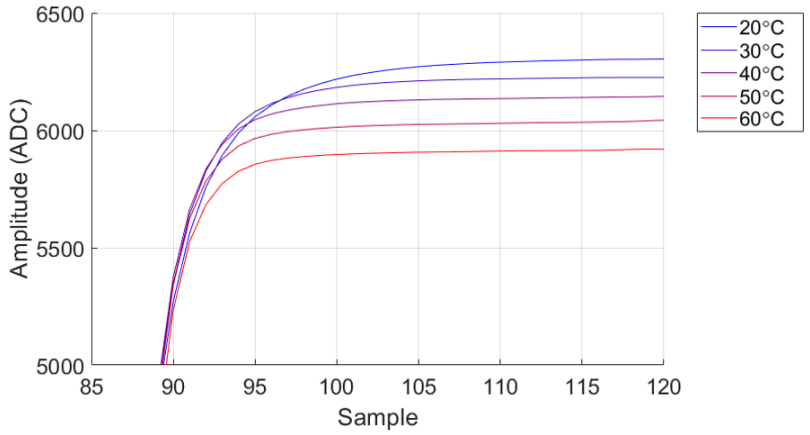

Figure 4.20: The rising turn of the mean anode SRFs as a function of temperature for Kromek CZT detector #14544-02. The sampling rate was 40 MHz.

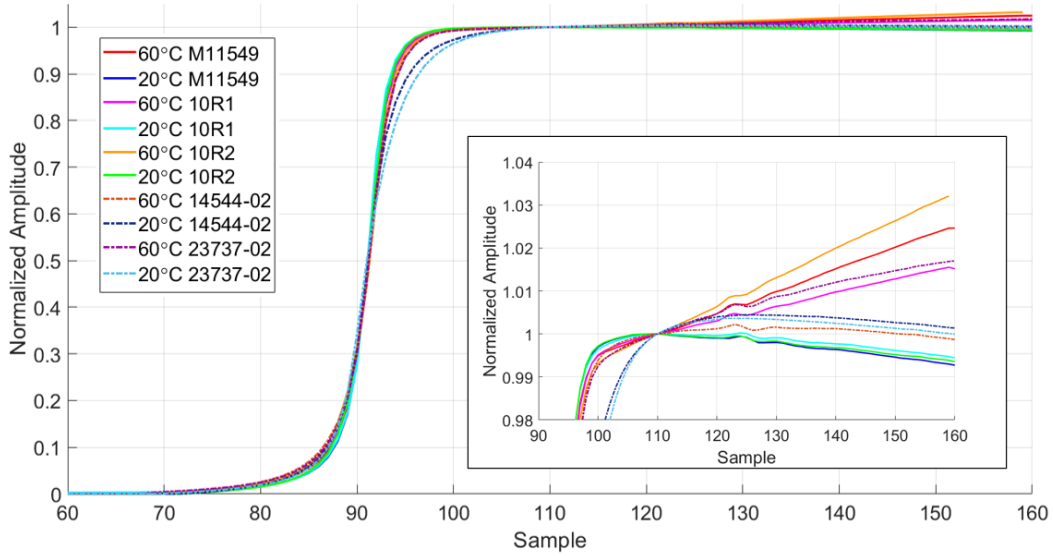

Figure 4.21: The normalized and aligned mean anode SRFs at 20°C and 60°C for the Redlen (solid lines) and Kromek (dashed lines) CZT detectors. The inset provides a zoomed in view of the anode tails. The sampling rate was 40MHz.

for detector M11549. This "anode tail rise" was only seen at amplitudes near the high end of the 700 keV dynamic range, causing non-linearity in the energy response. In the depth-corrected energy spectra, the 662 keV peak is used as the reference for the energy

calibration. This caused the low energy peaks from the ^{137}Cs X-rays and ^{241}Am to be underestimated at high temperatures, with the extent depending on the severity of the anode tail rise. At 60°C, the discrepancy in the gain of the 662 keV peak and 59.5 keV peak was ∼1%.

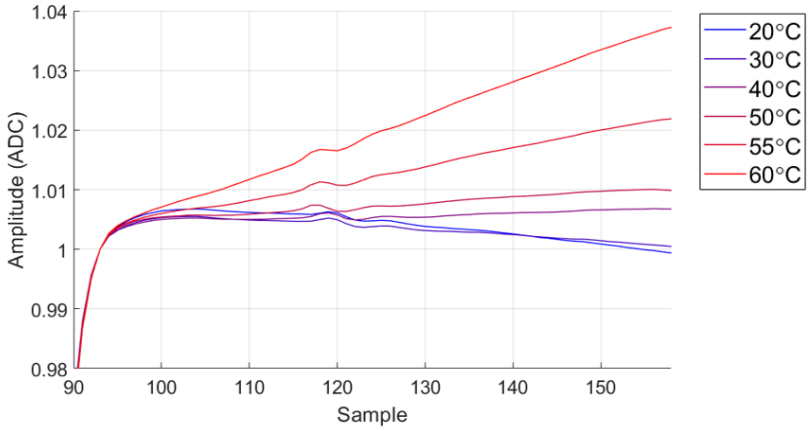

Figure 4.22: The tail region of the mean anode SRFs as a function of temperature for detector M11549. The sampling rate was 40MHz.

To quantify the anode tail rise per pixel, the anode SRFs at depth bin 40 (cathode-side interactions) was normalized to the value at sample 110 (40 MHz sampling rate) at each temperature, as shown in Fig 4.23. Sample 110 is a point in the waveform just shortly after collection of the electron cloud. The difference in the amplitude (relative to 20°C) of the normalized SRF at sample 160 multiplied by 100 gives the anode tail rise percentage. The degree of anode tail rise varied pixel-to-pixel and detector-to-detector, tending to be roughly proportional to the electronic noise of the pixel as shown in Fig. 4.24. The variation by pixel, detector, and amplitude makes it difficult to correct for the issue: a pixel-by-pixel non-linearity calibration would be needed at each temperature for every detector. This can be a rather time consuming process, requiring a large amount of data and multiple check sources.

While the SRFs at depth bin 40 were used in this analysis, it should be noted that the degree of anode tail rise appeared to be independent of the depth of interaction. This observation and the presence of anode tail rise in test pulses suggests that it is a problem with the electronics, rather than related to the CZT material. Since a correlation with electronic noise is seen, the issue could be related to high leakage as leakage contributes

to electronic noise. The ASIC was designed based on the expected leakage at room-temperature, about 1 nA per pixel. Based on the measured total leakage at 60°C, the per pixel leakage could be an order of magnitude larger (i.e. 10's of nA). Additionally, local variations in leakage could explain the pixel-to-pixel variation in anode tail rise; however, measurements of leakage on a per-pixel basis would be needed to confirm this hypothesis. High leakage can increase the DC voltage level of a channel's baseline. Thus, when the amplitude of an event is large (e.g. 662 keV) relative to the dynamic range and the baseline value is larger than normal, the total signal may come closer to the high-end of the dynamic range where the pre-amplifier response may no longer be linear. This could explain why high-amplitude events have the unexpected feature in the tails but the low-amplitude events do not.

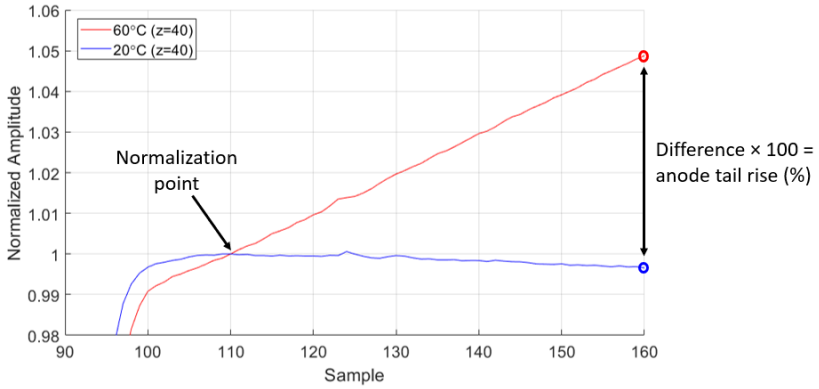

Figure 4.23: Example of how the anode tail rise (%) is calculated from the normalized anode SRFs.

Based on this hypothesis, additional measurements were taken for detector #23737-02 at 60°C using the next largest dynamic range setting, 3 MeV, to see if there were any improvements. The anode SRFs measured for all pixels using the 700 keV dynamic range and 3 MeV dynamic range are compared in Fig. 4.25. In general, there is less variability pixel-to-pixel in the slope of the anode tails when using the 3 MeV dynamic range. For the 3 MeV dynamic range measurement, the anode signals consistently have a small amount of decay in the tails at both high and low amplitudes. This slight decay is due to the pre-amplifier feedback resistance setting. In contrast, for the 700 keV dynamic range measurement, the anode signals have rise in the tail at high amplitudes, and more significant decay at low amplitudes. Therefore, the 3 MeV dynamic range can be used

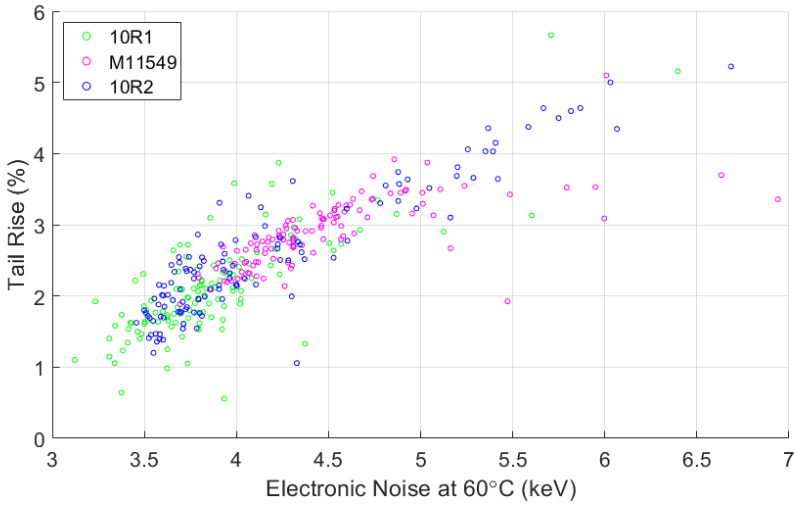

Figure 4.24: Anode tail rise (%) at 60°C as a function of electronic noise at 60°C on a pixel-by-pixel basis for Redlen CZT detectors.

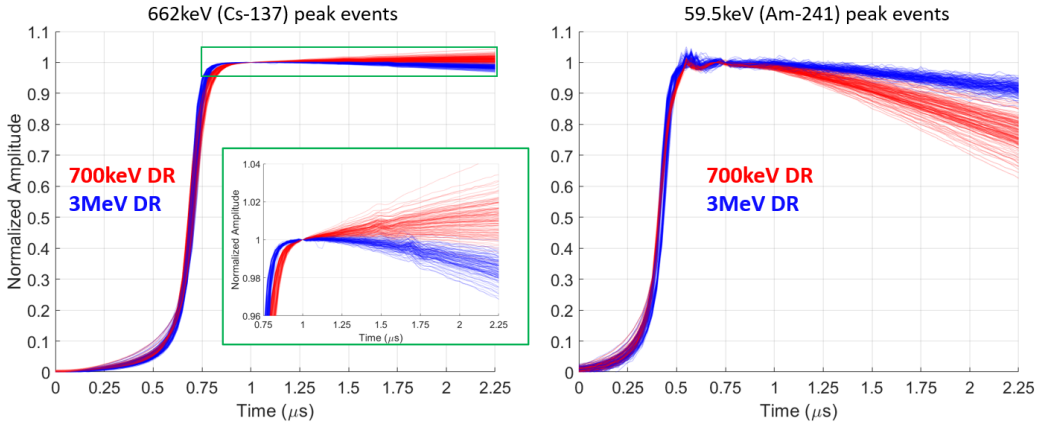

Figure 4.25: SRFs at 60°C for all anode pixels in detector #23737-02 with 700 keV dynamic range (red) and 3 MeV dynamic range (blue) ASIC settings. The SRFs for the two dynamic ranges are compared for both high (left) and low (right) amplitude events.

to help reduce non-linearity. Fig. 4.26 shows that there is significant improvement in the accuracy of the energy reconstruction of low energy peaks when using the 3 MeV dynamic range.

The downside of using a larger dynamic range is that the electronic noise increases, as mentioned in Section 4.3.1, which can worsen the energy resolution. However, it was

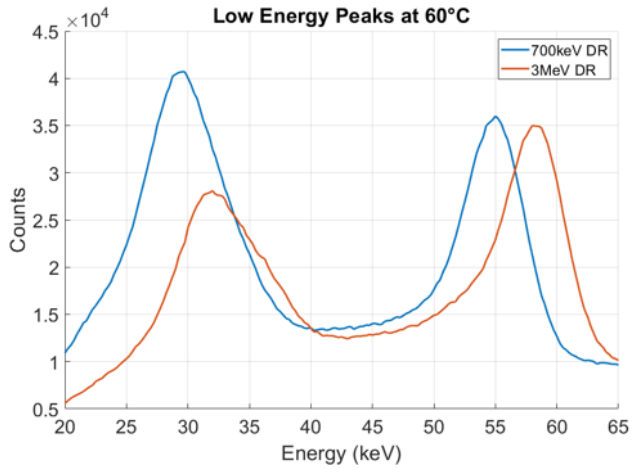

Figure 4.26: The low energy peaks (^{137}Cs X-rays at 32 keV and 36 keV and ^{241}Am 59.5 keV peak) in the anode energy spectra using the 700 keV dynamic range (blue) and 3 MeV dynamic range (orange) ASIC settings with detector #23737-02 at 60°C. The energy was reconstructed based on the amplitude of the ^{137}Cs 662 keV peak.

found that the benefits gained from the improved pre-amplifier stability using the 3 MeV dynamic range outweighed the effect of increased electronic noise as very similar energy resolution at 662 keV can be obtained using either the 3 MeV dynamic range or the 700 keV dynamic range without a non-linearity correction, as shown in Fig. 4.27. Therefore, to avoid time-consuming non-linearity corrections, a more pragmatic solution to the anode tail rise issue is to use a larger dynamic range setting.

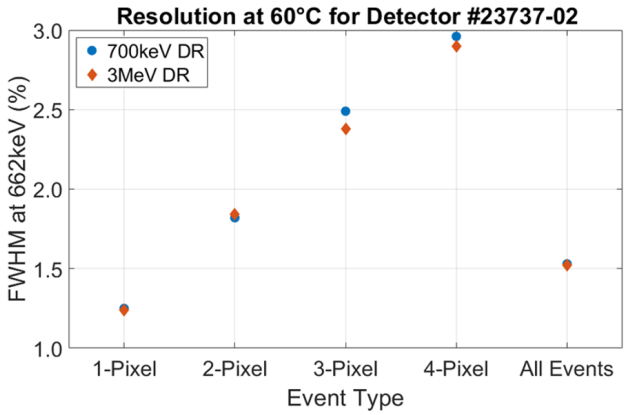

Figure 4.27: The depth-corrected energy resolution for detector #23737-02 at 60°C using the 700 keV (blue) and 3 MeV dynamic range (orange).

4.6 Gain

In previous work [20][16], it was shown that the electronic gain decreases with increased temperature and the relationship is approximately linear. Similarly, an approximately linear trend was seen in these measurements (Fig. 4.28), except there was some deviation at 50°C and above. Some variation in gain was expected due to the adjustment of the pre-amplifier feedback resistance setting and changes in the SRFs (Section 4.5.1) affecting the anode tail and thus the estimation of gain. However, some unexpected changes in gain were observed during the experiments, which will be discussed in the remainder of this section.

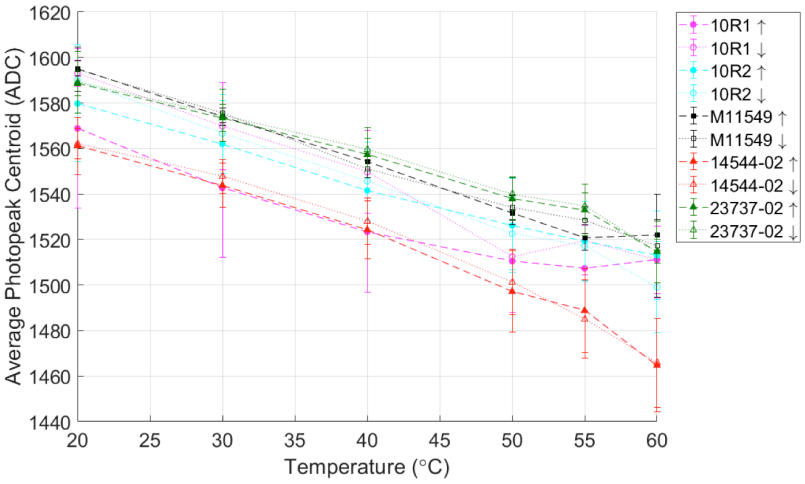

Figure 4.28: Gain (average 662 keV photopeak centroid, ADC) measured during the warming (↑) and cooling (↓) cycle for all detectors while at -2000V bias. Circle and triangle markers indicate detectors from Redlen and Kromek, respectively.

4.6.1 Gain Deficit

The raw anode spectrum for the standard Redlen CZT detector is shown in Fig. 4.29. A decrease in gain with increased temperature is seen for each peak. The broadening of peaks is most apparent for the low-energy peaks as their FWHM depends heavily on the electronic noise. The photopeak shape is consistent during heating and cooling which is in stark contrast to the raw photopeak during heating and cooling for the high-

temperature Redlen CZT #10R2 (Fig. 4.30). Initially at 20°C, there are multiple bumps in the peak due to large variations in gain pixel-to-pixel. At 60°C, the peak has a long flat top. Over extended time at 60°C and upon cooling, there is improvement in the peak shape until at 20°C, the shape is nearly the same as for the standard Redlen CZT. The change in the peak shape was due to a gain deficit issue. Both high-temperature Redlen CZT detectors initially had a significant number of gain deficit pixels which lead to a lower average gain during heating. Eventually, the higher temperatures cured the gain deficit in many pixels, causing a higher average gain during the cooling cycling. As shown in Fig. 4.28, this trend is only apparent for the high-temperature Redlen CZT detectors (#10R1 and #10R2), as the other detectors did not have gain deficit issues.

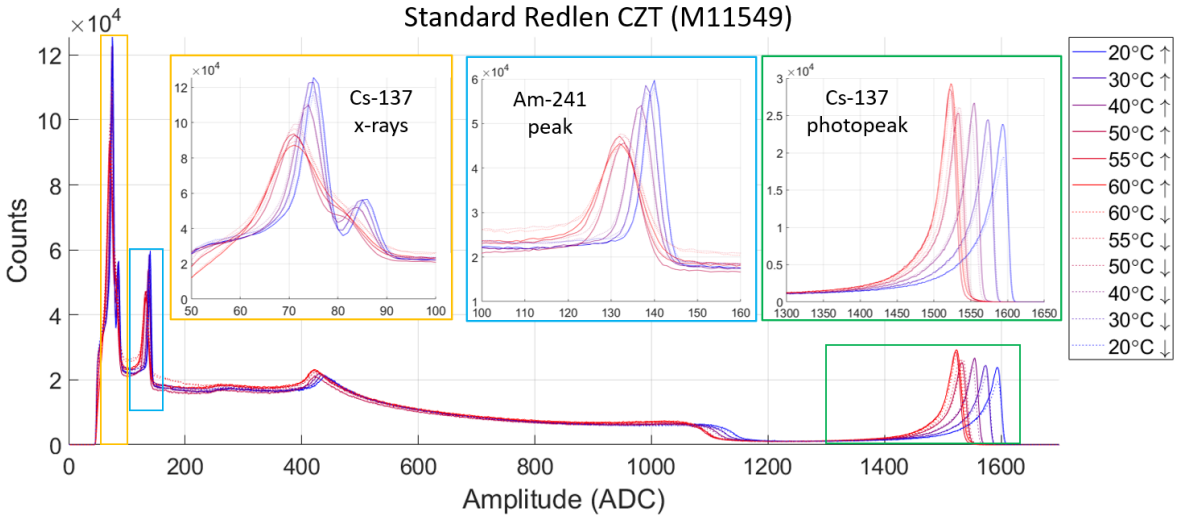

Figure 4.29: The raw anode spectrum as a function of temperature during the warming (↑) and cooling cycle (↓) for the standard Redlen CZT detector M11549. The bias was -2000V for all measurements.

The change in the distribution of gain on a per pixel basis as a function of temperature is shown in Fig. 4.31. All measurements were taken over a time period of less than two weeks (per detector). At higher temperatures, the spread of gain becomes wider and less peaked. Comparing the two measurements at 20°C, there are fewer pixels with values straying from the main peak after heating and cooling, indicating a decrease in the number of pixels with gain deficit. Unfortunately, the curing of gain deficit was only temporary. Fig. 4.32 shows the mapping of pixel gain at 20°C at multiple points in testing. Immediately after heating and cooling, it appears that the gain deficit is

"healed" for many pixels; however, the number of pixels with gain deficit increases after extended time at room-temperature and becomes worse than the initial state. This behavior is reminiscent of "heat shock" experiments by Xia [20]. Xia saw that quickly heating detectors to 80°C then immediately cooling them to room temperature would heal gain deficit, but only temporarily as gain deficit would reappear in the following weeks. Also interesting, in the third measurement, where the gain deficit is mostly cured, a few pixels that did not initially have gain deficit suddenly do. The gain appears to somewhat depend on the physical location of the pixel on the crystal, as the gain deficit issue appeared to spread to near-by pixels.

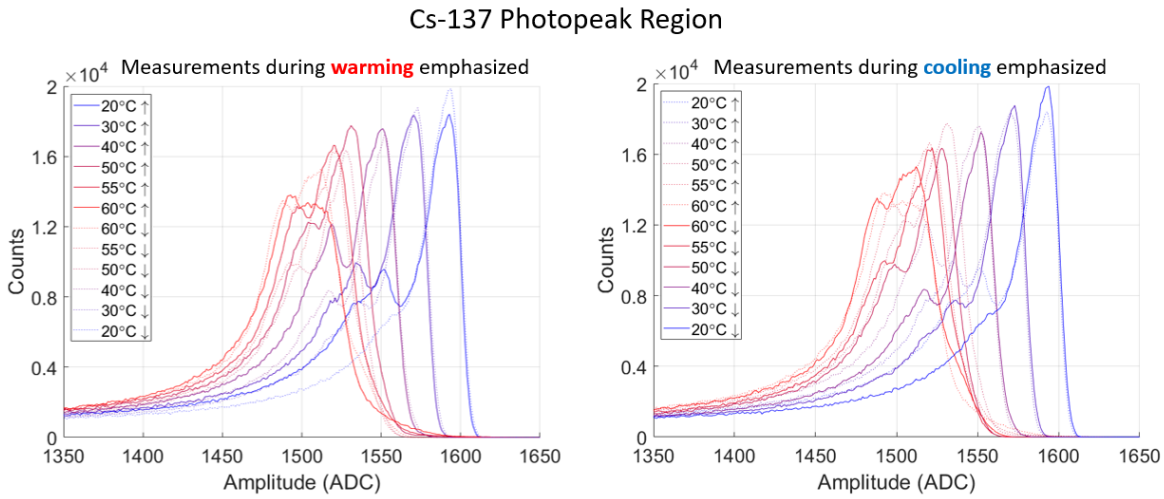

Figure 4.30: The 662 keV photopeak region in the raw anode spectrum as a function of temperature during the warming (↑, emphasized on left) and cooling cycle (↓, emphasized on right) for the high-temperature Redlen CZT detector #10R2. The bias was -2000V for all measurements.

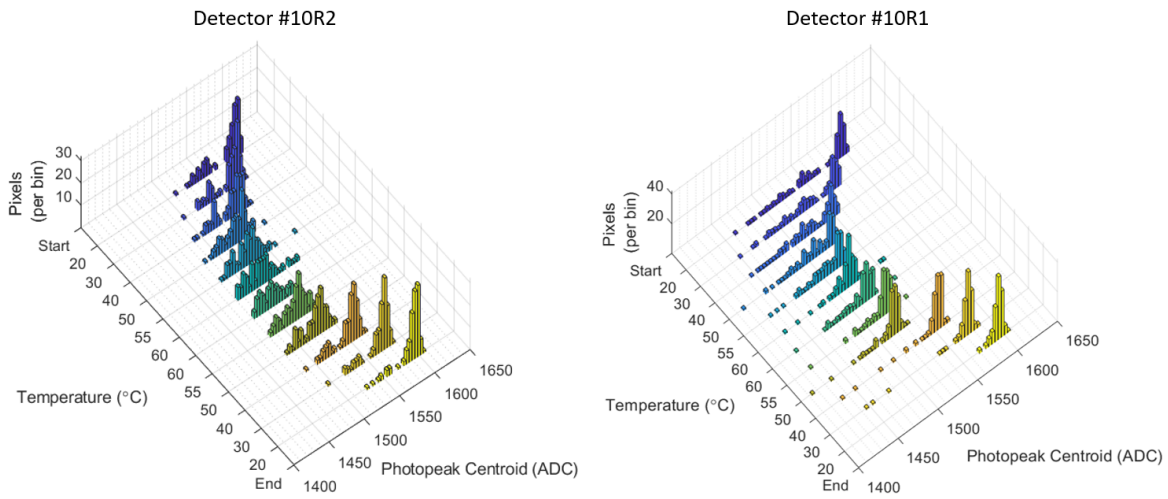

Figure 4.31: The distribution of pixel gain (photopeak centroid) throughout testing of high-temperature Redlen CZT detectors #10R2 (left) and #10R1 (right).

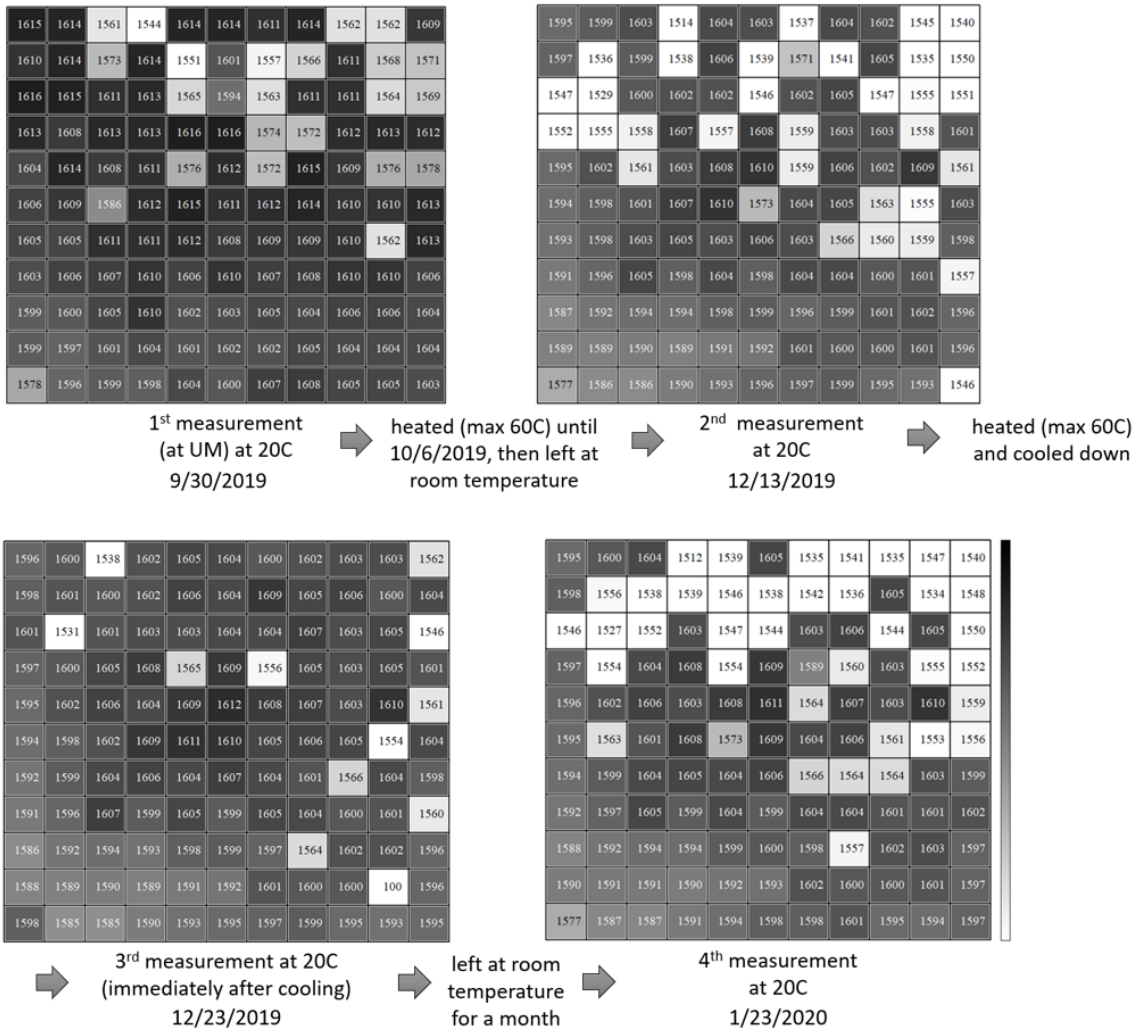

Figure 4.32: The mapping of pixel gain (anode spectrum cutoff) throughout testing of high-temperature Redlen CZT detector #10R2 (left). All measurements were taken at 20°C. The color bar range is 1554 ADC to 1624 ADC in all plots. The significantly lighter pixels indicate low gain / gain deficit.

4.6.2 Gain Switching

Double-peaking was observed in some pixels for the high-temperature Redlen CZT detectors. This double-peaking was observed throughout all depth bins, indicating it was possible that the gain shifted during the measurement. For each 1.5 h measurement, the spectrum was split into 20 time bins, which equates to counts collected from a period of ∼4.5 min in each bin (assuming count rate is approximately constant). Upon examining the time-separated spectra for individual pixels, shifts in the photopeak centroid location were observed for the pixels with double-peaking, as shown in Fig. 4.33. Some shifts occur immediately from one time bin to the next, while in other pixels the photopeak centroid gradually shifted over a few or several time bins. Both increases and decreases in photopeak centroid were observed. Previously, Kaye observed gain shifts between two discrete values in gain deficit pixels [26].

More odd behavior can be seen in Fig. 4.34, the distribution of gain throughout testing of detector M11549. As this detector did not have any gain deficit pixels, it followed a much tighter distribution of gain throughout heating. Strangely, the distribution shifted to higher gain at 60°C after experiencing a steady decline up to 55°C. A similar unexpected jump to lower gain was seen for detector #10R1 at 50°C (Fig. 4.31).

Detector M11549 did not have any obvious instances of individual pixels switching gain during measurements, as seen for detectors #10R1 and #10R2. However, during the measurement at 50°C, there was an overall switch in the peak centroid location, as shown in Fig. 4.35. In the matter of one time bin (∼18 s per time bin), the photopeak centroid shifted up ∼0.5 keV, then leveled off to reach a photopeak centroid ∼0.7 keV greater than its starting value. This shift occurred in all pixels, pointing to electronics as the cause.

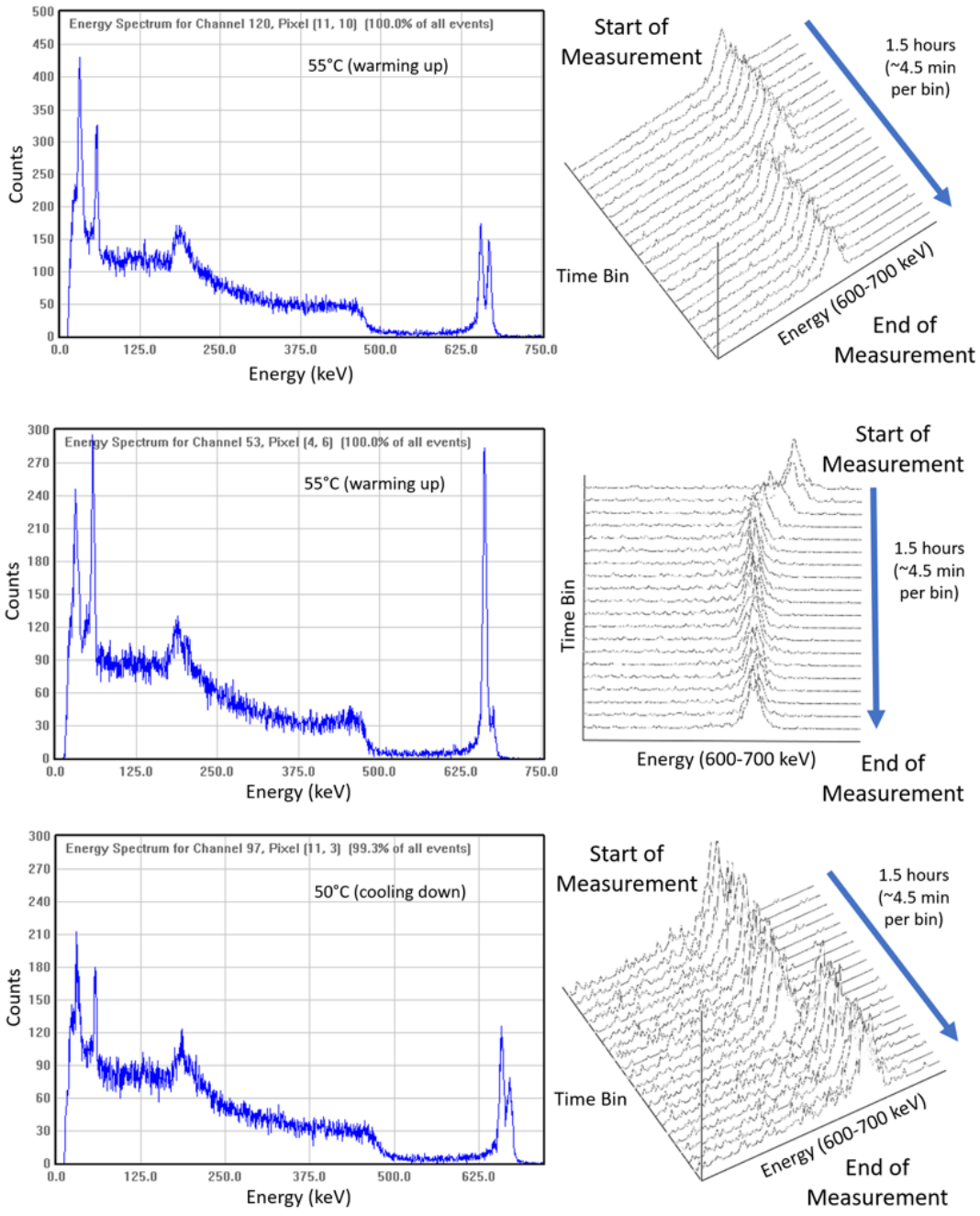

Figure 4.33: Examples of double-peaking in pixel anode spectra for detector #10R2 (left), and the corresponding time-separated spectra (right).

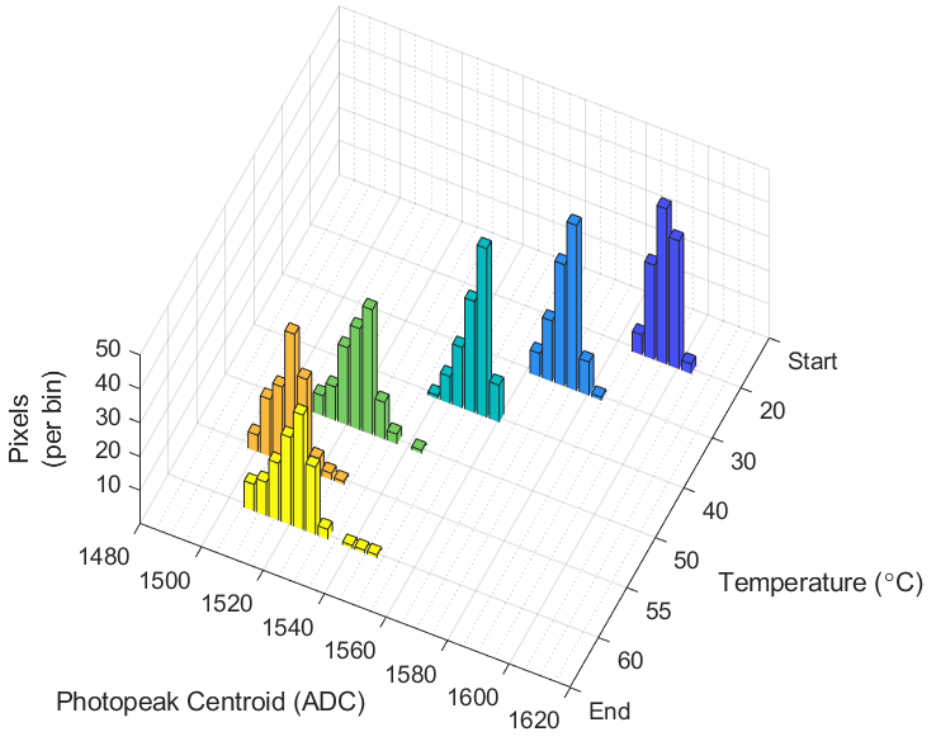

Figure 4.34: The distribution of pixel gain (photopeak centroid) throughout heating of standard Redlen CZT detector M11549.

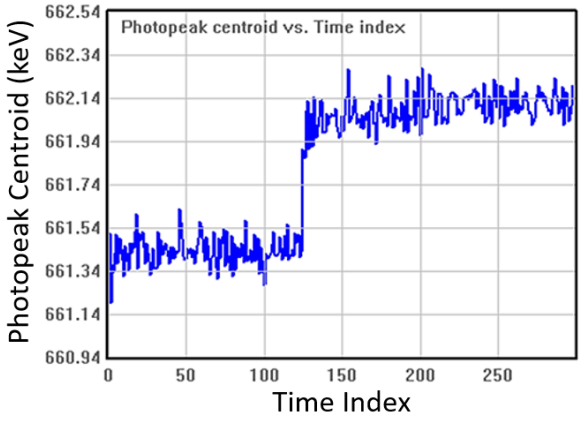

Figure 4.35: The overall photopeak centroid (keV) as a function of time during an hour and half measurement using detector M11549 at 50°C.

4.7 Stability of CZT at 60°C

4.7.1 Kromek CZT

Unlike the high-temperature Redlen CZT detectors, the Kromek CZT detectors appeared to be stable during the experiments described in Section 4.2. While this stability is promising, the time of each measurement was quite short, only 1.5 h, and the stability over longer periods of time at high temperature had not been previously studied. To address this, the stability of both Kromek CZT detectors during ∼24 h measurements of ^{137}Cs at 60°C was studied. The detector bias was constantly -2000V. The single-pixel energy resolution (Fig. 4.36) was very stable over 24 h for both detectors, very slightly improving over the course of the measurement. The gain (Fig. 4.37) slowly increased during the time of the measurement, ∼0.35 keV for detector #14544-02 and ∼0.15 keV for detector #23737-02. Percentage-wise, this is a very small change (<0.1%). The shape of the photopeak (Fig. 4.38) was consistent over the course of the measurement, with a slight improvement for detector #14544-02 just barely visible. Over the course of the measurement, the ASIC temperature increased by ∼0.1%. As discussed in Section 4.6, a slight decrease in gain would be expected, not an increase. This suggests the change in gain was not related to electronics, and instead may be related to a decrease in trapping over time at 60°C.

Figure 4.36: The depth-corrected single-pixel energy resolution for Kromek detectors #14544-02 and #23737-02 over a ∼24 h period at 60°C and -2000V bias.

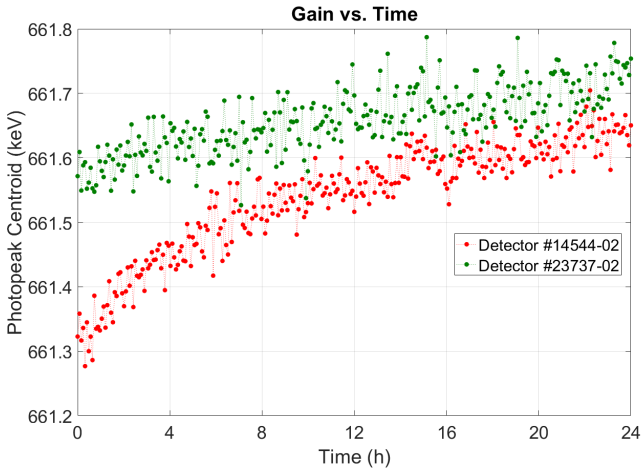

Figure 4.37: The gain for Kromek detectors #14544-02 and #23737-02 over a ∼24 h period at 60°C and -2000V bias.

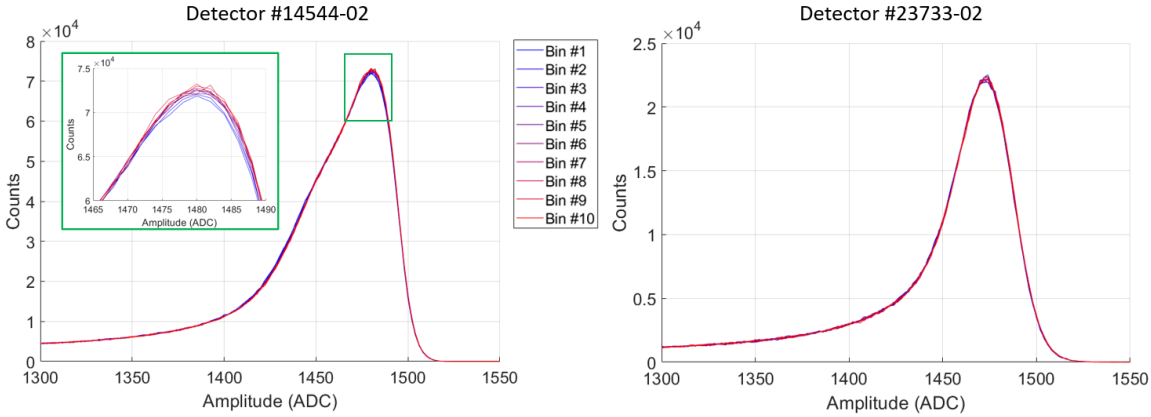

Figure 4.38: The 662 keV photopeak region for Kromek detectors #14544-02 (left) and #23737-02 (right) during a ∼24 h period at 60°C and -2000V bias. The data was split into 10 time bins, where bin #1 corresponds to the beginning of the measurement.

The gain, in terms of photopeak centroid, as a function of time on a pixel-by-pixel basis for detector #14544-02 is shown in Fig. 4.39. The variation in photopeak centroid was less than ∼1% even for the worst pixels. The standard deviation of the photopeak centroid was greater for pixels with worse resolution (resolution shown previously in Fig. 4.15). This suggests that the variation in gain is mainly due to statistics rather than an issue with the CZT material or contact stability at 60°C. Overall, the gain-

related issues seen for the Redlen detectors (Section 4.6) were not observed for the Kromek CZT detectors, even for longer measurements.

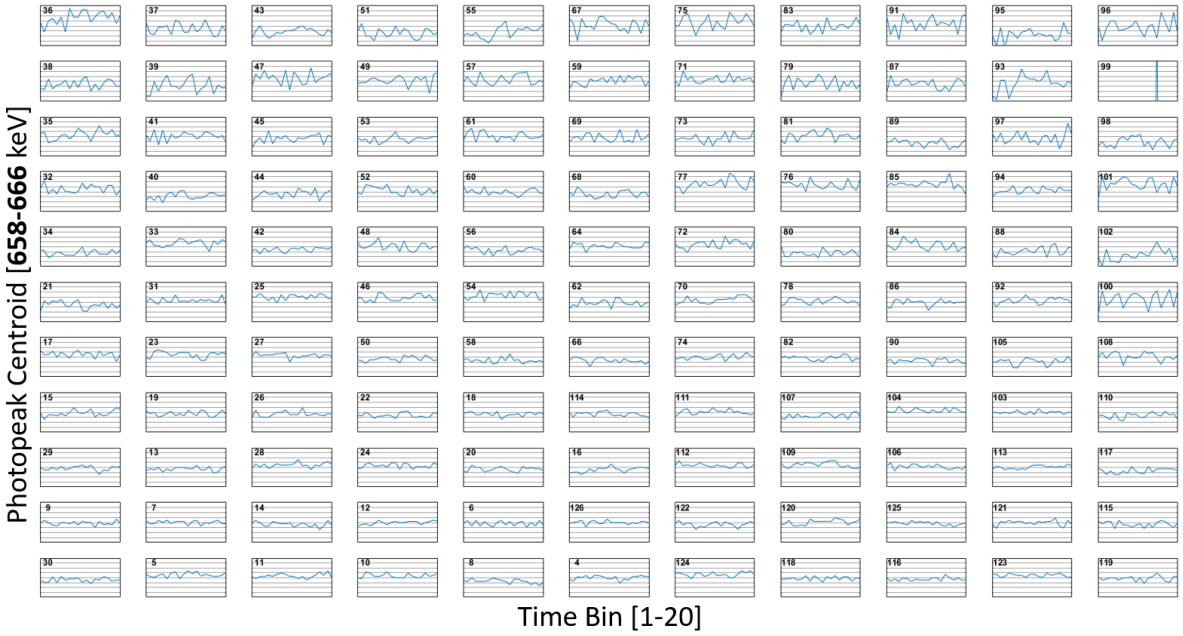

Figure 4.39: The gain on a pixel-by-pixel basis for detector #14544-02 over a ∼24h period at 60°C and -2000V bias. The data was split into 20 time bins.

4.7.2 New High-Temperature Redlen CZT

Later in the study, additional 2.2×2.2×1.0 cm^3 "high-temperature" CZT detectors were received from Redlen. Testing of one of these detectors (detector #M15050) showed that the increase in leakage current as a function of temperature was still similar to what was seen for the previous detectors. However, detector #M15050 had the best depth-corrected single-pixel energy resolution (FWHM at 662 keV) at 60°C with -2000V applied bias measured for any detector so far, 0.8% (for warming cycle measurement) and 0.78% (for cooling cycle measurement). The energy resolution for the best pixel was consistently 0.63% at 60°C, which was better than the resolution for six poor-performance pixels at 20°C. A 65 h ^{137}Cs measurement at 60°C was taken to test the stability of detector #M15050. The energy resolution slightly improved over 65 h as shown in Fig. 4.40.

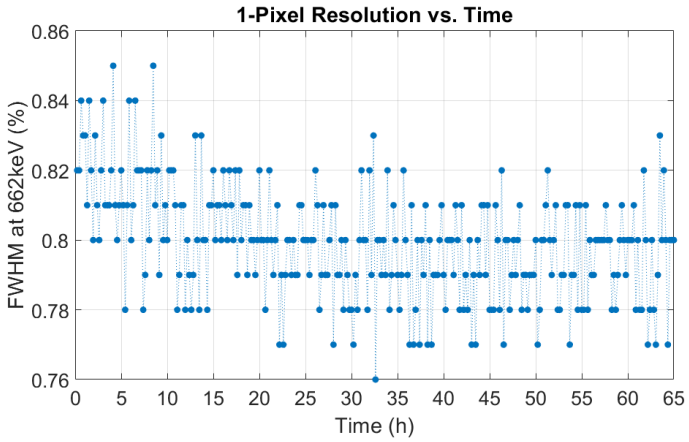

Figure 4.40: The depth-corrected single-pixel energy resolution for the new high-temperature Redlen CZT detector #M15050 over a 65 h period at 60°C and -2000V bias.

For detector #M15050, there were no anode pixels with gain deficit, which was an improvement compared to the previous "high-temperature" CZT detectors. Gain variation during measurements was low; however, gain slowly increased over 65 h at 60°C (Fig. 4.41). The increase in gain was more significant that the increase seen for the Kromek CZT, even when accounting for the length of the measurements. This could be due to different material quality and fabrication techniques used by the two vendors or possibly due to prior heating history. The Kromek detectors had been previously temperature tested (up to 60°C) before the 24 h stability measurements whereas this was the first time detector #M15050 was heated to 60°C at the University of Michigan (though temperature testing by the vendors may have occurred). Experiments carefully designed to determine the effects of heating history on stability are needed and could be the subject of future work.

The increase in gain for detector #M15050 over time was evident on a pixel-by-pixel basis and varied with depth. The gain as a function of depth for the first measurement at 60°C (prior to 65 h measurement), and a measurement approximately four days later are compared in Fig. 4.42. The improvement in gain increases with distance from the anode (z=0), indicating trapping in the detector decreases over time at 60°C. If the change in gain was purely electronic, the change in gain with depth would have been uniform. Also, the leakage measured before the 65 h measurement at 60°C was ∼1,575 nA and the leakage after was ∼1,555 nA, indicating that the resistivity of the detector

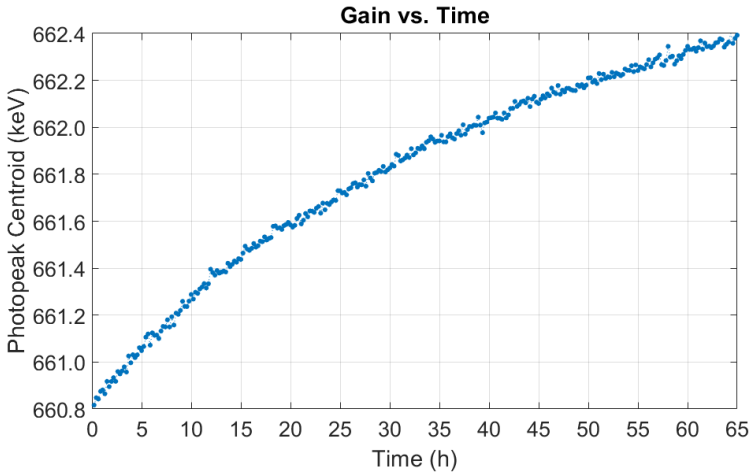

Figure 4.41: The gain for the new high-temperature Redlen CZT detector #M15050 over a 65 h period at 60°C and -2000V bias.

may have slightly increased. The results from this detector provides more solid evidence that an annealing effect occurs at 60°C.

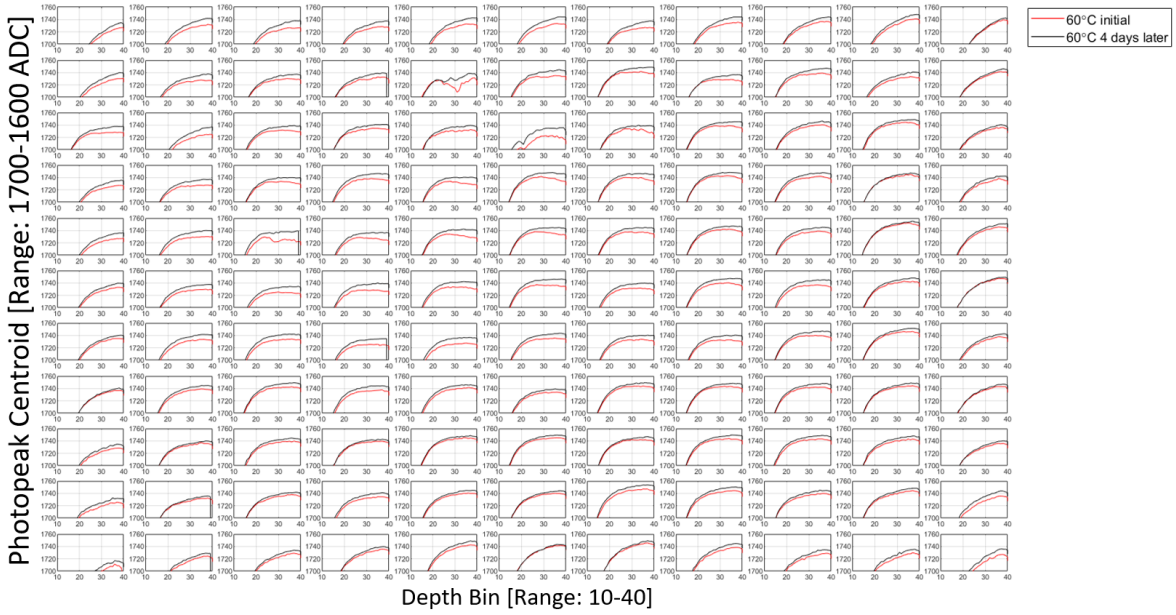

Figure 4.42: The gain as a function of depth for detector #M15050 initially at 60°C and after four days at 60°C.

4.8 Conclusions

While high-temperature operation faces several challenges—such as high leakage, high electronic noise, and gain instability—the testing of these 3D CZT detectors demonstrated that CZT can operate well above room-temperature (up to at least 60°C) without any cooling or temperature regulation. Single-pixel energy resolution below 1% FWHM at 662 keV at 60°C could be achieved for some detectors, which is still reasonable to perform high-resolution spectroscopy. There are many ways to improve performance at 60°C such as adjusting the pre-amplifier feedback, improving the stability of the cathode contact, decreasing bias, improving digital filtering, and making corrections for changes in gain over time.

Apart from gain-deficit issues, high-temperature Redlen CZT performed slightly better than the one standard Redlen CZT in terms of energy resolution at high temperature. Over the course of this study, Redlen was able to find a way to prevent gain-deficit issues (though details are proprietary). Overall, the Kromek detectors showed similar levels of leakage, electronic noise, and energy resolution degradation above room temperature compared to the Redlen CZT. The Kromek detectors had no gain-related issues. However, the two Kromek detectors showed signs of slower electron detrapping at room temperature. There appears to be annealing effects occurring at 60°C, in terms of temporary healing of gain deficit and decrease in trapping. This improves detector performance yet poses an issue for the long-term reliability of detector calibrations. It should be noted that the number of detectors tested in this study was small, so the findings for detectors from each CZT vendor are not necessarily representative of all detectors (or the highest quality detectors) from the vendor. Nonetheless, detectors from both vendors were capable of high-temperature operation up to 60°C.

Chapter 5

Efficiency at Low Temperatures

5.1 Introduction

Now that the operation of CZT in ambient temperatures ranging from 20°C to 60°C has been thoroughly discussed, the focus will shift to operation below room-temperature. The literature on CZT detectors at low temperatures (i.e. below 0°C) is rather limited [38] [39] [40] [41], especially for pixelated CZT [42], and not very recent (from over 15 years ago). The major challenges associated with high temperature operation (i.e. high leakage and high noise) are no longer an issue below room-temperature to the point that even better energy resolution can be obtained. However, an unexpected challenge at low temperatures is a significant drop in efficiency for some detectors. The stability of detector efficiency over a broad temperature range is critical for safeguards applications, where these detectors may be used to quantify the presence of special nuclear materials. An unexpected change in efficiency could result in an inaccurate quantification, and therefore poses a serious issue in this application space.

5.2 Experimental Setup

Four 2.2×2.2×1.0 cm^3 CZT detectors (Fig. 5.1) from Redlen were tested at 20°C and -10°C: detectors M53738 #1, M53733 #2, M53236 #3, and M53739 #4 (referred to as detectors #1, #2, #3, and #4 for brevity). These detectors were initially identified as having reduced efficiency more than the average detector below 0°C. The VAD UM v2.2 digital ASIC single board system was used for readout. The front-end enclosure of

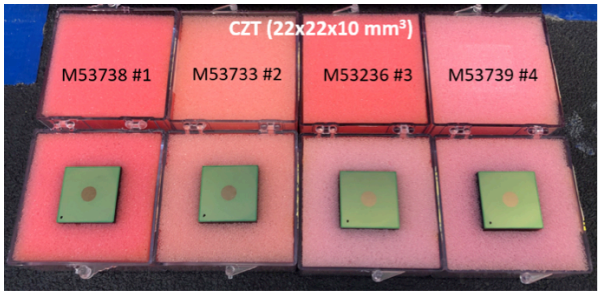

Figure 5.1: The four Redlen CZT detectors used in the low temperature efficiency study.

the system (containing the CZT and ASIC, and no temperature regulation) was placed inside an environmental chamber set to either 20°C or -10°C. Measurements were taken when the ASIC temperature was at an equilibrium. This is the same setup used for the high-temperature experiments.

Low energy sources (^{241}Am and ^{57}Co) and ^{137}Cs were used in this study. In measurements with ^{241}Am, the source was placed on the cathode-side of the detector, so that the majority of radiation interactions occurred near the cathode. Because the depth-of-interaction was similar for most events, a depth-gain correction was not necessary. This helped rule out the quality of the depth-gain correction as a contributing factor for changes in efficiency. ^{57}Co penetrates a bit further into CZT than ^{241}Am and was primarily used for collimator experiments. Flood irradiations with ^{137}Cs were performed as well to benchmark the system performance.

For these measurements, the count rate was limited to keep the dead-time low, the dead-time was recorded, the low energy threshold was low, and the guard ring was grounded. Measurements were taken with the cathode bias at the standard value used for the 1 cm-thick CZT (-2000V), as well as at lower and higher biases in additional measurements.

5.3 Distribution of Efficiency Loss

For flood ^{241}Am measurements, fewer counts were measured at -10°C compared to the counts measured at 20°C. Photopeak efficiency (50-65 keV) decreased by 4.9%, 8.4%, 8.5%, and 14.7% for detectors #1, #2, #3, and #4, respectively. The decrease in total

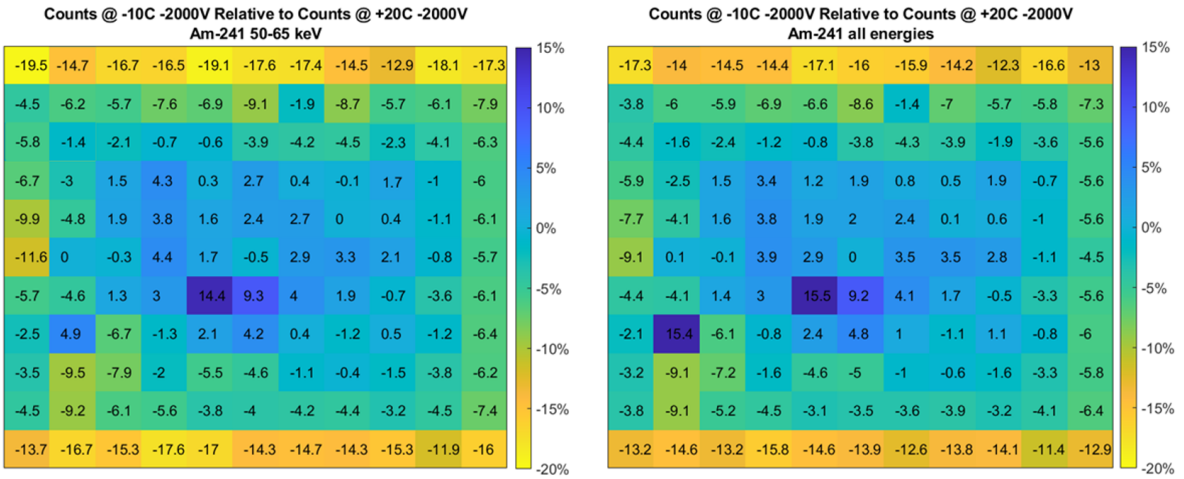

Figure 5.2: Pixel maps of ^{241}Am photopeak (50-65 keV) (left) and total (right) counts at -10°C relative to the respective counts at 20°C for detector #1. The bias was -2000V.

efficiency (all energies) was less severe; 4.3%, 2.6%, 5.2%, and 7.1% for detectors #1, #2, #3, and #4, respectively. The pixel-by-pixel distribution of efficiency at -10°C compared to at 20°C varied between detector #1 (Fig. 5.2) and detectors #2, #3, and #4 (Fig. 5.3). At -10°C, the first detector had efficiency loss mainly for pixels near the edges, and efficiency gain for pixels near the center. This distribution is thought to be most representative of the behavior of many detectors with low-temperature efficiency issues, so much of the analysis will focus on detector #1.

The other detectors had efficiency loss for the majority of the pixels, with varying values and distributions. In the most extreme case, some pixels lost up to 40% of the photopeak counts. The total efficiency loss was in general less significant than the photopeak efficiency loss and had a similar distribution. However, there were several pixels that had a significant increase in total counts at -10°C, especially for detectors #2, #3, and #4. In a few pixels, this increase spilled over into the photopeak region as well. These "hotspots" in counts will be further discussed in Section 5.7.

Changing the bias significantly affected the efficiency loss: results for detector #1 and detector #2 are shown in Fig. 5.4. The change in efficiency given is relative to the efficiency at 20°C -2000V bias (for each detector). For detector #1 at -2800V, the efficiency loss increased (to 8.9% for photopeak events and 8.8% for all events), especially towards the left edge of the detector. At -1200V, the efficiency loss was reduced for

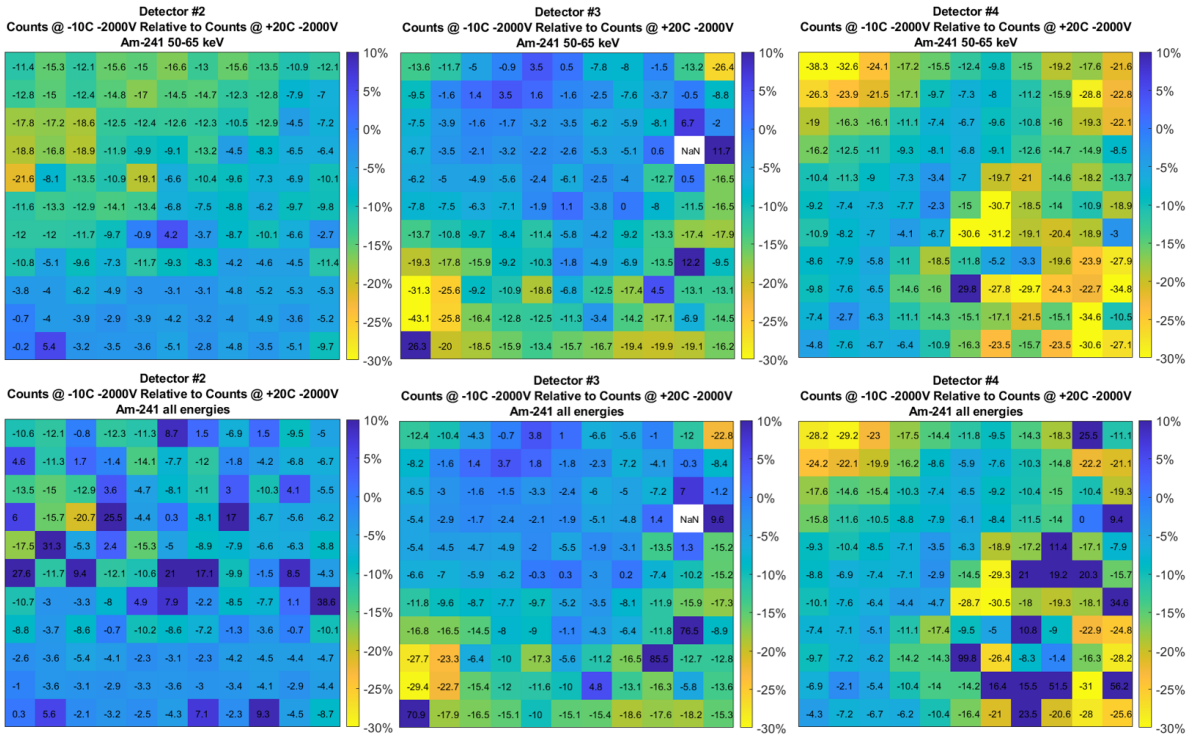

Figure 5.3: Pixel maps of ^{241}Am photopeak (50-65 keV) (top row) and total (bottom row) counts at -10°C relative to the respective counts at 20°C for detectors #2 (left), #3 (center), and #4 (right). The bias was -2000V. The color scale is the same (-30% to 10%) for all plots.

some pixels, especially towards the bottom edge. The total efficiency loss was reduced to 3.23%, but the photopeak efficiency loss was worse (8.5%) than at -2000V (likely because a correction for trapping was not applied). Detector #2 behaved similar to detector #1, but to an even greater degree. At -2500V, the photopeak efficiency loss was 29.6% overall and on a pixel-by-pixel basis reached as high as ∼50%. At -1500V, the majority of pixels actually had an increase in efficiency. The overall efficiency increased 3.0% for photopeak events and 1.1% for all events. In general, at -10°C, higher bias tended to increase efficiency loss and lower bias decreased efficiency loss (or resulted in efficiency gain). This was an unexpected result, as increasing bias typically improves charge collection efficiency.

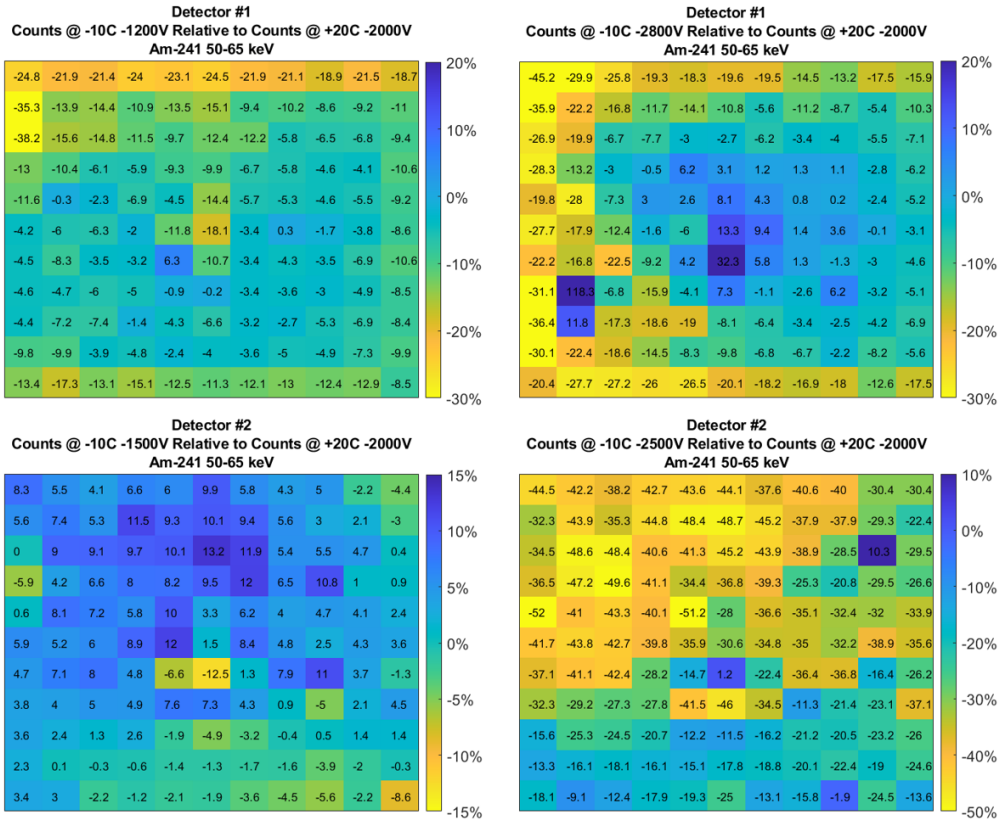

Figure 5.4: Pixel maps of ^{241}Am photopeak (50-65 keV) counts at -10°C relative to photopeak counts at 20°C (-2000V bias) for detector #1 (top) and #2 (bottom) at reduced (left) and increased (right) bias.

5.4 Consistency

When measurements were repeated for all detectors, similar results were obtained in terms of the general distribution and magnitude of efficiency loss, but sometimes there were small variations. For example, the relative photopeak efficiency measured from multiple measurements of an ^{241}Am source using detector #1 are shown in Fig. 5.5. All the measurements were 1 h long with -2000V bias. The relative efficiency loss was most similar for measurement sets #1 (4.9% for photopeak events, 4.3% for all events) and #3 (5.1% for photopeak events, 4.4% for all events). Set #2 had worse efficiency loss (6.5% for photopeak events, 5.7% for all events), especially towards the upper right region of the pixel map. A closer examination of the conditions before and after the measurements indicates that the efficiency may be affected by the testing history.

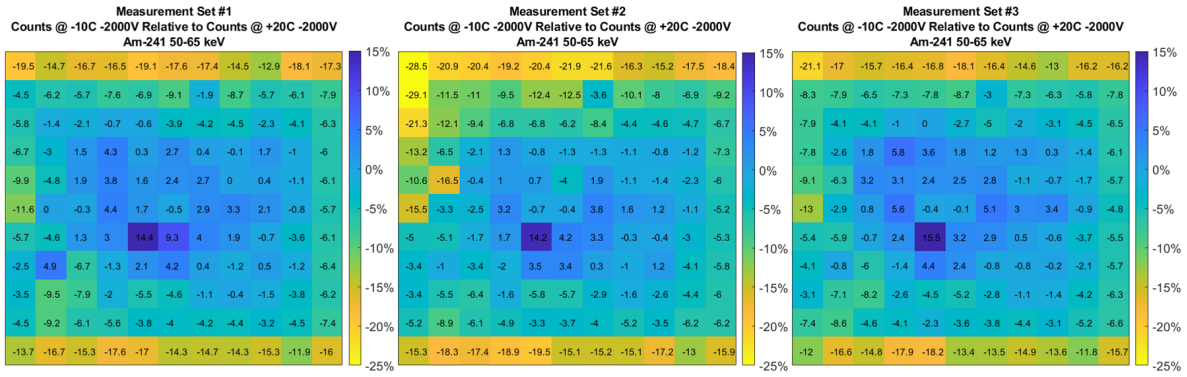

Figure 5.5: ^{241}Am photopeak (50-65 keV) counts measured at -10°C relative to at 20°C for measurement sets #1 (left), #2 (center), and #3 (right) for detector #1. Each measurement was 1 h long with the bias set to -2000V. The color bar range is -25% to 15% in all three plots.

A description of the context of each set of measurements shown in Fig. 5.5 are as follows:

- Set #1 (left): Prior to both measurements, the detector had been at -10°C for about three weeks and was biased to -2000V for about two weeks. Then the -10°C -2000V measurement was taken, the temperature was increased, and the 20°C -2000V measurement was taken (∼4.5 h after the -10°C measurement).

- Set #2 (center): A day after the last measurement in set #1, the detector was biased down and desiccant swapped out. The detector was biased back up and the 20°C -2000V measurement was taken. Then, the bias was increased to -2800V for a measurement at 20°C and after cooling, at -10°C. Then shortly after the 2800V -10°C measurement, the **bias was lowered to -2000V for the -10°C -2000V measurement**.

- Set #3 (right): After the last measurement in set #2, the bias was lowered to -1200V for a measurement. After 5 days, the **bias was increased to -2000V for the -10°C -2000V measurement**. The 20°C -2000V measurement from set #2 was used to do the efficiency comparison.

Considering these details, it appears that the worse efficiency seen for set #2 may be due to the high bias applied shortly before the measurement. Lowering the bias afterwards

appeared to help the detector "recover", as the efficiency loss returned to the level seen in set #1 for set #3, even though the detector had been at -10°C for the longest time for set #3. This observation provided a new "clue" in the investigation of efficiency loss, and motivated more measurements looking at changes over time at -10°C and with bias.

Also of interest is the behavior of the pixel at row 8, column 2, which will be referred to as pixel (8,2), that had a gain in efficiency in the first measurement set, but lost efficiency in the next two sets of measurements. This inconsistency was caused by a change in the energy spectrum. As shown in Fig. 5.6, a strange step is present below the photopeak in the spectrum of the first measurement taken at -10°C, which then disappears for the rest of the measurements at -2000V. In later measurements at -2800V (Fig. 5.7), the spectra for pixel (8,2) became severely distorted at both 20°C and -10°C. At -10°C -2800V, the issue spreads to a neighboring pixel, causing a similar bump in its spectrum. More detail about these hotspots in continuum counts are included in Section 5.7.

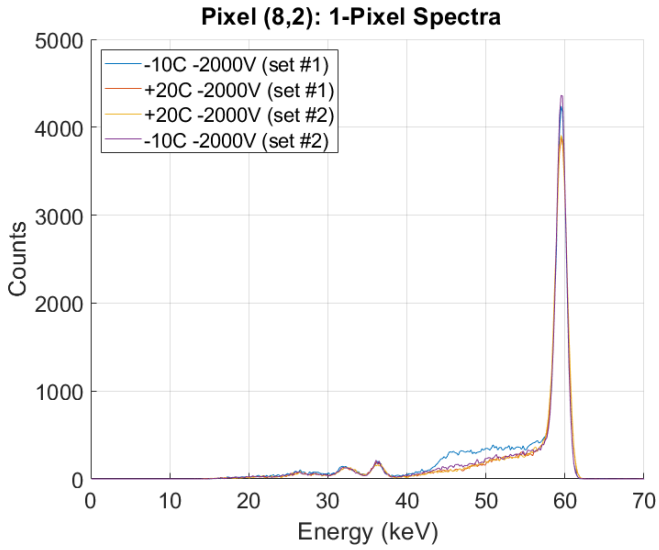

Figure 5.6: Single-pixel energy spectra for pixel (8,2) measured at 20°C and -10°C with -2000V bias for measurement sets #1 and #2.

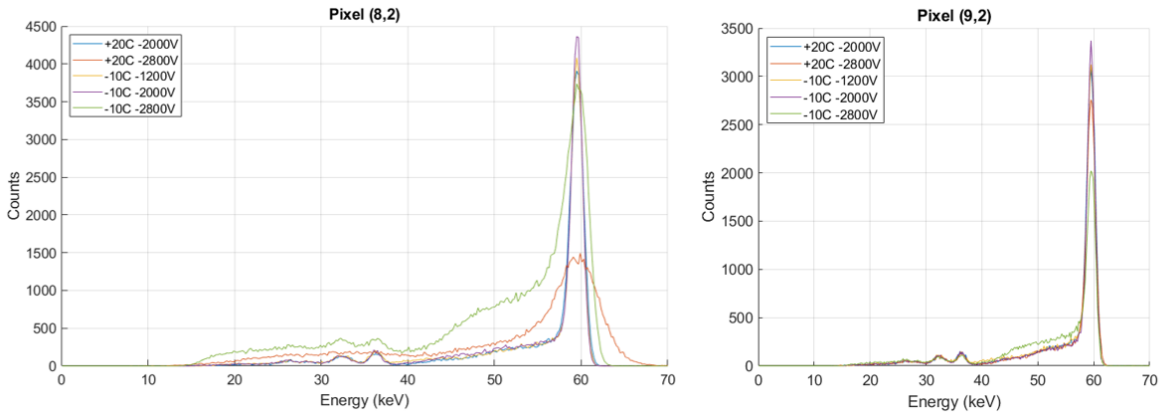

Figure 5.7: Single-pixel energy spectra for pixel (8,2) and neighbor pixel (9,2) measured at 20°C and -10°C with various bias settings.

5.5 System Response

For detector #1, there was a slight improvement in energy resolution from 0.48% to 0.43% FWHM at 662 keV when the detector was cooled from 20°C to -10°C. While resolution is expected to improve at lower temperatures due to reduced leakage and electronic noise, it appears that electric field uniformity was another factor affecting the resolution. At 20°C, there was a large region of the detector with poorer resolution that improved significantly with cooling (Fig. 5.8). In this region of the detector, the cathode waveforms were nonlinear, indicating significant distortion of the electric field in this region. At -10°C, the nonlinearity of the waveform is reduced (Fig. 5.9), and the drift time is shorter. This may indicate a change in the electric field, but it could also be due to an increase in electron mobility. As mentioned in Section 4.5, the rate of electron detrapping can become slower at lower temperatures. The SRFs for detector #1 (Fig. 5.10) show this is the case: near the collection point of the waveform, the shape is sharper at 20°C and rounder at -10°C.

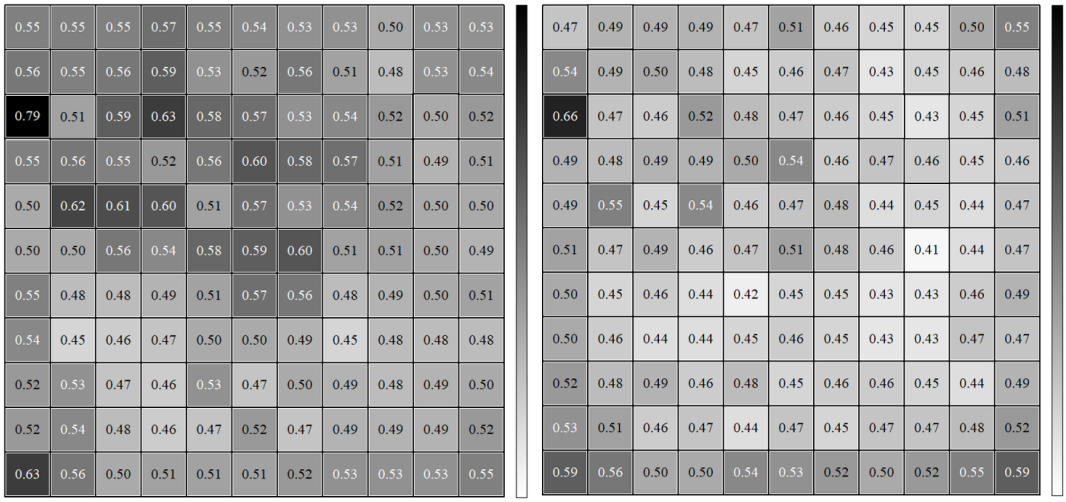

Figure 5.8: Depth-corrected single-pixel energy resolution (% FWHM at 662keV) at 20°C (left) and -10°C (right) for detector #1. The color bar range is 0.4%-0.7% for both plots.

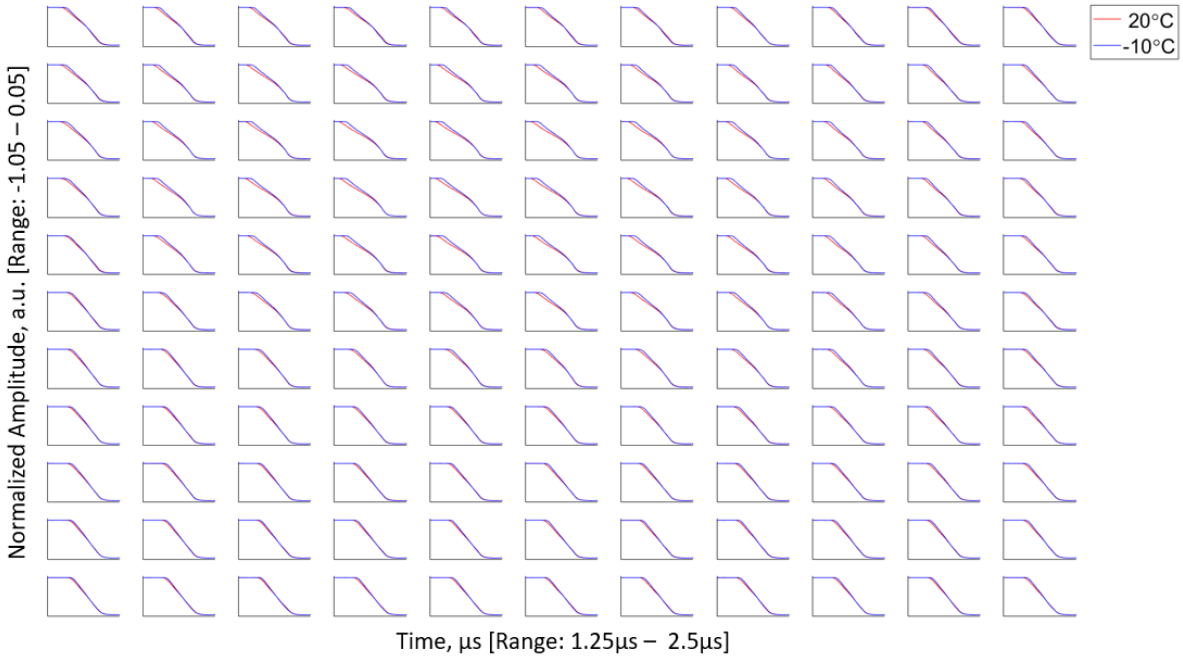

Figure 5.9: Normalized cathode SRFs (^{137}Cs cathode-side events) at -10°C and 20°C for detector #1. Bias was -2000V.

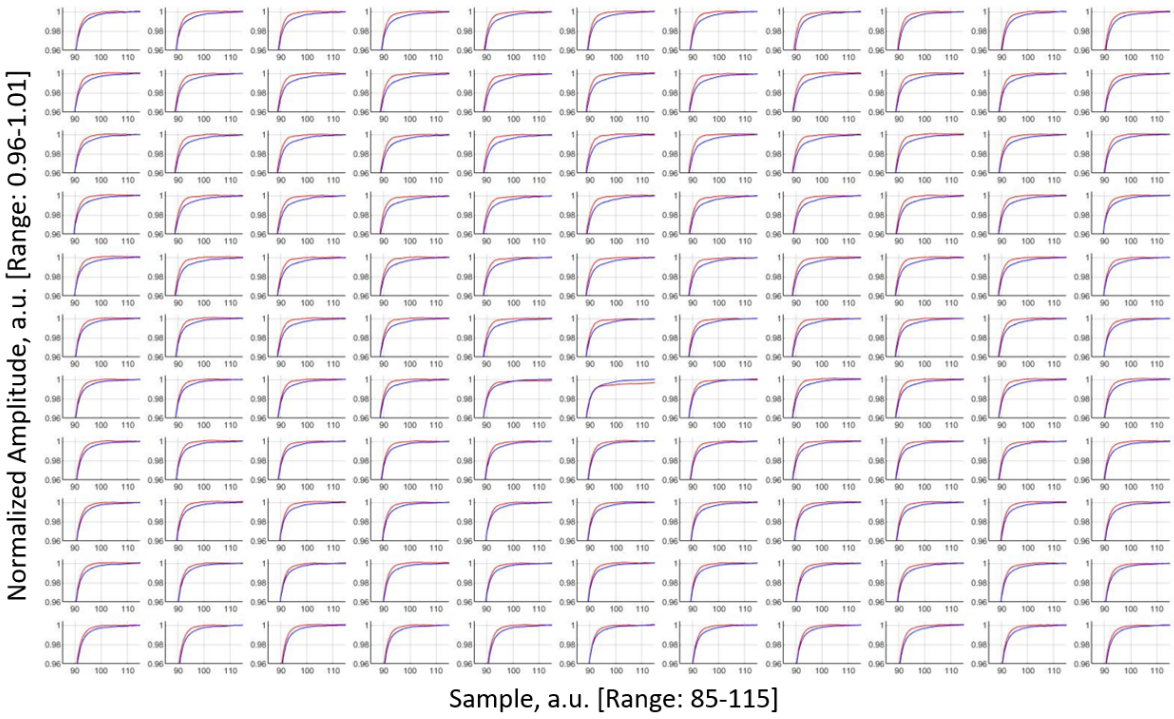

Figure 5.10: Comparison of the anode SRFs (from 662keV cathode-side events) at 20°C (red) and -10°C (blue) with bias at -2000V. The anode SRFs were normalized to sample 130, and the window is zoomed in on the "collection" turn of the waveform. The sampling rate was 40 MHz

5.6 Line Collimator Measurements

The lateral (x-y) position of an interaction is calculated using transient signals from neighboring non-collecting anodes. These signals are induced when the electron cloud is close to the anodes, so it is a measure of the x-y position of the location of charge collection. Typically, it is assumed that electron clouds drift relatively straight, so the x-y coordinate of collection can be an accurate estimation of the x-y coordinate of the interaction location. However, this is not always the case, as non-uniformities in the detector's operating electric field may alter the drift of charges. For detector #1, non-linear cathode waveforms indicate the electric field is not uniform and the distribution of efficiency loss indicated there may be a defocusing effect at low temperatures. To further probe the electric field of detector #1, extra measurements were taken with collimated ^{57}Co sources. A collimator (with an opening of approximately 300 μm) was set up above the cathode side of the detector so that a line of radiation would shine across a desired column or row of pixels. For the first position, the irradiation line passed through the 3rd column of pixels (as shown in the pixel map representations of data). For the second position, pixels in the 7th row were irradiated. For the first collimator position, the measurements were 3 h long, and for the second position the measurement time was increased to 6 h to improve statistics. It should be noted that the collimator positions are described based on the collection location of the majority of counts at 20°C, and that the true location of the collimated source with respect to the pixels is not actually well-known.

Non-uniformity was seen for both line collimator positions: instead of uniform straight lines of reconstructed interaction positions, there are bends in the line, uneven distributions of counts within each pixel, and even some instances of "pixel jumping" — charge being collected in neighboring pixels. The subpixel position reconstruction was similar at 20°C and -10°C, but upon closer examination, the distribution of counts on a subpixel scale shifted when the temperature was changed as shown in Fig. 5.11. The majority of single-pixel counts that were lost were from near-cathode side interactions. At -10°C, increasing the bias led to even greater distortions in the electron drift path, and the drift path was still not uniform at reduced bias. For the first collimator position (Fig. 5.12), many counts are steered towards neighboring pixels at increased bias. For the second position (Fig. 5.13), the effect of bias is more subtle, as the distribution

of counts changes mainly on a subpixel scale. The summed subpixel distributions are shown in Fig. 5.14. When looking at the distribution of the depth of interaction as a function of bias at -10°C, the trend is not as clear as when comparing measurements at 20°C and -10°C. The change is not significant in most pixels. In the first (edge) pixel in row 7 (not shown in figures), the loss in counts with increased bias appeared to occur in most depth bins, but these counts appeared to be gained in the nearest pixel in row 6. In the center pixel in row 7, which saw an increase in counts at higher bias, the counts gained appeared to be only from near-cathode side events.

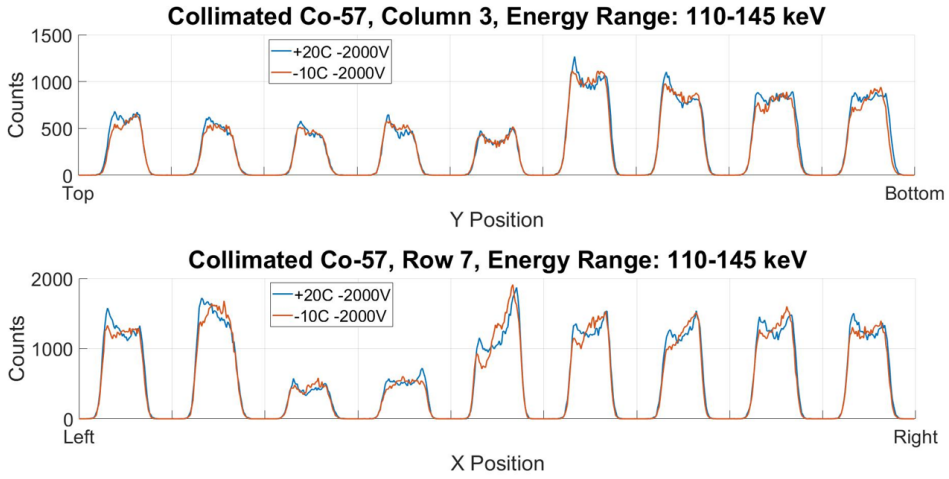

Figure 5.11: The subpixel distributions of photopeak counts at 20°C and -10°C summed for non-edge pixels in the column/row of interest when the ^{57}Co collimated source was aligned above the 3rd column of pixels (top) and above the 7th row (bottom) of pixels in separate measurements.

In an alternative collimator setup, the collimator (5.5 mm slit) and a ^{57}Co source were placed on the side of the detector, so that the depth of interaction could be any Z and attenuation by the detector occurs in the Y-direction (Fig. 5.15). The sum of the subpixel distribution of photopeak counts in the X and Y directions are shown in Fig. 5.16. From these figures, it is apparent that the loss is more significant toward the edge of the detector (Y-direction) and is relatively uniform in the X-direction. The loss in counts is continuous on a subpixel scale. There is not any movement of charges to the center of the detector nor outward in the X-direction, suggesting the counts lost near the edge were steered toward the side of the detector where they cannot be detected.

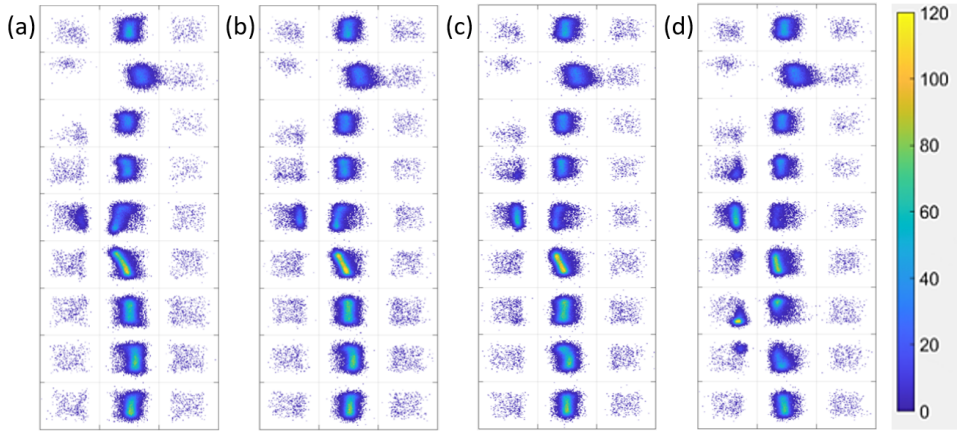

Figure 5.12: The subpixel distribution of photopeak counts at -10°C for non-edge pixels in columns 2 to 4 when the collimated source was aligned over the 3rd column of pixels. The bias was set to -1000V (a), -2000V (b), -2500V (c), and -2800V (d). Note that the subpixel reconstruction for row 2 was inaccurate due to an incorrect connector to pixel mapping.

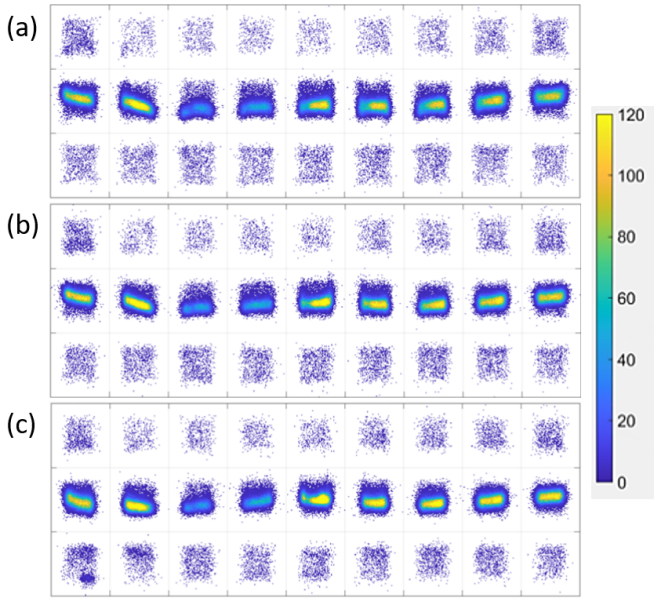

Figure 5.13: The subpixel distribution of photopeak counts at -10°C for non-edge pixels in rows 6 to 8 when the collimated source was aligned over the 7th row of pixels. The bias was set to -1200V (a), -2000V (b), and -2800V (c).

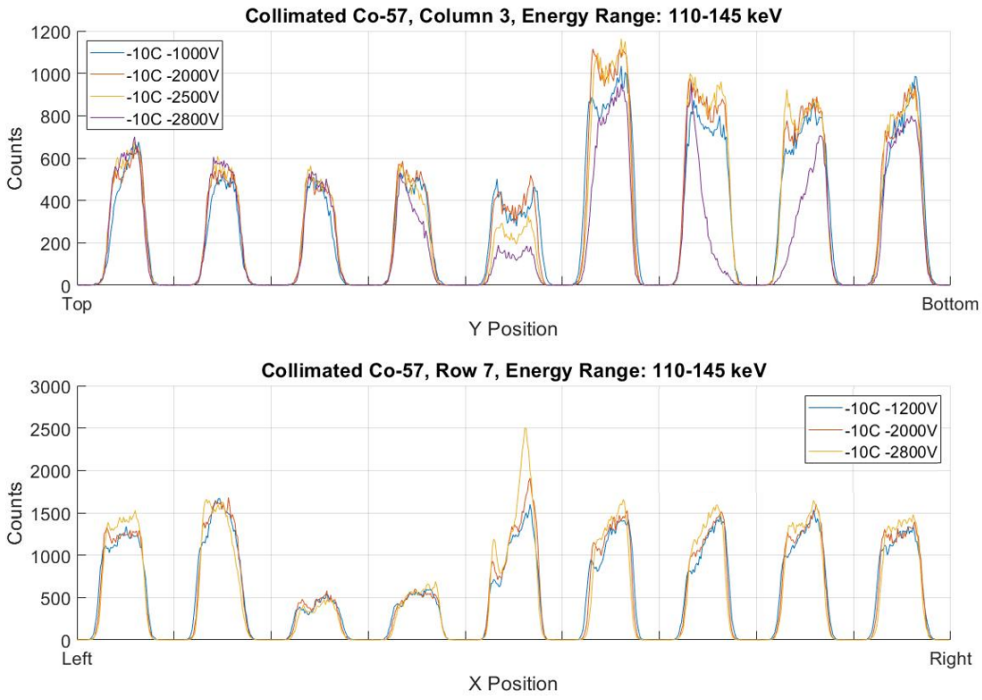

Figure 5.14: The subpixel distribution of photopeak counts summed for non-edge pixels in the column/row of interest when the ^{57}Co collimated source was aligned above the 3rd column of pixels (top) and above the 7th row (bottom) of pixels in separate measurements. The temperature was -10°C, and the bias was varied.

The loss of photopeak counts was uniform for all depths for the edge pixels. For pixels with less efficiency loss, the loss appeared to be greater towards the anode or cathode side and less at middle depths.

With the same collimator setup, a measurement was taken at -10°C with -2800V bias, then the detector was kept at that bias and temperature for 6 days before another measurement was taken. The efficiency loss slightly increased after 6 days, as shown in the subpixel count distribution in Fig. 5.17. Similarly, ^{137}Cs measurements (flood irradiations) at -10°C with -2000V were taken before and after the ^{57}Co measurements separated by 6 days. Then, the detector was biased down and left to rest (still at -10°C). After 1 day, the detector was biased up to -2000V and another ^{137}Cs measurement was taken. Based on the raw ^{137}Cs photopeak, shown in Fig. 5.18, there are changes in the detector performance. The behavior varied in different parts of the detector. For most pixels, the photopeak gain decreased after 6 days and then returned back to the initial

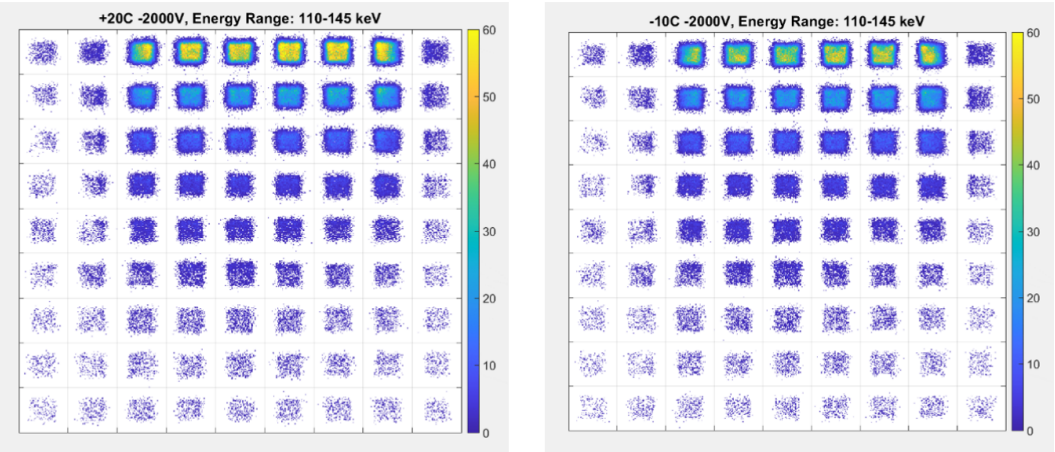

Figure 5.15: The subpixel distribution of photopeak counts for non-edge pixels at 20°C (left) and -10°C (right) with the collimated ^{57}Co impinging from the side of detector #1 (from the top in these plots).

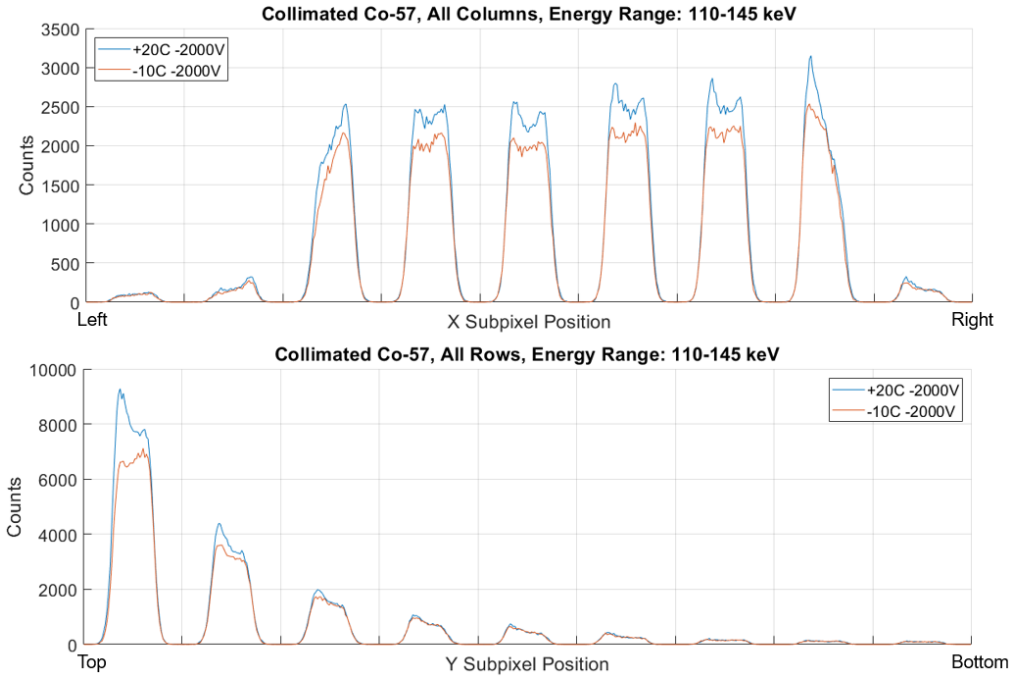

Figure 5.16: Comparison of the subpixel photopeak count distribution, summed over all columns (top) and all rows (bottom), for the measurements at 20°C and -10°C with the collimated ^{57}Co impinging from the side of detector #1.

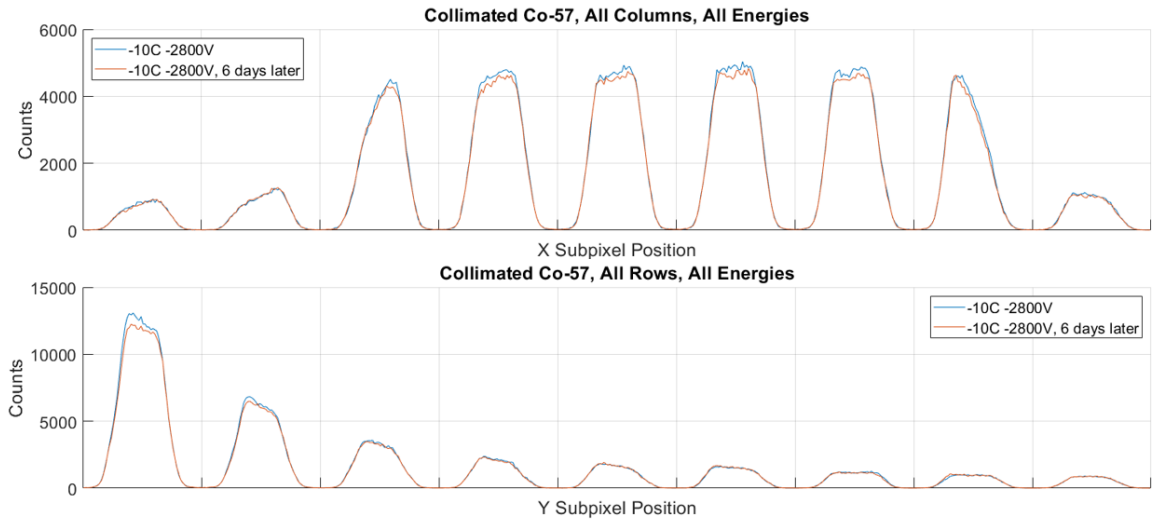

Figure 5.17: Comparison of the subpixel photopeak count distribution, summed over all columns (top) and all rows (bottom), for measurements at -10°C with -2800V bias taken 6 days apart with conditions kept constant in the meantime.

gain after a day of no bias. For pixels in the region of the detector with a non-uniform electric field, the gain was similar for the first measurement and the measurement 6 days later, and then increased after 1 day unbiased. The first measurement was not taken immediately after biasing up, instead the detector had been biased up and slowly cooled from 20°C to -10°C over a day. This may be the reason for the discrepancy. For example, the poorer region of the detector may have been more quickly affected by the cold temperature, causing the gain to be reduced already for the first measurement, whereas the rest of the detector took longer to see a reduction in gain so the gain was not yet reduced for the first measurement. Similar to the observations in Section 5.4, time at -10°C has a small effect but the effect of bias seems to be more significant.

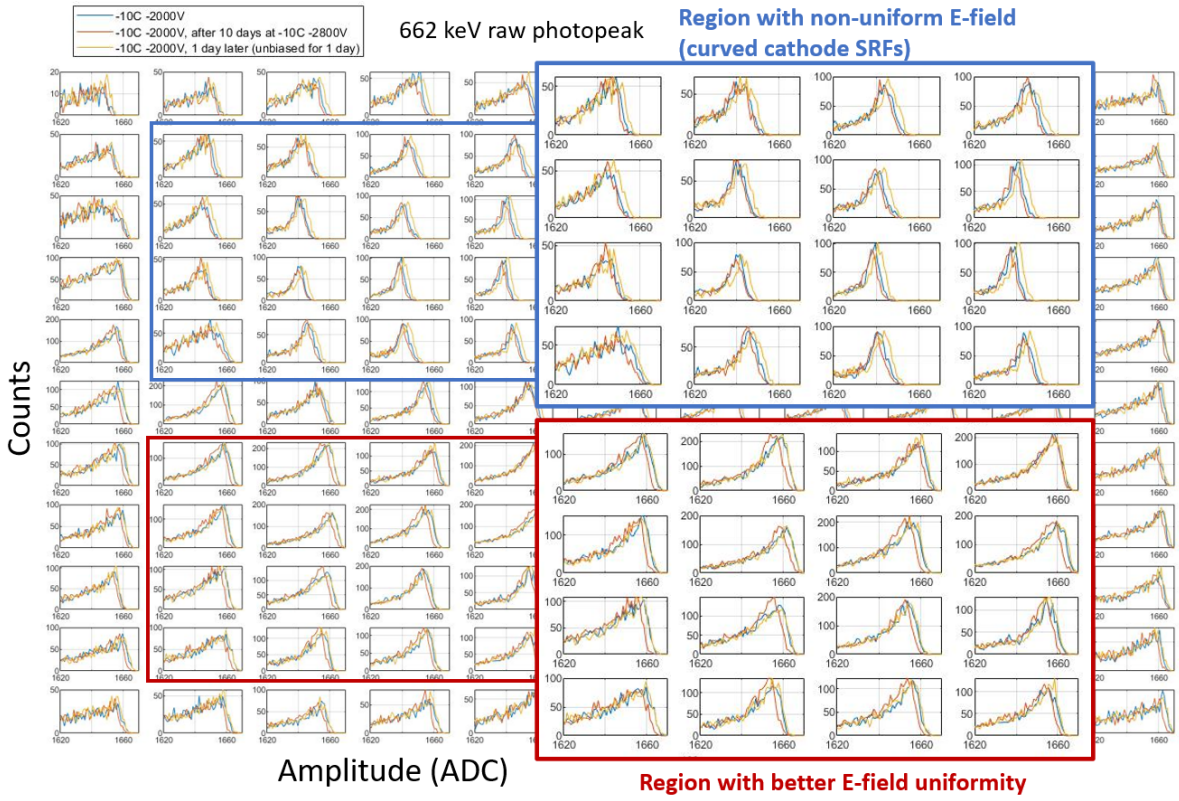

Figure 5.18: Comparision of the raw ^{137}Cs photopeak for three measurements, all taken at -10°C with -2000V bias. The second measurement was taken 6 days after the first (with -10°C and -2800V bias during the 6 days), and the third measurement was taken after 1 day with no bias applied (but still at -10°C). The first measurement is shown in blue, the second in red, and the third in yellow.

5.7 Hotspots

The "hotspots" in counts at -10°C, seen earlier for pixel (8,2) in detector #1 (Fig. 5.2) and for several pixels in the other three detectors (Fig. 5.3), have some defining features. Firstly, as mentioned in Section 5.4, the increase in counts tends to be in the continuum, but sometimes can spread into the photopeak region. This was shown as a function of temperature for pixel (8,2) earlier in Fig. 5.6 and for several pixels in detector #2 in Fig. 5.19a. Increasing the bias can increase the severity of this as well, as shown for pixel (8,2) earlier in Fig. 5.7 (at both -10°C and 20°C) and for several pixels in detector #2 at -10°C in Fig. 5.19b.

Second, in the depth-separated spectra, the unexpected counts in the continuum tend to have a CAR greater than 1, as shown for pixel (8,2) in Fig. 5.20. In this figure, there is a tail of high CAR values in the spectrum that extends from the photopeak. This feature is commonly seen in the depth-separated spectra of any detector and is created by charge sharing events. However, the highlighted region in Fig. 5.20 corresponding to the increase in continuum counts is a feature not seen in "good" detectors. For the depth-separated spectra on a pixel-by-pixel basis for detector #2 (Fig. 5.21), the unexpected feature is sometimes even more prominent and extends to even higher CAR values creating an "unexpected tail" feature that decays faster than the tail due to charge sharing. The decrease in CAR for the unexpected tail is associated with a decrease in the anode amplitude and, to a lesser degree, a decrease in the cathode amplitude as well. For charge sharing events, the cathode amplitude does not decrease, as the charge is lost between anode pixels (thus only anode amplitude is reduced) but the full charge is still detected by the cathode. Therefore, the decrease in cathode amplitude associated with the unexpected tail indicates that this effect is not due to charge sharing but rather represents a loss in charge during the drift through the bulk, not just in the near-anode region. It is also interesting that in a few pixels, the unexpected tails are even seen at 20°C (Fig. 5.21a), which indicates the issue is present at room-temperature as well, though to a lesser degree than at -10°C.

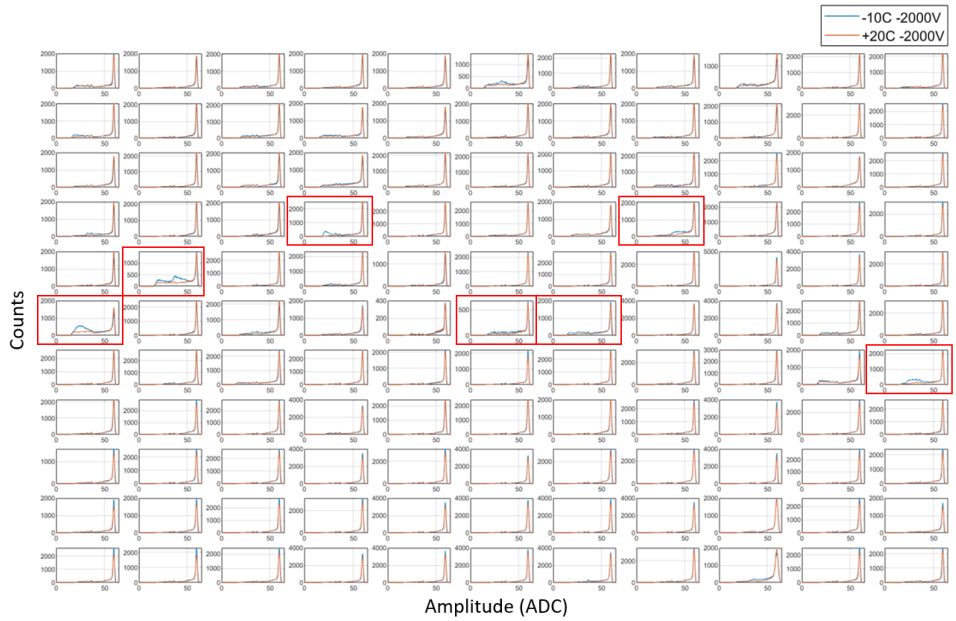

(a)

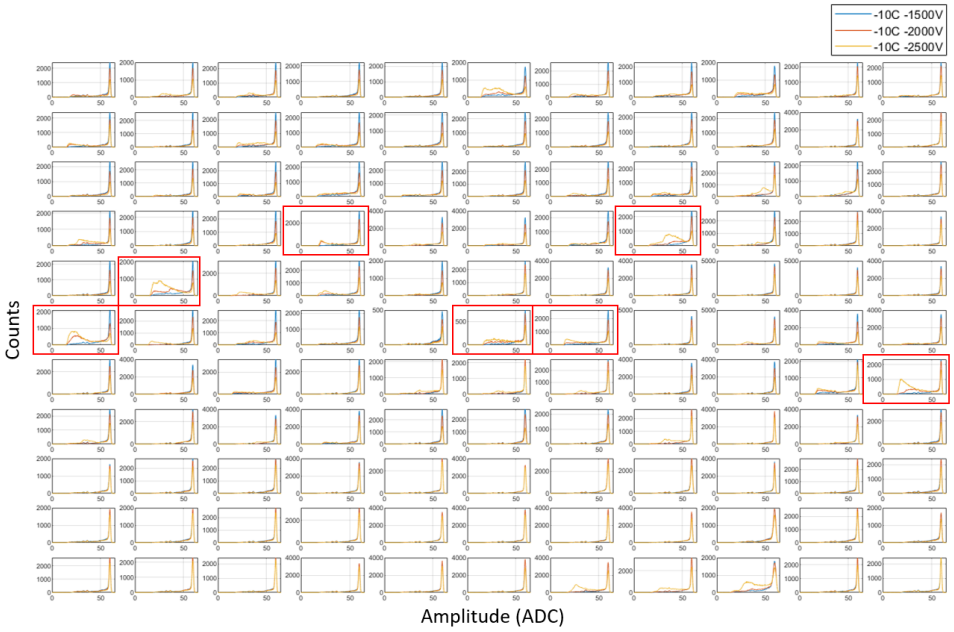

(b)

Figure 5.19: The single-pixel spectra on a pixel-by-pixel basis for detector #2 (a) for measurements at 20°C (red) and -10°C (blue), both with -2000V bias and (b) for measurements at -1500V (blue), -2000V (red), and -2500V (yellow) all at -10°C. Pixels that had an increase in total efficiency at -10°C (relative to at 20°C, with -2000V bias) of 17% or more are highlighted.

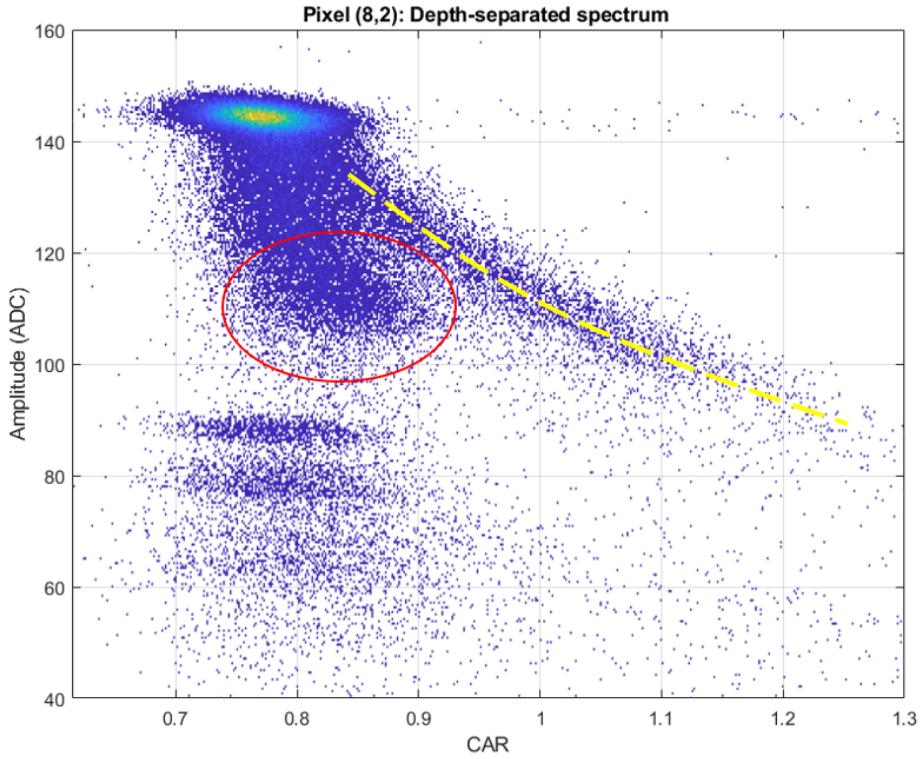

Figure 5.20: The single-pixel spectrum, as a function of CAR for pixel (8,2) from detector #1 measured at -10°C with -2000V bias. The dashed yellow line highlights the tail due to charge sharing, and the red circle indicates the unexpected feature in the spectrum.

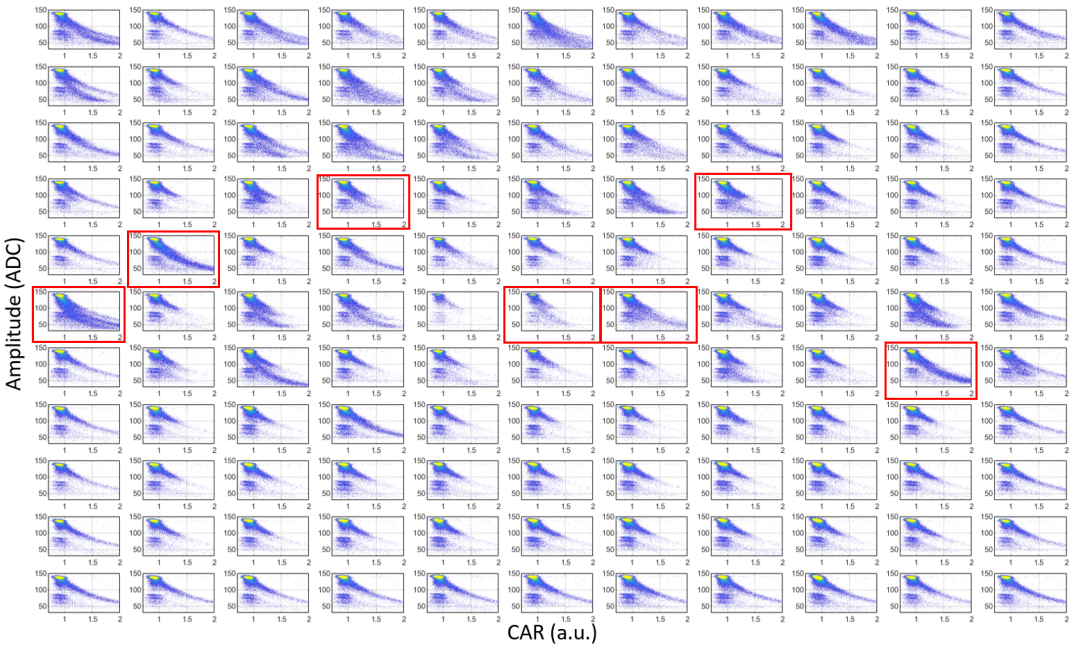

(a)

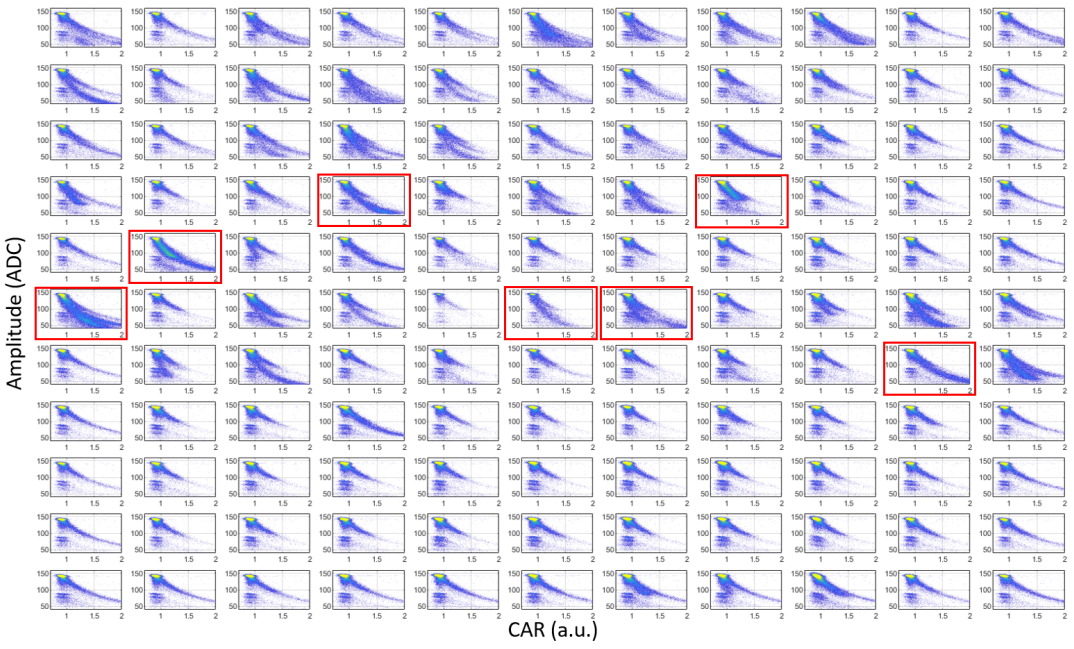

(b)

Figure 5.21: The single-pixel spectrum as a function of CAR on a pixel-by-pixel basis for detector #2 (a) at 20°C and (b) at -10°C, both with -2000V bias. Pixels that had an increase in total efficiency at -10°C (relative to at 20°C, with -2000V bias) of 17% or more are highlighted.

The third defining trait is that these hotspots appear at discrete subpixel locations. For example, Fig. 5.22 shows that the unexpected counts in the continuum for pixel (8.2) from detector #1 were mostly collected towards one corner of the pixel. For detector #2 there were several hotspots at seemingly random subpixel locations that appeared at -10°C (-2000V bias), as shown in Fig. 5.23. The hotspots grew in size and magnitude when bias was increased. Similarly, several hotspots were seen at -10°C for detectors #3 and #4. The number and magnitude of the hotspots grew when the bias was increased. The hotspot for pixel (8,2) in detector #1 appeared in the collimator measurements as well. At high bias, the hotspot appeared towards the right corner of the pixel for the first collimator position (pixel in first column, second row from bottom in Fig. 5.12d) and in the bottom corner of the pixel for the second collimator position (bottom left pixel in Fig. 5.13). For the second collimator position, the location of the hotspot is about a pixel pitch away from the original position of the collimated source, and there is no continuous distribution of counts leading to the point—it seems to truly be a "hotspot". It appears as though charge was steered laterally toward this location, possibly due to a strong local distortion in the electric field.

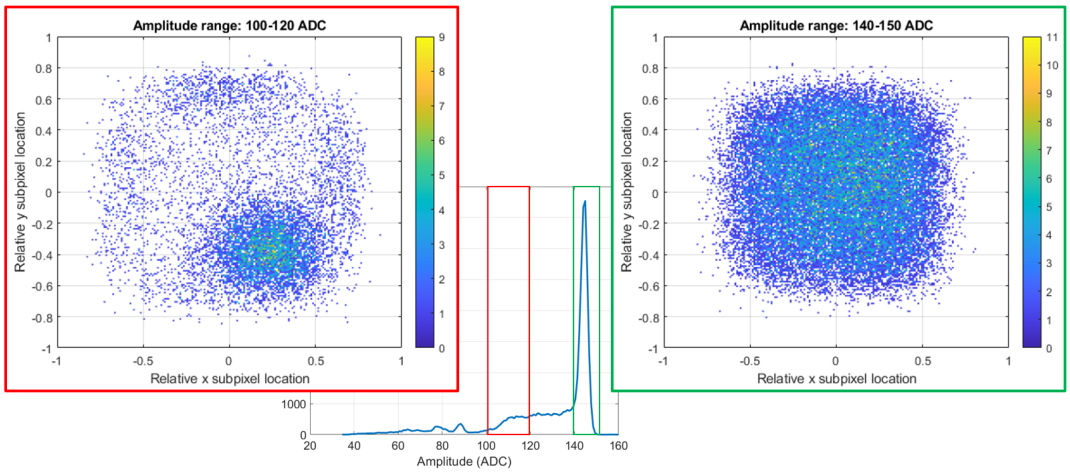

Figure 5.22: Pixel (8,2) subpixel position distribution for selected energy ranges from the first measurement at -10°C -2000V.

Interestingly, the position of these hotspots can change over time. For the measurements taken 6 days apart while the collimator was positioned to the side of the detector (Fig. 5.17 in Section 5.6), there were hotspots in the 2nd column as shown in Fig. 5.24. This column was not necessarily in the path of the collimated source (Fig. 5.15), so the

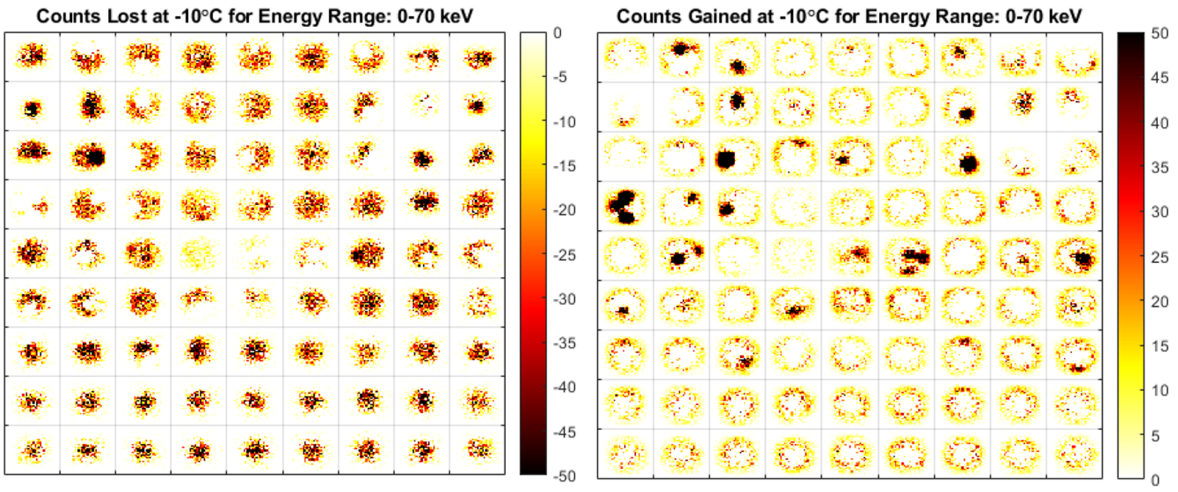

Figure 5.23: Subpixel net count distribution (counts at -10°C minus counts at 20°C) for detector #2. Two color scale bars are used to show counts lost (left) and counts gained (right). In the plot on the right, the ring-shaped feature in each pixel is an artifact of the subpixel reconstruction caused by the change in electronic noise with temperature.

number of counts was low. Over 6 days, one hotspot appeared to jump to a neighboring pixel. The other hotspot appeared to reduce over time; however, some counts may have been pushed to the gap between pixels (or to 2-pixel events).

The number of counts in the first hotspot region was large compared to the background counts, making it a prime candidate for waveform analysis. Fig. 5.25 compares the waveforms from the hotspot subpixel region and waveforms not from the hotspot, but in a region equidistant from the center of the pixel (so that the weighting potential should be similar for both regions). The rise of anode and cathode waveforms in both regions looked very similar and ordinary. This indicates that drift through the detector is very similar (though only movement in the Z direction is reflected, as the variation in the weighting potential in X and Y is negligible except when very close to the pixel). However, there appears to be some difference in the cathode tail. For waveforms from the hotspot region, there is a consistent negative slope in the cathode tail, whereas the tail is usually flat in the region outside of the hotspot. A negative slope in the tail is usually caused by electronics, because charge would need to move in the opposite way than expected to create such a signal (i.e. electron drift towards the cathode instead of anode). On the other hand, the electronics are the same for the whole pixel, so the

negative slope would be expected to occur uniformly in both subpixel regions if it was caused by electronics. This observation is very strange. A possible hypothesis is that a severe distortion in the electric field is causing a small amount of the charge to drift in the wrong direction. Simulations show that it is possible for internal electric fields to bend like this in extreme cases [43]. Alternatively, it could be that many electrons are quickly detrapped in most of the material but not in the hotspot region, causing a deficit. In this case, the detrapped electrons offset the pre-amplifier decay in the regions without hotspots. Additionally, the counts in the hotspot tend to primarily originate from the cathode side of the detector more so than counts outside the hotspot region, which is hypothesized to be because cathode-side events have more time and distance to be steered towards the hotspot location.

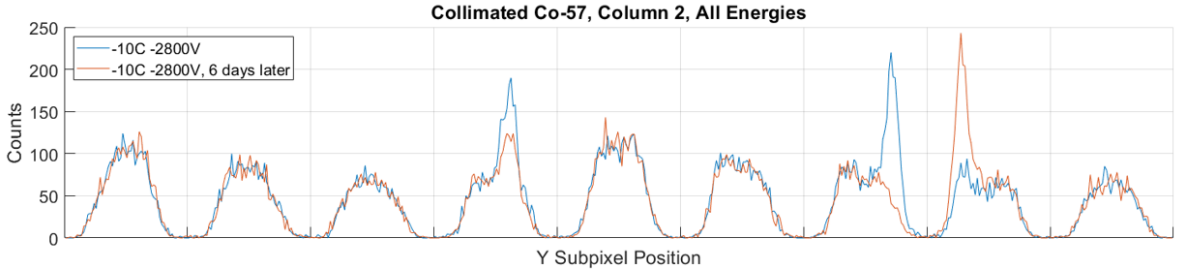

Figure 5.24: Comparison of the subpixel photopeak count distribution, summed over all rows in column 2, for measurements at -10°C with -2800V bias taken 6 days apart with conditions kept constant in the meantime.

5.8 Summary and Discussion

The effect of temperature on detector properties and performance may vary detector-by-detector. In this work, four 3D CZT detectors were tested at 20°C and -10°C to study changes in detector efficiency below room-temperature. From these experiments, there were several observations that can be summarized as follows:

- At -10°C compared to 20°C, there is a loss in efficiency near edges and gain of efficiency in the center for detector #1. For detectors #2, #3, and #4, the pixel-by-pixel distributions vary. Overall, there is a net efficiency loss at -10°C for all four detectors. For ^{241}Am measurements, the loss ranged from ∼5-15% for photopeak events (50-65 keV) and from ∼3-7% for all events.

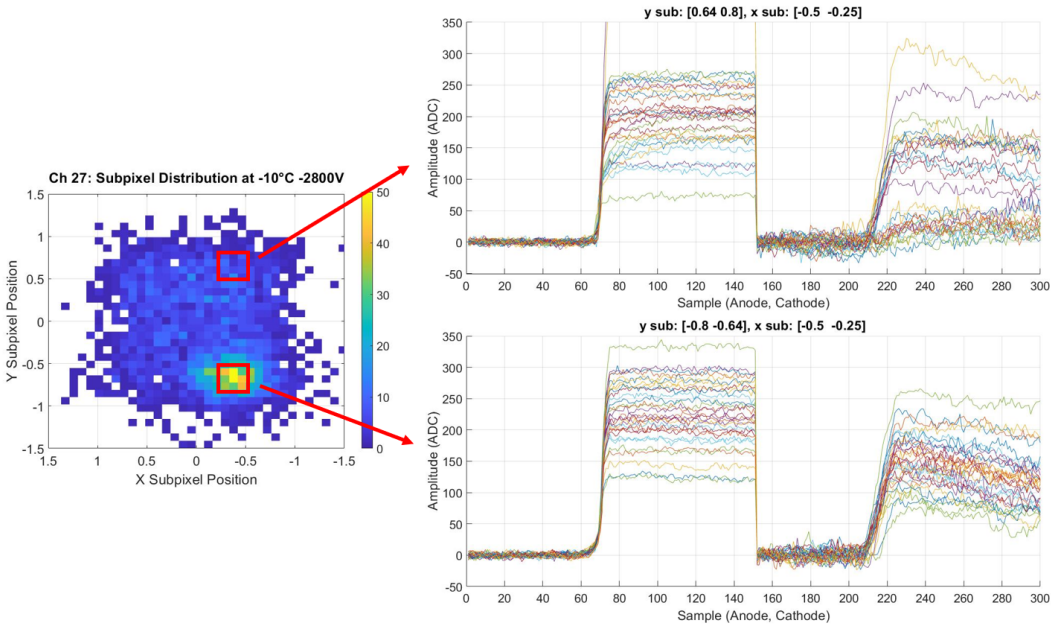

Figure 5.25: Comparison of the waveforms from a pixel at two subpixel locations: in a subpixel region with a hotspot of counts, and in a subpixel region with normal level of counts, yet equidistant from the center of the pixel as the other region. The sampling rate was 40 MHz. Anode and cathode waveforms are concatenated for easier display.

- At higher bias at -10°C, there is more severe efficiency loss. At lower bias at -10°C, there is slightly less efficiency loss (or efficiency gain).
- The efficiency loss is repeatable in general.
  - While not mentioned previously in this chapter, it should be noted that the relative efficiency measured in this work matched the results from testing performed by H3D Inc., which used different readout electronics. This finding plus dead time measurements indicated that the efficiency loss is unrelated to the electronics.
  - On the other hand, high bias and/or low temperature can worsen efficiency, and hotspots in counts can change over time and with bias. Reducing the bias can help recover performance.
- From line collimator measurements using detector #1:
  - There is some lateral movement in the drift / pixel jumping even at 20°C.

  - At 20°C compared to -10°C (both with -2000V bias), the subpixel position distribution changes.
  - At -10°C, increasing the bias significantly impacts the subpixel position distribution, and even causes some charge to be collected by neighboring pixels instead (significant lateral drift). Reducing the bias to -1000V helps reduce lateral movement but does not completely straighten the drift path.
  - When the detector was irradiated from the side with the collimated source, the loss in counts was more significant toward the edge of the detector, and an increase in counts was not detected elsewhere, indicating charge may be steered to the edges where it cannot be detected.

- There are hotspots of counts in subpixel maps at -10°C and at 20°C at high bias.
  - These events have reduced anode and cathode amplitudes, but the reduction of anode amplitude is more significant.
  - These events may have drifted laterally because hotspots can still appear in areas not directly irradiated.

While the exact cause of all these observations is difficult to declare, it is clear that temperature and bias affect charge collection (i.e. magnitude and distribution) and that there is severe non-uniformity in the electron drift path (i.e. non-uniform electric field) for all of these detectors. It is hypothesized that there are at least two different effects occurring. The first is a "global" effect, which is an overall defocusing of the electric field at low temperatures, which is the primary effect seen for detector #1. The observations that point to this is that the loss towards the edges is significant while there is little change in the center of the detector. In theory, a defocused electric field will cause electron charge clouds to be driven to the side surfaces of the detector, where they become trapped. Defocusing is observed for CZT (with small width-to-height ratio) and is described by Bolotnikov et al. in Ref. [44]. When the surface potential between the cathode and anode decreases faster than the potential in the bulk, a defocusing field is created (illustrated in Fig. 5.26). They theorize that this is caused by negative space charge in the bulk. Since the SRFs for detector #1 showed that the electron de-trapping rate was slower at low temperatures, it is reasonable to believe that more negative space charge could be accumulated in the bulk. Also, less accumulation of positive

charge in the bulk could provide the same effect (i.e. if hole movement increased at low temperature). Some hole movement was observed in detector #1 at both 20°C and -10°C, but the mobility lifetime of the holes was not carefully quantified. If defocusing at low temperatures is in fact the issue, a possible solution to boost efficiency at low temperatures would be to apply a significant bias to the guard ring to help steer charges in towards the edge pixels. Additionally, using larger $4\times4\times1.5$ cm^3 CZT may help improve the electric field uniformity towards the edges, as there is a greater width-to-height ratio [45].

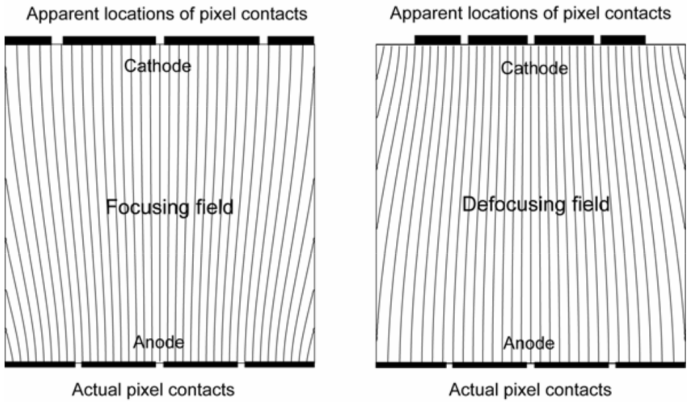

Figure 5.26: Electron trajectories modeled for a CZT sample, illustrating focusing and defocusing. Figure is from Ref. [44].

Unfortunately, there appears to be a secondary "local" effect occurring as well, which could explain why the efficiency loss is not just limited to the edges (especially in detectors #2-4) and why efficiency worsens at higher bias. Grain boundaries, disclocation walls, Te inclusions, and/or strains in the crystals due to defects can lead to local distortions in the internal electric field [46][44] [47][48][49]. In Ref. [48], local increases in counts in CZT (i.e. similar to the hotspots seen in this work) were postulated to be related to either sub-electrode scratches or some other crystalline defect. Optical images and the count density maps did not perfectly line up (shown in Fig. 5.27), which led them to believe that these features influenced the local electric field. Similarly, Bolotnikov et al. [44] concluded that certain material defects (i.e. strains and dislocation networks) do not trap charges, but instead affect the local electric field because they lead to local accumulations in space charge. As noted for the global effect, a change in space charge accumulation with temperature is possible for the CZT tested in this work

due to changes in electron detrapping. Another sign that space charge may be part of this issue is that reducing/turning off the bias helped recover detector performance because space charge will diffuse and recombine when the bias is off. Local changes became more extreme at high bias (more counts at discrete locations, and more loss over broad surrounding area), so perhaps increasing the electric field strength increases the effective collection volume of hotspots corresponding to defects and leads to greater disturbances in the non-uniformity of charge collection.

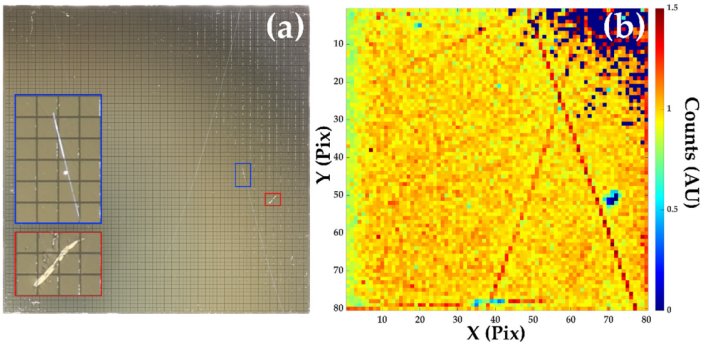

Figure 5.27: Optical image of pixels of a high-flux CZT detector (pixel pitch is 250 μm) (left) and intensity of counts produced from a flat-field X-ray exposure of the detector module (right). Some correlation between optically-visible defects and X-ray images are seen. Figure is from Ref. [48].

For the "local" effects, it is questionable whether applying a guard ring bias would be enough to reduce efficiency loss at low temperature, as it mainly affects the electric field near the edges of the detector. Therefore, a few more potential solutions are suggested. First, detectors with these issues could be routinely operated at reduced bias instead, as lower bias was shown to help reduce efficiency loss and minimize distortions in the electric field. Secondly, the hypothesis in Ref. [48] that the increase in intensity of counts may be related to sub-electrode scratches could be considered. In this case, detector #2, #3, and/or #4 could be sent to a vendor to have the sub-surface layer on the anode side polished off and re-fabricated to see if the locations of the hotspots and/or distortion of the electric field are affected. If they are affected, then improvements in fabrication techniques could help resolve the efficiency issue. If not, then defects in the bulk must be the issue, and improvements in the crystal growth (e.g. to reduce the number of defects) would be ideal to improve the yield of detectors that could be used

for quantification measurements in environments where the temperature may greatly vary. High-resolution X-ray beam mapping could also be performed on detectors #2-4 to determine which type of material defects may be responsible for the distortion in local electric fields.

Alternatively, techniques to help screen detectors that may have efficiency issues at low temperatures without having to test them at low temperatures may be of interest. Based on this work, identifying detectors with non-uniform electric fields would seem to be most helpful. Looking at the shape of digitized waveforms can help with the identification. However, when analog systems are used, this information is not available. In that case, non-uniformity of the electric field could be screened for by looking for non-linearity between drift time and CAR or by looking for unexpected tails in the depth-separated spectra which seems to indicate local electric field distortions (as seen for some pixels at 20°C in Fig. 5.21a). Also testing at higher bias at room-temperature could be helpful for identifying issues.

Chapter 6

Neutron Damage

6.1 Introduction

While CZT is known for gamma-ray detection, it can also be used for neutron detection. Thermal neutrons (<0.025 eV) can be detected indirectly, via measurements of gamma rays released during neutron capture or inelastic scatter. Due to the presence of Cd in CZT, most thermal neutrons will be captured near the outer edges of the detector. Fast neutrons can be detected due to elastic scattering with atomic nuclei. Neutron detection using CZT is discussed in Refs. [50] and [51]. However, sensitivity to fast neutrons also means that CZT is susceptible to neutron damage. In previous studies, it has been shown that exposure to fast neutrons can lead to an increase in electron trapping in CZT [34] [37] [51] [20]. However, there are relatively few studies published on the topic, especially for pixelated CZT. Understanding the effects of severe neutron damage on detector performance is important for assessing the viability of using CZT detectors in radiation-harsh environments and identifying potential ways to reduce degradation in performance of the detector. Experiments involving radiation damage in pixelated CZT are particularly of interest because the uniformity of damage can be studied as well.

6.2 Severe Neutron Damage

The effects of very high neutron exposure were studied using two 2.2×2.2×1.0 cm^3 CZT detectors from Redlen, M10641 and M10115 (Fig. 6.1). These detectors were exposed to a neutron fluence of 10^{12} n/cm^2 using a nuclear reactor (Watt spectrum). The neutron

exposure and initial testing was conducted by H3D Inc. This neutron fluence is a couple orders of magnitude larger than the fluences used in previous studies of neutron damage in pixelated CZT [37] and was intended to simulate what might be expected from a nuclear explosion. During irradiation, the detectors were unbiased and not plugged into any detector system. The detectors were irradiated from the side (neither the cathode nor anode side, but orientation was otherwise not tracked). Prior to neutron exposure, the energy resolution measured using the analog BNL ASIC was 0.69% FWHM at 662 keV for single-pixel events (0.88% for all events) for M10115, and 0.62% FWHM at 662 keV for single-pixel events (0.82% for all events) for M10641.

After the exposure, detector performance was evaluated via the VAD UM v2.2 system using a ^{137}Cs check source. These measurements were performed by Dr. Yuefeng Zhu. The gamma-ray spectroscopic capabilities of both detectors were severely degraded. The ^{137}Cs photopeak was absent in the raw anode energy spectra. The SRFs showed that the cathode and anode signals rose at the same time, indicating that only near-anode events were recorded. This was likely due to severe charge (electron) trapping in the bulk of the crystal, as electrons drifting in the bulk were unable to get close enough to the pixels to trigger the ASIC. The electron mobility-lifetime was estimated to be on the order of 10^{-5} cm^2/V. The electron mobility-lifetime is typically on the order of 10^{-2} cm^2/V for Redlen CZT (without neutron damage). After depth-correction was applied, a broad 662 keV photopeak could be seen in the single-pixel spectra: roughly 11% FWHM and 18% FWHM for detectors M10115 and M10641, respectively.

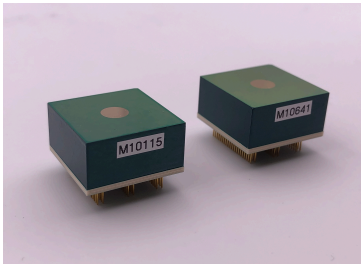

Figure 6.1: Redlen CZT detectors M10115 and M10641 used to study severe neutron damage.

6.3 Performance after Annealing

To improve the detector performance after neutron damage, M10641 and M10115 were annealed at 80°C for 156 h and 139 h, respectively. After annealing, detector M10115 was tested first, periodically over ten days while biased to -3000V and unbiased for random intervals. Unstable performance over time was observed, thus, detector M10641 was used to further investigate the time-dependence of performance. Several measurements, each 80 min long, were taken using detector M10641 during a 150 h period while under a constant bias of -3000V.

6.3.1 Detector M10115

When the detector was first biased up to -3000V after having been annealed for 139 h, the depth-corrected single-pixel energy resolution was 0.70% FWHM at 662 keV, which is nearly the resolution recorded prior to the neutron exposure. Unexpectedly, the energy resolution degraded over time while the bias was kept at -3000V. However, when the cathode bias was removed, the detector appeared to "heal" itself, with the extent of healing being more significant the longer the detector was left unbiased. Fig. 6.2 shows the change in energy resolution over 10 days where the detector was either biased to -3000V or unbiased for select periods of time.

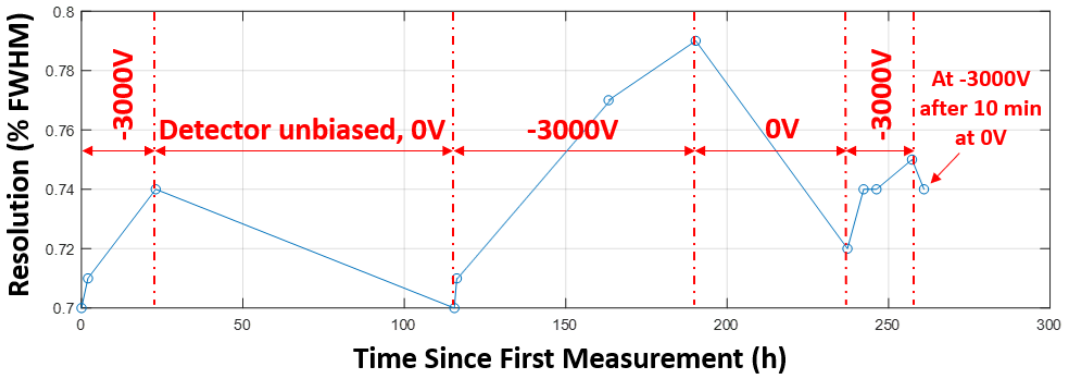

Figure 6.2: Depth-corrected single-pixel energy resolution at 662 keV for detector M10115 over 10 days. The detector bias during each time period is labeled.

6.3.2 Detector M10641

For detector M10641, similar behavior was seen. Annealing helped to improve the energy resolution to nearly pre-damage levels, but over time and under constant -3000V bias, the spectroscopic performance degraded. The raw ^{137}Cs spectra from several measurements over a 150 h time period are shown in Fig. 6.3. Over time, the 662 keV photopeak broadened, and its centroid decreased in amplitude. The energy resolution and gain over time are shown in Fig. 6.4. The single-pixel energy resolution degraded from 0.73% to 0.94% FWHM at 662 keV after approximately 150 h of bias. The broadening occurred uniformly throughout all depths, as shown in Fig. 6.5.

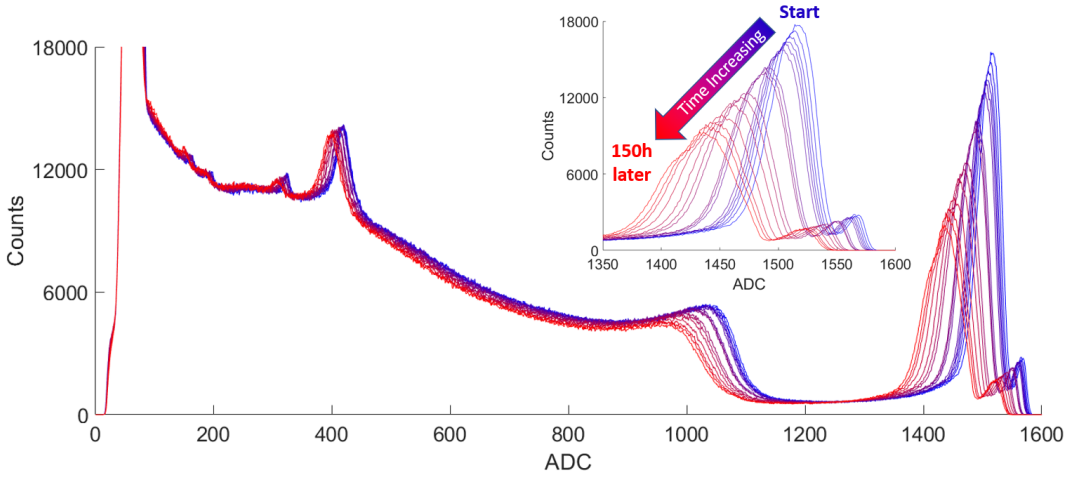

Figure 6.3: The raw ^{137}Cs energy spectra measured from shortly after biasing the detector (blue) to after being biased for approximately 150 h (red) for detector M10641. The inset highlights the photopeak region.

Another interesting feature in the raw spectra (Fig. 6.3) is the presence of two photopeaks. The raw spectra include all the spectra for 121 pixels without a correction for pixel-by-pixel variations in gain. The electronic gain of each ASIC channel can vary, which may result in multiple peaks in the raw spectra if the variation is large enough, which was shown earlier for the high-temperature CZT detectors (Section 4.6). However, the multiple peaks in the raw spectra here are due to a different effect. As shown in Fig. 6.6, the pixel-by-pixel gain variation follows a pattern, which is not expected if the variation is solely caused by differences in electronic gain. After neutron damage and annealing, the pixels in the center of the detector have much higher gain than the

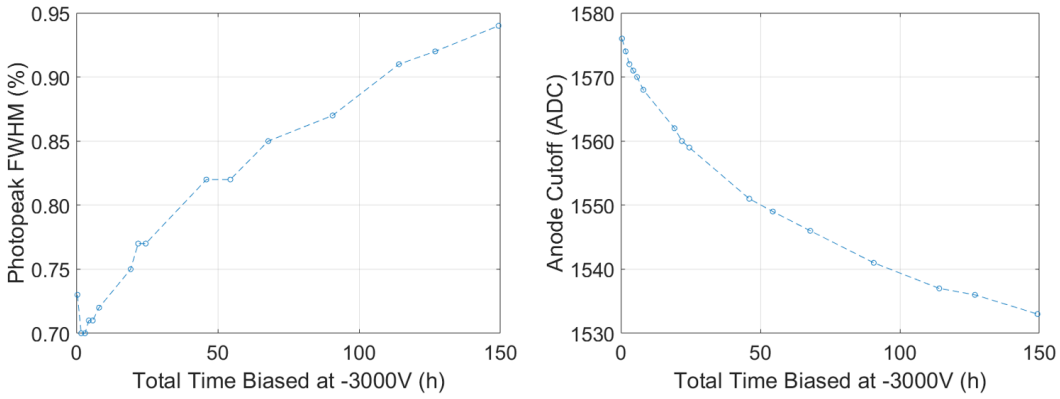

Figure 6.4: The single-pixel depth-corrected energy resolution FWHM at 662 keV (left), and gain in terms of anode spectrum cutoff (right) as a function of time under bias at -3000V for detector M10641.

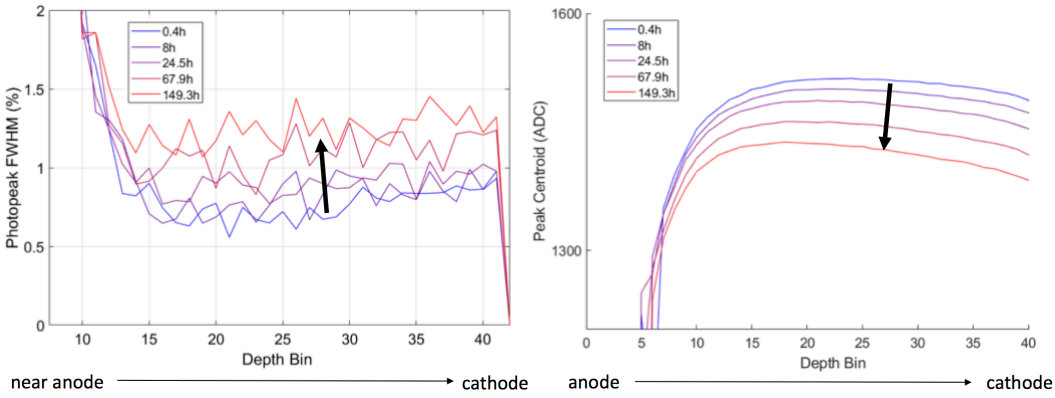

Figure 6.5: The single-pixel depth-corrected energy resolution FWHM at 662 keV (left), and gain in terms of peak centroid (right) as a function of depth over time under bias for an example pixel from detector M10641.

peripheral pixels, which causes the small peak with higher amplitude in the raw spectra. This non-uniformity will be discussed more in Section 6.5.

To further illustrate how the performance of M10641 changed with time under bias, Fig. 6.7 shows the cathode-side SRFs for the first and final measurement (150 h later). At the beginning of the measurement, the cathode signals were nonlinear and rounded towards the end of the electron drift which indicates that the electric field was nonuniform, and particularly weaker towards the anode side. Over time, the cathode signals became even more rounded towards the end of the drift, indicating that the deficit in

Figure 6.6: The pixel-by-pixel gain (anode high-energy cutoffs in ADC) for detector M10641 after neutron damage and annealing.

the electric field intensity near the anode becomes more severe over time. This is also reflected in the anode SRFs. After 150 h, the anode signal rose much more slowly which indicates that the drift velocity of electrons became slower in the near-anode region. Additionally, the degradation over time was more severe for pixels near the edge of the detector than for the center pixels.

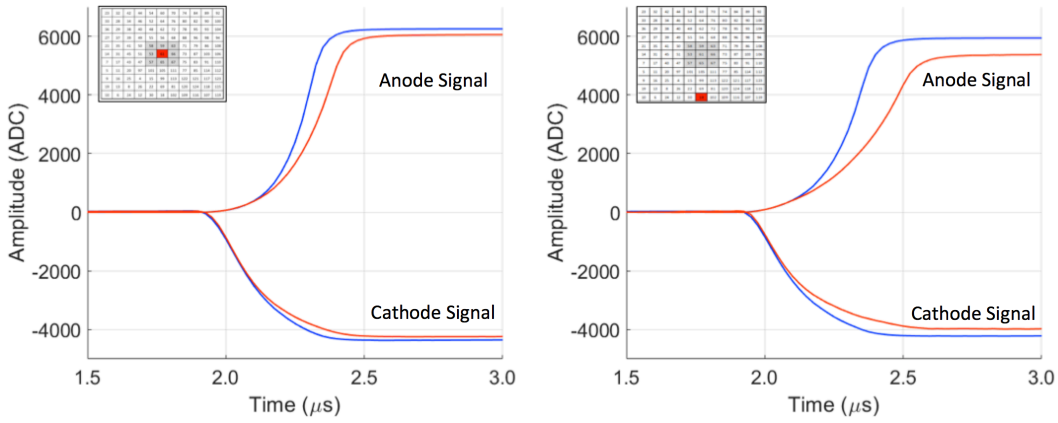

Figure 6.7: The cathode and anode SRFs (for cathode-side events) for the center pixel (left) and an edge pixel (right) for the first measurement (blue) and the measurement 150 h later (red).

The overall counts collected during each measurement (Fig. 6.8) gradually dropped over time under bias. Interestingly, only the number of single-pixel events declined over time, while the number of multi-pixel events increased. For single-pixel events,

the decrease in counts was greater for photopeak (662 keV) events than for events of all energies. The loss in single-pixel photopeak events was nearly compensated for by an increase in multi-pixel events. For the photopeak events at each depth, averaged over all pixels, losses slowly increased as distance away from the anode increased until a significant drop in counts was seen for the quarter of the bulk closest to the cathode. This effect could be due to electron cloud broadening/diffusion. The closer an event occurs towards the cathode-side and the larger the amplitude, the more likely the electron cloud will broaden enough to trigger more than one pixel, as the electron cloud size is proportional to energy and a longer drift path gives more time for diffusion and trapping/de-trapping.

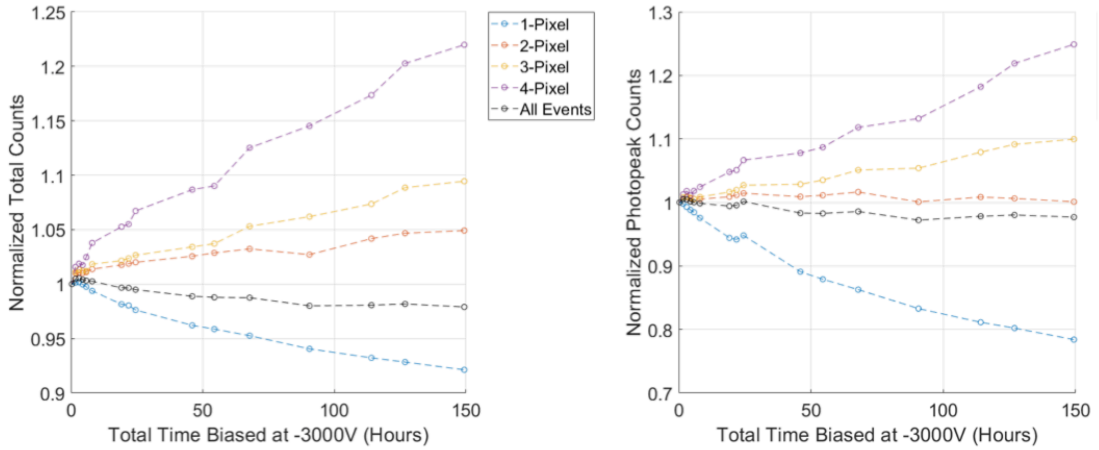

Figure 6.8: The total (left) and photopeak (right) counts over time under bias, relative to the first measurement.

6.3.3 Detector M10641: A Year Later

To determine whether the unstable behavior was temporary or long-term, detector M10641 was re-tested in a similar manner approximately a year later, in October 2020 (initial testing was in September 2019). Again, the VAD UM v2.2 system was used and the cathode was constantly biased to -3000V. Each calibration measurement was 80-min using a ^{137}Cs check source. Unlike in the previous measurements, an iSeg high-voltage power supply was used so that the total leakage could be measured, and the electronic noise was measured periodically.

After a year of rest (unbiased), the single-pixel energy resolution (FWHM at 662 keV) of detector M10641 was initially 0.71%. After time under bias, the resolution degraded in the same way as it had in September 2019, as shown in Fig. 6.9. The change in raw spectra over time (Fig. 6.10) was very similar to what was seen about a year earlier (Fig. 6.3). However, when directly comparing the raw spectra from 2019 and 2020 (Fig. 6.11), there are some notable differences. Firstly, a couple low-energy (<400 ADC) activation peaks are no longer present after a year, which was expected due to their relatively short half-lives. Second, the gain (high-energy anode cutoff) was significantly higher than the year before, but the increase in gain is seen only for the higher amplitude peak, which corresponds to the center pixels. The increase in gain is likely due to room-temperature annealing, which has also been observed in previous studies. Though the gain was higher in 2020 than 2019, it still showed a similar decrease over time under bias as shown in Fig. 6.12.

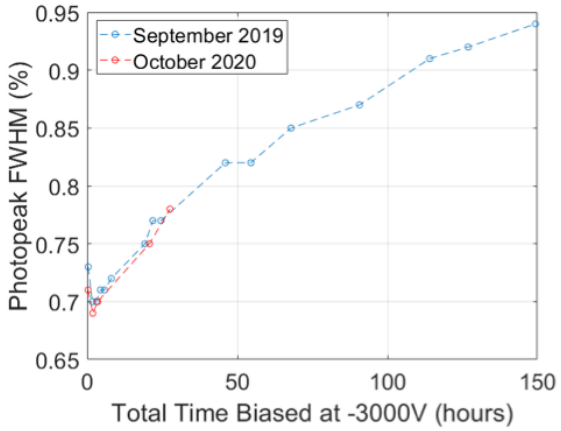

Figure 6.9: Comparison of the single-pixel energy resolution as a function of time under bias for detector M10641 for measurements about a year apart.

It should be noted that the decrease in gain during each individual measurement (80 min) was significant. The greatest rate of decline was seen for the measurement soonest after biasing up, and the rate slowed as time passed. While an overall decline in gain was consistent over all measurements, there were a couple measurements that saw an initial increase in gain over the first few minutes of the measurement. This behavior at the beginning of measurements is believed to be related to the amount of time before the measurement that the source had been placed near the detector. The source was placed

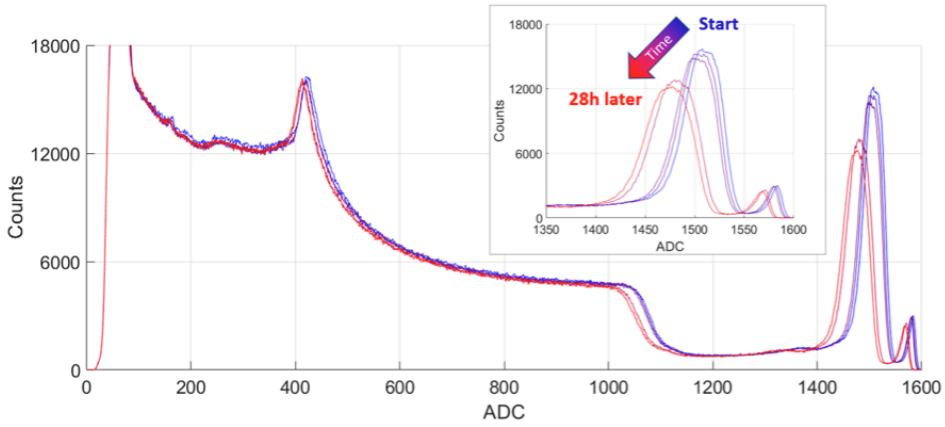

Figure 6.10: Transformation of the overall raw single-pixel energy spectra with time under bias during October 2020 measurements.

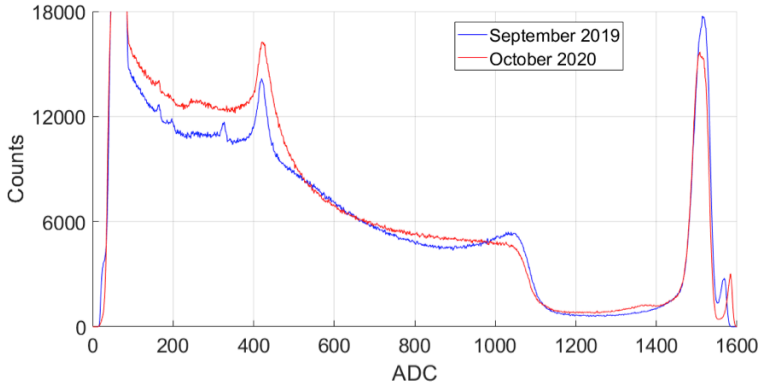

Figure 6.11: Comparison of the overall raw single-pixel energy spectra (measured shortly after biasing up) in September 2019 and October 2020. Measurement times were both 80 min, and ^{137}Cs source placement and activity (∼70 µCi) were similar.

near the detector at all times except when the electronic noise was measured before each measurement. The electronic noise measurement only takes a couple minutes (i.e. so a couple minutes pass without a source near the detector). However, after the source was returned, measurements were not always started immediately. For measurements that were started shortly after the electronic noise measurements (i.e. the source was near the detector for a short time before data collection began), an increase in gain is seen at the beginning of the measurement. When the source had been near the detector for a longer time prior to starting the measurement (i.e. when the time between the

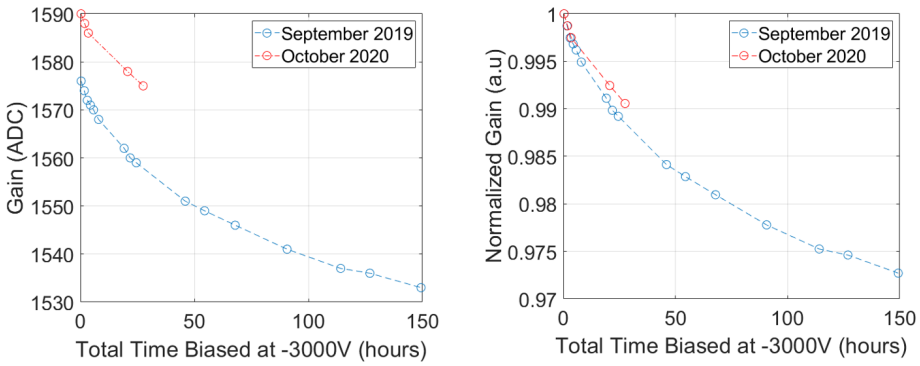

Figure 6.12: Comparison of gain as a function of time under bias for detector M10641 for measurements about a year apart. The absolute value of gain (anode cutoff, ADC) is shown on the left, and the gain normalized to the first measurement for each set of measurements is on the right.

electronic noise test and the start of measurement was greater, 7 min and 14 min), there was no increase in gain. Fig. 6.13 illustrates this effect.

This time dependence of source placement on the initial gain change was noted partway through the experiment, so the effect of the presence of the source long-term was tested. The source was removed for a 5 h period after the second to last measurement (after 21 h biased) and before the final measurement (after 27.6 h biased). The source was not removed in between all of the other measurements, except briefly to measure electronic noise. It appeared that removing the source did not have a significant impact on the trend of resolution degradation (Fig. 6.9) or decrease in gain (Fig. 6.12). While the source appeared to have a short-term effect on gain (Fig. 6.13), it did not impact the gain nor resolution long-term. This suggests that detector bias plays a more dominant role.

Lastly, the leakage measured during the experiment was very low, and slowly decreased ($\sim$3 nA) over the time of the experiment, as shown in Fig. 6.14. A small decrease in leakage over time biased is commonly observed for CZT without neutron damage, so this does not indicate an issue. The electronic noise (pixel baseline FWHM) in ADC dropped slightly during the experiment. When the electronic noise was converted to keV, it appeared to just slightly increase from 2.19 keV to 2.24 keV during the time of the experiment. However, this is probably due to the decrease in gain with

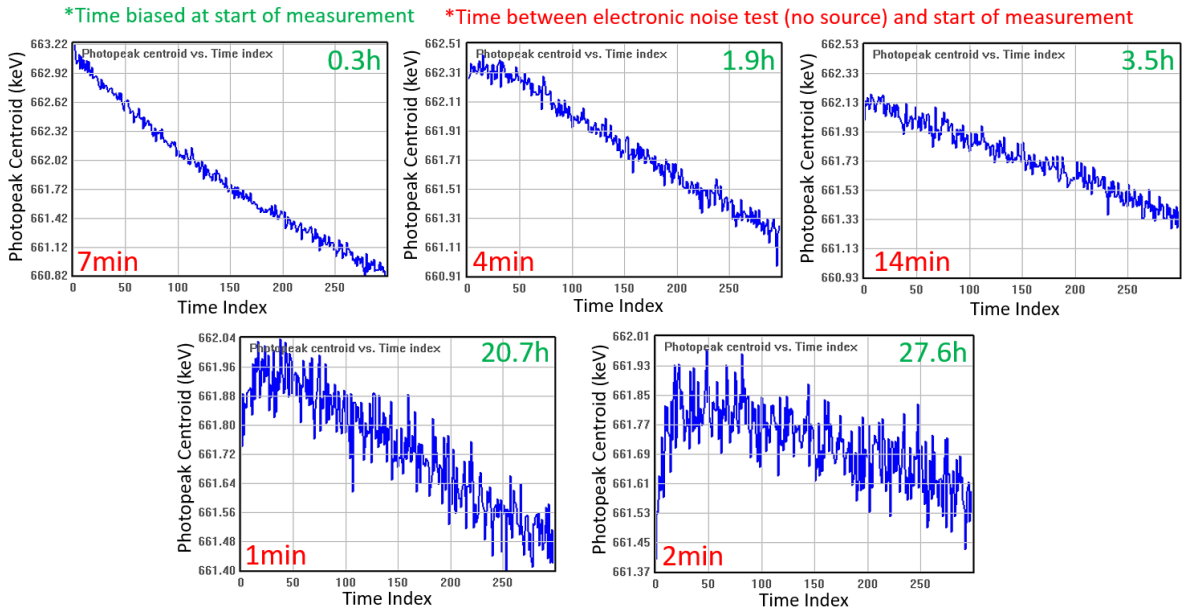

Figure 6.13: The change in gain during each 80 min measurement (divided into 300 time bins). The amount of time the detector had been biased at the start of the measurement is labeled in the top right corner (green), and the time between the electronic noise test and the start of the measurement is labeled in the bottom left corner (red).

time, as the gain is used for the conversion from ADC to keV. Either way, this increase in noise is too small to explain the degradation of energy resolution.

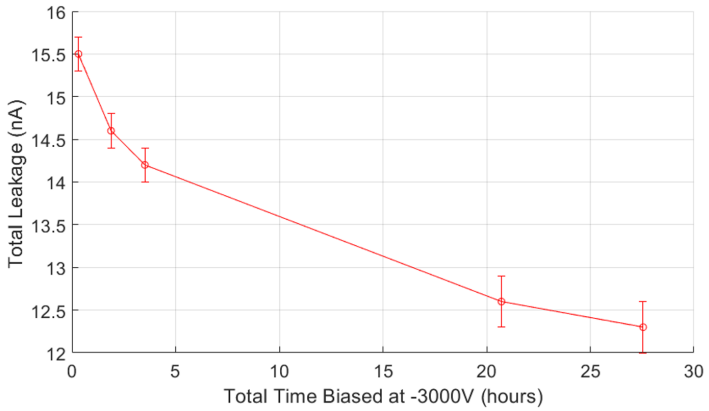

Figure 6.14: The total leakage measured periodically during the 28 h experiment in October 2020.

6.4 Conclusions on Annealing of Severe Neutron Damage

Firstly, annealing the detectors drastically reduced the amount of electron trapping induced by the severe neutron exposure and improved the energy resolution from greater than 10% to around 0.7% FWHM at 662 keV. An improvement in electron trapping was expected based on previous studies, and it was promising to see that the energy resolution could be almost fully recovered even after exposure to an extremely high neutron fluence (10^{12} n/cm^2). However, the unstable behavior after neutron damage and annealing has not been observed previously, and suggests that annealing is unable to completely cure the damage to the detector if the exposure is severe enough.

A list of the main changes in detector performance over time under bias after annealing are as follows:

- The gain of the photopeak decreases.
- Cathode SRFs become more round in the second half of the drift, and anode SRFs rise much more slowly.
- The number of single-pixel events decreases, and the number of multi-pixel events increases.
- The loss of single-pixel events is greatest for photopeak events near the cathode-side.
- Total leakage decreases.

Together, these factors suggest that over time (under constant bias), the electric field becomes weaker, especially in the near-anode region. Other observations were that:

- Resolution and gain degrade uniformly over all depths of interaction.
- Turning off the bias helped the detector recover.
- The presence of a source will initially increase the gain, but some equilibrium is reached within minutes, and the gain will decrease.
- Edge pixels perform worse to begin with and degrade faster.

- Total leakage current is low.

The uniformity of degradation with depth suggests that the issue occurs near the anode-side surface or at the electrode contacts, rather than throughout the bulk. On the other hand, the nonuniformity pixel-to-pixel suggests that material quality in the bulk may still play a role. The recovery of the performance after turning off the biasing and the effect of the presence of a source both suggest that space charge may be involved. For example, over time under bias, space charge may accumulate at the anode contacts. When the bias is shut off, the space charge will diffuse and recombine, and the performance is restored until space charge accumulates again after time under bias. Non-uniformity pixel-to-pixel, low total leakage, and the quick recovery via unbiasing the detector makes damage to the anode contacts itself seem unlikely. Damage to the contacts would be expected to be uniform, damaged pixels usually tend to have high leakage and have noisy waveforms, and it is difficult to propose a mechanism capable of quickly improving the contact by removing bias. Lastly, since the same behavior was seen when the detector was re-tested 1 year later, this newly observed effect could be described as long-term or permanent damage, as opposed to the increase in trapping typically observed due to appreciable amounts of neutron exposure that can be cured via annealing.

While the unstable behavior of CZT after an extreme neutron exposure is not ideal, the detectors can still be of use. Since the fluence was on the order of magnitude equivalent to what might be expected from an "emergency" scenario (i.e. nuclear explosion) or to long exposure to high levels of damaging radiation (i.e. years-long space flight), any other radiation detectors may be severely damaged as well. So it is important that without annealing, some spectroscopic performance can be recovered (though resolution is poor), and that with annealing, good energy resolution can be obtained again. Though energy resolution degrades over time under bias, the single-pixel energy resolution is still below 1% after more than 6 days under bias, which is still reasonable for a room-temperature semiconductor.

If very high resolution is needed, the spectra of just the center pixels could be used, or the detector bias could be switched off and on frequently. Additionally, accounting for the change in gain over the time of a measurement could help improve energy resolution. This could be done by using a known peak in the spectra as a reference for gain as a function of time. The reference could be a check source placed near the detector, or

perhaps peaks from activation products that have not yet decayed, considering that activation of CZT and surrounding materials is probable for such high neutron exposures. To use this technique, any non-linearity in the gain change as a function of energy would need to be considered.

6.5 Uniformity of Neutron Damage

As seen in the previous section and in unpublished work by Dr. Jiawei Xia, a strange phenomenon was observed where peripheral pixels appear to be more damaged than central pixels after exposure to neutrons. For center pixels, gain is higher and the increase of trapping due to neutron exposure is less significant. When creating a pixel map for either attribute, the best performance is at the center, and it degrades as distance from the center increases (Fig. 6.6). While better performance is most obvious for the center 3×3 pixels and a radial gradual change is seen even on the sub-pixel level. A circle-like pattern emerges, so this phenomenon will be referred to as the "circle effect". Applying bias during neutron exposure increases the severity of damage; however, the circle effect is still observed if there is no applied bias (just bare crystal alone) given that the neutron fluence is high enough. In these studies, Redlen CZT detectors were always used, so it is of interest to see if this phenomenon occurs for Kromek/eV Products CZT as well.

6.5.1 Experimental Setup

Kromek CZT detector #4E-7 was used for the next neutron damage test: this detector had physical damage to the cathode surface, very high electronic noise, significant trapping, and poor depth-corrected energy resolution, 1% FWHM at 662 keV. However, it had no gain issues and had relatively uniform trapping and gain, making it suitable for an experiment looking for non-uniformity in degradation due to neutron exposure. Detector #4E-7 was exposed to neutrons from a PuBe source for 63.5 h to try to study the circle effect. The source was ∼2 cm above the lid of the detector housing of the UM VAD benchtop system, as shown in Fig. 6.15. The detector was biased to -3000V throughout the exposure. The neutron fluence was estimated to be $\sim 10^9$ n/cm^2.

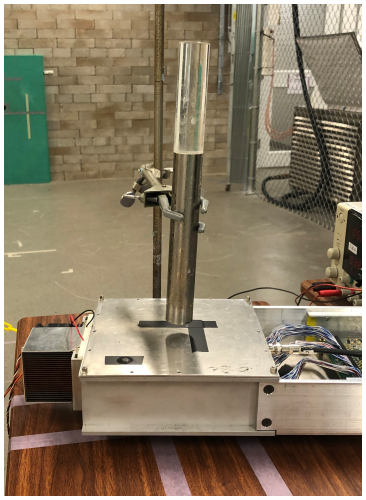

Figure 6.15: Detector #4E-7 in the UM VAD benchtop system, placed below the PuBe source. The PuBe source was located near the bottom of the rod.

6.5.2 Results

The single-pixel anode spectra (^{137}Cs) before and after neutron exposure are shown in Fig. 6.16. In the raw spectra, an increase in trapping is apparent. The corrected spectra did not change much, and the energy resolution only minimally worsened from 1.02% to 1.04%. The increase in trapping due to neutron exposure can be seen in the gain-depth curves, shown in Fig. 6.17. The trapping was significant enough to decrease the gain (anode cutoff) per pixel, as shown in Fig. 6.18. The increase of (extra) cathode-side electron trapping was calculated using relative gain-depth curves and is shown in Fig. 6.19. This shows good agreement with the previous findings: a neutron fluence of $\sim 10^9$ n/cm^2 caused about a 2% increase in extra electron trapping in Redlen CZT [20]. The technique used to estimate the increase in trapping was the same one used in the previous work, so it is a fair comparison.

The increase in trapping has a smooth gradient, with a greater increase on one side of the detector, likely due to the source placement. The source was so close to the detector that it is probable that the neutron fluence varied significantly across the detector. Otherwise, the changes in trapping and gain were relatively uniform, with degradation in the center pixels similar to the rest of the pixels. This indicates that the strange "circle effect" observed for Redlen CZT was not observed for this Kromek detector. Though

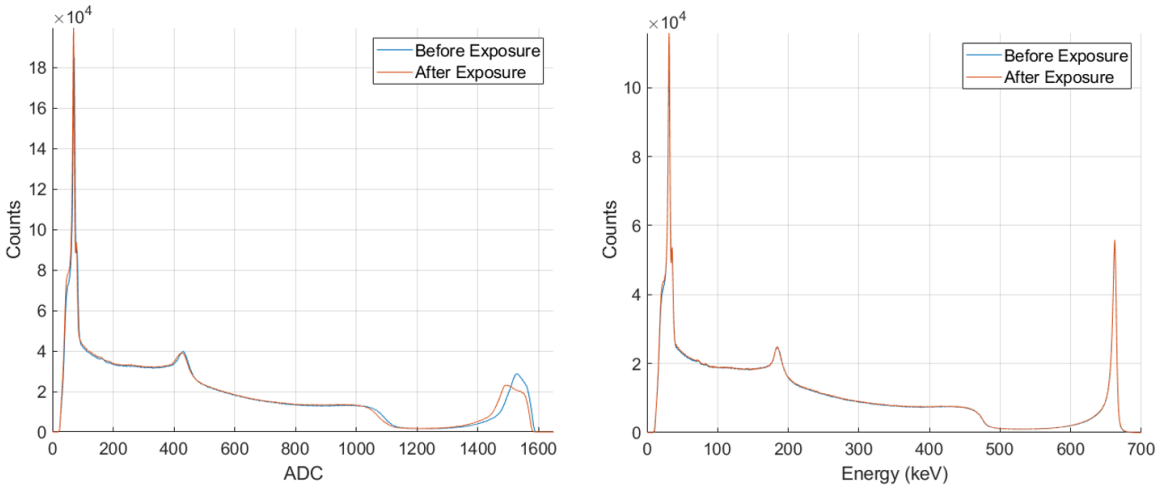

Figure 6.16: The raw (left) and corrected (right) anode spectra from before and after neutron fluence of $\sim 10^9$n/cm^2 for detector #4E-7.

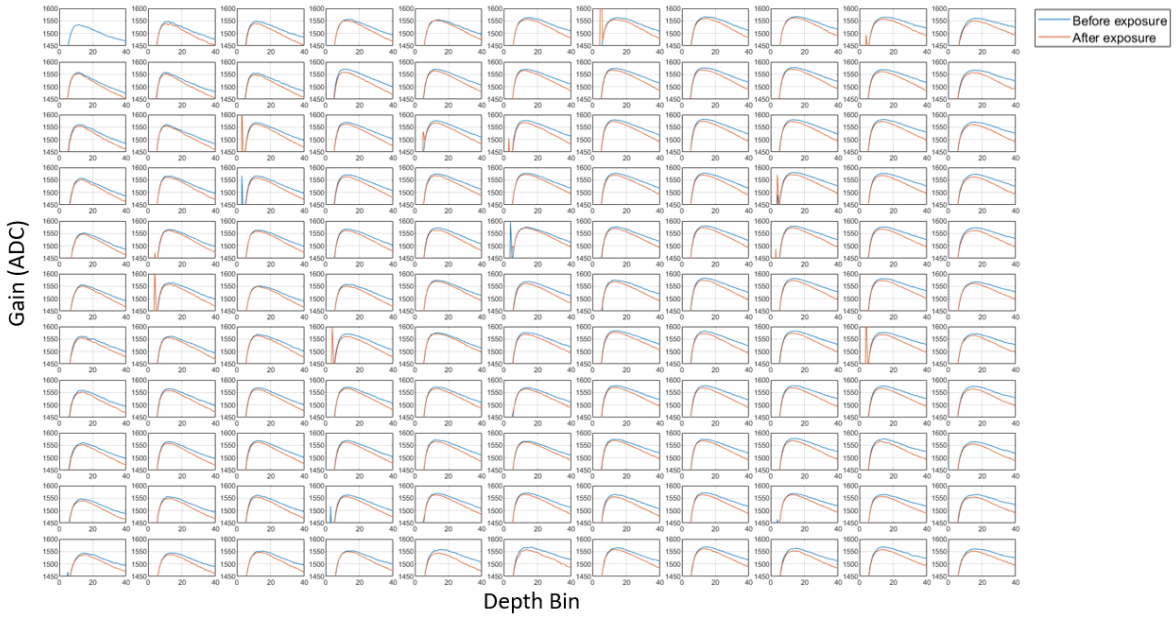

Figure 6.17: Gain-depth curves before and after neutron exposure on a pixel-by-pixel basis for detector #4E-7.

more experiments would be needed to see if this is consistently the case for Kromek CZT, the results from this detector suggest that the better performance in the center of Redlen CZT after neutron exposure is likely caused by some process used by Redlen

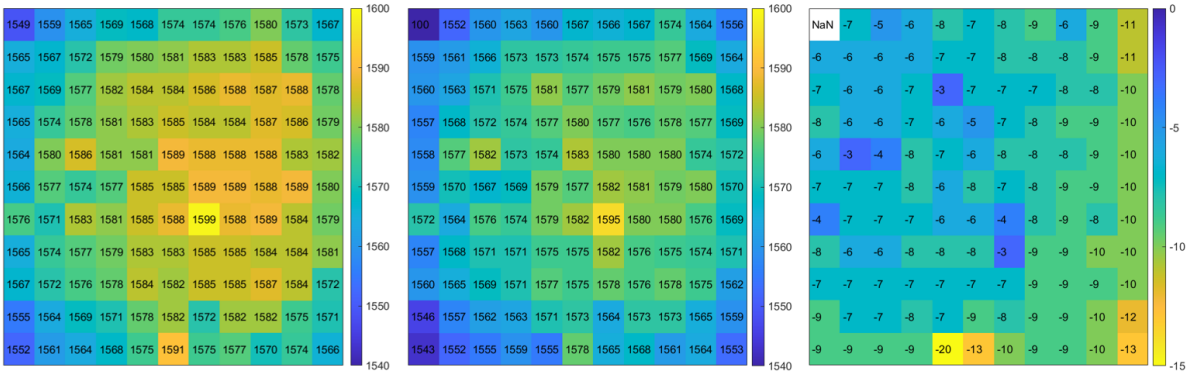

Figure 6.18: The pixel mapping of gain (anode cutoff, ADC) before neutron exposure (left), after neutron exposure (center), and the difference (right) for detector #4E-7.

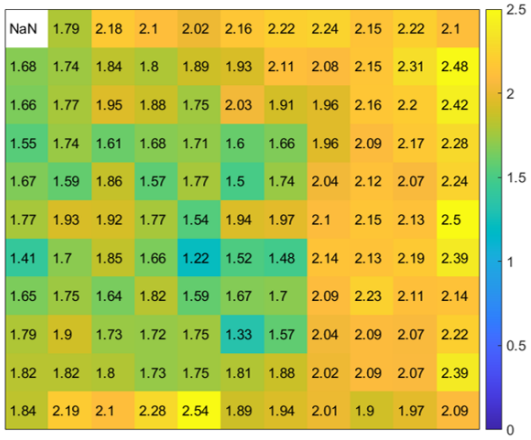

Figure 6.19: The increase of (extra) cathode-side electron trapping (%) due to neutron exposure. for detector #4E-7.

during the growth or fabrication of the CZT detector. It appears that there truly may be fewer impurities in the center of the Redlen CZT detectors. While less damage in the center of the Redlen detector is good because it indicates greater radiation hardness, the nonuniformity of detector response may pose an issue for calibrations. For example, anode pixels at the boundary between the "good" center pixels and the other pixels can have double peaking in their anode spectra due to the significant variation in gain under a single pixel, so subpixel calibrations may be required. Any nonuniformity on a scale finer than the detector's subpixel position resolution cannot be corrected for and will degrade energy resolution.

Chapter 7

High-Altitude Balloon Flight

7.1 Motivation for Space Applications

Gamma-ray spectrometers are regularly used in planetary science to probe the subsurface elemental composition of planetary bodies such as the Moon [52], Mars [53], Mercury [54], Venus [55], and asteroids Eros [56], Vesta and Ceres [57] [58]. Gamma rays emitted from planetary materials provide key information on the subsurface elemental composition that can be paired with mineralogical data to help understand the formation and evolution of the planetary body. These gamma rays are the result of both radioactive decay and interactions between the subsurface materials and an activation source (i.e. galactic cosmic rays or a pulsed neutron generator). Currently, the spatial resolution of mineralogical data such as data acquired by infra-red spectroscopy, X-ray diffraction and many other methods, is usually better than that achieved with gamma-ray spectrometers. The diameter of a spatial resolution element with the Mars Odyssey Gamma Ray Spectrometer (GRS) on the Martian surface is about 360 to 450 km [59]. To advance the state-of-the-art and enable the synthesis of elemental and mineralogical data at finer spatial scales, planetary gamma-ray spectrometers with near-HPGe energy resolution, imaging capabilities, high signal-to-noise ratio, high efficiency, low mass, low

This chapter is based on published work: Abraham et al., "Capability demonstration of a 3D CdZnTe detector on a high-altitude balloon flight," Nuclear Instruments and Methods in Physics Research Section A: Accelerators, Spectrometers, Detectors and Associated Equipment, Volume 1054, September 2023.

volume, and no cryogenic cooling are desirable. Large-volume, high resolution 3D CZT gamma-ray detectors using pixelated anodes are a suitable candidate to satisfy these requirements.

3D CZT detectors achieve around 0.5% FWHM at 662 keV for all events, which is comparable to the energy resolution achieved by HPGe used in space applications (0.3% FWHM at 662 keV for SPI [60] and RHESSI [61] and ∼0.5% FWHM at 662 keV for MESSENGER [62]). Unlike HPGe, CZT does not require cryogenic cooling, greatly reducing the mass, volume, and risk associated with a payload. Also, CZT has a greater atomic number and therefore higher stopping power.

In space, intense levels of mixed-radiation background can degrade the sensitivity of spectroscopic instruments. The 3D position sensitivity of CZT detectors can help enhance background rejection without an anticoincidence shield. Firstly, the 4π Compton imaging capability can be used to reject local gamma-ray background from scatter off spacecraft. Secondly, background events due to charged particles could be identified and rejected. While gamma-ray interactions have discrete interaction positions, charged particles deposit energy starting from one of the outward-facing surfaces of each CZT detector continuously along their path. The trail of energy deposition due to charged particles will therefore create a spatial signature that can be distinguished from the discrete gamma-ray interactions.

High-resolution large-volume 3D CZT detectors are commercially available and used in many relevant terrestrial applications, but have not yet been used in space applications, putting them at a Technology Readiness Level (TRL) of 4 [63]. CZT has successfully flown in previous space missions such as Swift-BAT [64], AstroSat [65], and NuSTAR [66]; however, the CZT used was much thinner (5 mm or less) and intended for X-ray detection. The significant difference in the size of the large-volume CZT is demonstrated in Fig. 7.1. Virtual Frisch-grid CZT, which can be up to ∼30 mm in thickness but limited in cross-section area, was proposed for gamma-ray telescope GECCO [67], but has not yet been space qualified. Compared to 3D CZT detectors using pixelated anodes, virtual Frisch-grid CZT has poorer energy resolution and position resolution for multi-interaction events and will require an anti-coincidence shield to reject background cosmic rays.

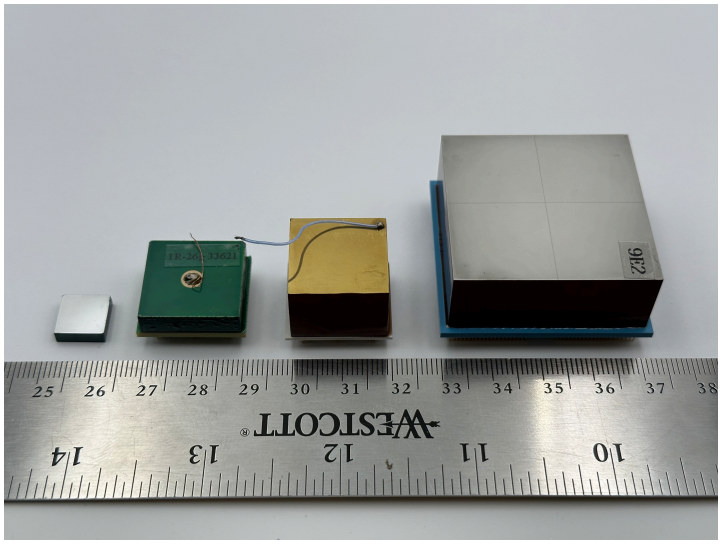

Figure 7.1: CZT of varying sizes, from left to right: 1×1×0.3 cm^3 (unbonded, volume ∼10 times greater than the CZT flown on Swift-BAT), 2×2×0.5 cm^3 (same thickness as thickest CZT flown in space), 2×2×1.5 cm^3 (size tested on high-altitude balloon flight) and 4×4×1.5 cm^3 (size proposed for future space missions).

7.2 Introduction

In collaboration between the University of Michigan and Los Alamos National Laboratory, a 3D position-sensing CZT detector prototype was built and integrated into a high-altitude balloon platform to evaluate its performance in a space-like mixed-radiation environment. The detector prototype, Orion Eagle, was designed to operate in near-vacuum environments without any temperature regulation. Orion Eagle was hand-launched from NASA's Columbia Scientific Balloon Facility (CSBF) at Fort Sumner, NM on September 26, 2021, and successfully operated throughout a 9 h flight, which reached 38.5 km in altitude. The flight met its objectives, successfully detecting atmospheric gamma rays and galactic cosmic rays, and raising the TRL from 4 to 6 for large-volume 3D CZT detector technology for space applications. Ionization tracks produced by charged particles create spatial signatures in the detector that are distinguishable from discrete gamma-ray interactions. Overall, the potential for background rejection capability, ambient-temperature operation, gamma-ray coded-aperture and Compton imaging, and near-HPGe energy resolution motivate the use of large-volume

3D CZT imaging spectrometers in future space missions.

A high-altitude balloon flight offered a cost-effective avenue to perform a capability demonstration of the Orion group's large-volume 3D CZT detector technology in a space-like environment for the very first time. The relatively small size and weight of CZT instruments made it a candidate for the relatively new hand-launch capability offered by NASA's CSBF. Compared to traditional small "piggyback" experiments hosted on larger balloon missions, hand-launch payloads are easier to integrate and launch, and suffer from less locally generated background due to the reduced overall mass. The high-altitude balloon flight aimed to show that with minor modifications, current 3D CZT systems can be adapted to operate in near-vacuum space-like environments and detect gamma rays while identifying charged particles to aide in the development of background discrimination algorithms.

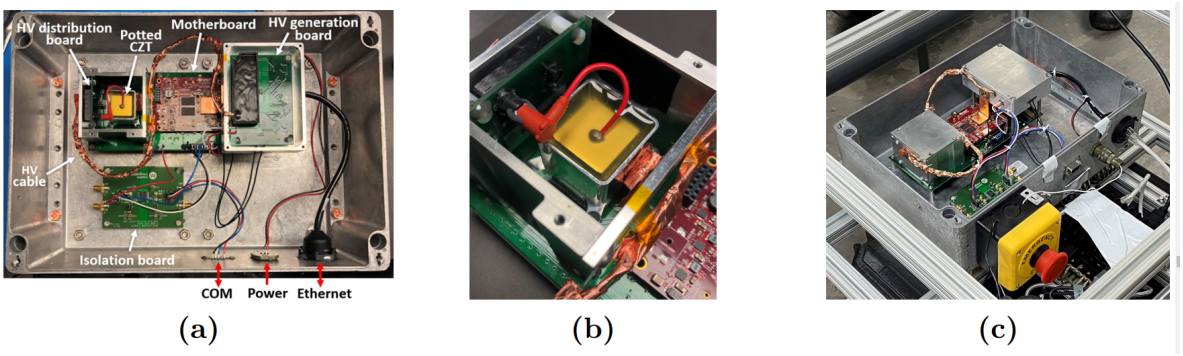

Figure 7.2: (a) Orion Eagle hardware with all enclosure lids removed. (b) Potted CZT detector with HV connector attached to the HV distribution board. (c) Orion Eagle with external connectors (emergency stop button, power, Ethernet) visible.

7.3 Payload

7.3.1 Orion Eagle Design

The design of Orion Eagle was based off Orion Solo. Due to the low-pressure environment expected during the high-altitude balloon flight, Orion Eagle (Fig. 7.2) has several additional design features not included in previous detector systems designated for in-laboratory or terrestrial use. Primarily, high-voltage design was of utmost importance.

During the operation, the cathode of the detector is biased to -3000V. Pressure changes during ascent/descent and the near-vacuum environment at float altitude are capable of causing high-voltage breakdown in air at small distances as predicted by Paschen's Law [68]. To mitigate risk, the layout of components on the high-voltage generation board and the distribution board were modified and contained in aluminum enclosures. All high-voltage components were potted. The CZT detector was potted with Scotchcast electrical resin 280 (3M) in an aluminum potting dam to provide high-voltage shielding (Fig. 7.2b). The wire and connectors carrying -3000V were rated for high-voltage (up to 12 kV) at high-altitude (up to 21 km) (manufactured by Connectronics Corps.). Orion Eagle was tested under -3000V bias in a small vacuum chamber pumped down to the anticipated float pressure ($\sim$266 Pa) prior to the flight. No issues were observed over six hours of operation at low air pressure.

Unlike other CZT systems that employ a fan and/or Peltier cooling to maintain room-temperature operation, Orion Eagle has no active temperature regulation to help reduce weight, power consumption, and risk. Copper pieces were used to dissipate heat from the components at greatest risk of overheating: the ASIC and FPGA. As discussed in earlier in this work, CZT detectors are capable of operating over a wide range of temperatures; however, calibration factors may drift with changes in temperature, so performing temperature calibrations are needed to help reduce degradation in energy resolution [16].

The top priority of this experiment was to successfully operate CZT in a near-space environment, which meant energy resolution was secondary. Due to limited time and low priority, temperature calibrations were not performed, and an issue with low frequency noise in the cathode signals was not fixed (which prevented the ability to accurately calculate the depth of interaction for 511 keV gamma-ray events, so a depth-correction could not be performed). Both of these factors degrade energy resolution even in a laboratory environment. For example, when the CZT detector was tested using a different readout system prior to potting, the depth-corrected energy resolution (FWHM at 662 keV) was 0.42% for single-pixel events, and the energy resolution degraded to 1.16% without depth-correction. Additionally, due to the risk of damage to the detector during the flight and possible harsh landing, only one CZT detector was used, and the detector selected was not one with the best performance nor the largest available size. The best detectors can achieve close to 0.3% FWHM at 662 keV for single-pixel events.

It should be noted that future CZT-based detector systems could instead use larger-volume CZT detectors ($4\times4\times1.5$ cm^3) [19] in an array to create an effective area higher than state-of-the-art HPGe used for planetary science missions [69]. The efficiency of ($2\times2\times1.5$ cm^3) CZT is described in detail in reference [70], and it is expected that the use of larger-volume single-crystal CZT can help improve efficiency.

Settings for flight

For the balloon flight, the Ideas v2.2 ASIC was operated in trigger-only readout mode with a sampling rate of 40 MHz and the largest available dynamic range setting of 9 MeV. A conservatively high low-energy threshold of 60 keV was chosen for the flight as a precautionary measure in case noise issues arose during the flight. For the balloon flight, events with 5 or more triggered pixels were also saved to demonstrate that CZT can measure high-energy charged particle tracks, which may trigger several pixels depending on the incident angle. Dual saving was implemented in case one of the external hard drives failed.

(a) **(b)** **(c)**

Figure 7.3: (a) Orion Eagle (aluminum enclosure) integrated into the gondola with the top insulation lid removed. (b) The payload on the flight-line shortly before launch. (c) The payload upside down after landing, still intact.

7.3.2 Integration

Orion Eagle is light (5 kg) and easily contained within a 33.2×23.3×11.0 cm^3 aluminum enclosure. This enclosure was integrated into a small gondola with an off-the-shelf compact fan-less computer, two external hard drives, and three 29.6V lithium-polymer batteries. The computer was used to run Orion Eagle's data acquisition software. Raw data (waveforms) was saved on-board via two external memory devices and retrieved after the flight for post-processing. The total power consumption of the whole system was around 20 W, mainly due to the computer and memory devices as Orion Eagle requires only ∼4 W. The gondola was 50.8×50.8×61.0 cm^3 (excluding handles) and had a simple but robust design, as it was intended to be a reusable testbed to hand-launch Los Alamos instrumentation. The gondola fully integrated and with insulation sidewalls taped on is shown in Fig. 7.3a.

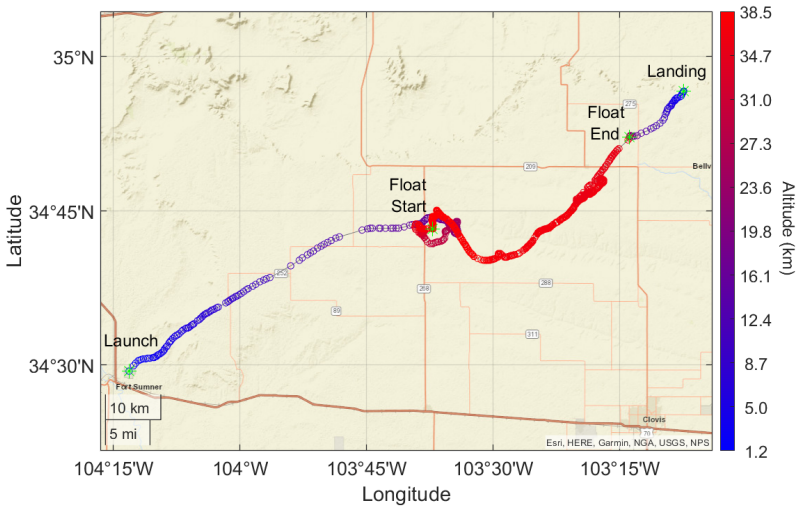

Figure 7.4: GPS coordinates provided by CSBF measured during the balloon flight starting in Fort Sumner, NM and ending ∼112 km northeast, near the New Mexico-Texas border.

7.4 High-Altitude Balloon Flight

The Orion Eagle payload (Fig. 7.3b) was successfully hand-launched at the NASA CSBF facility in Fort Sumner, NM on September 26th, 2021 at 7 am MDT. The float altitude

was reached 3.2 hours into the flight. During float, the altitude slowly dropped from 38.5 km to 35.4 km. After 5.4 hours at float the flight was terminated, and the payload descended back to the ground in 24 min. The flight path is shown in Fig. 7.4. Stratospheric turnaround conditions caused the balloon to circle in parts of the flight, which limited the latitudinal/longitudinal distance traveled. The payload landed ∼112 km northeast of the launch site in New Mexico near the Texas border. The temperature and altitude throughout the flight is shown in Fig. 7.5. All altitudes discussed are relative to sea level. Though the free air temperature reached below -60°C (measured via CSBF equipment), the temperature sensor on the instrument's ASIC measured between 20°C and 35°C during the flight. The ASIC temperature takes time to be impacted by changes in ambient temperature, so it lags behind the free air temperature during the ascent. The ASIC and other electronics generate some heat, which causes the ASIC temperature to reach equilibrium at a temperature greater than the ambient temperature outside the detector enclosure. However, at float altitude, the temperature gradually increased over time instead of reaching an equilibrium. This is likely due to poor heat dissipation caused by the near-vacuum environment (reduced convection). After the descent, the ASIC temperature decreased even though the free air temperature increased, which is likely due to improved heat dissipation.

7.5 Orion Eagle Flight Results

7.5.1 Detector Count Rate

Orion Eagle was turned on (biased to -3000V) and acquiring data about an hour prior to launch. There was no communication between Orion Eagle and CSBF during the flight. Orion Eagle was equipped to receive a pulse to control the high voltage power and send a return status (via an off-the-shelf isolation board shown in Fig. 7.2a); however, this feature was not used to reduce risk. All power successfully remained on until Orion Eagle was manually powered off during recovery of the payload. Orion Eagle was functional with no signs of damage afterwards (Fig. 7.3c).

The event rate on the day of the flight is shown in Fig. 7.6. The event rate was averaged over one-minute intervals, and additionally separated by the number of anode pixels triggered during each event. Typically, the ASIC can process thousands of counts

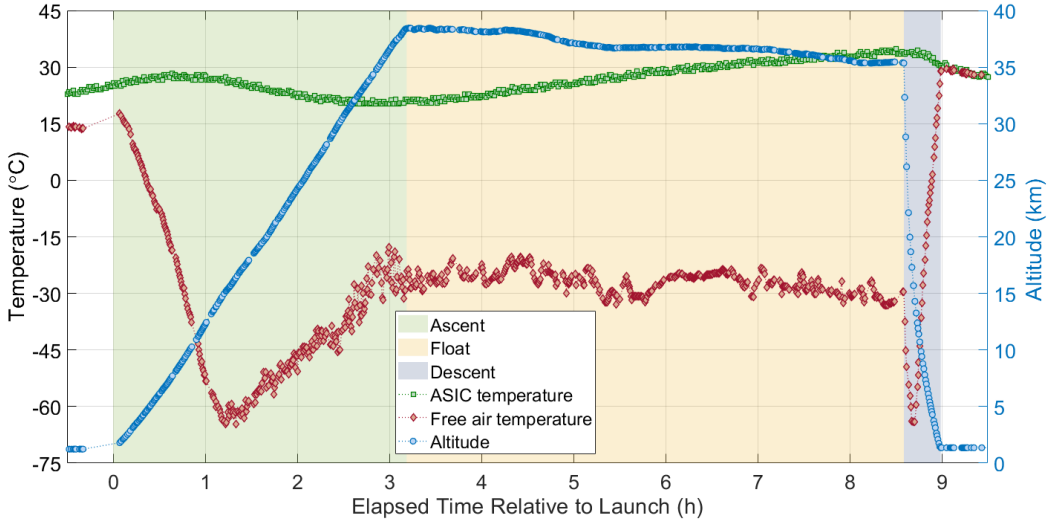

Figure 7.5: Conditions during the flight: free air temperature, Orion Eagle ASIC temperature, and altitude. Altitude and free air temperature were provided by CSBF.

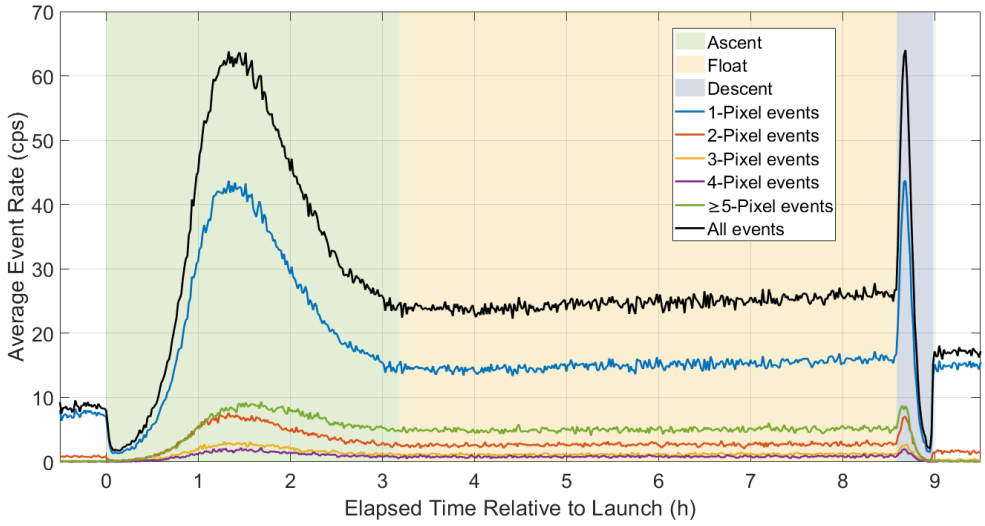

Figure 7.6: Average event rate as a function of time relative to the high-altitude balloon launch. The events are categorized by number of pixels triggered.

per second; thus, the count rates measured during the flight were relatively very low,

and the detector dead time is small (<1.5%). The overall detector count rate was steady during the float, only slightly increasing over time, and the maximum count rate was reached during the ascent and descent. The altitude profiles shown in Fig. 7.7 demonstrate that the change in average count rate during the flight was altitude related. The altitude profiles match the general trend measured in previous balloon flights with radiation detectors [71] [72] [73] and generated by atmospheric simulations [74]. The count rate initially increases with altitude, peaks at ∼17.5 km (near the Regener-Pfotzer maximum [75] which is where the maximum intensity of radiation in the atmosphere is expected) and then decreases above the peak altitude. This trend is consistent for both the ascent and descent. It should be noted that due to the quick nature of the descent (34 km drop in 24 min), the statistics are sparser. The change of altitude within each minute (over which the event rate is averaged over) may have skewed the first few data points at the beginning of the descent where the drop was fastest.

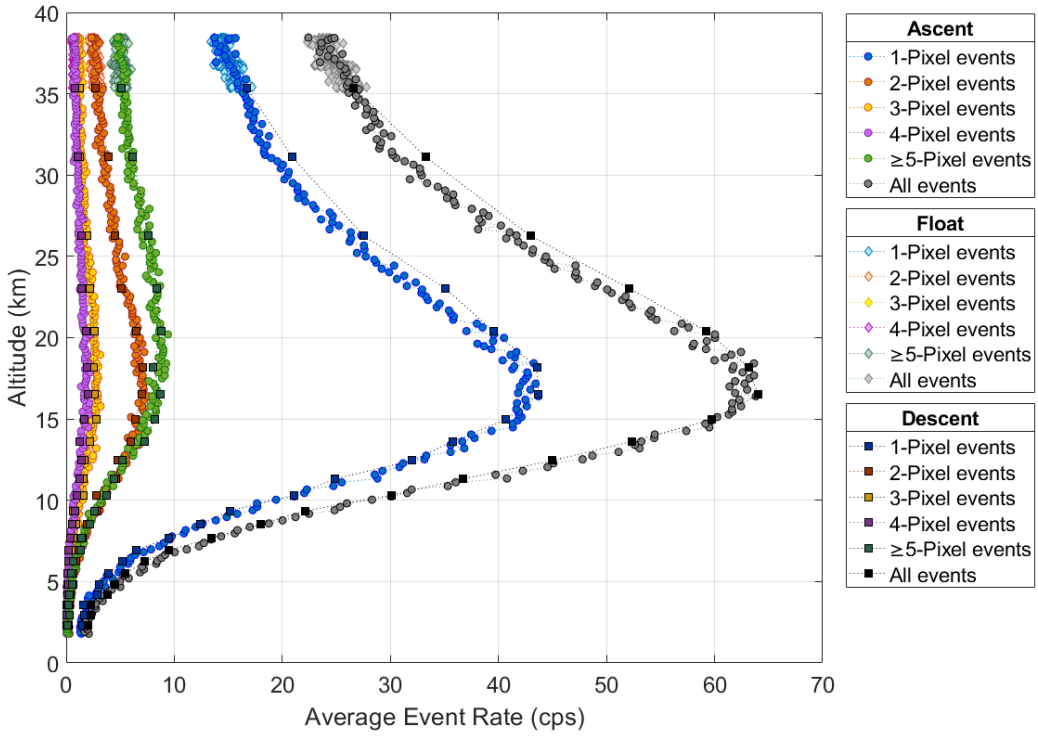

Figure 7.7: Altitude profiles of event rate (averaged every minute) for Orion Eagle's ascent (circles), float (diamonds), and descent (squares).

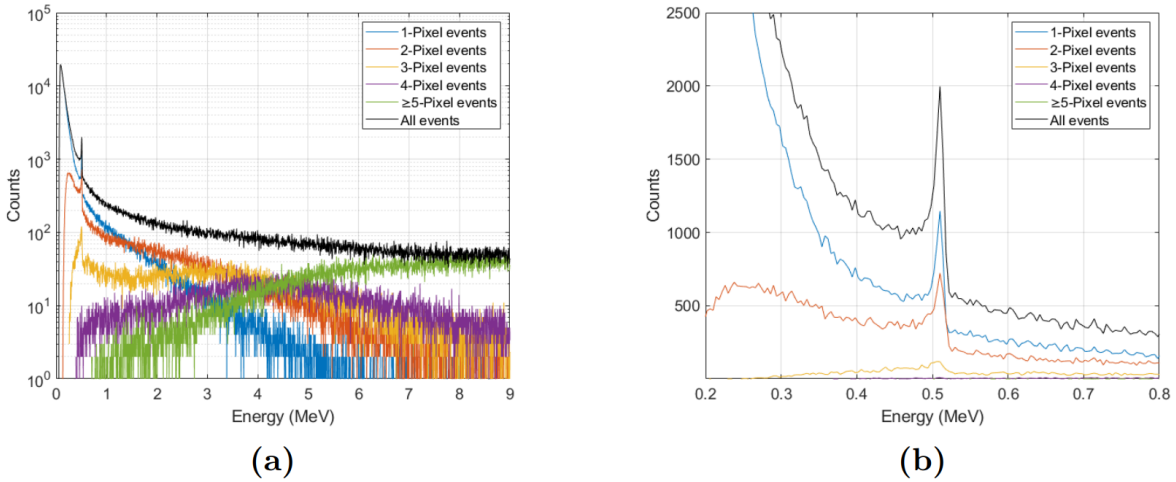

Figure 7.8: The anode energy spectra measured during the flight (ascent, float, and descent combined) broken down by event type for (a) the whole dynamic range in log scale and (b) focused on the 511 keV peak on a linear scale.

7.5.2 Spectroscopy

The anode energy spectrum measured during the flight is shown in Fig. 7.8. The overall spectrum clearly has a peak at 511 keV, the expected electron-positron annihilation line, and is otherwise a broad continuum with many low energy counts. This energy distribution is similar to observations from other atmospheric gamma-ray high-altitude balloon measurements and simulations [73] [76] [77] [78]. For 1, 2, 3, and 4-pixel events, the spectra drop off at sequentially higher energies. For 5-or-more-pixel events, the continuum increases and levels off at high energies likely due to the large energy depositions from heavy charged particles. The peak is easily identifiable and consistently present during the majority of the flight (Fig. 7.9), indicating the successful operation of the detector. In Fig. 7.9b, variations in the 511 keV peak centroid over the time of the flight can be seen, likely due to changes in temperature. In the spectrum as a function of altitude measured during the ascent (Fig. 7.10), the 511 keV peak first becomes discernable just below 10 km.

From a ^{22}Na calibration measurement prior to the balloon flight, the FWHM of the 511 keV peak for single-pixel events was 6.1 keV (temperature was 28.8°C ± 1.1°C). The data was only corrected for channel-by-channel gain variations and had no corrections

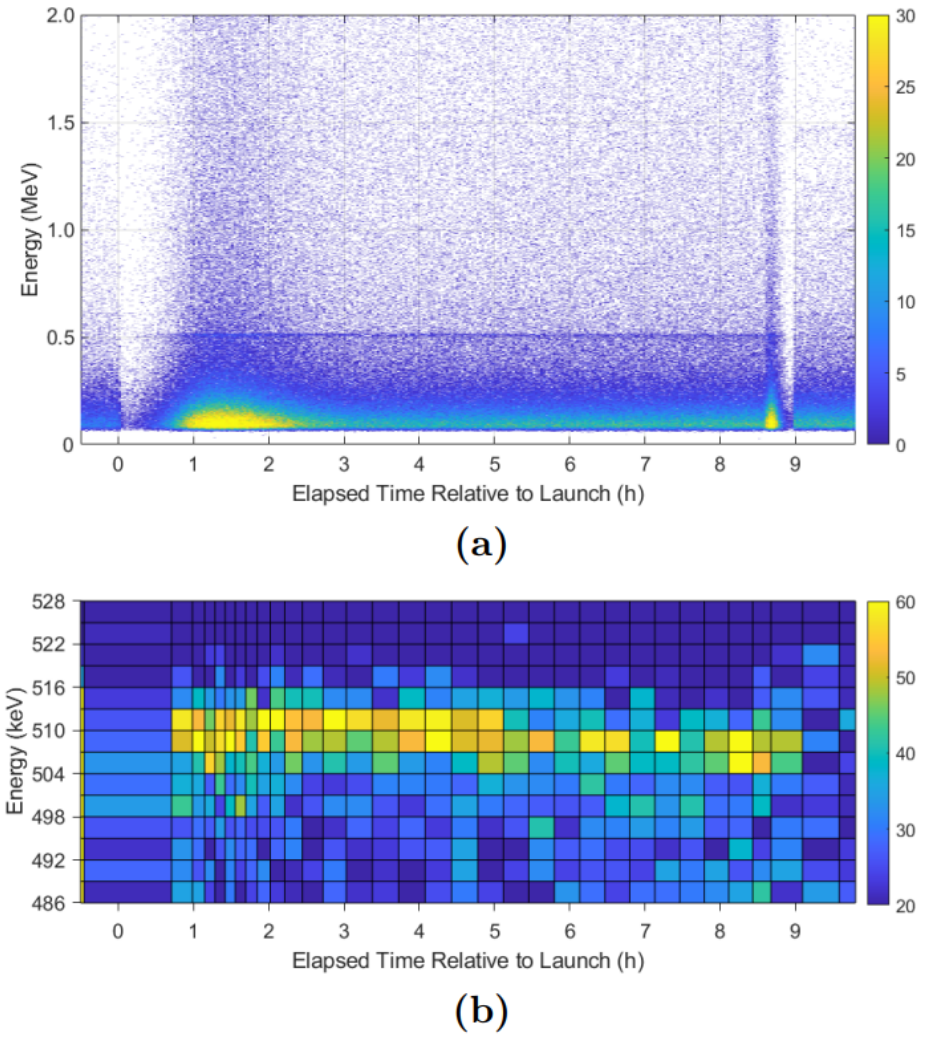

Figure 7.9: The anode energy spectrum for all events over time relative to the launch (a) in the range of 0-2 MeV, where each bin is 1 keV by 2 min, and (b) focused on the 511 keV peak where each bin is 3 keV by a variable time bin to compensate for differences in count rate (∼30k counts over all energies per time bin). Float altitude was reached at 3.2 h, the descent began at 8.6 h, and the payload landed at 9 h.

for temperature or depth-gain variations, which is why the 511 keV peak has poorer energy resolution than normally achieved with 3D CZT in laboratory settings. The 511 keV photopeak measured during the flight (Fig. 7.8b) was broader, with a FWHM of 11.2 keV for single-pixel events. The broadening of the peak was likely due to a much

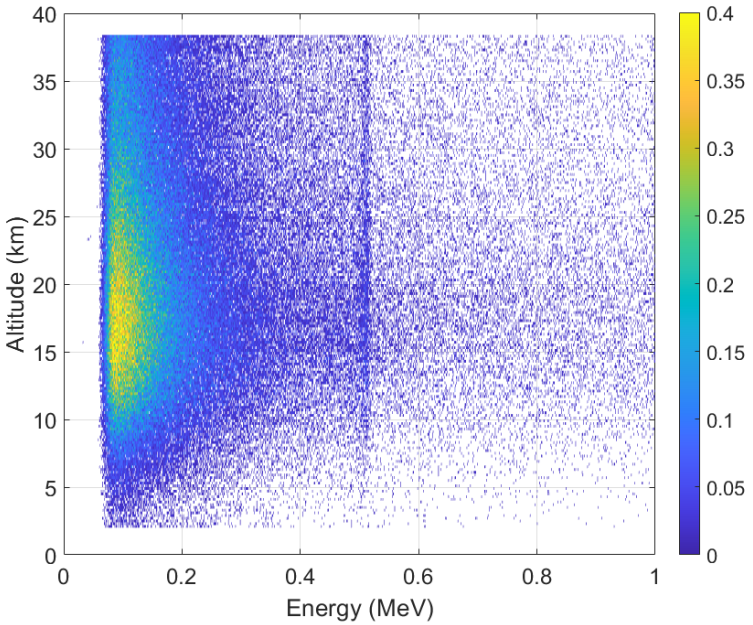

Figure 7.10: The anode energy spectrum for all events as a function of altitude measured during the ascent. The color bar gives the counts per second per bin, where each bin is 1 keV by 0.2 km.

greater variation in temperature during the flight. In a ^{22}Na calibration measurement after the flight, the FWHM of the 511 keV peak for single-pixel events was 6.2 keV (temperature was 26.1°C ± 0.6°C). The average channel gain was 0.3% greater after the flight. These changes are negligible, especially when considering the difference in temperature during the calibration measurements. This indicates that the detector was not damaged during the flight. If there was damage (either mechanical or radiation-induced), the gain would have significantly decreased. Additionally, no activation peaks were observed during the flight or in post-flight background measurements. Due to the short time frame of the flight, neither radiation damage nor activation were expected based on previous studies [79].

As shown previously in Fig. 7.5, the temperature ranged from 20°C to 35°C during the flight. For an increase in temperature of 15°C, a decrease in gain of almost ∼2% is expected based on findings earlier in this work (Section 4.6) and in Ref. [16]. The gain corresponds to the amplitude of the photopeak centroid. For example, if calibration factors determined at 20°C were applied to data from a measurement at 35°C, the

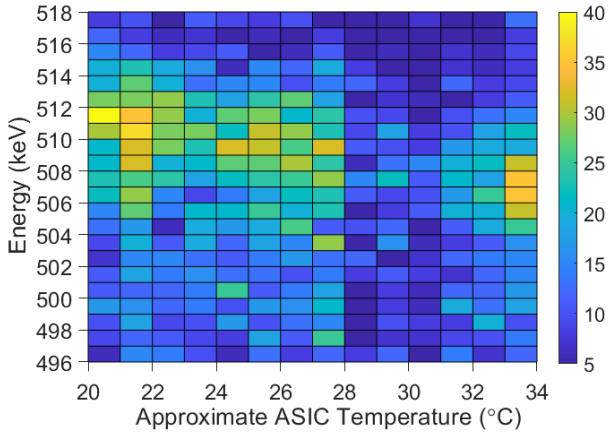

Figure 7.11: The distribution of the in-flight 511 keV peak as a function of the approximate ASIC temperature. Each bin is 1 keV by 1°C.

reconstructed energy of the 511 keV peak would be underestimated by ∼10 keV. If the temperature is stable, the change in gain would have little effect on the FWHM of the peak. However, if the temperature gradually drifts between 20°C and 35°C, like in the case of the balloon flight, the peak will be spread over a ∼10 keV range if the change in gain is not accounted for. This could be seen in Fig. 7.9b and in Fig. 7.11, the distribution of the 511 keV peak during the flight as a function of ASIC temperature. The ASIC temperature is an approximation in this figure: the temperature sensor was not very precise (±0.5°C error), the temperature was only sampled every minute so values for each radiation event had to be interpolated, and the temperature of the ASIC may not truly reflect the detector temperature when the temperature changes quickly [16]. This approximation and the lack of depth-correction may be the reason for varying spread in the photopeak for different temperature bins. Nevertheless, it is reasonable to conclude that the broadening of the 511 keV peak during the flight was within the error expected due to changes with temperature.

The background event rate after landing was approximately 2 times higher than prior to the launch. The elevated event rate was not observed during the descent, suggesting it is caused by differences in natural background activity and/or the proximity to the ground rather than activation of the payload. Though statistics are poor, the spectrum after landing (Fig. 7.12) appears to have a peak near 1.46 MeV and a corresponding Compton edge/continuum, which is likely from naturally occurring ^{40}K. Prior to the

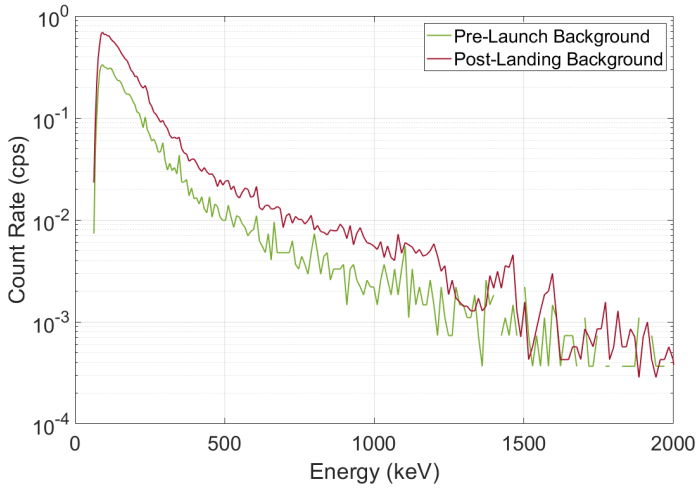

Figure 7.12: The single-pixel energy spectra measured from background prior to launch at the launch site and after the flight at the landing site.

flight, the payload was upright on its legs and hoisted up on cardboard (Fig. 7.3b), and the detector was near the top of the gondola. After the impact of landing, the payload ended up resting upside down, which places the detector much closer to the ground (Fig. 7.3c).

7.6 Charged Particle Detection

During the flight, the majority of events were single-pixel events, which correspond mainly to low energy gamma-ray interactions (i.e. photoelectric absorption). Charged particles passing perpendicularly through the anode/cathode planes under a single pixel will fall under the single-pixel event category as well. Charged particles will continuously deposit energy in the detector along their path, essentially creating a line charge. Following the Shockley-Ramo theorem, the expected signal induced from a line charge under a single pixel is different from that of a point charge (i.e. approximation of gamma-ray interaction) in a pixelated detector. Waveforms from Orion Eagle's flight can demonstrate these differences as shown in Fig. 7.13.

For gamma-ray interactions, the cathode signal will increase linearly as soon as the charge begins to drift, and the anode signal rises very quickly only when the charge is in close proximity to the collecting pixel anode. For gamma-ray interactions in the bulk of

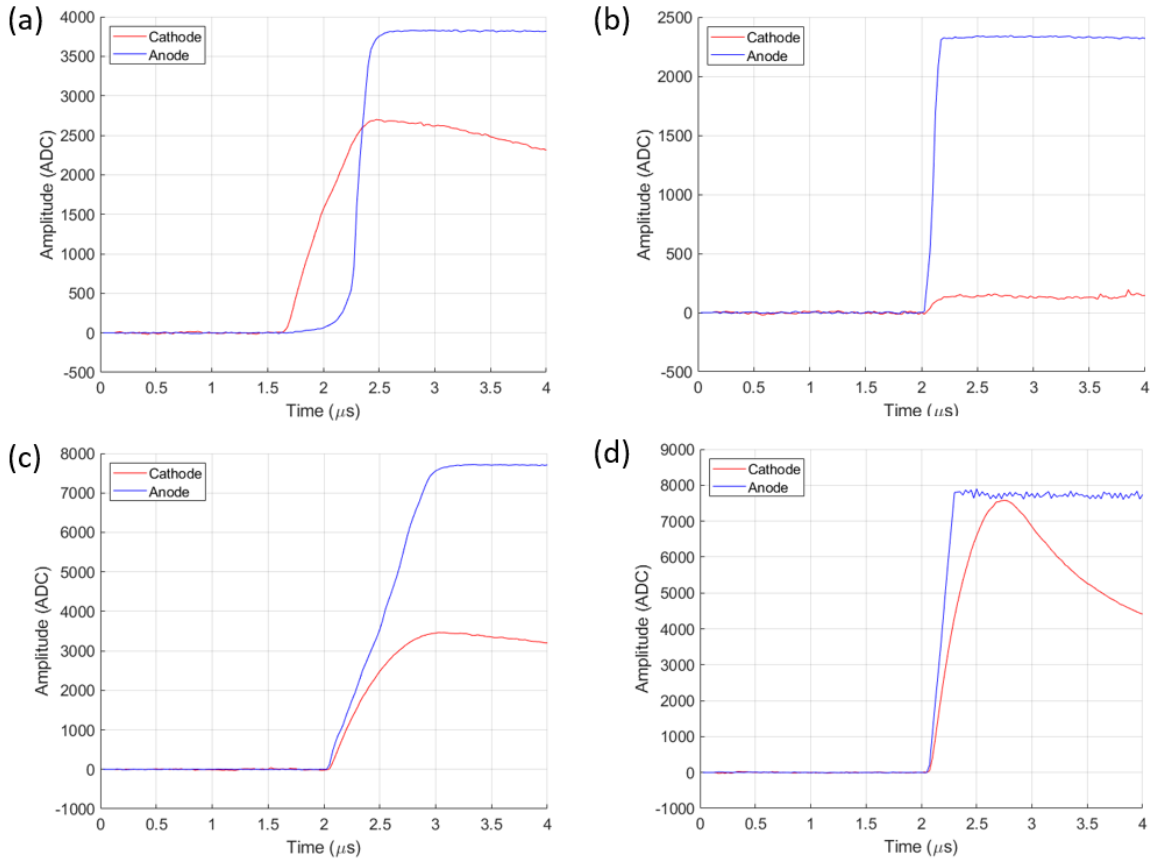

Figure 7.13: Examples of waveforms measured during Orion Eagle's flight corresponding to (a) a gamma-ray interaction in the detector bulk, (b) a near-anode gamma-ray interaction, (c) a heavy charged particle interaction, and (d) a heavy charged particle interaction depositing >9 MeV that saturated the anode and cathode pre-amplifiers. Signal decay in the cathode tails in (a) and (c) is due to the cathode pre-amplifier feedback resistance setting whereas in (d) it is due to saturation of the pre-amplifier.

the detector (Fig. 7.13a), the anode signal will rise later than the cathode signal and will have some curvature. The extent of curvature in anode signals depends on the depth of interaction, as it is caused by variation in the anode weighting potential (curve at beginning of signal rise) and the amount of electron trapping/detrapping (rounding at the end of signal rise). For a near-anode gamma-ray interaction (Fig. 7.13b), the charge begins in close proximity to the collecting pixel so the anode and cathode signals will rise at the same time. Due to the short drift distance, the amount of curvature in the

Table 7.1: Summary of the anode and cathode signal characteristics expected for different interaction types.

Interaction particle type/location	Anode signal			Cathode signal			Relative start time
	Amplitude	Shape	Rise time	Amplitude	Shape	Rise time	
Gamma-ray (in bulk)	*Variable*	*Some curvature*	*Short*	*Variable*	*Linear*	*Variable*	*Cathode rises first*
Gamma-ray(near-anode)	*Variable*	*Minimal curvature*	*Very Short*	*Low*	*Linear*	*Short*	*Both rise at same time*
Charged particle (all depths)	*High*	*Linear*	*Long*	*High*	*Rounded*	*Long*	*Both rise at same time*

anode signal is limited, and the cathode amplitude will be small relative to the energy deposited.

For a charged particle passing vertically through the detector under a single pixel, the collecting anode signal will increase linearly, the cathode signal will be rounded, and both signals should begin to visibly rise at the same time (Fig. 7.13c). The slope of the anode signal will be proportional to the energy deposited by the charged particle. An example of a charged particle event with very high energy is shown in Fig. 7.13d. In this case, the amount of energy deposited is so large that the pre-amplifiers saturate. In the anode channel, this causes the signal to be clipped. For the cathode channel, discharge occurs, causing a rapid decay in the tail of the cathode signal. Events that saturate the anode pre-amplifier are easy to identify due to the high amplitude. Only 1.3% of single-pixel events during the flight caused saturation of the anode signal.

For events that do not saturate the anode pre-amplifier, charged particle events can be identified by abnormally long anode signal rise times, simultaneous rise of anode and cathode signals, and large amplitudes. Differences in signal shapes (i.e. linearity, curvature) can be considered as well. For near-anode gamma-ray events and high energy charged particle events, the timing and shape of anode signals may be similar. In this scenario and for events that saturate the anode pre-amplifier, the cathode amplitude can help classify the events, as the amplitude will be very low for near-anode gamma-ray events, and high for the charged particle events. The differences in characteristics of the cathode and anode signals can be used for discrimination between gamma-rays and charged particles. Table 7.1 summarizes these characteristics. It should be noted that these are the characteristics expected in an ideal detector system. In practice, the shape of signals can be affected by noise, pre-amplifier settings, poor detector material quality, and non-uniformity in the detector's electric field.

At altitudes above 15 km, 5-or-more-pixel events were the second most probable

event type, likely due to the increased presence of charged particles, which are primarily protons [74]. Heavy charged particle interactions incident from most angles will fall under this category. For the 5-or-more-pixel events, the 3D position sensitivity of CZT can be leveraged to visualize charged particles passing through the detector to help separate them from gamma-ray interactions based on differences in spatial signatures. Multiple gamma-ray interactions result in multiple discrete energy depositions, whereas heavy charged particles continuously deposit energy along their path, creating linear ionization tracks. Fig. 7.14 shows a few examples of linear ionization tracks measured by Orion Eagle. These are rough estimations of the electron cloud distribution, and do not account for weighting potential crosstalk, charge sharing, and local electric field distortions due to large electron clouds. For applications where charged particles are not of interest, events triggering several pixels should not be saved to help reject most charged particles and reduce detector dead time as data size grows large for these events. If charged particles are of interest, the 3D reconstructions of the ionization path could be used to estimate the dE/dx (energy loss per unit path length), which could consequently be used to estimate the energy of the particle if its identity is known.

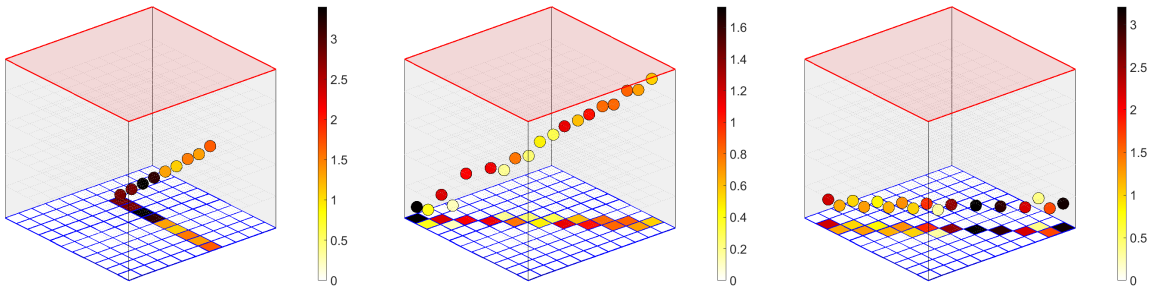

Figure 7.14: Visualization of charged particle tracks passing through Orion Eagle's single CZT detector. The red face represents the planar cathode. The 11×11 blue grid represents the pixelated anodes, with triggered anodes colored based on the energy deposition. The colored circle markers represent the reconstructed interaction location and energy. The color bar shows the range of the estimated energy deposition per pixel in MeV.

7.7 Conclusions

The high-altitude balloon flight of Orion Eagle demonstrates that 3D CZT detectors can successfully operate in a near-space environment. Modifications to detector design allowed operation in the near-vacuum environment without failure of the high voltage. The detector count rate consistently varied with altitude and peaked at the altitude of the Regener-Pfotzer maximum. The 511 keV electron-positron annihilation line was consistently present as expected, demonstrating the stability of the detector's spectroscopic capability. Cosmic rays were detected, most notably shown by the increase in 5-or-more pixel events at elevated altitudes. The dataset obtained by Orion Eagle can be used to visualize the differences in spatial signatures for gamma-rays and charged particles, which can help the development of particle discrimination algorithms and will be discussed in more detail in Chapter 8. The successful operation of Orion Eagle and the increase of TRL from 4 to 6 further motivates the use of high-resolution large-volume 3D CZT detectors in space applications.

Chapter 8

Particle ID

8.1 Background

Over a decade ago, Xu [80] first identified muon tracks in a single 3D CZT detector, and Kaye [81] showed an example of a muon track traversing through an array of 3D CZT detectors. These muon interactions triggered multiple pixels, leaving a visible track. Near sea-level, the flux of these events are low, and the energy deposited will be high compared to other natural radiation background sources, making muon events easy to distinguish [15]. In the upper atmosphere and in space, the relative flux of charged particles can be significant, and the energy of gamma-ray lines of interest could be comparable to the energy deposited by charged particles. Since there has been growing interest in using large-volume 3D CZT for space applications [67] [82] [83], it is important to consider how particle ID could be performed in such scenarios. The dataset collected from the balloon flight in Chapter 7 can be used to explore different techniques.

8.2 Single-Pixel Events

As discussed in Section 7.6, in the case that a charged particle is incident perpendicular to the anode and cathode, it is possible for only one pixel to trigger, and the signature of the signal induced on the pixel has some defining features. Previously, Xia [20] revisited methods introduced by Zhu [24] to reconstruct the electron cloud distribution of a muon interaction under a single pixel in CZT. Electron cloud reconstruction could help with particle ID; however, there are issues with the current methods that impede

the accuracy and practicality (e.g. computationally expensive).

In this section, waveform analysis techniques are proposed to help identify single-pixel charged particle events. These methods are split into two categories: "conventional methods" that rely on digital signal processing and PCA, an unsupervised machine learning technique introduced in Chapter 2. The particles of interest are those with long ionization tracks such as muons and protons. Other charged particles like betas and alphas will only travel small distances in CZT, and can be discarded based on their proximity to the edge of detectors, as noted in Ref. [81]. The techniques were tested on the data set acquired during the high-altitude balloon flight. Before some of this analysis could be performed, extra corrections for the noisy cathode waveforms were performed.

8.2.1 Correction of Cathode Waveforms

The cathode signals from Orion Eagle were non-ideal due to unresolved low-frequency noise in the signal that could not be fixed in time for the balloon flight. Even though mainly large amplitude anode events are relevant to this analysis, there is still a wide range of cathode amplitudes due to the cathode weighting potential. The default techniques for timing and amplitude pick off do not work very well, especially since the signals oscillate up and down (Fig. 8.1). Therefore, a different approach was taken. Prior to the flight, the cathode waveforms at a lower sampling frequency with no source present indicated that the cathode noise resembles a low frequency sine wave. Therefore, for radiation events, fitting the cathode baseline to a sine wave and subtracting it out can help remove the noise. To do so, first the length of the baseline must be determined. The derivative of the cathode signal was taken to determine the starting point of the cathode signal rise (also shown in Fig. 8.1) for each event so that the number of samples used for the fit could be maximized. Based on the estimated frequency of the noise, fitting parameters were constrained to help fit the data in the baseline region to a sine wave, as shown in Fig. 8.2. Apart from the speed of the computation, this technique worked very well in fixing the majority of cathode signals, as shown in Fig. 8.2. Now, the fixed cathode waveforms can be used to get a better estimate of both amplitude and timing.

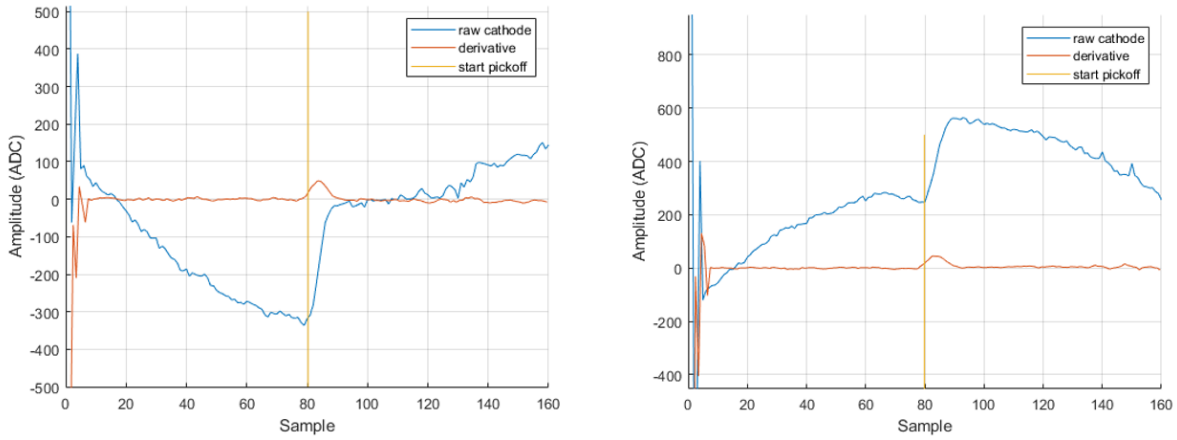

Figure 8.1: Examples of the noisy cathode waveforms and the signal start time picked off using the differential signal.

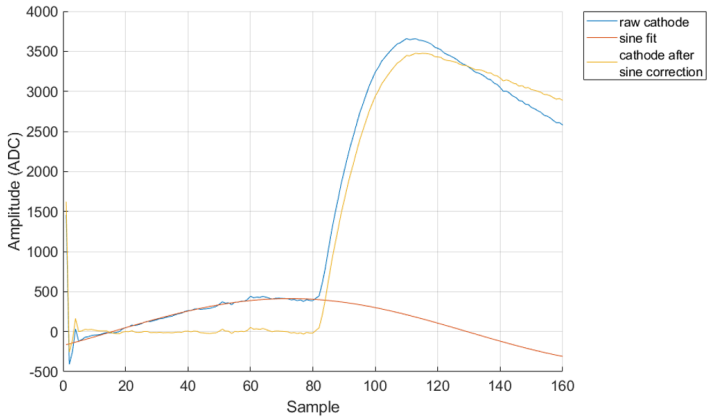

Figure 8.2: Example of correcting a noisy cathode signal by fitting a sine wave to the baseline.

8.2.2 Conventional Approach

Method #1: Compare Anode Amplitude Pick Off Techniques

A simple way to help identify charged particle events is to compare the anode amplitude calculated using different amplitude pick off techniques. As mentioned earlier in Section 2.2.1, amplitude can be picked off using a trapezoidal filter or with simple subtraction. The trapezoidal filter is very sensitive to long rise times, i.e. if the drift rise is longer than the stage / flat top of the trapezoidal filter (400 ns for anode waveforms), the amplitude will be underestimated. Simple subtraction would be the better measure

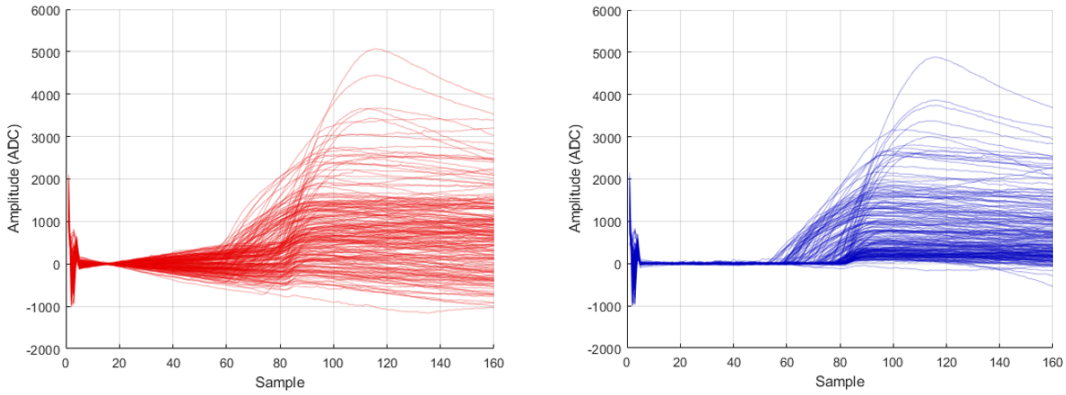

Figure 8.3: Cathode waveforms before (left) and after (right) the sine baseline correction.

of amplitude as long as the bounds of the baseline and tail region are selected properly. As mentioned in Section 7.6, the anode signals from charged particle events should have long rise times so the amplitude estimated would vary based on the pick off technique used.

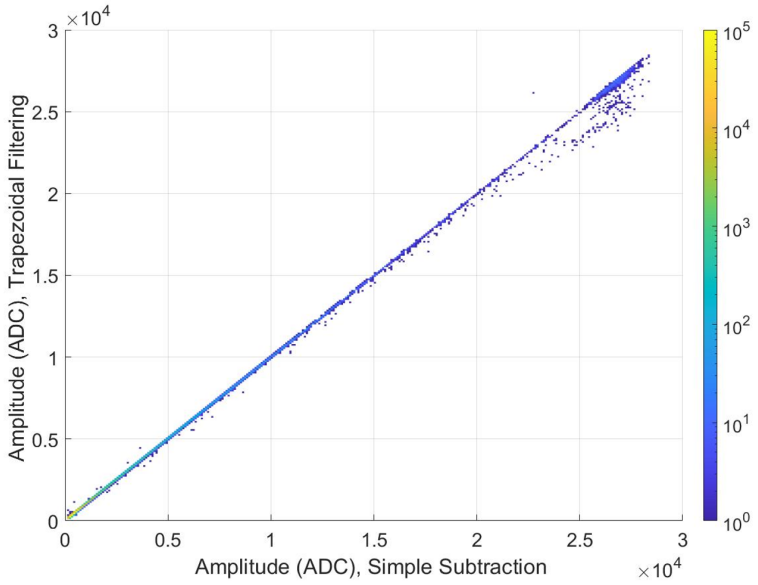

Figure 8.4: Comparison of the amplitude calculated via trapezoidal filtering and via simple subtraction for the high-altitude balloon flight data.

Fig. 8.4 shows that while the relationship between anode amplitudes calculated using

simple subtraction and trapezoidal filtering is usually 1:1, there begins to be some divergence at very high energies (this plot includes the full dynamic range, up to ∼9 MeV). Based on visual inspection of waveforms, the data points that fall far below the line of proportionality look like either charged particle events (long, linear anode signals) or multiple gamma-ray events occurring under a single pixel (multiple discrete rises, each shaped like gamma-ray induced anode waveforms). In either case, this technique could be used to reject such events that will degrade the typical anode spectrum created using trapezoidal filtering. The benefit of this method is that it requires only one additional form of waveform processing computation. However, it may still miss some events (e.g. if charged particle energy is very high, the waveform may be clipped so the full rise is not included), and it may be desirable to separate the charged particle events and multiple gamma-ray single-pixel events. Only data with amplitudes over 5,000 ADC (greater than roughly 1.8 MeV) are considered in the rest of this analysis.

Method #2: Anode Rise Time vs. Timing Difference

Next, the timing characteristics of the anode and cathode signals can be leveraged to gain more information. As mentioned in Chapter 7, a charged particle passing fully through the detector perpendicularly should have a long rise time, and the cathode and anode signals should begin to rise at the same time. These two features are not shared by gamma-ray events so they can be useful for particle discrimination. For this analysis, the timing was picked off differently than for typical measurements. Since all the events considered are high energy, the anode waveforms have a very high signal-to-noise ratio so filtering them is unnecessary, and the raw waveform can be used directly to more precisely pick off timing. The anode rise time was considered to be the time when the anode waveform is between 10% and 90% of the final anode amplitude. To determine the cathode signal rise "start" time, the fixed cathode waveform was smoothed and differentiated, and the rising-edge half-maximum of the differentiated waveform was picked off.

Fig. 8.5 shows the anode rise time as a function of the timing difference between the start of the anode signal rise and start of the cathode signal rise. An interesting distribution is revealed. For gamma rays, the timing difference is essentially the drift time and is proportional to the depth of interaction. Anode-side interactions have short

timing differences, and cathode-side events have longer timing differences. Therefore, the lower band corresponds to gamma-ray events, as the anode rise time varies only slightly with the depth of interaction / timing difference. For charged particles passing through the whole detector (i.e. muons and protons), the timing difference should be small and the anode rise time should equal the time for an electron to drift through the whole detector (1.5 cm). There are some events that appear in this region on the plot, and the shape of the corresponding waveforms match the expectations for a charged particle interaction.

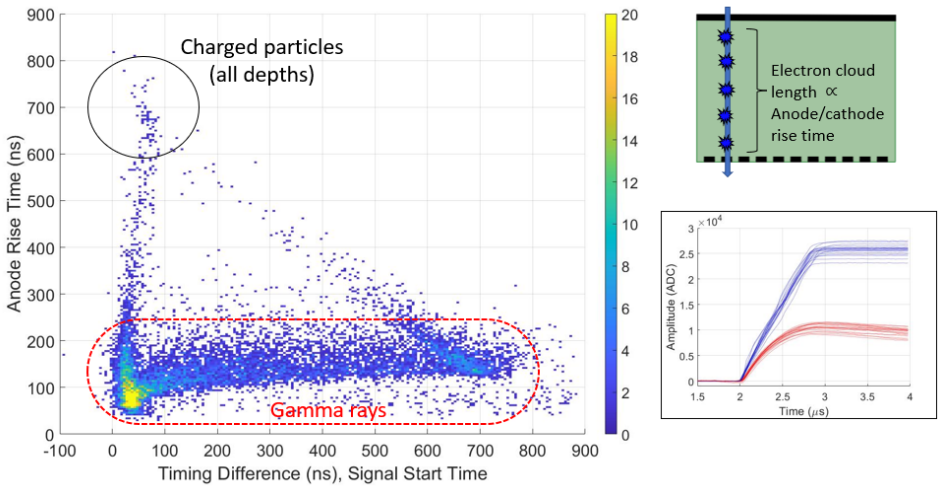

Figure 8.5: Anode rise time as a function of timing difference between the anode and cathode signal start times for single-pixel events with anode amplitudes greater than roughly 1.8 MeV. The waveforms shown on the right correspond to data points circled in black.

However, there is data that falls in two bands between the obvious gamma ray events and charged particle events, as highlighted in Fig. 8.6. The vertical band (where the timing difference is small and the anode rise time greatly varies) corresponds to large electron clouds extending from the anode side of the detector, as the anode and cathode signals should rise at the same time. The electron cloud length is proportional to the anode or cathode rise time in this case. The other band (where the anode rise time and timing difference have an inverse relationship) corresponds to large electron clouds extending from the cathode side of the detector. The cathode signal rises immediately, but the anode signal will not rise until the electron cloud reaches the near-anode region.

In this case, the anode rise time is proportional to the electron cloud length. The longer the electron cloud length, the shorter the difference in start times (which is why the inverse relationship exists). In this discussion, using the term "electron cloud" is intentional, as these events cannot be explicitly declared either a charged particle event or gamma-ray event, especially in the region where the two bands overlap with the lower "gamma-ray" band. For high-energy gamma-ray interactions, the electron cloud created can be quite large, resulting in long anode rise times (seen in the center of the three bands). If a high-energy gamma-ray interaction occurs near the anode or cathode side, it currently cannot be discerned from the electron cloud created by a charged particle that does not penetrate very far into the detector (i.e. alphas or betas). Advancements in electron cloud reconstruction techniques (like those discussed by Zhu [24] and Xia [20]) could possibly help with this in the future.

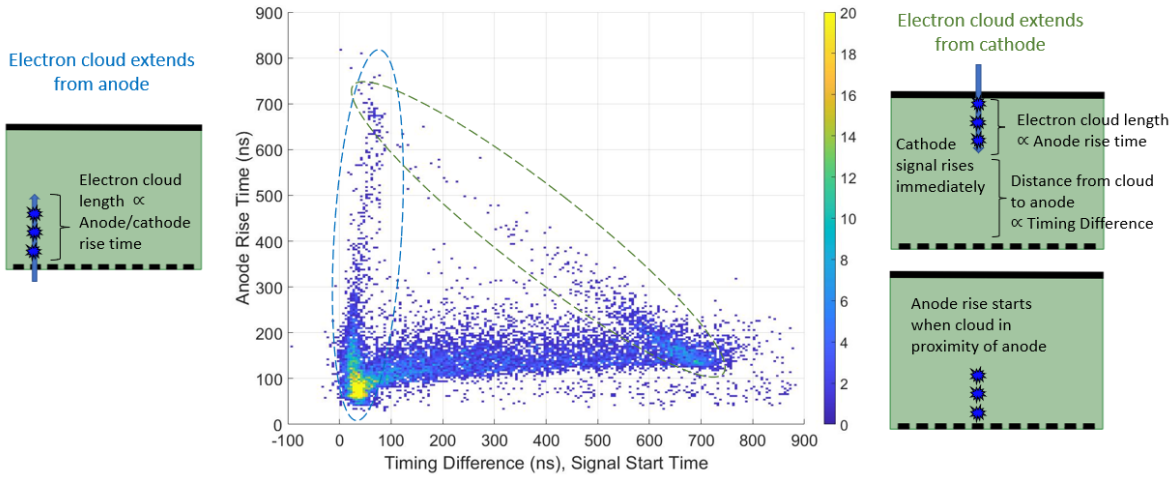

Figure 8.6: Anode rise time as a function of timing difference between the anode and cathode signal start times for single-pixel events. The circled regions correspond to electron clouds extending from the anode side (schematic on left) and from the cathode side (schematic on right).

Another explanation for the two bands in Fig. 8.6 is that charged particles are not necessarily stopped in the detector, but instead exit through the sides of the detector. Since only single-pixel events are considered, this could only be possible for interactions in the edge pixels. Fig. 8.7 shows a comparison of the distribution for edge and non-edge pixels. Also, events where the anode pre-amplifier saturated were removed, as this could cause an underestimated anode rise time. In this figure, the edge pixel distribution still

has all three bands and many counts. For the non-edge pixel distribution, there are fewer counts and there still appears to be some charged particles passing through all depths. The band related to large electron clouds extending from the cathode side is gone, yet there are large electron clouds extending from the anode side. The reason for this is likely diffusion and the fact that only single-pixel events are being considered. If a high-energy deposition occurs at the cathode side, it is more likely to diffuse and ultimately trigger more than one pixel. The edge pixels have a little more leeway as charge induced on the guard ring does not result in a trigger. Fig. 8.8, the distribution for two-pixel non-edge events shows that the "triangle" shape distribution can appear for the non-edge pixels, thus it is probable that there are still some charged particles stopped in the detector. Future work needs to more carefully consider charge-sharing events to be able to identify more charge particle events.

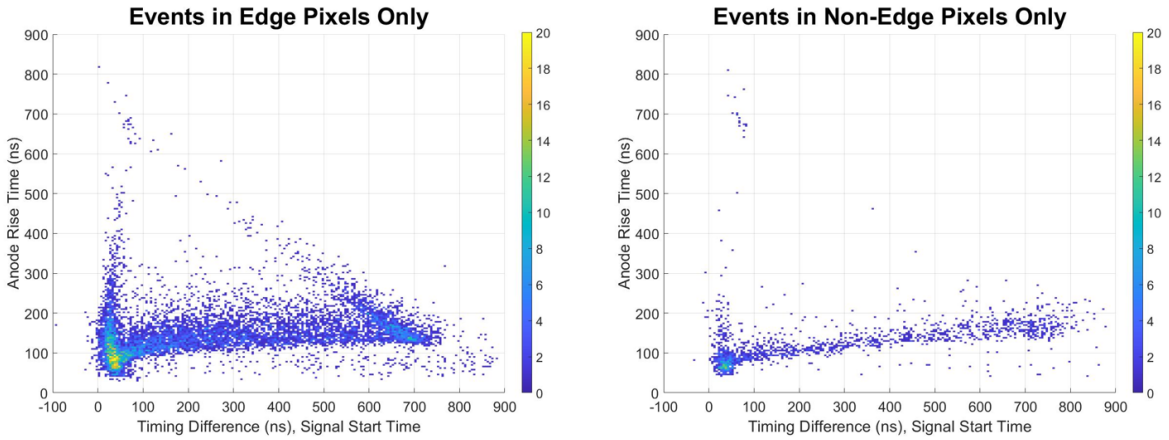

Figure 8.7: Anode rise time as a function of timing difference between the anode and cathode signal start times for single-pixel events occurring in edge pixels (left) and non-edge pixels (right).

8.2.3 PCA

The digitized waveforms contain a wealth of information that is difficult to fully utilize using conventional methods. Therefore, to try to extract as much information as possible, PCA can be used. This may help reject charged particle events while preserving as many gamma-ray events from the cathode and anode side as possible. Also, it may help identify events with multiple gamma-ray interactions under a single-pixel that could be

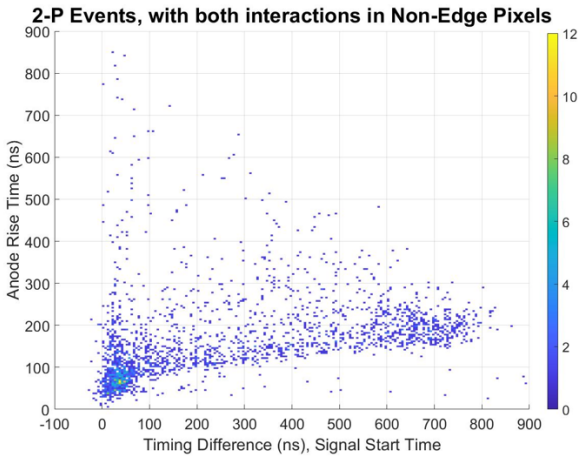

Figure 8.8: Anode rise time as a function of timing difference between the anode and cathode signal start times for two-pixel events with both events occurring in non-edge pixels.

labeled as charged particle events using the conventional methods. For initial proof-of-concept analysis, only very high-energy events were considered as there should be a relatively large share of charged particle events. Then for events over a broader range of energies, PCA is compared to conventional method #2.

Near-Saturation and Saturated Events

Only single-pixel anode events with very high amplitudes ($>2.5\times10^4$ ADC or roughly 9 MeV or more) were selected, normalized by their amplitude, and aligned by the sample corresponding to 2% of their maximum value. The eigenvectors for the first five anode principal components were calculated and shown in Fig. 8.9. The shape of the eigenvectors suggests that the different components are looking at sequentially higher order derivatives of the anode waveforms. Fig. 8.10 shows the distribution of the first four anode principal components. The second component shows potential for use as a discriminator due to its bimodal distribution, but it is unclear where to draw a line between the distributions. When plotted against the third and fourth principal components (Fig. 8.11), the separation between the distributions becomes clearer. Parabolas were drawn by visual inspection to separate the data into three groups. The separation is shown in color across different variations of principal component plots in Fig. 8.12. The three categories represent events that are (1) most likely charged particles, (2) most

likely gamma-rays, and (3) either gamma-rays with near-anode interaction locations or very high energy charged particles. The term "most likely" is used because this is all experimental data and the actual particle type is not known; however, the shape of the waveforms matches these descriptions, as shown in Fig. 8.13.

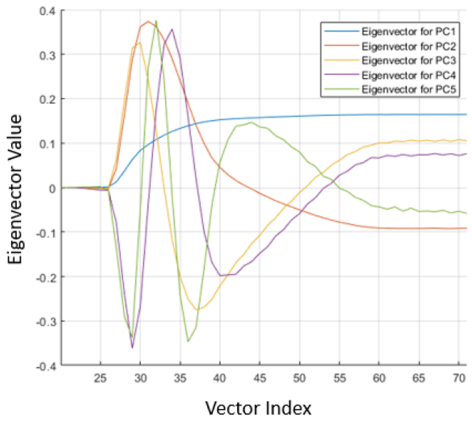

Figure 8.9: Eigenvectors for the first five principal components using the anode waveforms.

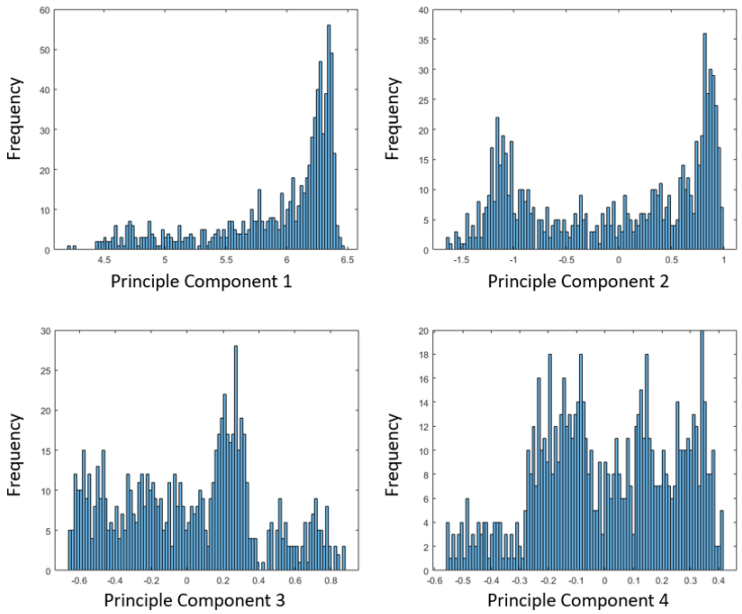

Figure 8.10: Distribution of the first four principal components for single-pixel events.

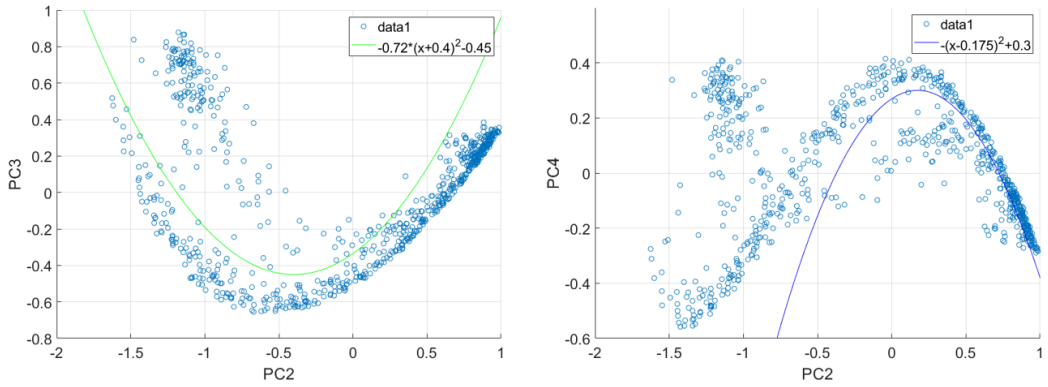

Figure 8.11: The second principal component plotted against the third (left) and fourth (right) principal components. Parabolas used for discrimination are included.

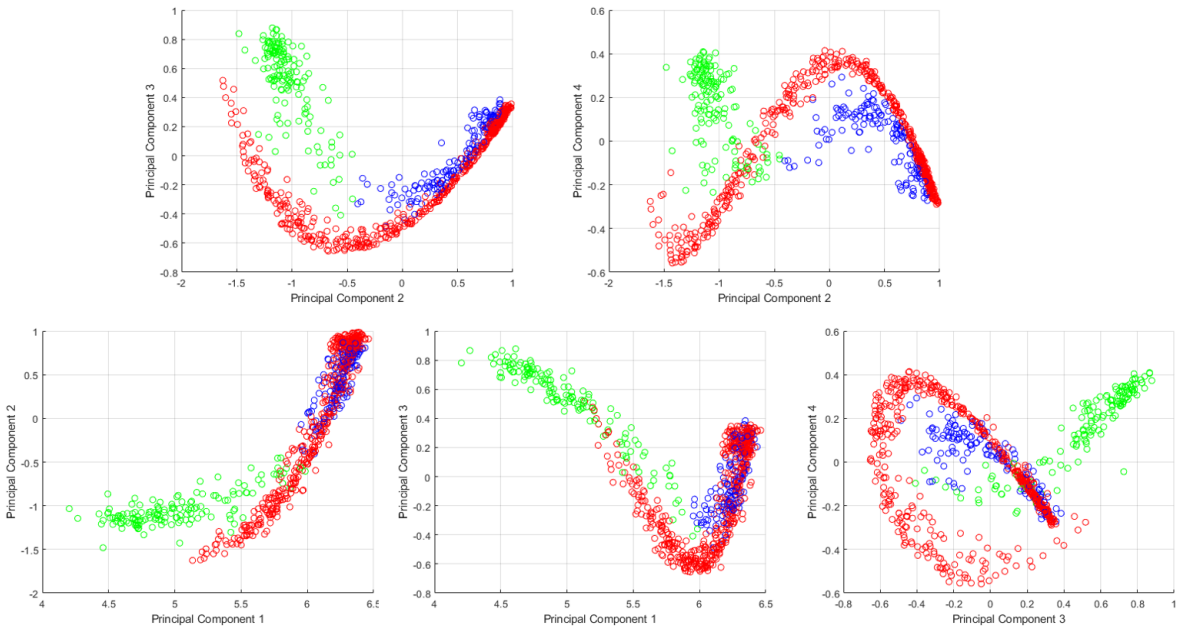

Figure 8.12: Comparison of principal components for the data split into three different categories using the parabolas shown in Fig. 8.11.

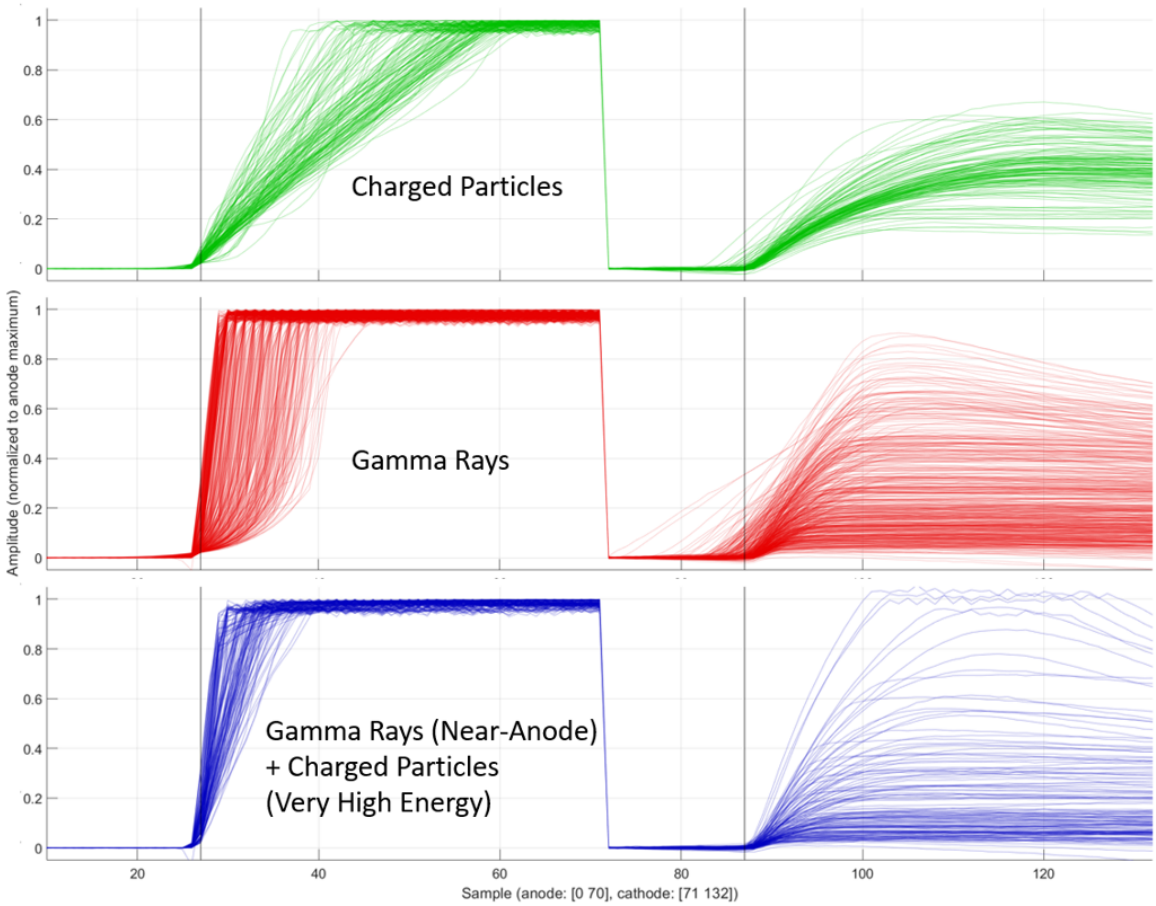

Figure 8.13: Anode and cathode waveforms from the data split into three different categories using the anode signal principal components, matching the colors shown in Fig. 8.12.

The trouble with category (3) is that as the energy of a charged particle increases, its anode signal, while still linear, begins to more closely resemble the anode signal for an anode-side high energy gamma-ray event. The saturation of waveforms adds an extra element of difficulty due to the loss of information that could provide additional clues. In this case, it can be beneficial to use information from the cathode signal. The lower amplitude cathode signals should correspond to the anode-side gamma-ray events, and the rounder cathode signals should correspond to charged particle events. For the cathode signals (aligned based on the anode signals), the first and second principal components are most useful and shown in Fig. 8.14. Plotting the two components against each other (Fig. 8.15), a discrimination line could be drawn which would only be applied to category (3) data. Events falling below the line are proposed to be charged particles and above the line are proposed to be gamma-ray events. Even by eye, it is hard to tell if the categorization is correct for some waveforms. However, based on this analysis, it appears that this data set was comprised of roughly 23% charged particle events and 77% gamma-ray events. Comparison to simulation would be able to help benchmark the accuracy of this technique.

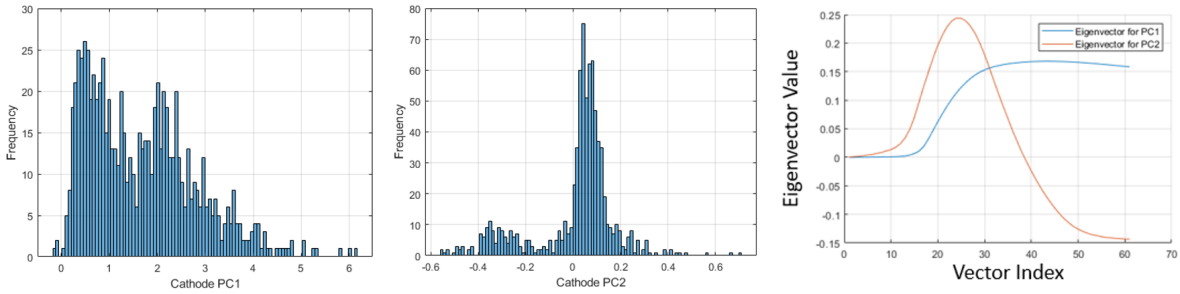

Figure 8.14: Distributions of the first two principal components of the cathode signals (left, center), and their corresponding eigenvectors (right).

8.2.4 Comparison of Methods

Using conventional method #2, regions were roughly selected and assigned a color to represent the probable event type. Then the PCA method was applied to the same data, and the distribution of the principal components was plotted using the event type color assignments chosen using method #2 for comparison of the results, as shown in

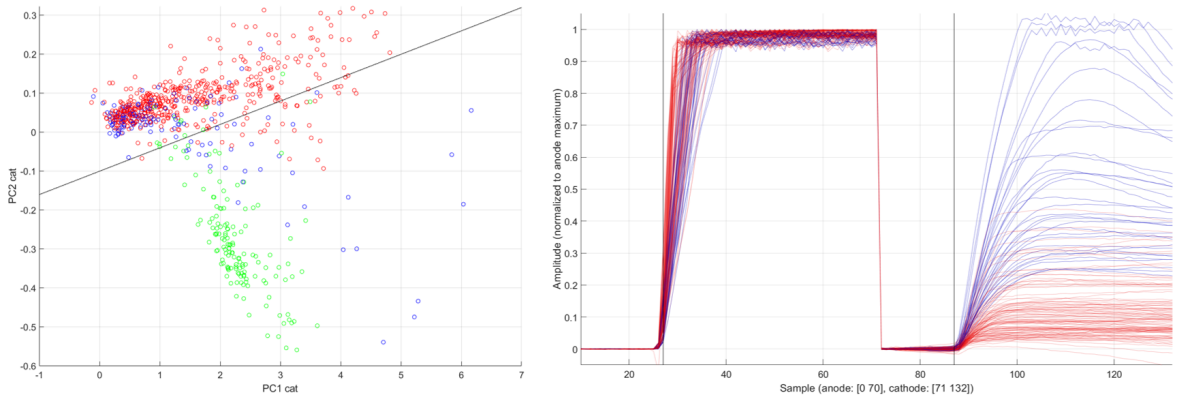

Figure 8.15: Left: First principal component vs. second principal component for cathode signals. Colors match the categories shown in previous figures. A discrimination line was added for the category with uncertain particle type based on anode information only (category 3 or blue data points). Right: Category 3 waveforms with events above the line colored red and events below the line colored blue.

Fig. 8.16. This further confirms that the labeling of the PCA bands was valid. For the events where the particle type was determined to be uncertain (purple) using method #2, there seemed to be greater spread in the distributions of the principal components. This suggests that PCA may be able to provide easier discrimination of these events, as it is more obvious when they fall outside of the gamma ray band in the PCA plots, especially for the non-edge events.

8.2.5 Summary and Future Work

Overall, the digitized waveforms from 3D CZT can provide information to help with particle identification. Conventional method #1 compares anode amplitude using different pick off techniques, which can help easily discard events with unexpected pulse shapes but does not provide much information. Conventional method #2 compares anode rise times and timing of anode and cathode signals. This clearly demonstrated the presence of charged particles, indicates how far the particle's generated electron cloud extends in the CZT, and can be used to help identify high-energy gamma-ray events with large electron clouds. The PCA method leverages information from signal shape. The anode signals alone can provide enough information to help with particle discrimination. PCA

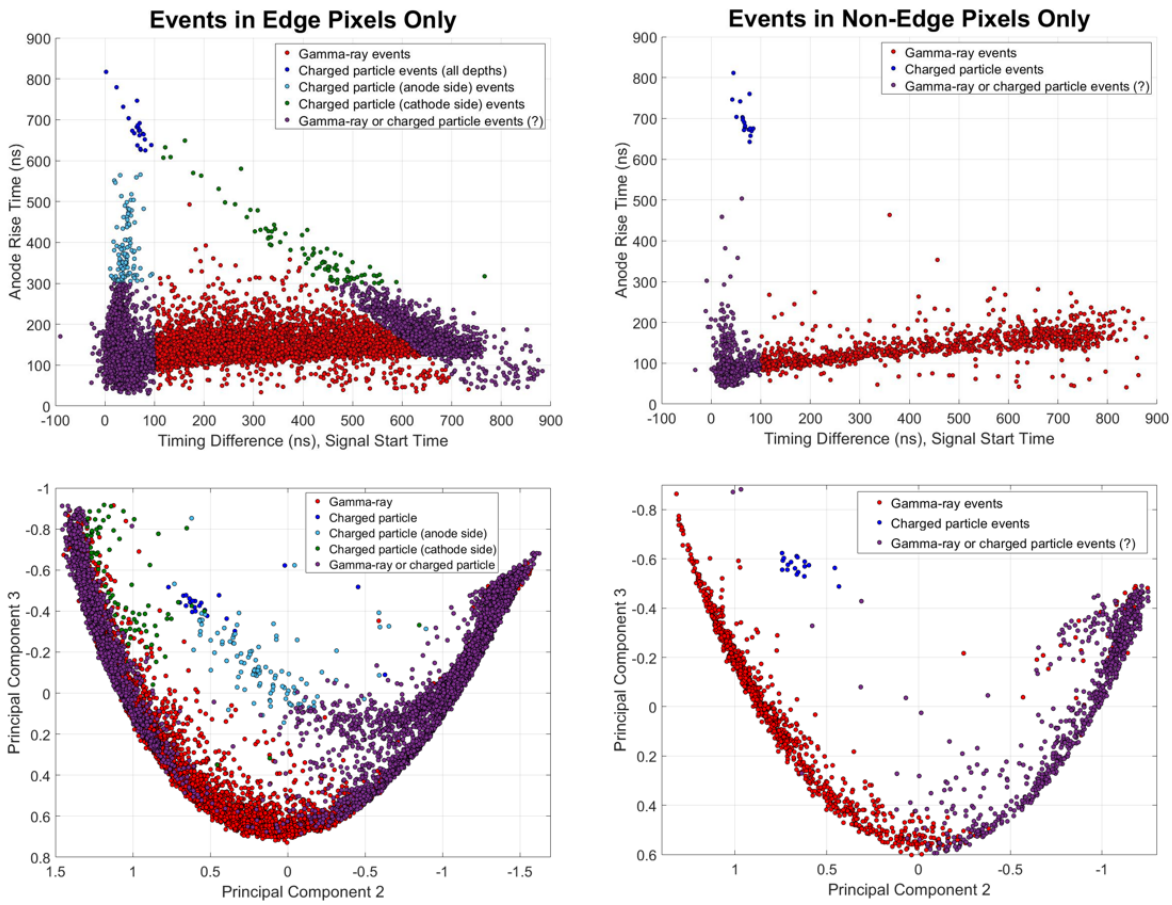

Figure 8.16: Comparison of conventional method #2 and PCA method for the single-pixel events (with anode amplitudes greater than roughly 1.8 MeV). The assigned colors and particle type were chosen based on the results for conventional method #2.

is especially helpful for saturated pulses, as inaccurate information is obtained with the conventional methods.

The limitation of using CZT for particle discrimination is that the electron cloud distributions cannot be reconstructed as well as it could be with a particle tracking detector. Waveforms provide some information due to the understanding of signal induction in the detector, but the reality is that other factors can affect pulse shapes too (e.g. detector non-uniformity and electronics) and this makes it more difficult to classify the events. The use of simulations to help choose thresholds for discrimination would be ideal to help optimize the particle discrimination and determine if the successful par-

ticle identification rate would be sufficient for practical applications. Also, the analysis discussed in this work needs to be extended to multi-pixel events.

8.3 Discussion on 5-or-more Pixel Events

Some additional analysis on 5-or-more pixel events was performed. During the balloon flight of Orion Eagle, there were many events triggering 5-or-more pixels (Fig. 8.17). Typically, these events are rare, but at high altitudes, past the bulk of the atmosphere, there is a greater flux of charged particles. Charge particles can trigger long tracks of multiple pixels depending on the incident angle and energy. For each 5-or-more pixel event, the vast majority of triggered anodes always had triggers in at least one neighboring pixel (0 value in Fig. 8.18). For gamma-ray events, there should be discrete locations of energy deposition rather than the continuous track created by charged particles. In principal, that would mean that most pixels triggered due to gamma-ray events will not have triggers in the neighbor pixels. However, at high-energies, more charge sharing occurs so this complicates the analysis.

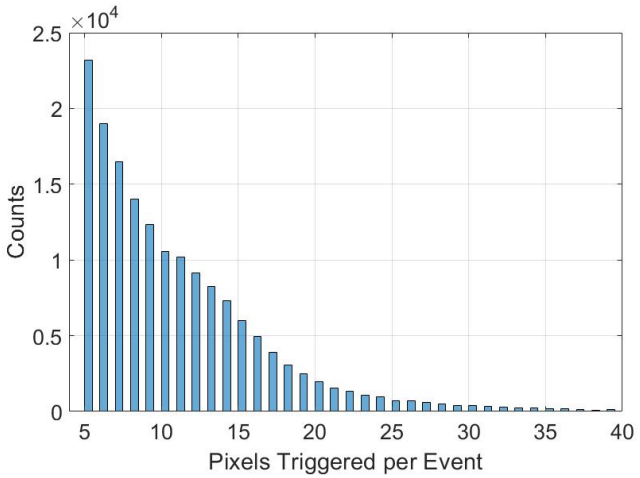

Figure 8.17: Number of pixels triggered per event for the 5-or-more pixel event data from the high-altitude balloon flight.

The electron cloud size was roughly estimated for the 5-or-more pixel event data (Fig. 8.19) based on the maximum distance between points in the estimated electron cloud. Subpixel sensing was not used, so the x, y location of points in the cloud cor-

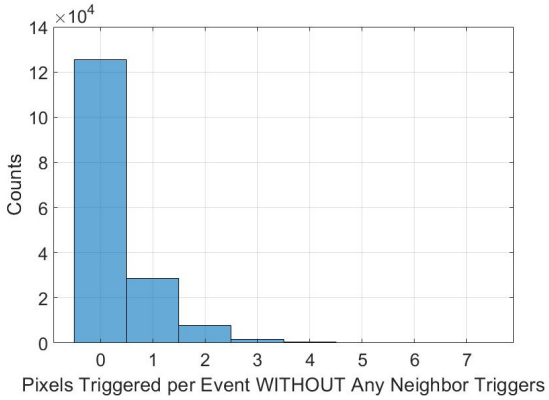

Figure 8.18: Number of pixels triggered in an event that did not have at least one trigger in a neighboring pixel. For a value of 0, every pixel triggered in an event had a trigger in a neighboring pixel.

responded to the coordinates of the center of the pixel trigger. Depth z was calculated using timing and converted to an approximate depth (anode/cathode side locations were estimated using the distribution of timing of events). This all was a rough estimation, but general trends can still be seen. In Fig. 8.19, events with smaller electron clouds are more likely to be gamma-ray events, whereas larger electron clouds are more likely charged particle events. At high energies, the size of electron clouds produced from gamma-ray interactions can span multiple pixels. Therefore, it may be useful to look at the electron cloud size as a function of energy deposited (Fig. 8.20). This could be compared to simulations to help guide gamma/charged particle discrimination (see Refs. [27] and [24] for simulation results up to 10 MeV and 3 MeV, respectively). Also, depending on the angle a charged particle passes through the detector, as few as 1 pixel could trigger. In this case, waveform analysis is helpful, as discussed in the previous section.

When assuming that the energy was deposited uniformly in each electron cloud, a rough estimate of dE/dx can be calculated (Fig. 8.21). The dE/dx could also be calculated on a finer scale since the energy is known at each 3D point (for example, see Ref. [84]). However, with the rough estimation, the results are on the right order of magnitude, and match the expected shape (similar to plots in Ref. [84]). At float, it was expected that the charged particles are mostly protons, and the average proton energy would be roughly 200 MeV. In CZT, for 200 MeV protons, the dE/dx is expected to

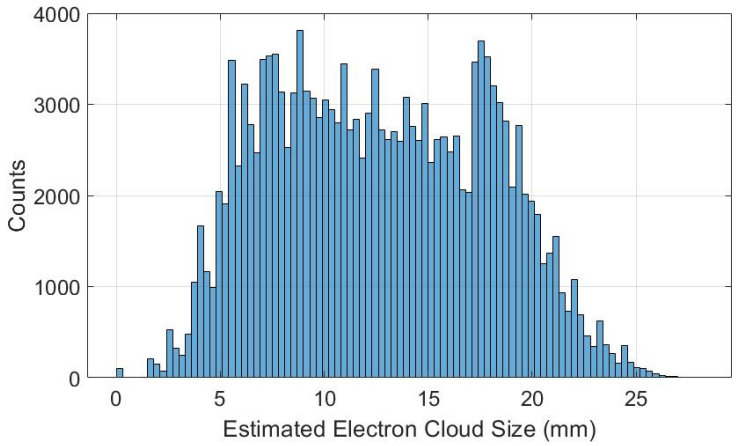

Figure 8.19: Distribution of the estimated electron cloud size.

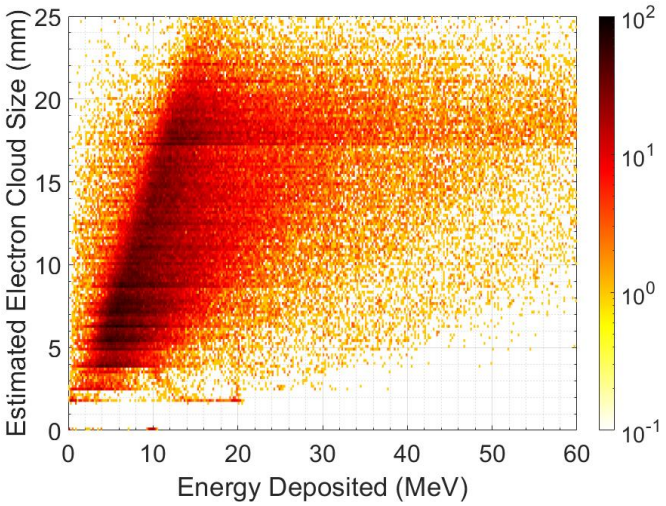

Figure 8.20: The estimated electron cloud size as a function of energy based on the 5-or-more pixel events from the balloon flight.

be ∼1.5 MeV/mm (calculated via SRIM). Fig. 8.21 shows a close match to this. The ADC to energy conversion was performed using the 511 keV peak which adds some uncertainty, as it is best to calibrate the energy with a similar type of source [1].

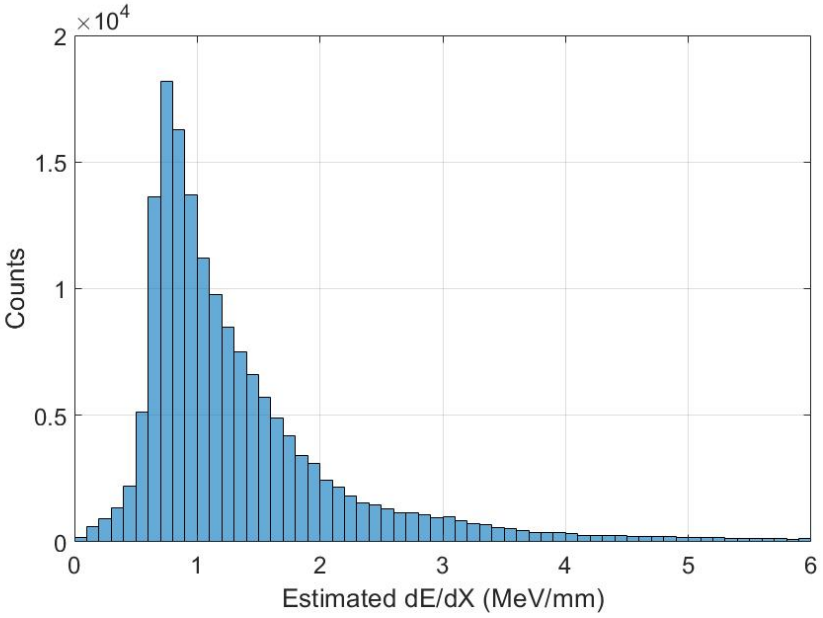

Figure 8.21: The distribution of approximate dE/dx values for the 5-or-more pixel events from the balloon flight.

Chapter 9

Conclusions

9.1 Summary

In this work, the effect of extreme environments on 3D CZT was studied in terms of temperature, neutron damage, and near-space.

Previous work looking at annealing of CZT without neutron damage was expanded on. Improvements in both CZT material properties and the electrode contacts were observed, and the largest improvement in depth-corrected energy resolution was 0.09% for a detector with heavy electron trapping. Annealing at 80°C can be beneficial for 5R-generation Redlen CZT detectors, especially if the detectors have issues related to trapping. For detectors with severe neutron damage (10^{12} n/cm^2 fluence), annealing improved the energy resolution from over 10% to below 1% FWHM at 662 keV. However, there was unexpected unstable performance over time under bias after annealing. Suggestions to deal with this issue are provided in Chapter 6.

To study the operation of 3D CZT at high temperatures, detectors were tested at ambient temperatures ranging from 20°C to 60°C. While leakage at room temperature was around ∼50 nA, it rose to over 1 μA at 60°C. High leakage increased electronic noise, leading to a degradation in energy resolution. At 60°C, depth-corrected energy resolution was ∼0.85% for the high-temperature Redlen CZT, ∼1% for the standard Redlen CZT, and just below 1.3% for the standard Kromek CZT. The sample size was small, so this does not necessarily represent the expected performance for all detectors from each vendor. The high leakage also led to a decrease in the effective applied bias, which caused slower drift of the electrons. Issues during high-temperature operation

were identified and remedies to help improve performance were suggested. For Kromek detectors, changes in electron de-trapping were observed.

At low temperature (-10°C), efficiency loss in four detectors was studied. There were at least two mechanisms of loss identified, both related to the internal electric field. The first mechanism was defocusing of the electric field that led to loss near the edges. The second was related to strong local variations in the electric field. Charge clouds were focused to "hotspot" subpixel locations, and in the process, lost a significant amount of charge, causing the event to fall outside the photopeak region or possibly below the low energy threshold in the worst case. At low temperature, high bias worsened efficiency loss, and low bias reduced efficiency loss.

A detector system with a single 2×2×1.5 cm^3 CZT detector was designed, built, and tested on a high-altitude balloon flight. The detector successfully operated in the near-space environment and measured atmospheric radiation (gamma rays and charged particles) throughout the flight. Charged particle discrimination techniques were explored using data from the balloon flight.

9.2 Significance and Future Work

In this work, energy resolution below 1% FWHM at 662 keV for single-pixel events could be achieved at 60°C; however, it would be desirable to reach below 1% for **all** events. Findings from the high-temperature experiments can help guide the development of detector systems that could meet such a specification. It was found that bulk leakage is the main contributor to leakage and that detector leakage was the main cause for the increase in noise at high temperatures. This indicates that CZT vendors need to devote efforts towards reducing the bulk leakage rather than the surface leakage. In the past, surface leakage was typically the dominant issue, so processing and handling of the surfaces was important. Now, development of blocking contacts may be needed. Even if leakage cannot be further reduced, there are still other ways to improve performance at high temperatures. As shown in this work, reducing the operating bias helps reduce leakage and improve energy resolution. Even lower biases and thorough optimization of digital signal processing and event reconstruction could potentially help further improve the energy resolution at 60°C. Additionally, the annealing experiments suggest that "pre-annealing" detectors at 80°C prior to operating above room temperature could help

improve the stability of the detector material and contacts as issues could be "annealed out" ahead of time.

Though an exact cause of the electric field issues at low temperatures (-10°C) could not be identified, possible ways to help reduce the efficiency loss can still be suggested based on this work (discussed in detail at the end of Chapter 5). If future experiments show that these techniques are able to consistently reduce efficiency loss at low temperatures, that would be a very significant contribution, as it would greatly improve the yield of CZT detectors that could be used for quantitative measurements over a wide range of temperatures (e.g. for use by IAEA inspectors).

For neutron damage, a new issue was observed: time under bias (after damage and annealing) led to a degradation in performance. These detectors were annealed several days at 80°C, and even after a year of annealing at room temperature, the problem still existed. It would be interesting to see if annealing at 80°C again but for a longer amount of time (i.e. weeks) could help resolve the issue. If not, this experiment would suggest that the fluence of 10^{12} n/cm^2 causes a form of permanent damage to the CZT that needs to be further understood. More neutron damage experiments with other CZT detectors would be needed to see if it is reproducible. Also of interest, is that the center of the Redlen detector performed better in this experiment and in previous unpublished work. Testing of a Kromek CZT detector did not show similar behavior, indicating the better performance in the center of Redlen CZT could actually be due to higher material quality. Informing Redlen of this could possibly lead to improvement in the material quality over a larger area, since they may be able to determine the step in their processes of making the CZT detector that improved the material quality of the center.

The successful flight of Orion Eagle, the greater understanding of temperature and radiation effects, and the exploration of charged particle discrimination techniques motivate the use of large-volume 3D CZT in space. The possible impacts of using CZT in space applications are quite large, as these detectors could contribute to discoveries in planetary science or MeV astrophysics, and also could be used for space-based nuclear detonation detection. It is very likely that the 3D CZT technology from the University of Michigan will make it into space in the near future [85].

Bibliography

[1] G. F. Knoll. *Radiation detection and measurement*. 3rd ed. New York: Wiley, 2000. 802 pp.

[2] W. Shockley. "Currents to Conductors Induced by a Moving Point Charge". In: *Journal of Applied Physics* 9.10 (Oct. 1, 1938), pp. 635–636. DOI: 10.1063/1.1710367.

[3] S. Ramo. "Currents Induced by Electron Motion". In: *Proceedings of the IRE* 27.9 (Sept. 1939), pp. 584–585. DOI: 10.1109/JRPROC.1939.228757.

[4] C. Jen. "On the Induced Current and Energy Balance in Electronics". In: *Proceedings of the IRE* 29.6 (June 1941), pp. 345–349. DOI: 10.1109/JRPROC.1941.230316.

[5] G. Cavalleri, E. Gatti, G. Fabri, and V. Svelto. "Extension of Ramo's theorem as applied to induced charge in semiconductor detectors". In: *Nuclear Instruments and Methods* 92.1 (Mar. 1, 1971), pp. 137–140. DOI: 10.1016/0029-554X(71)90235-7.

[6] Z. He. "Review of the Shockley–Ramo theorem and its application in semiconductor gamma-ray detectors". In: *Nuclear Instruments and Methods in Physics Research Section A: Accelerators, Spectrometers, Detectors and Associated Equipment* 463.1 (May 2001), pp. 250–267. DOI: 10.1016/S0168-9002(01)00223-6.

[7] D. S. McGregor, Z. He, H. A. Seifert, D. K. Wehe, and R. A. Rojeski. "Single charge carrier type sensing with a parallel strip pseudo-Frisch-grid CdZnTe semiconductor radiation detector". In: *Applied Physics Letters* 72.7 (Feb. 16, 1998), pp. 792–794. DOI: 10.1063/1.120895.

[8] A. E. Bolotnikov, K. Ackley, G. S. Camarda, C. Cherches, Y. Cui, G. De Geronimo, J. Fried, D. Hodges, A. Hossain, W. Lee, G. Mahler, M. Maritato, M. Petryk, U. Roy, C. Salwen, E. Vernon, G. Yang, and R. B. James. "An array of virtual Frisch-grid CdZnTe detectors and a front-end application-specific integrated circuit for large-area position-sensitive gamma-ray cameras". In: *Review of Scientific Instruments* 86.7 (July 28, 2015), p. 073114. DOI: 10.1063/1.4927455.

[9] P. N. Luke. "Single-polarity charge sensing in ionization detectors using coplanar electrodes". In: *Applied Physics Letters* 65.22 (Nov. 28, 1994), pp. 2884–2886. DOI: 10.1063/1.112523.

[10] P. Luke. “Unipolar charge sensing with coplanar electrodes-application to semiconductor detectors”. In: *IEEE Transactions on Nuclear Science* 42.4 (Aug. 1995), pp. 207–213. DOI: 10.1109/23.467848.

[11] Z. He, G. F. Knoll, D. K. Wehe, and J. Miyamoto. “Position-sensitive single carrier CdZnTe detectors”. In: *Nuclear Instruments and Methods in Physics Research Section A: Accelerators, Spectrometers, Detectors and Associated Equipment* 388.1 (Mar. 21, 1997), pp. 180–185. DOI: 10.1016/S0168-9002(97)00318-5.

[12] Z. He, W. Li, G. F. Knoll, D. K. Wehe, J. Berry, and C. M. Stahle. “3-D position sensitive CdZnTe gamma-ray spectrometers”. In: (1999).

[13] Y. Ma, S. Xiao, G. Yang, and L. Zhang. “Design and study of a coplanar grid array CdZnTe detector for improved spatial resolution”. In: *Applied Radiation and Isotopes* 94 (Dec. 1, 2014), pp. 314–318. DOI: 10.1016/j.apradiso.2014.09.003.

[14] H. Chen, S. A. Awadalla, R. Redden, G. Bindley, A. E. Bolotnikov, G. S. Camarda, G. Carini, and R. B. James. “High-Performance, Large-Volume THM CdZnTe Detectors for Medical Imaging and Homeland Security Applications”. In: *2006 IEEE Nuclear Science Symposium Conference Record*. 2006 IEEE Nuclear Science Symposium Conference Record. Vol. 6. Oct. 2006, pp. 3629–3637. DOI: 10.1109/NSSMIC.2006.353781.

[15] M. Streicher, S. Brown, Y. Zhu, D. Goodman, and Z. He. “Special Nuclear Material Characterization Using Digital 3-D Position Sensitive CdZnTe Detectors and High Purity Germanium Spectrometers”. In: *IEEE Transactions on Nuclear Science* 63.5 (Oct. 2016), pp. 2649–2656. DOI: 10.1109/TNS.2016.2593631.

[16] J. Xia, Y. Zhu, and Z. He. “Efficient temperature corrections for gamma-ray energy reconstruction in 3-D position-sensitive CdZnTe detectors”. In: *Nuclear Instruments and Methods in Physics Research Section A: Accelerators, Spectrometers, Detectors and Associated Equipment* 954 (Feb. 2020), p. 161340. DOI: 10.1016/j.nima.2018.10.018.

[17] Z. Chen. “Quantitative Measurement and Development of Back-end Processing System-on-Chip for the Pixelated CdZnTe Detector”. PhD thesis. University of Michigan, 2022. DOI: 10.7302/6886.

[18] M. Petryk. “Algorithms and Electronics for Processing Data from Pixelated Semiconductor Gamma-Ray Detectors”. PhD thesis. University of Michigan, 2023.

[19] Y. Zhu and Z. He. “Performance of Larger-Volume 40 × 40 × 10- and 40 × 40 × 15-mm^3 CdZnTe Detectors”. In: *IEEE Transactions on Nuclear Science* 68.2 (Feb. 2021), pp. 250–255. DOI: 10.1109/TNS.2021.3052133.

[20] J. Xia. “Interaction Reconstruction in Digital 3-D CdZnTe Under Various Circumstances”. PhD thesis. University of Michigan, 2019.

[21] W. Koehler. “Thallium Bromide as an Alternative Material for Room-Temperature Gamma-Ray Spectroscopy and Imaging”. PhD thesis. University of Michigan, 2016.

[22] S. P. O’Neal. “Advancements in TlBr for Gamma-Ray Detection and Imaging”. PhD thesis. University of Michigan, 2018.

[23] C. O. Leak. “Techniques for Pixelated Ambipolar-Sensitive Semiconductor Gamma-Ray Spectrometers”. PhD thesis. University of Michigan, 2021.

[24] Y. Zhu. “Digital Signal Processing Methods for Pixelated 3-D Position Sensitive Room-Temperature Semiconductor Detectors”. PhD thesis. University of Michigan, 2012.

[25] Y. Zhu, S. E. Anderson, and Z. He. “Sub-Pixel Position Sensing for Pixelated, 3-D Position Sensitive, Wide Band-Gap, Semiconductor, Gamma-Ray Detectors”. In: *IEEE Transactions on Nuclear Science* 58.3 (June 2011), pp. 1400–1409. DOI: 10.1109/TNS.2011.2132738.

[26] W. R. Kaye. “Energy and Position Reconstruction in Pixelated CdZnTe Detectors”. PhD thesis. University of Michigan, 2012.

[27] D. Shy. “Super-MeV Compton Imaging and 3D Gamma-Ray Imaging Using Pixelated CdZnTe”. PhD thesis. University of Michigan, 2020.

[28] B. Williams. “Applications of Principal Component Analysis for Position-Sensitive Semiconductor Detectors”. PhD thesis. University of Michigan, 2019.

[29] M. J. Myjak and C. E. Seifert. “Real-Time Compton Imaging for the Gamma-Tracker Handheld CdZnTe Detector”. In: *IEEE Transactions on Nuclear Science* 55.2 (Apr. 2008), pp. 769–777. DOI: 10.1109/TNS.2007.915008.

[30] S. Joshi. “Coded Aperture Imaging Applied to Pixelated CdZnTe Detectors”. PhD thesis. University of Michigan, 2014.

[31] S. T. Brown, D. Goodman, J. Chu, B. Williams, M. R. Williamson, and Z. He. “Time-Encoded Gamma-Ray Imaging Using a 3-D Position-Sensitive CdZnTe Detector Array”. In: *IEEE TRANSACTIONS ON NUCLEAR SCIENCE* 67.2 (2020).

[32] D. Shy, M. Petryk, Z. Chen, S. Thompson, and Z. He. “Time encoded imaging of extended gamma-ray sources in 3D using the OrionUM pixelated CdZnTe with subpixel estimation and depth of interaction corrections”. In: *Journal of Instrumentation* 16.3 (Mar. 8, 2021), P03013. DOI: 10.1088/1748-0221/16/03/P03013.

[33] D. Shy, J. Xia, and Z. He. “Artifacts in High-Energy Compton Imaging With 3-D Position-Sensitive CdZnTe”. In: *IEEE Transactions on Nuclear Science* 67.8 (Aug. 2020), pp. 1920–1928. DOI: 10.1109/TNS.2020.3005834.

[34] L. M. Bartlett, C. M. Stahle, P. K. Shu, L. M. Barbier, S. D. Barthelmy, N. A. Gehrels, J. F. Krizmanic, P. Kurczynski, D. M. Palmer, A. M. Parsons, B. J. Teegarden, and J. Tueller. "Radiation damage and activation of CdZnTe by intermediate energy neutrons". In: *Hard X-Ray/Gamma-Ray and Neutron Optics, Sensors, and Applications*. Hard X-Ray/Gamma-Ray and Neutron Optics, Sensors, and Applications. Vol. 2859. SPIE, July 19, 1996, pp. 10–16. DOI: 10.1117/12.245137.

[35] L. S. Varnell, W. A. Mahoney, E. L. Hull, J. F. Butler, and A. S. Wong. "Radiation effects in CdZnTe gamma-ray detectors produced by 199-MeV protons". In: 2806 (Oct. 1, 1996), pp. 424–431. DOI: 10.1117/12.254014.

[36] I. Kuvvetli, C. Budtz-Joergensen, U. Korsbech, and H. J. Jensen. "Radiation damage effects in CZT drift strip detectors". In: *X-Ray and Gamma-Ray Telescopes and Instruments for Astronomy*. X-Ray and Gamma-Ray Telescopes and Instruments for Astronomy. Vol. 4851. SPIE, Mar. 11, 2003, pp. 984–992. DOI: 10.1117/12.461293.

[37] Y. Eisen and A. Shor. "Fast Neutron Damage of a Pixelated CdZnTe Gamma Ray Spectrometer". In: *IEEE Transactions on Nuclear Science* 56.4 (Aug. 2009), pp. 1700–1705. DOI: 10.1109/TNS.2009.2020599.

[38] W. Murray, K. Krueger, M. Rawool-Sullivan, L. Ussery, and C. Whitley. "Temperature effects on CdZnTe detector performance". In: *1998 IEEE Nuclear Science Symposium Conference Record. 1998 IEEE Nuclear Science Symposium and Medical Imaging Conference (Cat. No.98CH36255)*. 1998 IEEE Nuclear Science Symposium Conference Record. 1998 IEEE Nuclear Science Symposium and Medical Imaging Conference (Cat. No.98CH36255). Vol. 1. Nov. 1998, 643–645 vol.1. DOI: 10.1109/NSSMIC.1998.775221.

[39] B. Sturm, Zhong He, T. Zurbuchen, and P. Koehn. "Investigation of the asymmetric characteristics and temperature effects of CdZnTe detectors". In: *IEEE Transactions on Nuclear Science* 52.5 (Oct. 2005), pp. 2068–2075. DOI: 10.1109/TNS.2005.856728.

[40] M. Amman, J. Lee, and P. Luke. "Temperature Study of CdZnTe Coplanar-Grid Detectors". In: *IEEE Transactions on Nuclear Science* 53.5 (Oct. 2006), pp. 3035–3040. DOI: 10.1109/TNS.2006.879909.

[41] B. W. Sturm. "GAMMA-RAY SPECTROSCOPY USING DEPTH-SENSING COPLANAR GRID CdZnTe SEMICONDUCTOR DETECTORS". PhD thesis. University of Michigan, 2007.

[42] I. Jung, H. Krawczynski, A. Burger, M. Guo, and M. Groza. "Detailed studies of pixelated CZT detectors grown with the modified horizontal Bridgman method". In: *Astroparticle Physics* 28.4 (Dec. 1, 2007), pp. 397–408. DOI: 10.1016/j.astropartphys.2007.08.004.

[43] D. S. Bale, S. A. Soldner, and C. Szeles. "A mechanism for dynamic lateral polarization in CdZnTe under high flux x-ray irradiation". In: *Applied Physics Letters* 92.8 (Feb. 25, 2008), p. 082101. DOI: 10.1063/1.2883924.

[44] A. E. Bolotnikov, G. S. Camarda, Y. Cui, A. Hossain, G. Yang, H. W. Yao, and R. B. James. "Internal Electric-Field-Lines Distribution in CdZnTe Detectors Measured Using X-Ray Mapping". In: *IEEE Transactions on Nuclear Science* 56.3 (June 2009), pp. 791–794. DOI: 10.1109/TNS.2008.2007904.

[45] G. Yang, A. E. Bolotnikov, G. S. Camarda, Y. Cui, A. Hossain, K. Kim, and R. B. James. "Electric field distribution of cadmium zinc telluride (CZT) detectors". In: SPIE Optical Engineering + Applications. Ed. by R. B. James, L. A. Franks, and A. Burger. San Diego, CA, Aug. 20, 2009, p. 74490C. DOI: 10.1117/12.826909.

[46] H. W. Yao, R. B. James, E. Lee, R. Olsen, H. Hermon, and R. Anderson. "Optical studies of the internal electric field distributions, crystal defects, and detector performance of CdZnTe radiation detectors". In: *Proceedings of SPIE 3446, Hard X-Ray and Gamma-Ray Detector Physics and Applications,* SPIE's International Symposium on Optical Science, Engineering, and Instrumentation. San Diego, CA, United States, July 1, 1998. DOI: doi:10.1117/12.312889.

[47] N. Sadeghi. "The Effect of Crystal Defects on the Performance of High-flux CZT X-ray Detectors". PhD thesis. University of Tehran, 2012.

[48] M. C. Veale, P. Booker, S. Cross, M. D. Hart, L. Jowitt, J. Lipp, A. Schneider, P. Seller, R. M. Wheater, M. D. Wilson, C. C. T. Hansson, K. Iniewski, P. Marthandam, and G. Prekas. "Characterization of the Uniformity of High-Flux CdZnTe Material". In: *Sensors* 20.10 (May 12, 2020), p. 2747. DOI: 10.3390/s20102747.

[49] W. Chen, R. Guo, Y. Tong, L. Liu, S. Zhou, and J. Lin. "Influence of grain boundary on electric field distribution in CdZnTe crystal". In: *Ninth Symposium on Novel Photoelectronic Detection Technology and Applications*. Ninth Symposium on Novel Photoelectronic Detection Technology and Applications. Vol. 12617. SPIE, Apr. 4, 2023, pp. 244–249. DOI: 10.1117/12.2663350.

[50] D. Goodman. "Passive Characterization of Unknown Spaces Using Large-Volume Pixelated CdZnTe". PhD thesis. University of Michigan, 2019.

[51] M. W. Streicher. "Applications of Digitized 3-D Position-Sensitive CdZnTe Spectrometers for National Security and Nuclear Nonproliferation". PhD thesis. University of Michigan, 2017.

[52] D. J. Lawrence, W. C. Feldman, B. L. Barraclough, A. B. Binder, R. C. Elphic, S. Maurice, and D. R. Thomsen. "Global Elemental Maps of the Moon: The Lunar Prospector Gamma-Ray Spectrometer". In: *Science* 281.5382 (Sept. 4, 1998), pp. 1484–1489. DOI: 10.1126/science.281.5382.1484.

[53] L. G. Evans, R. C. Reedy, R. D. Starr, K. E. Kerry, and W. V. Boynton. "Analysis of gamma ray spectra measured by Mars Odyssey". In: *Journal of Geophysical Research: Planets* 111 (E3 2006). DOI: 10.1029/2005JE002657.

[54] L. G. Evans, P. N. Peplowski, E. A. Rhodes, D. J. Lawrence, T. J. McCoy, L. R. Nittler, S. C. Solomon, A. L. Sprague, K. R. Stockstill-Cahill, R. D. Starr, S. Z. Weider, W. V. Boynton, D. K. Hamara, and J. O. Goldsten. "Major-element abundances on the surface of Mercury: Results from the MESSENGER Gamma-Ray Spectrometer". In: *Journal of Geophysical Research: Planets* 117 (E12 2012). DOI: 10.1029/2012JE004178.

[55] Y. A. Surkov, F. F. Kirnozov, V. N. Glazov, A. G. Dunchenko, L. P. Tatsy, and O. P. Sobornov. "Uranium, thorium, and potassium in the Venusian rocks at the landing sites of Vega 1 and 2". In: *Journal of Geophysical Research: Solid Earth* 92 (B4 1987), E537–E540. DOI: 10.1029/JB092iB04p0E537.

[56] P. N. Peplowski, D. Bazell, L. G. Evans, J. O. Goldsten, D. J. Lawrence, and L. R. Nittler. "Hydrogen and major element concentrations on 433 Eros: Evidence for an L- or LL-chondrite-like surface composition". In: *Meteoritics & Planetary Science* 50.3 (2015), pp. 353–367. DOI: 10.1111/maps.12434.

[57] T. H. Prettyman, N. Yamashita, M. J. Toplis, H. Y. McSween, N. Schörghofer, S. Marchi, W. C. Feldman, J. Castillo-Rogez, O. Forni, D. J. Lawrence, E. Ammannito, B. L. Ehlmann, H. G. Sizemore, S. P. Joy, C. A. Polanskey, M. D. Rayman, C. A. Raymond, and C. T. Russell. "Extensive water ice within Ceres' aqueously altered regolith: Evidence from nuclear spectroscopy". In: *Science* 355.6320 (Jan. 6, 2017), pp. 55–59. DOI: 10.1126/science.aah6765.

[58] T. H. Prettyman, D. W. Mittlefehldt, N. Yamashita, D. J. Lawrence, A. W. Beck, W. C. Feldman, T. J. McCoy, H. Y. McSween, M. J. Toplis, T. N. Titus, P. Tricarico, R. C. Reedy, J. S. Hendricks, O. Forni, L. Le Corre, J.-Y. Li, H. Mizzon, V. Reddy, C. A. Raymond, and C. T. Russell. "Elemental Mapping by Dawn Reveals Exogenic H in Vesta's Regolith". In: *Science* 338.6104 (Oct. 12, 2012), pp. 242–246. DOI: 10.1126/science.1225354.

[59] W. Boynton, W. Feldman, I. Mitrofanov, L. Evans, R. Reedy, S. Squyres, R. Starr, J. Trombka, C. d'Uston, J. Arnold, P. Englert, A. Metzger, H. Wänke, J. Brückner, D. Drake, C. Shinohara, C. Fellows, D. Hamara, K. Harshman, K. Kerry, C. Turner, M. Ward, H. Barthe, K. Fuller, S. Storms, G. Thornton, J. Longmire, M. Litvak, and A. Ton'chev. "The Mars Odyssey Gamma-Ray Spectrometer Instrument Suite". In: *Space Science Reviews* 110.1 (Jan. 1, 2004), pp. 37–83. DOI: 10.1023/B:SPAC.0000021007.76126.15.

[60] J. Roques, S. Schanne, A. Von Kienlin, J. Knödlseder, R. Briet, L. Bouchet, P. Paul, S. Boggs, P. Caraveo, M. Cassé, B. Cordier, R. Diehl, P. Durouchoux, P. Jean, P. Leleux, G. Lichti, P. Mandrou, J. Matteson, F. Sanchez, V. Schönfelder,

G. Skinner, A. Strong, B. Teegarden, G. Vedrenne, P. Von Ballmoos, and C. Wunderer. "SPI/INTEGRAL in-flight performance". In: *Astronomy and Astrophysics* 411.1 (2003), pp. L91–L100. DOI: 10.1051/0004-6361:20031501.

[61] D. Smith, R. Lin, P. Turin, D. Curtis, J. Primbsch, R. Campbell, R. Abiad, P. Schroeder, C. Cork, E. Hull, D. Landis, N. Madden, D. Malone, R. Pehl, T. Raudorf, P. Sangsingkeow, R. Boyle, I. Banks, K. Shirey, and R. Schwartz. "The RHESSI Spectrometer". In: *Solar Physics* 210.1 (Nov. 1, 2002), pp. 33–60. DOI: 10.1023/A:1022400716414.

[62] J. Goldsten, E. Rhodes, W. Boynton, W. Feldman, D. Lawrence, J. Trombka, D. Smith, L. Evans, J. White, N. Madden, P. Berg, G. Murphy, R. Gurnee, K. Strohbehn, B. Williams, E. Schaefer, C. Monaco, C. Cork, J. Del Eckels, W. Miller, M. Burks, L. Hagler, S. Deteresa, and M. Witte. "The MESSENGER gamma-ray and neutron spectrometer". In: *Space Science Reviews* 131.1 (2007), pp. 339–391. DOI: 10.1007/s11214-007-9262-7.

[63] S. R. Hirshorn, L. D. Voss, and L. K. Bromley. *NASA Systems Engineering Handbook*. Feb. 17, 2017.

[64] S. D. Barthelmy, L. M. Barbier, J. R. Cummings, E. E. Fenimore, N. Gehrels, D. Hullinger, H. A. Krimm, C. B. Markwardt, D. M. Palmer, A. Parsons, G. Sato, M. Suzuki, T. Takahashi, M. Tashiro, and J. Tueller. "The Burst Alert Telescope (BAT) on the SWIFT Midex Mission". In: *Space Science Reviews* 120.3 (Oct. 1, 2005), pp. 143–164. DOI: 10.1007/s11214-005-5096-3.

[65] V. Bhalerao, D. Bhattacharya, A. Vibhute, P. Pawar, A. R. Rao, M. K. Hingar, R. Khanna, A. P. K. Kutty, J. P. Malkar, M. H. Patil, Y. K. Arora, S. Sinha, P. Priya, E. Samuel, S. Sreekumar, P. Vinod, N. P. S. Mithun, S. V. Vadawale, N. Vagshette, K. H. Navalgund, K. S. Sarma, R. Pandiyan, S. Seetha, and K. Subbarao. "The Cadmium Zinc Telluride Imager on AstroSat". In: *Journal of Astrophysics and Astronomy* 38.2 (June 2017), p. 31. DOI: 10.1007/s12036-017-9447-8.

[66] F. A. Harrison, W. W. Craig, F. E. Christensen, C. J. Hailey, W. W. Zhang, S. E. Boggs, D. Stern, W. R. Cook, K. Forster, P. Giommi, B. W. Grefenstette, Y. Kim, T. Kitaguchi, J. E. Koglin, K. K. Madsen, P. H. Mao, H. Miyasaka, K. Mori, M. Perri, M. J. Pivovaroff, S. Puccetti, V. R. Rana, N. J. Westergaard, J. Willis, A. Zoglauer, H. An, M. Bachetti, N. M. Barrière, E. C. Bellm, V. Bhalerao, N. F. Brejnholt, F. Fuerst, C. C. Liebe, C. B. Markwardt, M. Nynka, J. K. Vogel, D. J. Walton, D. R. Wik, D. M. Alexander, L. R. Cominsky, A. E. Hornschemeier, A. Hornstrup, V. M. Kaspi, G. M. Madejski, G. Matt, S. Molendi, D. M. Smith, J. A. Tomsick, M. Ajello, D. R. Ballantyne, M. Baloković, D. Barret, F. E. Bauer, R. D. Blandford, W. N. Brandt, L. W. Brenneman, J. Chiang, D. Chakrabarty, J. Chenevez, A. Comastri, F. Dufour, M. Elvis, A. C. Fabian, D. Farrah, C. L. Fryer, E. V. Gotthelf, J. E. Grindlay, D. J. Helfand, R. Krivonos, D. L. Meier,

J. M. Miller, L. Natalucci, P. Ogle, E. O. Ofek, A. Ptak, S. P. Reynolds, J. R. Rigby, G. Tagliaferri, S. E. Thorsett, E. Treister, and C. M. Urry. "THE NUCLEAR SPECTROSCOPIC ESCOPE ARRAY (NuSTAR) HIGH-ENERGY X-RAY MISSION". In: *The Astrophysical Journal* 770.2 (May 2013), p. 103. DOI: 10.1088/0004-637X/770/2/103.

[67] A. Moiseev. "New Mission Concept: Galactic Explorer with a Coded Aperture Mask Compton Telescope (GECCO)". In: 43 (Jan. 1, 2021), p. 1372.

[68] F. Paschen. "Ueber die zum Funkenübergang in Luft, Wasserstoff und Kohlensäure bei verschiedenen Drucken erforderliche Potentialdifferenz". In: *Annalen der Physik* 273.5 (1889), pp. 69–96. DOI: 10.1002/andp.18892730505.

[69] S. F. Nowicki, Z. He, Y. Zhu, A. M. Parsons, T. H. Prettyman, S. A. Storms, and S. A. Wender. "Ambient-Temperature Imaging Gamma-Ray Spectrometer (TIGRS) for High-Sensitivity Planetary Elemental Mapping". In: Lunar and Planetary Science Conference. Mar. 1, 2021, p. 1702.

[70] Z. Chen, Y. Zhu, and Z. He. "Intrinsic photopeak efficiency measurement and simulation for pixelated CdZnTe detector". In: *Nuclear Instruments and Methods in Physics Research Section A: Accelerators, Spectrometers, Detectors and Associated Equipment* 980 (Nov. 2020), p. 164501. DOI: 10.1016/j.nima.2020.164501.

[71] H. V. Neher. "Cosmic-ray particles that changed from 1954 to 1958 to 1965". In: *Journal of Geophysical Research (1896-1977)* 72.5 (1967), pp. 1527–1539. DOI: 10.1029/JZ072i005p01527.

[72] C. J. Mertens, G. P. Gronoff, R. B. Norman, B. M. Hayes, T. C. Lusby, T. Straume, W. K. Tobiska, A. Hands, K. Ryden, E. Benton, S. Wiley, B. Gersey, R. Wilkins, and X. Xu. "Cosmic radiation dose measurements from the RaD-X flight campaign". In: *Space Weather* 14.10 (2016), pp. 874–898. DOI: 10.1002/2016SW001407.

[73] M. Julien, J. M. Ryan, P. F. Bloser, J. S. Legere, C. M. Bancroft, M. L. McConnell, R. M. Kippen, and S. Tornga. "Balloon flight results of a FAst compton telescope (FAC)". In: *2012 IEEE Nuclear Science Symposium and Medical Imaging Conference Record (NSS/MIC)*. 2012 IEEE Nuclear Science Symposium and Medical Imaging Conference Record (NSS/MIC). Oct. 2012, pp. 1893–1900. DOI: 10.1109/NSSMIC.2012.6551439.

[74] F. Lei, S. Clucas, C. Dyer, and P. Truscott. "An atmospheric radiation model based on response matrices generated by detailed Monte Carlo Simulations of cosmic ray interactions". In: *IEEE Transactions on Nuclear Science* 51.6 (Dec. 2004), pp. 3442–3451. DOI: 10.1109/TNS.2004.839131.

[75] E. Regener and G. Pfotzer. "Vertical Intensity of Cosmic Rays by Threefold Coincidences in the Stratosphere". In: *Nature* 136.3444 (Nov. 1935), pp. 718–719. DOI: 10.1038/136718a0.

[76] J. D. Bowen, M. E. Bandstra, S. E. Boggs, A. Zoglauer, C. B. Wunderer, M. S. Amman, and P. N. Luke. "Depth dependent background measurements with NCT". In: *2007 IEEE Nuclear Science Symposium Conference Record*. 2007 IEEE Nuclear Science Symposium Conference Record. Vol. 1. Oct. 2007, pp. 436–444. DOI: 10.1109/NSSMIC.2007.4436364.

[77] C. A. Kierans, S. E. Boggs, A. Zoglauer, A. W. Lowell, C. Sleator, J. Beechert, T. J. Brandt, P. Jean, H. Lazar, J. Roberts, T. Siegert, J. A. Tomsick, and P. v. Ballmoos. "Detection of the 511 keV Galactic Positron Annihilation Line with COSI". In: *The Astrophysical Journal* 895.1 (May 2020), p. 44. DOI: 10.3847/1538-4357/ab89a9.

[78] A. Akyüz, D. Bhattacharya, K. W. Chuang, D. D. Dixon, T. J. O'Neill, O. T. Tümer, R. S. White, and A. D. Zych. "Atmospheric gamma rays at geomagnetic latitudes of −29° and +43°". In: *Journal of Geophysical Research: Space Physics* 102 (A8 1997), pp. 17359–17364. DOI: 10.1029/97JA01147.

[79] A. Bolotnikov, G. Carini, M. Chekhlov, A. Dellapenna, J. Fried, J. Haupt, S. Herrmann, I. Kotov, D. Medvedev, A. Moiseev, G. Pinaroli, A. Rusek, M. Sasaki, M. Sivertz, L. Smith, and E. Yates. "Radiation effects induced by the energetic protons in 8x8x32 mm3 CdZnTe detectors". In: *Nuclear Instruments and Methods in Physics Research Section A: Accelerators, Spectrometers, Detectors and Associated Equipment* 1039 (Sept. 2022), p. 166927. DOI: 10.1016/j.nima.2022.166927.

[80] D. Xu. "GAMMA-RAY IMAGING AND POLARIZATION MEASUREMENT USING 3-D POSITION-SENSITIVE CdZnTe DETECTORS". PhD thesis. University of Michigan, 2006.

[81] W. Kaye, F. Zhang, Y. A. Boucher, W. Wang, J. C. Kim, Y. Zhu, and Z. He. "Event classification in 3D position sensitive pixelated CdZnTe detectors". In: *2011 IEEE Nuclear Science Symposium Conference Record*. 2011 IEEE Nuclear Science Symposium Conference Record. Oct. 2011, pp. 4756–4760. DOI: 10.1109/NSSMIC.2011.6154709.

[82] J. McEnery, E. Ferrara, E. Hays, J. Mitchell, A. Moiseev, R. Ojha, J. Racusin, A. Smith, D. J. Thompson, M. Ajello, D. Hartmann, R. Johnson, V. Connaughton, J. E. Grove, R. Woolf, E. Wulf, L. Baldini, N. Omodei, and M. Hui. "Allsky Medium Energy GammaRay Observatory (AMEGO): A MediumEnergy Gamma-ray Surveyor". In: *Astro2020 APC White Paper* (2019).

[83] G. Lucchetta, M. Ackermann, D. Berge, and R. Bühler. *Introducing the MeVCube concept: a CubeSat for MeV observations*. Apr. 4, 2022.

[84] M. Kroupa, A. A. Bahadori, T. Campbell-Ricketts, S. P. George, and C. Zeitlin. "Kinetic energy reconstruction with a single layer particle telescope". In: *Applied Physics Letters* 112.13 (Mar. 26, 2018), p. 134103. DOI: 10.1063/1.5024920.

[85] D. Shy. “The cadmium zinc TElluride Radiation Imager (TERI): An Instrument to Space Qualify Large-Volume Pixelated CdZnTe”. Ann Arbor, MI, May 20, 2023.